EXPERIMENTAL ANALYSIS OF CO_2-DILUTED GAS FLAMES FOR CARBON CAPTURE

By:

Eirini Karagianni

A thesis submitted in partial fulfilment of the requirements for the degree of

Doctor of Philosophy

The University of Sheffield

Faculty of Engineering

Department of Mechanical Engineering

June 2017

Acknowledgements

Abstract

Current extreme weather events are evidence of the global climate change and its effects on the environment. Although natural gas is a "greener" fuel compared to solid fuels, its continuous uncontrolled use will increase further the atmospheric CO_2 emissions above sustainable levels. Natural gas fired power plants equipped with a carbon capture plant can serve as a short, and medium, term solution to mitigate global warming.

Several research studies have shown that post-combustion capture technology is a readily available option to reduce drastically the CO_2 emissions. However, its associated energy demand for separating CO_2 from the other exhaust gases is high and needs to be reduced. Therefore, recirculating part of the exhaust gases to the inlet of gas turbine combustors increases significantly the exit CO_2 concentration which is the driving force of the capture plant. This fundamental study focuses on the implications of the addition of CO_2 on fuel-lean natural gas non-premixed flames. The thermal and chemical effects of adding CO_2 in the air stream on the flame chemistry, properties, stability and the formation of pollutant emissions represent the main aim of the present study.

Two experimental campaigns were performed in this study and in-flame, post-flame and exit measurements of major and minor combustion species and the flame temperature are performed utilising an in-house built combustion chamber. Experimental results concluded that CO_2 has a considerable impact on the combustion process even at relatively low dilution levels. However, the effects of the dilution can be controlled in a beneficial way for the efficiency of the combustion systems.

Furthermore, the assessment of the performance of a 1D numerical model on predicting the implications of the addition of CO_2 on the flame chemistry was part of this study. The numerical results concluded that robust complex combustion models are needed to examine CO_2-diluted combustion systems and it is evident that detailed chemical reaction mechanisms are as necessary as the inclusion of the interaction between turbulence and chemistry.

Table of Contents

List of Figures

List of Tables

Nomenclature

Roman Letters

a_s Strain Rate (s^{-1})

c_{pi} Specific Heat Capacity of Species i at Constant Pressure (J/ kg K)

C_p Heat Capacity at Constant Pressure (J/K)

d Characteristic Length or Distance (m)

D Diameter (m)

Da Damköhler Number (-)

D_i Diffusion Coefficient (m^2/s)

D_T Thermal Coefficient (W/m^2 K)

E_A Activation Energy (kJ/mol)

$EINO_x$ Emission Index of NO_x Emissions (g/kg)

E_{total} Total Error (-)

h Enthalpy (J)

$j_{i\alpha}$ Molecular Diffusion Flux of Species (mol/ m^2 s)

Le_i Lewis number (-)

$M\alpha$ Mach Number (-)

MW Molecular Weight (g/mol)

P Pressure (atm)

q_R Radiative Heat Flux (W/m^2)

$\dot{Q}_{cat}$ Rate of Heat Transfer due to Surface-induced Catalytic Reactions(W)

$\dot{Q}_{conv}$ Rate of Convection Heat Transfer (W)

$\dot{Q}_{rad}$ Rate of Radiative Heat Transfer (W)

$\dot{Q}_{cond}$ Rate of Conduction Heat Transfer (W)

Re   Reynolds Number (-)

T_{TC} Measured Thermocouple Temperature (K)

u_α Component of Velocity Vector (m/s)

U   Velocity (m/s)

V   Volume (m^3)

x_α Spatial Coordinate (-)

x_{NO_x} Mole Fraction of NO_x Emissions (-)

Y or Y_i Mass Fraction of Species (-)

$Y_{c,j}$ Mass Fraction of the Carbon Atoms in the Fuel Jet Stream (-)

Z   Mixture Fraction (-)

Z_{st} Stoichiometric Mixture Fraction (-)

Greek Letters

β Beta-standard for Calibration Gases

ΔT_{rad} Temperature Radiation Correction (K)

ε Emissivity (-)

λ Thermal Conductivity (W/m K)

η Dynamic Viscosity (kg/m s)

ν' Stoichiometric Coefficient (-)

ν Speed of Sound (m/s)

ρ Density (kg/m^3)

σ   Stefan-Boltzmann Constant (5.67 10^{-8} W/ m^2 K^4)

τ_D Characteristic Diffusion Time Scale (s)

τ_C Characteristic Chemical Time Scale (s)

Φ   Equivalence Ratio (-)

χ_{st} Scalar Dissipation (s^{-1})

$\dot{\omega}_i$ Net Mass Chemical Reaction Rate of Species (kg/ m^3 s)

Abbreviations

CAD	Computer-Aided Design
CARS	Coherent Anti-Stokes Raman Spectroscopy
CCGT	Combined Cycle Gas Turbine
CCS	Carbon Capture and Storage
CFD	Computational Fluid Dynamics
CRZ	Central Recirculation Zone
EGR	Exhaust Gas Recirculation
EI	Emission Index
EOR	Enhanced Oil Recovery
FID	Flame Ionisation Detection Analyser
FLA	Flamelet Model
FSD	Full Scale Deflection
FTIR	Fourier Transform Infrared
GHG	Greenhouse Gases
GT	Gas Turbine
HMDSO	Hexamethyldisiloxane
LabView	Laboratory Virtual Instrument Engineering Workbench
LIF	Laser-Induced Fluorescence
LNG	Liquefied Natural Gas
NGCC	Natural Gas Combined Cycle
OPPDIF	Opposed-Flow Diffusion Flames Code
ORZ	Outer Recirculation Zone

PID   Proportional, Integral, Derivative

PCC   Post-combustion Capture

PTFE   Polytetrafluoroethylene

TC   Thermocouple

THC   Total Hydrocarbons

UHC   Unburnt Hydrocarbons

UV   Ultraviolet Light

CHAPTER 1- Introduction

1.1 Climate Change and World Energy Review

The rise in global population, human activities and living standards has resulted in the expansion of the world economy and the rapid growth of the world energy demand. The energy consumption will increase by 34 % between 2014 and 2035 (BP Energy Outlook, 2016). As at the same time renewables are taking up a bigger share in the energy mixture to meet the increasing energy demands (from 3 % to 9 % in 2035), so too is the consumption of fossil fuels to avoid any serious disruption to the global economy. In 2014, 86 % of the total energy needs were covered by burning fossil fuels but the predictions for 2035 show that the share of fossil fuels will be about 80 % (BP Energy Outlook, 2016). This indicates the reduced future dependency on fossil fuels but they still continue to be the dominant source of energy. The benefit is that the composition of the fuel mixture will change significantly in the future as coal usage will drop and renewables will gain more space. Natural gas becomes the fastest growing fossil fuel and the second largest fuel source due to the growth of the supply of shale gas and liquefied natural gas (LNG), its flexibility as a fuel and its lower emissions than other fossil fuels. Figure 1-1 illustrates these aforementioned facts regarding the change in the fuel mixture and the annual fuel demand growth.

More than half of the predicted global energy demand originates from the power sector, thus resulting in the immediate need for taking actions to decarbonise the emissions from burning fossil fuels. By 2035, energy-related emissions are projected to increase from 31.2 Gt in 2011 to 37.2 Gt; a total increase of 20 % (IEA World Energy Outlook, 2013). This figure is in contrast to the necessity of limiting global warming, which is observed by the gradual increase in the global mean surface temperature. The increase in the overall temperature of the Earth's atmosphere, along with changes in the frequency or intensity of rainfall and heat waves, ocean and land ice loss and sea level rise are evidence of the real problem of climate change (IPCC, 2013). Further careless increase in the emissions of greenhouse gases (GHG), such as carbon dioxide, CO_2, methane, CH_4, and nitrous oxide, N_2O, will cause additional warming and changes in the climate system. Their atmospheric concentration has increased enormously in the last 800,000 years and in fact CO_2, mainly from burning fossil fuels, has increased by 40 % compared to the pre-industrial levels (IPCC, 2013).

The combustion of fossil fuels produces mainly CO_2, carbon monoxide, CO, nitrogen oxides, NO_x, sulphur dioxide, SO_2, and soot particles, which are all more or less related to the pollution of the atmosphere. However, serious concern is focused on CO_2 as it has been identified as one of the main pollutant species and its reduction from large point sources, such as fossil-fuelled power plants, would be of vital importance in meeting the internationally agreed target of keeping the average temperature rise below 2 ^{o}C with respect to pre-industrial levels.
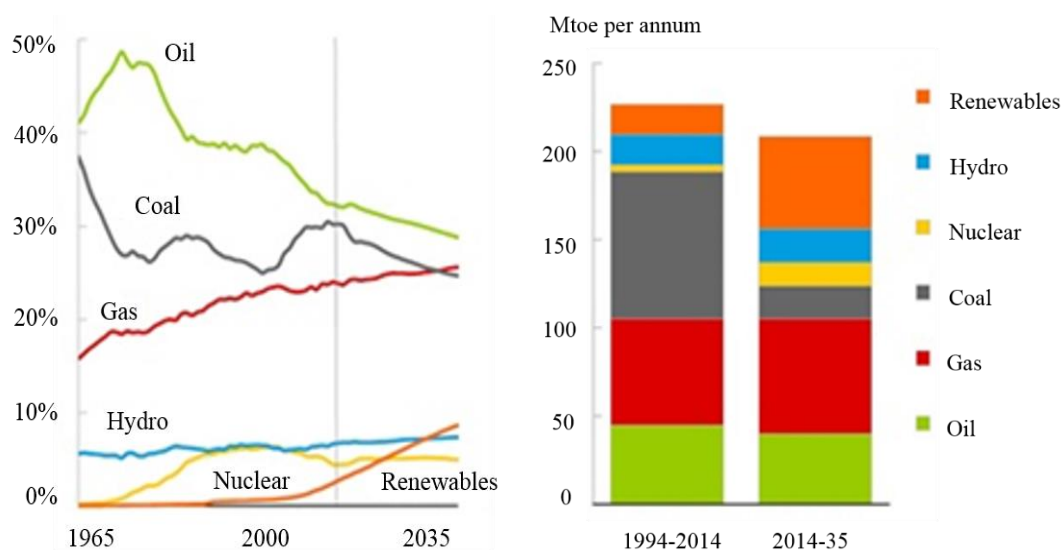
Figure 1-1 Fuel source shares in energy demand (left) and fuel annual growth by different fuel source (right) as reported in BP Energy Outlook (2016).

In order to eliminate the CO_2 emissions from the power sector, which is currently responsible for more than two-thirds of the global GHG emissions, decarbonisation measures must be put into force (IEA World Energy Outlook, 2013). Mitigation of climate change means improving the efficiency of the energy systems, the shift from dirty fossil fuels, e.g. coal, to less carbon intensive fuels, e.g. gas, and the investment and growth of renewables and nuclear energy. However, the technique that could possibly achieve large reductions in the short term is trapping the CO_2 produced by power generation and other heavy industries and storing it in deep geological formations.

1.2   Carbon Capture and Storage (CCS)

In order to have a realistic chance to meet the 2 ^{o}C temperature limit target, the CO_2 emissions from power plants, especially coal-fired ones, must fall drastically by 2050. On one hand, coal is cheap and plentiful and gas prices have not yet stabilised and on

the other hand, gas-fired plants are cleaner but still produce a lot of CO$_2$. Nevertheless, the need to meet the continuously increasing energy demand is urgent due to population and economy growth. Therefore, the present situation allows for implementing carbon capture into the existing, and any new, power plants as a short-term solution. Carbon capture and storage technology (CCS) can act as a reliable solution for energy supply and promises long-term stabilisation of the CO$_2$ concentration in the atmosphere, thus avoiding the potential harmful consequences of global warming. It is the only currently available technique that allows very deep cuts on the CO$_2$ emissions of the largest emitters, the power generation industry and heavy industries, such as cement, iron and steel plants, and refineries.

The implementation stage of CCS at a commercial level is at an early stage yet as only one power plant equipped with CCS is currently in operation worldwide, the SaskPower's Boundary Dam project in Canada. There are some important barriers keeping the global CCS development behind; incentives for selling the captured CO$_2$ are missing, lack of funds for demonstration projects and the high imposed cost of the capture plant. The incentive of carbon capture is the profit from selling the captured CO$_2$ usually to oil companies for enhancing the oil recovery process (EOR) but usually this is not feasible as existing power plants are located far from storage sites or transportation infrastructure is at an early stage. Both the CCS retrofit cost and the energy penalty imposed on the power plant are holding the future of CCS development behind. The reduction in the final energy output of the power plant equipped with CCS as resulted from the highly energy demanding processes of the CCS full chain stages is a challenging obstacle. The full CCS chain comprises of the capture/separation, compression, transportation and injection stages. In response to the above barriers, the single CCS commercial project has shown that the operating costs for CCS could be reduced and future demonstration projects can reveal this likelihood of cheaper capture methods. Furthermore, setting a robust carbon price combined with a functioning cap-and-trade emission scheme can speed up the transition to a low carbon economy (Global CCS Institute, 2014).

Carbon capture and storage technology should be seen as a chain of subsequent processes, starting with the separation (capture) of CO$_2$ from the rest of the exhaust gases produced by power generation systems or industrial processes. After compressing the captured CO$_2$ to a liquid state, it is transported to a suitable location for injection into a safe long-term storage site; deep saline formations or hydrocarbon

reservoirs for the enhancement of the oil recovery process. There are three possible methods for capturing CO_2:

i. Pre-combustion capture, where the separation of carbon from the fuel takes place prior to combustion. Partial oxidation of the fuel produces syngas, a mixture of carbon monoxide and hydrogen. Then, by adding water the syngas mixture is converted to CO_2 and additional H_2, which needs to be separated from CO_2 by a physical or chemical absorption process. The H_2-rich stream is burnt to produce energy due to the high reactivity of the hydrogen.

ii. Post-combustion capture, where the CO_2 is separated from the rest of the exhaust gases by physical or chemical processes after the combustion process has taken place.

iii. Oxy-fuel combustion capture, where fuel is burnt with pure oxygen instead of air and the flue gas stream contains only carbon dioxide and water. Condensing the flue gas stream gives a pure stream of carbon dioxide.

1.3 Gas-CCS

The focus of this study is on the gaseous power generation systems since natural gas-fired power plants are "greener" than coal plants and gas will continue to play a major role in the energy mixture over the next decades, as discussed in Section 1.1. Although natural gas-fired plants emit significantly less CO_2, NO_x and CO and yield a higher combustion efficiency, the target for reducing substantially the greenhouse gas emissions from large point sources cannot be met without capturing the CO_2 emissions from the stacks of gas plants and transferring them to a long-term safe site. Consequently, gas-fired plants combined with CCS can offer a short, and medium term, feasible solution to meet the energy growing demands and the internationally agreed temperature limit by 2050.

Post-combustion capture technology uses traditional separation methods to recover 85 to 95 % of the CO_2 generated and thus becomes a readily available technology for existing and new power plants (Griffin et al., 2008). For the separation of CO_2 from the rest of the exhaust gases, a substantial amount of the energy produced by the power plant is needed. However, the major challenge for the post-combustion method is that air-fired combined cycle gas turbine plants (CCGT) produce large volumes of exhaust gases with a very low CO_2 concentration because they operate in very fuel-lean

conditions in order to protect the turbine system from the hot exhaust gases. Consequently, the CO_2 partial pressure is very low due to the low CO_2 concentration of the gas turbine flue gases (typically 3–4 % in volume if natural gas is used as a fuel source) and the size, cost and energy demands of the capture plant become in turn the strongest barriers for this technology (Griffin et al., 2008, IEAGHG, 2012). Therefore, the industry is now looking into the investigation of novel gas turbine cycles for CO_2 separation with the ultimate goal of developing a zero-emissions gas turbine (GT). Exhaust gas capture of CO_2 in a CCGT equipped with exhaust gas recycle (EGR) is an attractive technological option. Adding a part of the exhaust gas to the inlet of the gas turbine combustor, increases the CO_2 concentration and hence its partial pressure at the exit of the combustor. As reported by Griffin et al. (2008), this cycle option, due to the recirculation, achieves a reduced volumetric flow of the exhaust gas treated by the capture plant and a raised CO_2 exit concentration (6-10 % in volume) which can substantially improve the efficiency and reduce the cost/size of the capture plant. In contrast, the impacts of the composition of the new working fluid on the kinetics, emissions, combustion stability and turbomachinery need to be considered thoroughly (Li et al., 2011a). A recent techno-economic study investigated the technical feasibility, cost and performance of implementing post-combustion CCS on retrofitted or newly built natural gas combined cycle plants (NGCC) (Dillon et al., 2013). The second proposed cycle option is the integration of an air separation unit to simulate oxy-fuel combustion in a CCGT which requires substantial modifications on the turbomachinery parts (Griffin and Mantzaras, 2009). A comparative study between NGCC with post-combustion CO_2 capture (PCC) and oxy-fuel combustion combined cycles was performed with respect to the loss of electrical energy per kg CO_2 captured (Mletzko et al., 2016). Also, the last cycle approach is the injection of steam into a GT which needs further modifications on the system but its impact on the combustion process can be beneficial (Griffin and Mantzaras, 2009). Other ways of increasing the CO_2 concentration in the exhaust stream of CCGT were numerically investigated by Li et al. (2011b) who focused mainly on the cycle and combustion efficiency, and the modifications on the GT components.

There is no single technological option for zero emissions but rather a variety of approaches that need to be investigated further. Gas turbines, as a proven technology and with a fast-growing portion in the power generation industry, could significantly contribute to the reduction of greenhouse gas emissions. Due to the aforementioned

reasons, the focus of this study is on the impacts of EGR on the combustion process as experimentally investigated by injecting CO$_2$ into the combustion air stream.

1.4   Aims and Objectives

Exhaust emissions from power plants are proved to be harmful to the environment and their reduction is mandatory to meet the CO$_2$ emissions reduction goals which will keep the surface temperature within the 2°C safe rise limit, an internationally shared target. Emission reduction in power generation systems is particularly challenging considering the different fuel composition, combustor geometries and firing modes. All these parameters have an important effect on the formation mechanism of the pollutant emissions and alter the combustion process. Controlling the effect of these parameters leads to the development of gaseous combustion systems with reduced exhaust gases and weakens in turn the contribution of the power generation industry to climate change, global warming and air pollution. If carbon capture is applied to gas turbine units, gas can continue to be used as a primary fuel source for many years and ensure a reliable energy supply. For the best performance of the capture and the power plant, the CO$_2$ concentration of the feed stream to the chemical separation plant must be maximised. Therefore, part of the gas turbine exhaust stream is recirculated back to the combustor inlet to increase its outlet concentration. This is the most common firing mode of modern gas turbine systems to improve the overall plant efficiency. However, the diluted oxidiser mixture alters the combustion efficiency.

The aim of this study is to examine CO$_2$-diluted natural gas flames as applicable to gaseous combustors for the enhancement of the carbon capture process. This study consists mainly of experiments using an in-house built combustion chamber to investigate the effects of different CO$_2$ dilution levels on the flame chemistry, flame properties, flame stability and pollutant formation mechanisms. Similar experimental studies have not been reported with detailed in-flame, post-flame and exit measurements and therefore, the value of this study is to complete these research gaps. The fundamental understanding of the thermal and chemical effects of adding CO$_2$ in the combustion process is the knowledge gap aimed to be completed in this study. Moreover, numerical calculations using a detailed kinetic mechanism for natural gas combustion are carried out which give a deeper insight into the changes of the combustion chemistry with dilution. In summary, the objective of the current study is to enhance the fundamental understanding of the effects of adding CO$_2$ in the inlet of

a gas burner on the flame chemistry and properties by collecting detailed experimental measurements from confined natural gas non-premixed and non-preheated flames.

1.5 Thesis Structure

This thesis is composed of seven chapters, a summary of each is described below:

Chapter 1 introduces the problem of climate change and its human-made causes. CCS aims at reducing the CO$_2$ emissions from gas fired power plants whose contribution to global warming is significant. Through outlining the CCS mitigation options, the aims and objectives of this study are addressed.

Chapter 2 presents an overview of the published literature studies which assess the impacts of adding CO$_2$ on the combustion process. Furthermore, the research gaps in the available published studies are highlighted and how these knowledge gaps will be filled by the completion of this study is defined.

Chapter 3 is divided into two main parts. The first part is concerned with the experimental setup, techniques and methodology used throughout this study to collect and analyse the experimental data presented in Chapters 4 and 5. The second part describes the theory of the numerical model used to predict the implications of the CO$_2$ dilution and produce the data presented in Chapter 6.

Chapter 4 presents the results obtained from the first experimental campaign, named as "Flame A". A detailed analysis and discussion of the collected data is included along with the main conclusions on the impact of CO$_2$ in the combustion process.

Chapter 5 presents the experimental data and findings obtained from the second experimental campaign, named as "Flame B". Useful conclusions on the implications of the added CO$_2$ in the air stream are discussed.

The final purpose of this study was to assess the extent to which an available 1D numerical model can predict the changes in the flame chemistry and properties due to CO$_2$ dilution. In Chapter 6, the numerical results are presented and discussed. A comparison of the numerical results with the experimental data of Chapter 5 is performed and important information on the performance of the utilised model is extracted.

Chapter 7 summarises the conclusions of this thesis and includes suggestions for further work on the same research topic.

CHAPTER 2- Literature Review

2.1 Introduction

The analysis of CO$_2$-diluted natural gas flames for the enhancement of the carbon capture processes requires the understanding of the effects of the addition of CO$_2$ on the combustion chemistry. A detailed description of the different flame types and their characteristics is presented as the mixing type of the fuel and oxidiser streams plays an important role on the combustion efficiency, emissions and flame stability. Moreover, the formation mechanisms of the main pollutant emissions under air and CO$_2$-enhanced environments are outlined to understand the changes in the flame and thus in the combustion chemistry due to the dilution, thermal and chemical effects of CO$_2$. Furthermore, the presented literature review includes the research work that is done on investigating the impact of CO$_2$ on the combustion efficiency, exhaust emissions, enhancement of the post-combustion process and the overall efficiency of a power plant when equipped with a capture plant. Finally, the research gaps that led this study to be identified are presented in this chapter.

2.2 Classification of Flames

A combustion process couples chemical and physical phenomena; the combustion initiates with an exothermic reaction and involves the transport of mass and energy. Depending on the design of the combustion system, the flames are classified in the following three categories:

i.   Premixed flames, when the fuel and the oxidiser streams are mixed before burning.
ii. Non-premixed flames, when combustion and mixing occurs at the same time.
iii. Partially-premixed flames, the combination of a non-premixed and a premixed flame.

These three categories are further divided into laminar or turbulent flows, according to the type of the fluid flow (Warnatz et al., 1996, Griffiths and Barnard, 1995, Turns, 1996, Glassman and Yetter, 2008). In premixed flames, the fuel and the oxidiser streams are mixed before combustion initiates; the Bunsen burner is an example of a

premixed burner. In these systems, reactions between a gaseous fuel and an oxidant stream are rapid, exothermic and propagate in a thin zone at a low burning velocity (Griffiths and Barnard, 1995). In non-premixed flames (also called diffusion flames), the fuel and the oxidiser are mixed where combustion occurs, an example of such flames is a candle flame. Combustion takes place at the interface between the two reactant streams, fuel and oxidiser, and the dominant process is the mixing of the fuel and oxidiser (Griffiths and Barnard, 1995). Finally, in partially-premixed flames, there is more than one stream of fuel and oxidiser, usually there is a pilot flame, which is non-premixed, and multiple fuel jet injection points. There are other types of flames, such as piloted flames, flames stabilised by strong recirculation zones as formed by swirling flows, flames stabilised on bluff-bodies and flames stabilised by both recirculation zones and bluff-bodies (Turns, 1996). In this study, particular focus is given on jet flames due to their simple geometrical characteristics.

2.2.1. Non-premixed vs. premixed flames

This section gives a brief description of the main differences between premixed and non-premixed flames. Most gas turbine combustors operate in partially-premixed and/or diffusion mode to ensure a stable combustion process despite the regular changes in the ambient conditions and operating pressure. In addition, non-premixed combustion yields more stable flames, is significantly less sensitive to transient variations in temperature, pressure and/or load and these systems are stable enough during abrupt changes in the air-to-fuel ratio. Moreover, diffusion flames are safer to handle because the fuel and oxidiser are mixed and burnt inside the combustor and flashback phenomena are less likely. However, non-premixed combustion is not an ideal burning process because diffusion flames burn in near stoichiometric conditions and this results in higher flame temperatures, which inevitably increase NO$_x$ emissions, and in a higher thermal load inside the primary zone of a gas turbine combustor (Lefebvre and Ballal, 2010).

2.2.1.1. Premixed flames

In Figure 2-1, temperature and concentration profiles of reactants and products are depicted for a premixed adiabatic flame. The heat release from the exothermic chemical reactions in the system is responsible for the temperature increase, for the faster reaction rates and the higher heat release in the reaction zone. When reactants

are consumed, the reactions come to an end and the temperature eventually becomes constant in the products zone. Intermediate species are usually produced in the reaction zone and are related to short residence times (Griffiths and Barnard, 1995).
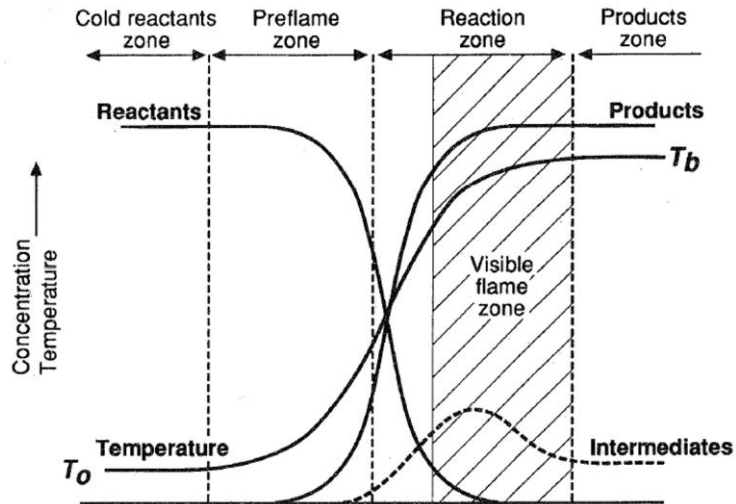
Figure 2-1 Schematic of the concentration and temperature profile in a typical premixed adiabatic flame (Griffiths and Barnard, 1995).

2.2.1.2. Non-premixed flames

When fuel and oxidiser enter the flame zone from separate streams, they react as fast as they mix. Mixing occurs mainly by molecular diffusion, and combustion takes place at the interface of these two streams. Figure 2-2 shows a schematic of non-premixed jet flames, which shows how the fuel diffuses into the oxidiser side at a stoichiometric proportion and combustion occurs at the boundary layer where most of the combustion reactions take place. Heat transport and mass diffusion promote active species, such as hydroxyl radicals, to diffuse into the fuel-rich zone and decompose the fuel molecules to initiate chain branching reactions (Griffiths and Barnard, 1995).

The flame front is the location of the maximum products concentration and flame temperature; maximum flame temperature is slightly lower than the adiabatic one due to heat losses. Diffusion flames exhibit a wider reaction region and reactants are not present at the flame front, which indicates fast chemical reaction rates. In non-premixed combustion systems, burning depends only on the mixing process which is slower than the reactions; mixing is the determining step.

Diffusion flames can be divided into laminar and turbulent flames using the Reynolds number, Re, as an indicator, described by Equation (2-1).

$$Re = \frac{\rho \, U \, d}{\eta}$$
(Equation 2-1)

where ρ is the fluid density (kg/m^3), U is the fluid velocity (m/s), d is a characteristic length (m) and η is the dynamic viscosity of the fluid (Pa s).
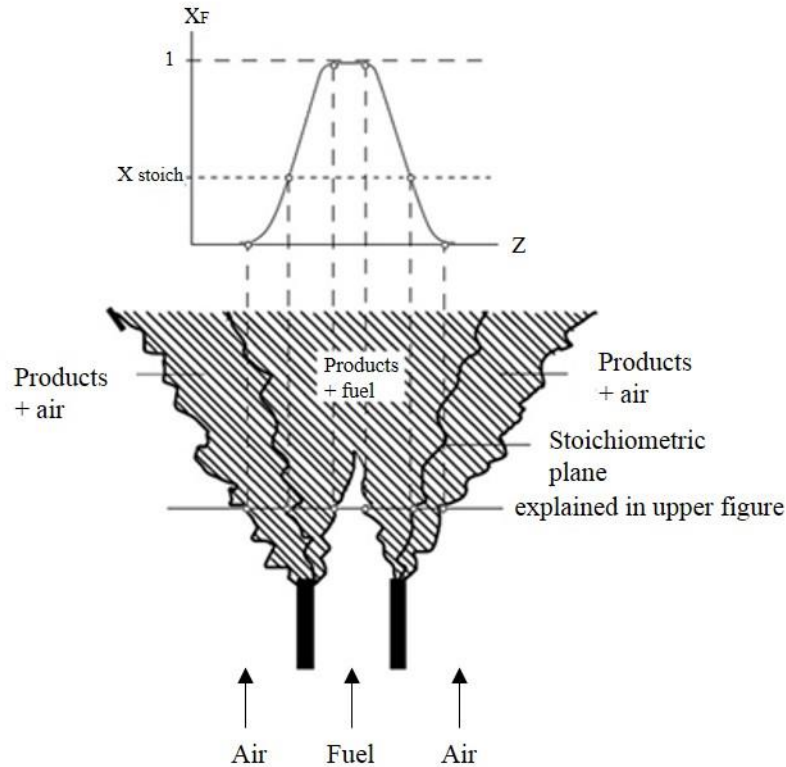
Figure 2-2 Structure of a turbulent non-premixed jet flame (Warnatz et al., 1996).

The Reynolds number is defined as the ratio between the inertial and the viscous forces and is inversely proportional to the dynamic viscosity which changes substantially within the combustion zone. Turbulent flows are characterised by high Re numbers and laminar flows by low numbers (Borghi, 1988, Griffiths and Barnard, 1995). In laminar flames, mixing occurs solely by molecular diffusion whereas in turbulent flames, eddies are formed, enhancing greatly the mixing rate. Any type of fuel (solid, liquid or gas) can be used and either a gas flowing stream or quiescent atmosphere can be used as an oxidiser flow (Glassman and Yetter, 2008, Griffiths and Barnard, 1995).

Non-premixed hydrocarbon flames are more luminous because they are sooty flames (contain luminous particles). The luminosity of the flame base is low, indicated by the blue colour, forming a soot-free region. Further upstream, the flame becomes brighter due to soot formation and the colour becomes yellowish. Methane and natural gas are less sooty fuels compared to other gaseous fuels, such as propane, and the length of

the soot-free region is longer than in other gaseous fuels (Turns, 1996). In addition, part of the flame radiation originates from the luminosity of these carbon particles (Warnatz et al., 1996).

The aforementioned characteristics of the non-premixed flames are schematically shown in Figure 2-3. Hottel and Hawthorne (1948) were the first to investigate laminar hydrogen-air diffusion flames and examined the radial distribution of the species concentration. The fuel flows internally and is surrounded by oxygen and this is the reason for the fuel concentration being maximum on the jet centreline and minimum on the flame boundary. On the other hand, the oxygen concentration is maximum outside of the flame boundary layer and close to zero at the flame front where most reactions occur and the products concentration reaches their maximum (Hottel and Hawthorne, 1948).
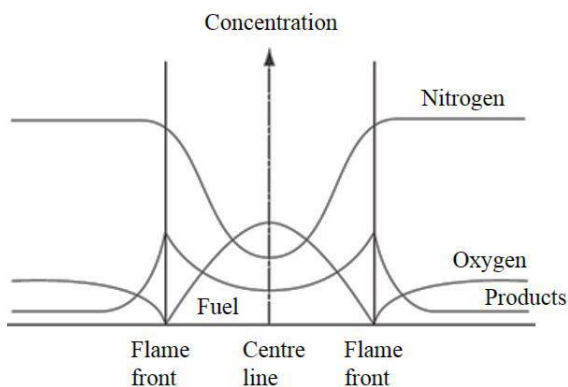
Figure 2-3 Schematic of the spatial concentration profiles of fuel, oxygen and products of a laminar diffusion flame (Hottel and Hawthorne, 1948).

Laminar diffusion flames are long flames with a cylindrical shape and their mixing rate is slower than the rate in turbulent flames. They are used in applications where the distribution of heat along large regions in a combustion rig is required (Hottel and Hawthorne, 1948). They consist of two diffusion-convection zones, as shown in Figure 2-4, which are formed at both sides of the reaction zone and the temperature and species vary across the zones. Laminar flames are steady flames which are stabilised where the two separated flows, the oxidant and the fuel, are mixed and create a thin boundary layer (Borghi, 1988). In this study, only turbulent non-premixed flames are experimentally investigated.

At relative low jet velocities, laminar flows exist where mixing of reactants is weak, the flame is long, smooth with a sharp-edged shape and the flame height increases almost linearly when increasing the jet exit velocity as shown in Figure 2-5. Above a

certain jet velocity, the flame tip appears to have the shape of a brush (known as the "breakpoint"). The velocity increases and flame height decreases as the turbulence becomes more intense until a fully developed turbulent flame is formed.
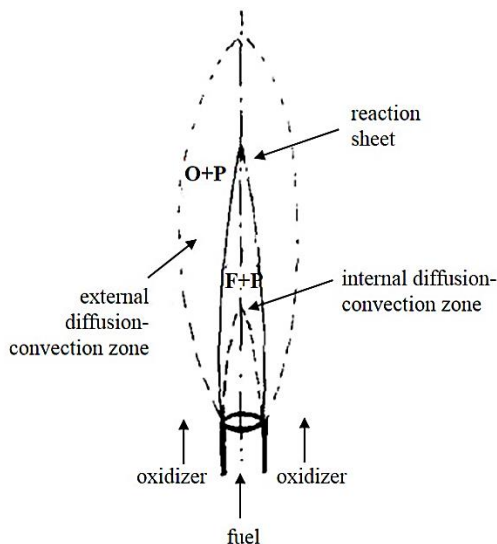
Figure 2-4 Structure of a laminar diffusion flame (Borghi, 1988).
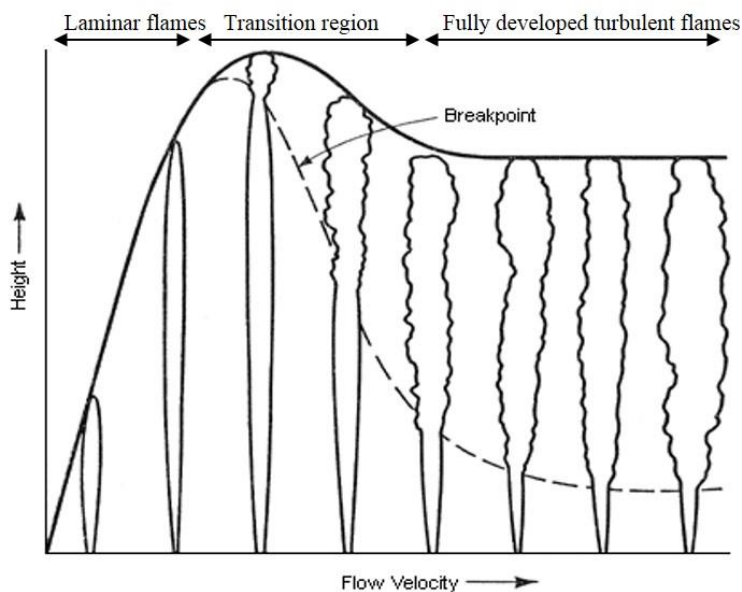
Figure 2-5 Diffusion flame structure depicted as a function of flame height and flow velocity (Hottel and Hawthorne, 1948).

The decrease in flame height is a result of increased turbulent mixing which enhances air entrainment through eddies. In turbulent flames, the flame height remains constant and independent of any additional increase in the jet velocity. A turbulent flame makes more noise, its visible flame zone spreads outwards (thicker flame width) and is less luminous compared to laminar flames because the turbulence produces better mixing and decreases the soot formation rate (Hottel and Hawthorne, 1948). Above a certain

increase in the flow velocity, turbulent flames may detach from the burner nozzle; lifted flames. When the jet velocity increases above a certain value, specific for each system, the lifted flame eventually extinguishes (known as the blow-out phenomenon).

The main characteristics of a turbulent flow are randomness and flow irregularity, the molecular diffusivity in turbulent flows enhances and promotes rapid mixing and transfer of mass and heat. Turbulent mixing leads to a fast and more intense mixing of the fluid micro particles in the reaction zone through eddies that are formed and cause the burning process to be faster. The velocity difference of the fuel and air streams generate a shear layer along their interface of the two fluids and its interaction with the surrounding air generates the turbulent eddies. These eddies are also responsible for the flame 'flickering' behaviour (Griffiths and Barnard, 1995). The smaller scale eddies that are formed, are mixed through molecular diffusion and therefore two types of mixing are responsible for turbulent flames, namely eddy and molecular diffusion (Warnatz et al., 1996).

2.2.2. Jet non-premixed flames

Turbulent jet flames provide a well-defined and relatively simple flow field despite the complexities originating from the interaction between turbulence and chemistry. The goal of studying and understanding jet flames is to develop and validate models which could couple this interaction for simple systems. When fundamental knowledge is gained, then more complex reacting flows can be investigated, such as turbulent swirling and recirculating flows. One of the main features of jet flames is the influence of the initial jet diameter and fuel flow rate on the size of the flame and the flame stability.

There are two critical flow conditions related to the stability of lifted jet flames, lift-off and blow-out phenomena. At low flow rates the flame is laminar and the flame is touching the burner nozzle (attached flames). When a turbulent flame detaches from the burner nozzle, it is called a nearly-lifted flame, and depending on the system (jet diameter, fuel composition) the appearance of a turbulent diffusion flame will change. Above a critical flow rate (or velocity), the diffusion flame will become further-lifted and stabilise downstream of the jet exit. Lift-off height is defined as the distance between the burner exit and the lowest point of the lifted flame base. Any further

increase in the fuel flow rate will eventually blow-out the flame which practically means that self-sustained combustion is not possible (Turns, 1996).

2.2.2.1. Configuration of jet flames

When a jet of pure fuel issues from a pipe or nozzle, a jet diffusion flame is formed. Jet diffusion flames were fully presented by Griffiths and Barnard (1995) who characterised them according to the air-to-fuel velocity ratio. There are two types of jet flames, the simple and the co-flow ones. Simple jet flames consist of a jet of fuel which flows into a quiescent atmosphere and co-flow jet flames consist of both streams of fuel and oxidant moving upwards (concentric setup) into still air. Close to the boundary of the fuel and oxidant streams, turbulence creates eddies of combustion products which separate these streams and slows down the diffusion (Griffiths and Barnard, 1995).

In co-flow jet flames, the fuel and the oxidant are flowing through concentric pipes. When the oxidiser flow rate (in the outer annulus) is above the stoichiometrically required amount for complete combustion, the flame is long and such flames are called over-ventilated. If the oxidiser flow rate is below that amount, a shorter and wider flame is formed and is called under-ventilated. Both types are illustrated in Figure 2-6 (Glassman and Yetter, 2008).
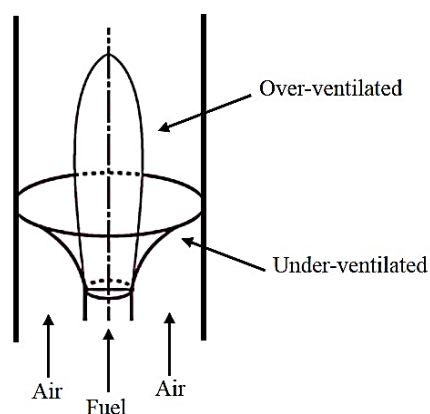
Figure 2-6 A representation of the configuration of co-flow jet flames (Glassman and Yetter, 2008).

2.2.2.2. Stabilisation theories on lifted non-premixed flames

Lifted flames are used in systems where a distance between the burner nozzle and the flame is needed to avoid damage to the nozzle material. A burner stabilised jet flame can become lifted when the jet exit velocity or the surrounding co-flow air velocity is

increased above a critical value, characteristic for each system. Once the flame is lifted, it can stabilise downstream and a "stable" lifted jet flame can be obtained. A lifted jet flame can exist over a range of exit velocities above which the flame blows-out (Lyons, 2007). Extensive analysis on stabilisation of lifted flames has been conducted and is discussed in this section.

Lifted laminar jet flames

Premixed flames propagate through regions of flammable mixtures whereas diffusion flames spread across the interface created by diffusion of the fuel and oxidiser flows. Various studies have concluded that laminar jet flames propagate partially due to premixing occurring upstream of the flame base. Phillips (1965) was one of the first experimentalists that confirmed the structure of triple laminar flames (or also called tri-brachial flames). The edge-flame theory is based on the triple flame structure comprising of three flame fronts; a fuel-rich flame close to the jet stream, a fuel-lean flame on the oxidant side and the remaining fuel is burnt in a diffusion flame further downstream (Lyons, 2007). Plessing et al. (1998) observed the flame luminosity of the triple flame through flame imaging and as seen in Figure 2-7, the diffusion flame has a broad luminous zone between the other two thinner zones.
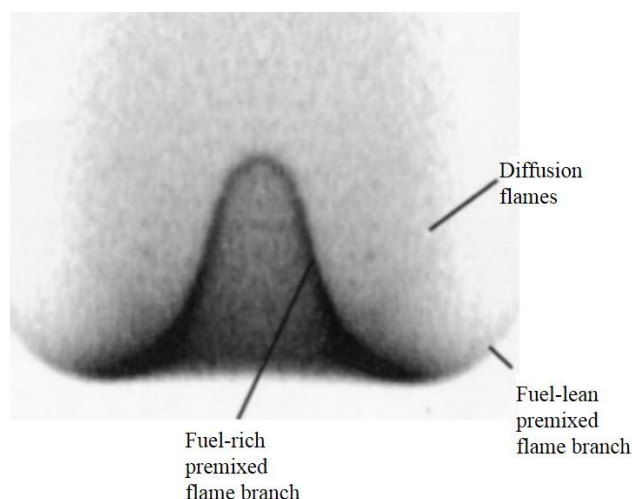
Figure 2-7 Flame image showing the triple flame structure of a lifted laminar jet flame (Ko and Chung, 1999).

Plessing et al. (1998) also investigated the heat exchange between the three flame branches. Other studies on tri-brachial flame structure examined the characteristics of the propagation speed, the influence of the mixture fraction gradient and the tendency

of lifted flames to stabilise around the tri-brachial stabilisation point and were conducted by Ko and Chung (1999), Lee and Chung (1997) and Kim et al. (2007).

Turbulent lifted flames

The first review that summarised published experimental and theoretical studies on the stability of turbulent lifted jet flames was carried out by Pitts (1988) who concluded that none of the theories could fully explain the stabilisation mechanism of a lifted flame. A summary of the main theories is as follows:

(i) The Premixed or Flamelet Model was first proposed by Vanquickenborne and van Tiggelen (1966). The concept of the model supports that the initially non-premixed fuel-air mixture is fully premixed at the base of a lifted flame. The starting position of a lifted jet flame is where the local burning velocity becomes almost equal to the local mean jet velocity due to turbulence; this burning velocity resembles that of a premixed flame under the same turbulent conditions (Vanquickenborne and van Tiggelen, 1966). The turbulent burning velocity is a function of the laminar burning velocity and for hydrocarbon fuels it is found to be maximum close to the stoichiometric plane. Consequently, lifted flames are stabilised where combustion is controlled by premixing of the fuel-air mixture or where the mean fuel mass fraction is that required for stoichiometric burning (Lyons, 2007; Vanquickenborne and van Tiggelen, 1966).

Eickhoff et al. (1985) revealed that 40-50% of the fuel flow rate was found to be already mixed upstream of the stabilisation zone and downstream of this location no change in the species concentration was found. This clearly showed that mixing becomes weak when combustion initiates. Pitts (1988) pointed out the weakness of this model to take into account the existence of large scale structures in turbulent jets, known as turbulent eddies. Furthermore, this model is valid for lift-off heights greater than forty jet diameter radius (Lawn, 2009). Lyons (2007) reported that when the above criterion is met, large eddies start to play a crucial role in flame stabilisation because they allow the propagation of the flame downwards against the mean velocity of the reactants. Burgess and Lawn (1999) had earlier reported that the propagation of turbulent lifted jets occurs around the periphery of large eddies which is in full agreement with the later results of Lyons (2007).

(ii) The Extinction Flame or Critical Dissipation Rate Model was initially proposed by Peters and Williams (1983). In this model, a turbulent flow is considered to

comprise of multiple laminar flames, known as flamelets. The flamelet concept is valid when chemistry is faster than diffusion and combustion occurs in asymptotically thin flamelets (Peters, 1986). Peters and Williams (1983) first reported that lift-off phenomena are controlled by local quenching of the laminar diffusion flamelets. Also, they reported that flame stretching and flow inhomogeneities are responsible for local quenching through turbulent mixing of the fuel jet with the flame (Peters and Williams, 1983).

Recent studies have attempted to explain the above theory by demonstrating the relationship between flame stretching, local extinction, strain rate and stabilisation of lifted flames. Schefer et al. (1994a) suggested that a balance between premixed or partially-premixed flame propagation and local extinction phenomena contributes to the stabilisation mechanism, similarly to that reported in Kelman et al. (1998). The interaction of large scale vortices with the flame causes the movement of the flame base due to intense flame stretching. Movement of large vortices cause the entrainment of cold air which forces the flame base to move further downstream (Kelman et al., 1998). The new downstream location increases the mixing time of the fuel jet and the flame and consequently, flame stretching leads to local flame extinction phenomena in the stabilisation region (Kelman et al., 1998).

The study carried out by Schefer et al. (1994b) is in contrast to the above results as they found that lifted flames exist in regions where scalar dissipation values are below the extinction critical value. Their conclusion is that local stoichiometry controls the stabilisation and scalar dissipation does not play an important role. Ignition of a fresh mixture by mixing with hot products occurs due to the interaction of the formed eddies in the central fuel jet and the instantaneous flame zone. A more recent study by Lyons et al. (2005) confirmed the quenching phenomena by observing ″flame holes″ upstream of the flame front through CH PLIF imaging. Local extinction can generate these flame holes which are caused by large strain rates (high values of the scalar dissipation) and help in partial premixing of fuel and oxidiser in non-premixed systems. Lawn (2009) confirmed that low stretching rates cause local extinction and stretching only reduces the flame front propagation rate. Therefore, flame stabilisation occurs when the scalar dissipation is below a critical value (Lyons, 2007).

(iii) The Large Eddy Model was first introduced by Broadwell et al. (1984). Turbulent jets comprise of large scale structures, the turbulent eddies, which are formed along

the jet mixing layer. Due to the movement of these eddies, entrainment of hot gases and fresh air are introduced into the unreacted fuel rich jet, thus assisting the flame to stabilise. Flame lift-off is due to the local flame quenching caused by enhanced mixing through the eddies that form mixtures beyond flammability limits. Therefore, stabilisation is based on the balance between a characteristic chemical reaction time and molecular mixing times of entrained hot gases into fresh reactants (Broadwell et al., 1984). Through simultaneous laser techniques, Su et al. (2006) investigated how the upstream point of the lifted flame base is related to flame stabilisation. The results could identify a high temperature interface at the flame base and the location of the stabilisation point which lies closer to the jet centreline, rather than any other upstream point on the stoichiometric interface, because the local composition of the mixture could support the combustion. Scalar dissipation values were also determined and near the stoichiometric interface they did not exceed the equivalent quenching rate. Thus, the dissipation rate reveals that stabilisation is based mainly on partial premixing rather than diffusion quenching (Su et al., 2006).

2.2.3. Swirl-stabilised non-premixed flames

Swirl-stabilised jet flows are formed by the introduction of a spiralling motion to the flow; this is achieved by introducing a tangential velocity component to a perfectly axial flow. The tangential velocity creates a rotational flow motion which results in high adverse pressure gradients; this is a characteristic of swirling flames which explains many of their features. This pressure gradient is responsible for the formation of internal recirculation zones (also known as toroidal vortices) contributing to the stabilisation of the flames and to the enhancement of the fuel-air mixing rate by increasing the contact region between the fuel and the air streams (Turns, 1996, Chen and Driscoll, 1989). Therefore, turbulent flames inside swirl combustors are stabilised due to the presence of central (CRZ) and outer recirculation zones (ORZ) which recycle combustion products back to the inlet of the combustor. A swirl-induced recirculation zone acts as a continuous ignition source transferring thermal energy from the hot exhaust gases to the inlet colder reactants and contains many chemical radicals (Turns, 1996). Industrial gas burners usually accommodate both tangential air inlets and a set of swirled vanes, which are usually fitted into the air rather than the fuel flow stream, to control the degree of swirl by adjusting the air flow rate and to yield enhanced mixing and stable flames (Turns, 1996).

Driscoll et al. (1987) was one of the first researchers that related the recirculation strength to the mixing rates, flame length, NO emissions and blow-out limits. Driscoll et al. (1987) and similarly, Chen and Driscoll (1989) found that as the swirl strength of a flow increases, the flame length of a jet flame can be reduced by a factor of about five. According to Turns (1996), swirling flows are important in designing modern gas combustors because swirl assists in minimising the pollutant emissions. Rapid and strong mixing yields in shorter residence times and so, lower NO$_x$, and higher CO emissions due to the entrainment of cold air causing the quenching of the combustion reactions yielding in poor combustion efficiency (Turns, 1996, Cheng et al., 1998).

2.2.4. Bluff-body stabilised non-premixed flames

Bluff-body stabilised flames consist of a very complex flow field, especially the recirculation zone created on a bluff-body and thus extensive experimental and numerical research is required to fully understand these flows. However, this type of flow yields excellent mixing characteristics, improved flame stability and ease of combustion control. Most studies on these flames concentrate on the investigation of the structure and flow pattern of the recirculation zone formed in bluff-body stabilised flames due to its complexity and key role in flame stabilisation. Many parameters control the structure of these flames, such as the fuel-air velocity ratio, stoichiometric mixture fraction, heat release rate and bluff-body to jet diameter ratio. Masri and Bilger (1985) studied the chemical kinetic mechanisms occurring in these flames and also, observed a double toroidal structure which is usually formed on the bluff-body surface and is responsible for the recirculation zone and for the flame stabilisation. The double structure of the recirculation zone was studied in detail by Masri et al. (1994) who examined the flow field of bluff-body stabilised CH$_4$/CO and CH$_4$/H$_2$ flames. Two distinct regions form the recirculation zone, the larger outer region which entrains enough air closer to the fuel jet and provides the inner region (also known as inner vortex) with a combustible, near stoichiometric fuel-air mixture. The recirculating air mixes well with the fuel jet in the inner vortex region where combustion is intense, the temperature and mass fractions of the combustion products are maximum (Masri et al., 1994). Another study on these flames was conducted by Masri et al. (1998) who performed laser diagnostic techniques to produce instantaneous and quantitative images of scalar variables in diffusion bluff-body stabilised flames which agreed on the existence of the double reaction zones within the recirculation zone.

2.3   Formation Mechanisms of Pollutants in Air Combustion

Continuous burning of fossil fuels produces exhaust gases that are harmful to the environment and some of them have been identified as the major contributors to global warming. The main combustion products are carbon dioxide (CO_2) and water vapour (H_2O). However, other important generated by-products are nitrogen oxides (NO_x), which are toxic gases for our health and harmful to the environment as they contribute to the formation of photochemical smog and ozone depletion. In addition, other pollutants are the unburnt hydrocarbons (UHC), when they are combined with NO_x, they form the photochemical smog, the carbon monoxide (CO) which can cause suffocation in a high concentration by reducing the capacity of the blood to absorb O_2 and the soot particles which are harmful to the respiratory human system (US Environmental Protection Agency, 1998).

2.3.1. NO$_x$ formation mechanism

In this section, the formation mechanisms of nitrogen oxides, denoted by NO_x, is presented. There are two sources of nitrogen in the combustion systems, the combustion air and nitrogen-based fuels. Both nitric oxide, denoted by NO, and nitrogen dioxide, denoted by NO_2, are named as nitrogen oxides, causing photochemical smog, ozone destruction and serious respiratory problems to humans. In addition, nitrous oxides, or N_2O, can be formed during combustion of gaseous fuels and they are a harmful pollutant (US Environmental Protection Agency, 1998). Consequently, combustion researchers are nowadays interested in the development of low nitrogen oxide burners, the so-called Dry Low Emission technology, to reduce NO_x emissions from gas fired turbines. Measured concentrations of various pollutant emissions can differ substantially from their calculated equilibrium values, which is the reason for investigating their chemical kinetic mechanisms. The kinetics of the nitric oxide formation reactions are affected by the oxygen availability and the flame temperature level, parameters that fluctuate greatly in turbulent reactive flows. In combustion systems, NO is formed firstly and under specific temperature and pressure conditions it is oxidised to NO_2. The formation of the mixture NO and NO_2, which is reported as total NO_x in flames, occurs via the following four mechanisms (Lefebvre and Ballal, 2010, Miller and Bowman, 1989):

i.   Reaction between atmospheric oxygen and nitrogen at regions with high flame temperatures. This mechanism was initially proposed by Zeldovich, its formation rate depends on the combustion temperature and is known as "thermal NO mechanism" (Boyce, 2012).

ii. Oxidation of the chemically bound nitrogen, mostly in solid and liquid fuels. The formation rate of this mechanism is a function of the fuel composition and is known as "fuel NO mechanism" (Boyce, 2012).

iii. Reaction between carbon or hydrocarbon radicals and atmospheric nitrogen. This mechanism was initially suggested by Fennimore, its formation rate depends on the mixture stoichiometry and is known as "prompt NO mechanism" (Fenimore, 1971).

iv. Formation of nitrous oxide emissions which produces NO emissions (Lefebvre and Ballal, 2010).

In gaseous combustion systems, fuel NO$_x$ is absent and NO$_x$ emissions are mainly generated via the thermal route, and less by the prompt path. However, the absence of fuel NO$_x$ do not necessarily imply that gaseous fuels have lower total NO$_x$ emissions as they can reach quite high flame temperatures (Lefebvre and Ballal, 2010).

2.3.1.1. Thermal nitric oxide (NO)

The thermal NO$_x$ formation mechanism occurs when nitrogen reacts with oxygen under elevated temperatures existent mainly in the post-flame regions. Zeldovich proposed the principle reactions for the formation of thermal NO emissions and the extended mechanism is described here. The atomic species of N$_2$ and O$_2$ in the following reactions are a result of the decomposition of their molecules during chain reactions (Lefebvre and Ballal, 2010, Lee et al., 2004):

$$O + N_2 \leftrightarrow NO + N \qquad\qquad (R\ 2\text{-}1)$$

$$N + O_2 \leftrightarrow NO + O \qquad\qquad (R\ 2\text{-}2)$$

$$N + OH \leftrightarrow NO + H \qquad\qquad (R\ 2\text{-}3)$$

The rate constants of the above reverse reactions reveal that reaction (R 2-1) is the rate determining step since it has the lowest reaction rate constant, a very high activation energy (E$_A$= 314 kJ/mol) for breaking the triple bond of N$_2$ molecule (the dissociation energy required is 941 kJ/mol) and thus its peak concentration is found where also the temperature peak is found (ElKady, 2005, Hayhurst and Vince, 1980). Therefore, this

mechanism is called the ″thermal″ NO formation mechanism. For natural gas combustion systems, the thermal route is the main mechanism for producing NO$_x$ emissions, is highly dependent on the combustion temperature and as such is dominant in stoichiometric mixtures. According to Turns (1995, 1996) and Lefebvre and Ballal (2010), the thermal formation mechanism occurs only at temperatures above 1800-1850 K. Lefebvre and Ballal (2010) mentioned that the peak concentration of NO emissions is found to be in the fuel-lean regions of a flame although in fuel-rich regions the flame temperature is higher. This can be explained when considering that nitrogen competes with fuel to engage oxygen atoms but fuel molecules attack oxygen in the fuel-rich side of a flame (Lefebvre and Ballal, 2010). In conclusion, this mechanism accounts for up to 80 % of the total NO$_x$ emissions, is dominant in non-premixed flames, is highly dependent on temperature but also linearly dependent on oxygen availability, as reported in Bowman (1992). From the reaction rates of the Zeldovich mechanism it can be concluded that it is a relatively slow kinetic mechanism, thus turbulence and chemical kinetics play an important role in predicting thermal NO. As reported by Hayhurst and Vince (1980), measured NO levels are found to be higher than the predicted ones suggesting that Zeldovich mechanism underpredicts the NO formation rates.

2.3.1.2. Prompt nitric oxide (NO)

Emissions of nitric oxides are also found in regions where the criteria for the thermal pathway cannot be met, such as in the primary reaction zone where flame temperature cannot reach 1800 K. As a result, another formation pathway for NO occurs in regions of lower flame temperatures. This mechanism is called prompt and is a faster NO formation method as it is much less dependent on flame temperature. Fenimore (1971) suggested that hydrocarbon radicals react with molecular nitrogen according to the reaction (R 2-4) which is dominant in flame regions of temperatures about 1000 K. The reaction (R 2-4) indicates that the peak formation rate of prompt NO is located where the maximum CH concentration is found; intermediate species are usually forming at the flame front (Warnatz et al., 1996). Consequently, the prompt mechanism does not depend on the temperature but on the mixture stoichiometry (fuel-rich conditions), and NO forms during a short residence time. The initiation reaction of the Fenimore reaction pathway is as follows:

$$CH + N_2 \leftrightarrow HCN + N \qquad\qquad\qquad (R\ 2\text{-}4)$$

This mechanism consists of (i) the breaking up of hydrocarbon molecules, (ii) the reaction of fuel molecules, CH_i, with N_2 molecules, and (iii) the oxidation of hydrocyanic acid, HCN, and nitrogen atoms to finally form NO. The oxidation of HCN involves a sequence of reactions to form NO, such as $HCN \rightarrow CN \rightarrow NCO \rightarrow NO$ and is rapid only under fuel-lean conditions. In addition, the oxidation of nitrogen atoms to form NO follows mainly the reaction (R 2-2) (Lefebvre and Ballal, 2010). Bowman (1992) concluded that prompt NO contributes to about 50% of the total NO_x emissions and is a dominant mechanism in fuel-rich hydrocarbon flames.

2.3.1.3. Nitrogen oxide (NO₂)

Miller and Bowman (1989) reported that the NO/NO_2 conversion occurs in low flame temperature regions, for methane flames the effectiveness of this conversion is above 1000 K. In addition, NO will eventually be converted to NO_2 in the atmosphere due to quenching. The formation reaction of NO_2 contains NO as a precursor and the destruction mechanism of NO_2 produces NO and is also described as follows:

$$NO + HO_2 \leftrightarrow NO_2 + OH \qquad \text{(R 2-5)}$$

$$NO_2 + H \leftrightarrow NO + OH \qquad \text{(R 2-6)}$$

$$NO_2 + O \leftrightarrow NO + O_2 \qquad \text{(R 2-7)}$$

Reaction (R 2-5) describes the formation of nitrogen dioxide occurring mainly due to the decomposition of fuel molecules producing active species, such as the hydroperoxyl, HO_2. Nitric oxide is transported through molecular diffusion from high temperature regions to lower temperature ones to react with HO_2 and form NO_2. Peak concentrations of NO_2 are found at downstream regions of the flame zone, regions with temperatures below 1500 K or at post-flame regions where combustion products are mixed with fresh reactants. Finally, the destruction mechanism of NO_2 is rapid under elevated temperatures and depends on the availability of radicals, such as O and H (Miller and Bowman, 1989, Bowman, 1992).

2.3.1.4. Nitrous oxide (N₂O)

Nitrous oxide emissions are formed based on the availability of oxygen atoms and molecular nitrogen, reacting via a three-body reaction, reaction (R 2-8). The nitrous oxides species subsequently react either with the oxygen atoms to form NO via reaction (R 2-9) or with hydrogen atoms via reaction (R 2-10) or with carbon

monoxide via reaction (R 2-11) (Lefebvre and Ballal, 2010). However, this mechanism does not increase significantly the total generated NO emissions but in fuel-lean conditions the formation of CH can be suppressed which would yield less prompt NO emissions and the low temperatures related to fuel-lean regions would also suppress the formation of thermal NO emissions (Bowman, 1992). In conclusion, the N$_2$O route is an important mechanism at low equivalence ratio mixtures and thus low temperature regions. These conditions are found mostly in gas turbine systems (lean premixed combustors) and less often in gas burners, as considered in this thesis (Bowman, 1992, Michaud et al., 1992). The main reactions describing this mechanism are the following (Warnatz et al., 1996, Lee et al., 2004):

$$O + N_2 + M \leftrightarrow N_2O + M \qquad \text{(R 2-8)}$$

$$N_2O + O \leftrightarrow 2NO \qquad \text{(R 2-9)}$$

$$N_2O + H \leftrightarrow NO + NH \qquad \text{(R 2-10)}$$

$$N_2O + CO \leftrightarrow NO + NCO \qquad \text{(R 2-11)}$$

2.3.1.5. NO$_x$ formation in non-premixed flames

As shown in Figure 2-2, at the stoichiometric plane of non-premixed flames, high flame temperatures are present resulting in relatively high NO$_x$ emissions; a strong relationship between temperature and thermal NO mechanism. Furthermore, close to this stoichiometric plane, the concentration of the O and OH radicals is at maximum which is also in favour of the thermal NO$_x$ formation reactions as explained in Section 2.3.1.1. In contrast, in premixed flames most mixtures are fuel-lean resulting in temperatures below the stoichiometric flame temperature. Therefore, the NO$_x$ emissions are higher in diffusion flames compared to the premixed systems. However, diffusion flames are more stable flames and thus are valuable in industrial applications. First Kent and Bilger (1973), and later Bilger and Beck (1975), observed in hydrogen diffusion flames that the peak of NO is located at fuel-rich regions. Similarly reported in Turns (1995), peak production rates are found on fuel-rich regions in hydrogen diffusion flames. Also, he presented that for methane-air flames the prompt NO route can play a major role in the total NO emissions.

These early data on NO$_x$ emissions peaking on fuel-rich flame zones are not in agreement with the studies of Drake et al. (1987), Correa (1992) and Røkke (2006). These studies supported that maximum NO$_x$ formation rates occur in regions of high

temperature and high concentration of O atoms (conditions occurring in near stoichiometric flame zones). Due to these discrepancies in the experimental and modelling studies, a concrete conclusion, whether the differences in fuel composition, in flow conditions and possible probe sampling errors are responsible, cannot be made.

Drake et al. (1987) proposed that thermal NO reaches its maximum concentration at the stoichiometric plane in diffusion flames but could not prove the shift of NO_x emissions in fuel-rich regions. They assumed that the ″rich-shift″ might be due to errors in the probe sampling methods, used by earlier studies. Later, Drake and Blint (1991) used various modelling approaches to investigate the nitric oxide formation mechanisms in counterflow laminar $CH_4/N_2/air$ flames. Their numerical work revealed that the Fenimore mechanism generates up to 70 % of the total calculated NO_x emissions and assumed to be the same in all the configurations of hydrocarbon diffusion flames. Similarly, Smyth (1996) examined the NO formation and destruction mechanisms in a laminar co-flowing methane-air diffusion flame. He determined that the prompt route contributes to the formation of NO as much as the thermal mechanism but the instantaneous formation rate for prompt NO emissions is significantly larger than the thermal route rate close to the burner nozzle where CH_i radicals are plentiful. Røkke (2006) conclusions on the NO_x emissions for diffusion flames are the following: (i) the NO_x concentration peak is close to stoichiometry rather than at fuel-lean or rich regions, and (ii) the prompt NO and N_2O routes are less significant in turbulent diffusion flames. Correa (1992) reviewed many of the available studies on turbulent non-premixed combustion and supported that thermal NO emissions dominate in turbulent diffusion flames whereas rest reaction pathways become more important in laminar diffusion flames.

2.3.2. Carbon monoxide (CO), unburnt hydrocarbons (UHC) and carbon dioxide (CO₂) formation/destruction mechanisms

Carbon monoxide, CO, is an undesirable combustion by-product along with unburnt hydrocarbon, UHC, emissions because their presence reveals poor combustion efficiency. If the fuel is not mixed well with the oxygen within the flame zone, regional pockets of fuel are formed with limited access to oxygen yielding in an incomplete combustion. Consequently, premixed combustion enhances the mixing process resulting in lower amounts of CO/UHC compared to diffusion systems. However,

premixed combustors operate under fuel-leaner conditions, lower flame temperatures and slower reaction rates which slow down the oxidation of CO/UHC to CO_2 and H_2O (Turns and Bandaru, 1993). Carbon dioxide is the end product formed when a hydrocarbon fuel is burnt in near or above stoichiometric conditions. It is evidenced that CO_2 is fuelling climate change and thus in most countries its emissions are regulated (Baukal and Charles, 2013). Its production implies good mixing between the fuel and the oxidant in the reaction zone and thus is accompanied by low carbon monoxide emissions.

Initially carbon monoxide is formed by the rapid reaction of hydrocarbons with oxygen in the reaction zone and then it is found in significant amounts in: (i) fuel-rich flames where an insufficient amount of O_2 is present, (ii) very fuel-lean flames, where oxidation of CO is not initiated due to relatively low flame temperatures and so, low burning rates, (iii) stoichiometric or slightly fuel-lean flames where dissociation of CO_2 is favourable and (iv) when entrainment of cold air causes the quenching of post-flame gases. The actual CO oxidation process occurs at high flame temperatures and is described mainly by the following reversible reactions (Westbrook and Dryer, 1984, Lefebvre and Ballal, 2010, Mullinger and Jenkins, 2008):

$$CO + OH \leftrightarrow CO_2 + H \qquad\qquad\qquad\text{(R 2-12)}$$

$$CO + HO_2 \leftrightarrow CO_2 + OH \qquad\qquad\qquad\text{(R 2-13)}$$

Between these two reactions, Reaction (R 2-12) consumes almost all of the CO and produces most of the CO_2 that is present in a reacting system; its reaction rate depends strongly on the availability of OH radicals. Furthermore, Bowman (1975) reported that the reaction rate constant of the forward reaction (R 2-12) is almost temperature independent below 1000K and becomes dependent in flame temperatures above 1500 K. Also, reaction (R 2-12) is the most important reaction associated with the direct participation of CO_2 within a flame. Various studies have reported other CO oxidation reactions but their relative importance in hydrocarbon flames is contradictory, such as the study of Westenberg and DeHaas (1972) and Westbrook and Dryer (1981).

The availability of OH radicals depends on the controversy between reactions (R 2-12), the reverse reaction of the reaction (R 2-13) and reactions between hydrocarbons, HC, with OH since the latter reactions have a higher reaction rate. As a result, the presence of hydrocarbons is not in favour of CO oxidation and only if all the

hydrocarbon species are consumed, the OH radicals become available and then carbon monoxide can be oxidised to CO_2 (Westbrook and Dryer, 1984). It is worth noticing that all these reactions inhibit the single most important chain branching reaction in reactive flows, reaction (R 2-14), which produces the important radical species, such as O, H and OH (Westbrook and Dryer, 1984). Reduction in the concentration of radicals results in reduction in the fuel burning rate and overall combustion rate (Liu et al., 2003):

$$H + O_2 \leftrightarrow O + OH \qquad\qquad \text{(R 2-14)}$$

The pyrolysis and oxidation mechanism of methane has been studied extensively by Westbrook and Dryer (1984) and later by Lee et al. (2001) and Park et al. (2002), who summarised the main reaction pathways for methane-air and methane-air-CO_2 mixtures. A complete methane oxidation mechanism should include radical recombination reactions since during oxidation of methane large amounts of HC are formed, containing two or more carbon atoms. Especially, C_2 species, such as ethane, C_2H_6, ethylene, C_2H_4, and acetylene, C_2H_2, are formed. Methane oxidation can occur via two methods, thermal decomposition or via reactions with the active radicals O, H and OH. Both methods produce methyl radicals, CH_3, and thus methyl oxidation pathways should be considered, too. Methyl oxidation reactions can yield to methoxy radicals, CH_3O, and/or formaldehyde, CH_2O, or methyl radical recombination reactions which yield to ethane, ethyl and ethylene. It was reported that in fuel-lean or stoichiometric mixtures almost 30% of the methyl radicals are consumed by recombination reactions whereas in fuel-rich mixtures, this percentage increases to 80% (Westbrook and Dryer, 1984).

2.4 CO$_2$-Diluted Combustion Systems

Gas-fired power plants emit significantly less pollutant emissions and yield higher combustion efficiency compared to coal-fired plants as natural gas is a much cleaner fuel than any solid fuel. As a result, gas-fired plants that have implemented CCS technology can provide a clear reduction in global CO_2 emissions. To achieve the CO_2 reduction goals for power generation systems utilising gas turbines, exhaust gas recirculation (EGR), combined with a post-combustion capture system, is the most common mitigation option. A post-combustion capture plant uses traditional chemical processes to separate CO_2 from the other gases and can easily be retrofitted to existing

power plants. The chemical capture plant is highly demanding in energy consumption, due to mainly the reboiler energy demands, resulting in significant penalties associated with the efficiency of the power plant. In addition, the regeneration of the solvent requires a substantial amount of heat (endothermic reactions) in terms of thermal energy which is usually produced by low steam turbines in a combined cycle plant (CCGT). This is another factor contributing to the increase in the energy penalty of the power plant and reduction of the overall electrical efficiency (Bolland and Sæther, 1992, Burdet et al., 2010). Therefore, the gas separation processes are highly dependent on the concentration of the CO$_2$ in the feed stream and its volumetric flow and thus the operational and capital costs and size of the capture plant become dependent on the exit CO$_2$ concentration; the higher the CO$_2$ concentration, the higher the CO$_2$ partial pressure which is the driving force of the chemical separation processes. As such, the purpose of the partial recirculation of the exhaust gas stream of the gas turbine is to increase the concentration of CO$_2$ in the inlet stream of the capture plant and to reduce the total volumetric flow of the feed stream (Bolland and Mathieu, 1998). Bolland and Mathieu (1998) showed that a 40 % recirculation ratio results in a 43 % decrease in the mass flow rate of the exhaust gas stream prior to entering the CO$_2$ capture plant compared to its flow rate without recirculation.

The biggest challenge for the operation of the gas turbine systems is the material constraint of their blades as they need to resist the very high combustion temperatures. This is the reason why gas turbine (GT) combustors operate in lean or very lean conditions as most of the excess air amount is needed for cooling the exhaust gases before entering the GT unit rather than for the combustion process itself. As a result, the generated exhaust stream is a highly diluted CO$_2$ stream which becomes in turn the challenge for the capture plant to deal effectively with large volumes of diluted exhaust gases (Li et al., 2011b).

The importance of combining gaseous combustion systems with exhaust gas recirculation is of great importance for the development and implementation of CCS in existing power generation systems. However, EGR has important effects on the combustion process and the operability limits of the gas turbine combustors as the properties of the working fluid are now different to the composition of the typical combustion air. Diluting combustion air with CO$_2$ results in changes in the operability limits of the gas turbine combustors, changes in the flame chemistry along with changes in the flame temperature and exhaust emissions. As a result, understanding

these fundamental changes and proposing changes in the operation of gas turbines are needed. Although a large number of experimental and numerical studies have been conducted towards this goal, there is still a lack of sufficient experimental data that describes fully the combustion process inside a combustor. Most available data are taken at the exit of a GT combustor or at the exit of the turbine because it is difficult to have full access to the various sections of a GT combustor. Therefore, the objective of this study is to fill this gap by providing as much as possible information on the compositional and temperature profile of various species of non-premixed natural gas flames enclosed in a combustion chamber as applicable in GT combustors.

Many experimental studies, utilising different types of gas turbine combustors, have focused on the risks and challenges associated with combustion when applying EGR. The challenges include, for example, operational changes or redesigning the gas turbine to increase residence time, operational limitations of the compressor and/or recuperator, the success of complete mixing of the inlet air compressor and recirculation stream, or differences in heat transfer and composition of the new working fluid mixture, or effects on the exit temperature and exhaust emissions, which could yield combustion efficiency penalties in the case of incomplete combustion (Røkke and Hustad, 2005). Also, numerical analysis has been conducted to assist in the understanding of the benefits from combining EGR with a post-combustion capture plant from the performance, operability and efficiency point of view (Sander et al., 2011). From these studies, it can be concluded that EGR is applicable without major modifications to the current design of the combustors; a maximum ratio of about 40 % EGR for moderately fuel-lean mixtures has been tested experimentally which corresponds to an exit CO$_2$ level at about 10 % in volume and O$_2$ exit levels below 2 % in volume (ElKady et al., 2011). Similar studies on the feasibility of EGR for the enhancement of carbon capture, have concluded that a 35 % EGR does not cause significant operability and stability issues at the combustor; this ratio corresponds to an inlet oxidiser composition of 17 % O$_2$ and 3 % CO$_2$ in volume (ElKady et al., 2008, ElKady et al., 2009, Ditaranto et al., 2009). At 35 % EGR, the maximum CO$_2$ concentration found in the primary zone of the combustor can be 8 % in volume and at 40 % EGR the lowest achievable level of O$_2$ can be less than 4 % in volume. Different combustor designs and differences in the firing mode (pilot or partially or fully premixed mode) play the most vital role in the operational limits of the combustor and in the composition of the inlet oxidiser composition (ElKady et al., 2008, ElKady

et al., 2009). The lowest technically acceptable O$_2$ concentration in the gas turbine combustor inlet is the determining factor for the maximum recirculation ratio of the exhaust gas stream (Burdet et al., 2010).

The recycled part of the exhaust gas stream leads further to an apparently higher CO$_2$ concentration at the exit of the combustor along with a lower inlet O$_2$ concentration which reduces the reaction rates and suppresses the peak flame temperature. These are the two parameters that play a key role in the reduction in the thermal NO$_x$ pathway formation rate in diffusion systems; the lower adiabatic flame temperature due to higher CO$_2$ heat capacity and the lower O$_2$ concentration. In addition, it has been noted that the NO formation mechanism is affected more by the replacement of O$_2$ in the combustion air stream rather than the lack of high flame temperatures (Røkke and Hustad, 2005, ElKady et al., 2011, Guethe et al., 2011). A more detailed analysis on the understanding of NO$_x$ reduction processes when mixing fuel with part of the turbine exhaust gas was conducted by Ditaranto et al. (2009).

On the other hand, using EGR has considerable weaknesses, such as increased emissions of CO and THC. Less consumption of CO can be chemically attributed to either lack of oxygen for completion of the CO oxidation mechanism in fuel-rich flames or dissociation of CO$_2$ in stoichiometric or moderately fuel-lean flames or insufficient residence time or low pressure and temperature or low flame temperature and low burning rates in the primary zone of a combustor leading to incomplete combustion of the fuel in very fuel-lean mixtures. Carbon monoxide behaves the same in air combustion and EGR mode but increases when increasing the EGR ratio and its minimum concentration appears to be at higher flame temperature regions as the EGR percentage increases (ElKady et al., 2008, Evulet et al., 2009, Burdet et al., 2010, ElKady et al., 2011). Carbon dioxide replaces part of the oxygen in the inlet air and low levels of O$_2$ affect the flame velocity which can exhibit flame instabilities and potentially to flame blown-out. These two weak features appear to be the limiting parameters when deciding the maximum EGR ratio (Røkke and Hustad, 2005, ElKady et al., 2011). Combustors operating in diffusion or partially-premixed mode can operate in a wider range of limits and are less prone to flame instabilities when changes in the composition of the working fluid occur, such as operating in an O$_2$ depleted environment, but on the other hand, these systems produce less NO$_x$ emissions (Røkke and Hustad, 2005, ElKady et al., 2008, ElKady et al., 2009).

2.5 Formation Mechanisms of Pollutants in CO_2-Diluted Combustion

A diluent added into the combustion air stream can lower the flame temperature (thermal effects), reduce the concentration of reactive species (dilution effects) and its participation in the chemical reactions (chemical effects) can alter substantially the combustion process (Park et al., 2002, Liu et al., 2001). The thermal contribution of an additive is due to the different physical properties, such as its specific heat, thermal conductivity and absorption coefficient (for radiating species) (Liu et al., 2001). For that reason, various studies on the role of additives in the air stream are of paramount importance but there is lack of deep understanding of how the combustion chemistry and the flame structure changes despite earlier efforts.

The most challenging part in the experimental studies is to measure major and minor species and the temperature within the reactive flow field; most studies were concentrated on the exit exhaust emissions. The difficulties arise from uncertainties in gas analysis principles, flame perturbation by inserting sampling and thermocouple probes, species cross interference when multiple species are present and technical difficulties in taking gas samples from various positions within the hot environment of a flame. As a result, the aim of this study is to address these gaps by creating flame maps of the concentration and distribution of major species, as many as possible minor species and the flame temperature profile under different percentage ratios of CO_2 in the oxidiser stream.

The challenges arising from burning in a CO_2-enhanced combustion air are the effects of CO_2 addition on the burning process of the fresh reactants mixture, the flame temperature, flame stability and formation of pollutant emissions. As discussed in Section 2.3.2, the addition of CO_2 affects negatively the burning velocity through the reduction in the concentration of the radicals (Liu et al., 2003).

2.5.1. CO_2 thermal effects

As shown in the numerical study of Park et al. (2002), the peak flame temperature decreases with the dilution of combustion air. This study investigated the dilution effects of H_2O, CO_2 and N_2 addition to the air stream and found that the strongest influence is caused by CO_2 although water has the highest heat capacity among them. Consequently, the combination of the thermal and chemical effects of these diluents have a strong impact on the flame temperature. Park et al. (2002) concluded that the

thermal effects of CO_2 and H_2O are stronger compared to the effects of N_2 as was attributed to the higher radiative absorption coefficients of carbon dioxide and water. Lee et al. (2001) have concluded that CO_2 affects significantly the flame volume and reaction zone thickness and as such the radiative heat loss of the flame changes accordingly and in turn thus influences the flame temperature.

2.5.2. CO_2 chemical effects

Carbon dioxide has different chemical, transport, thermal and radiative properties compared to nitrogen, the main substance of air. Its chemical reactivity has gained significant research interest in many studies because it is valuable to understand its influence on the flame structure and chemistry. As it is not possible experimentally to detach the chemical effects of CO_2 from its thermal ones, a few numerical studies have invented the introduction of the imaginary chemically inert CO_2 which has the same thermodynamic, transport and radiative properties as CO_2 but it does not take part in the chemical reactions. This is an easy way to separate the thermal and the chemical contribution of CO_2 in a complicated combustion process. Dilution effects imply the relative decrease in the O_2 concentration in the oxidiser stream and consequently, the reduction in the concentration of chain active species, such as OH (Liu et al., 2001).

Liu et al. (2001) proposed two numerical models, one that accounted for all the chemical reactions that CO_2 is involved and the other which introduced this imaginary inert counterpart of CO_2. Both models were compared against the typical air combustion model to demonstrate the thermal contribution of CO_2. The main outcome was that CO_2 directly participates in the chemical reactions by inhibiting the formation of NO and N_2O (mainly due to the temperature dependency of the NO formation mechanism) and promoting the conversion of CO_2 by reacting with H atoms to produce OH, which encourages the oxidation of soot precursors and as a result, the suppression of soot formation (Liu et al., 2001). Comparison of flame temperature plots with and without the N_2 replacement with CO_2, and the fictitious CO_2 in the oxidiser stream revealed that apart from the different thermal properties of CO_2, its chemical participation in reactions yields a substantial reduction in the flame temperature.

The numerical study of Park et al. (2002) explained how the thermal and chemical effects of additives are interrelated and responsible for the changes in the flame structure. To illustrate this complex interaction, they studied the effects of both H_2O

and CO_2. The dissociation process of each species via third-body reactions and/or thermal decomposition in high flame temperature regions is different. As a measure of the progress of combustion, the chain initiation reaction, (R 2-14), is mostly used (Park et al., 2002). When H_2O breaks down, chain carrier radicals are formed, enhancing the reaction (R 2-14). On the other hand, when CO_2 breaks down, hydrocarbon intermediates are produced, thus inhibiting chain reactions; the H atoms attack much faster the hydrocarbons (Park et al., 2002).

2.5.2.1 CO_2 dilution effects on UHC emissions

In Section 2.3.2, the main oxidation pathways of methane were explained and in this section, the effects of adding CO_2 in these reaction pathways is examined. Calculated mole fractions of various C_1 and C_2 species have shown that the formation of C_1 species has been restrained whereas the diluent addition favours the increase of the concentration of some C_2 species (Park et al., 2002).

As observed in Lee et al. (2001), the peak concentration of hydrocarbon species shifts to the oxidiser side when CO_2 is added to the air stream where active radicals, such as O, H and OH, are in abundance. Reactions (R 2-15) and (R 2-16) reveal the direct chemical effects of the addition of CO_2 in the oxidation of methane (Liu et al., 2001):

$$CO_2 + H \rightarrow CO + OH \qquad\qquad \text{(R 2-15)}$$

$$CO_2 + CH \rightarrow HCO + CO \qquad\qquad \text{(R 2-16)}$$

Reaction (R 2-15) is mainly responsible for the increased concentration of hydroxyl and is the principle oxidation reaction at high temperatures in hydrocarbon flames. As illustrated in the numerical study of Lee et al. (2001), the first oxidation path of CH_3 forms CH_2 and CH which are directly related to the formation of N and HCN. As described in Section 2.3.1.2, the CH species contribute to the formation of prompt NO. Therefore, the changes in the reaction paths of the hydrocarbon intermediates affect dramatically the formation and destruction method of prompt NO emissions (Park et al., 2002). It is apparent that the chemical participation of CO_2 alters the oxidation process of methane and thus the combustion reaction rate.

2.5.2.2 CO_2 dilution effects on NO_x emissions

Another numerical study that adopts the same concept of the CO_2-counterpart gas was completed by Lee et al. (2001) which observed the effects of CO_2 addition on methane-

air flame structure and NO formation and destruction mechanisms. These numerical results confirmed the reduction of the flame temperature which causes an increase in the mole fraction of CH_4, as the fuel oxidation mechanisms are suppressed, and a significant decrease in the NO concentration when the amount of the added CO_2 is increased. As was explained in Section 2.5.2.1, the reaction pathways of methane are significantly altered by the addition of CO_2, thus causing a change in the production of the hydrocarbon products. The decrease in hydrocarbon species gives rise to the reduction of N and HCN and prompt NO emissions, as displayed in the major reaction pathways for methane-air flames in Park et al. (2002). In CH_4-air-CO_2 flames, prompt NO are dominant compared to the thermal NO emissions and it is therefore apparent that the addition of CO_2 changes the CH_4 reaction pathways in a favourable way for total NO_x emissions (Lee et al., 2001).

2.5.2.3 CO_2 dilution effects on CO emissions

Increase in carbon monoxide emissions is usually related to insufficient residence times as needed for complete oxidation of CO to CO_2. Other possible reasons are flame quenching at the flame front due to the strong turbulence, strong radiation heat loss, and dilution with cool air or cooler products recycled into the post-flame regions. In gas turbine combustors, CO emissions are increased at low load and in very fuel-lean conditions where unsteady flames are dominant and local quenching is very likely to occur. Therefore, under such conditions, Goldin et al. (2012) suggested that only a numerical model that incorporates unsteady behaviour of the combustion process is appropriate to predict accurately the CO emissions.

2.6   Research Gaps

Many experimental and numerical studies have investigated the effects of CO_2 as imposed on the gas turbine combustors (operability limits and exhaust emissions), on the capture plant (performance, size, cost and efficiency) and finally, on the performance of the gas turbine power generation systems (power output, overall efficiency, energy penalty). From these studies, the identified research gaps are as follows:

i.   Major species have been measured at the exit of the combustor or at the exit of the turbine system.

ii. There is lack of in-flame measurements of major and minor species and particularly there is no published work using an FTIR analyser for flame data.

iii. Limited number of experimental studies are available for confined flames and there is no published work on confined CO$_2$-diluted flames.

2.7 Summary

This chapter provided an overview of the flame types, flame stabilisation methods and the formation mechanisms of the pollutant emissions under air and CO$_2$-diluted combustion environments. Furthermore, considerable amount of literature has been published on the investigation of CO$_2$-diluted combustion systems for the improvement of the performance of a carbon capture plant. Finally, the research gaps on investigating the changes caused by CO$_2$ dilution on the flame chemistry were identified and the following chapters explain the contribution of this study towards filling these gaps.

CHAPTER 3- Experimental Facilities and Numerical Model

3.1 Introduction

The first part of this chapter focuses on the experimental setup, the techniques and instrumentation used to generate the results presented and analysed in Chapters 4 and 5. It also includes a description of the methodology employed for collecting and analysing the captured data and a summary of the experimental errors. The second part of the chapter presents a 1D numerical model that incorporates a detailed chemical kinetic mechanism and the interaction of the turbulence with the chemistry. The numerical results are presented and discussed in Chapter 6.

3.2 Burner Test Rig

The 10 kW burner rig used in this experimental work consists of a simple diffusion burner, a rectangular chamber and a series of heaters. The purpose of this investigation is to study natural gas flames in a well-enclosed environment that would ensure the amount of air introduced to the flame is known and the flame is free of any distortions compared to an open flame. The burner was originally built with a perspex enclosure to investigate the effects of various diluent gases on the combustion of low calorific value fuels. As such, modifications on the burner rig were necessary due to the high temperature application of this study. Therefore, a well-insulated mild steel chamber was fabricated with a convergent open end at its top part for the exhaust gases to be vented into the chimney duct after being diluted with fresh air from a fan, as seen in Figures 3-1 (a) and (b). Initially, the three heater elements, as described in Section 3.2.3, were utilised to preheat the oxidant stream but during initial tests they were burnt out and for health and safety issues they could not be replaced without major modifications.

3.2.1 Diffusion burner

The design of the utilised diffusion burner was based on the same model used at the Sandia National Laboratory in Livermore and the BOC Group Technical Centre in

USA. A number of previous studies have also utilised the same burner, as for example, Howard (1998) investigated oxygen-enriched methane flames.

Figure 3-1 Photographs of the (a) old and (b) the modified combustion chamber.

This burner can only be used with gaseous fuels and consists of a central fuel tubing mounted within a low velocity co-flow. The uniform shrouded flow is created through different types of flow straighteners; thin-walled honey combs, sets of fine-wire meshes and a contraction section, as depicted in Figure 3-2. Stainless steel tubing, 18" length and 4.57 mm internal diameter, is used throughout this study for the supply of natural gas. For simple jet flames, the fuel jet originates from the central tube and supplies a high-speed flow of natural gas into the shrouded oxidant stream. Please refer to Appendix A for further information on the desired development of this burner.
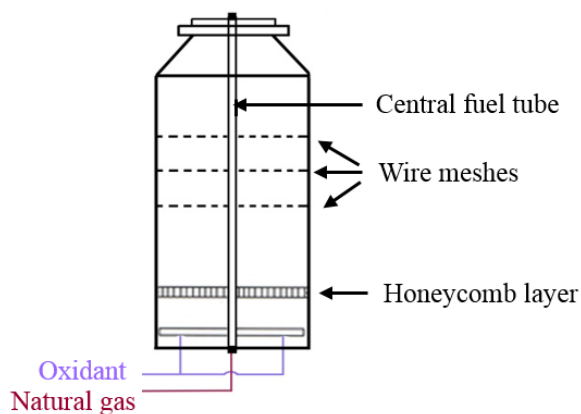
Figure 3-2 Schematic of the diffusion burner.

3.2.2   Combustion chamber

A mild steel combustion chamber is designed to accommodate natural gas flames within an enclosed, controlled environment to investigate the effect of the addition of CO$_2$ into the combustion process. The cross section of the chamber was square with side dimension of 240 mm and its height was about 1.7 m, including the top convergent part. For flame visualisation, a circular quartz window is used on one side, as seen in Figure 3-3 (left hand side). The design ensured a gas tight combustion system by including high temperature gaskets, compression fittings and a top tapered section. Please refer to Appendix B for more information on the development of this rig. The chamber is designed as such to allow for temperature and gas sampling probes to traverse in two dimensions, axially and radially. Multiple probes can be fitted into the chamber, thus allowing for sampling within the whole flame length (including the flame tip) and at the exit of the chamber creating 2D flame maps, as shown in Figure 3-3. The main body of the chamber was double insulated internally and externally by using a rock-wool blanket with external foil-faced surface to prevent from fibre inhalation. Figure 3-4 shows the internal insulation, which consisted of a 25 mm compressible ceramic refractory fibre blanket and a 25 mm ceramic refractory fibre board.
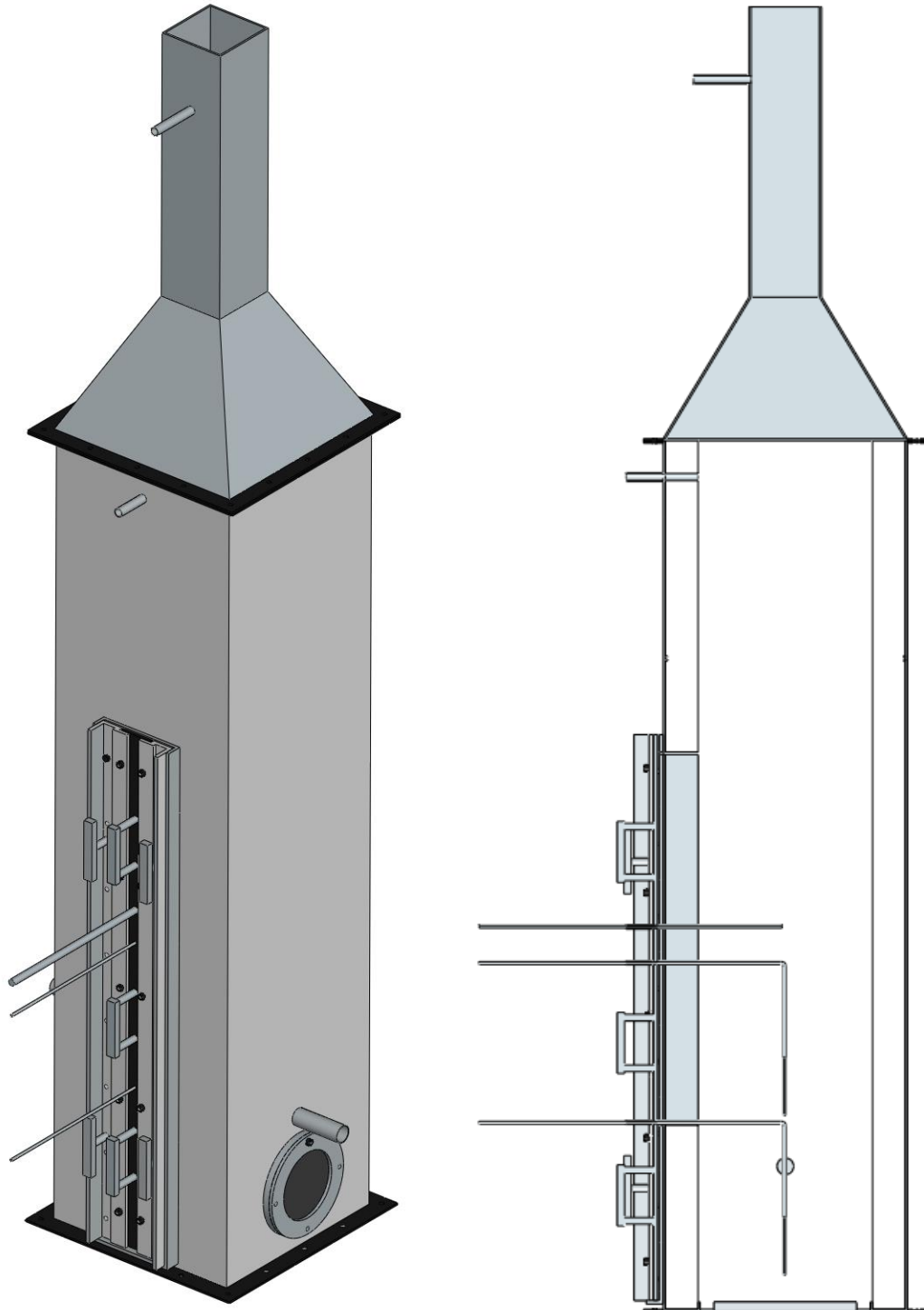
Figure 3-3 Drawings of the design of the in-house built chamber.

Figure 3-4 Photograph of the internal insulation of the utilised chamber.

3.2.3   Heaters

As seen in Figures 3-5 and 3-6, a series of heaters are connected to the burner housing to meet the needs for preheating the oxidiser stream. Figure 3-5 shows a photograph of the heaters setup and Figure 3-6 is a photograph of the last heater (heater band) which is wrapped around the burner housing. The power rating of the heater band is 3 kW and is supplied by Hedin ltd. The middle heater is an in-line heater off 6 kW power supplied by Sylvania and the first heater is off 0.75 kW, supplied by RS Components. During the initial experiments two heaters were burnt out and the third was not sufficient to preheat the oxidiser flow to the required elevated temperatures. All heaters were controlled via PID controllers.

3.2.4   Fuel supply

Natural gas was supplied by the main supply line and its flow rate was measured using a manual flow controller. A UV flame detection probe was installed around 2 " above the burner exit and with the use of two solenoid valves the fuel supply could be shut down automatically in case of flame failure or extinction. The composition of natural

gas was not constant during the tests and thus an average composition was used for the mass balance calculations, which is shown in Table 3-1.

Table 3-1 Mean composition of natural gas

Mean dry calorific value (MJ/m³)	39.84
Gas substances (vol %)	
Nitrogen	0.92
Carbon dioxide	1.74
Methane	89.45
Ethane	5.76
Propane	1.58
Iso-butane	0.21
N-butane	0.21
Neo-pentane	0.00
Iso-pentane	0.05
N-pentane	0.03
Hexane	0.05

Figure 3-5 Photograph of the heaters setup.
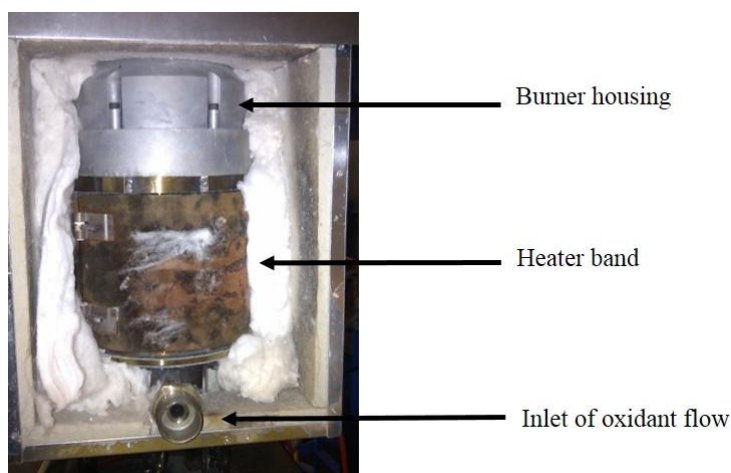
Figure 3-6 Photograph of the heater band.

3.2.5 Oxidiser supply

Combustion air was supplied by a compressor/chiller system and regulated at a pressure of 3 bar. The compressor system included a humidifier for removing moisture. A pressure gauge was installed also at the outlet of the air flow controller to estimate the pressure of the flow going into the burner. Carbon dioxide was supplied by BOC Gases and pressure gauges were installed at the supply line and at the outlet of the CO$_2$ flow controller. A mixed gas pipe was fitted for the CO$_2$ dilution tests where the air flow was mixed with CO$_2$ prior to the burner entry.

3.3 Experimental Techniques

The combustion chamber is designed for detailed in-flame, post-flame and exit measurements and thus full characterisation of the natural gas combustion process is achieved through a range of experimental techniques. The design of the chamber is such that multiple gas sampling probes and/or thermocouple probes could traverse along the chamber in two dimensions allowing for axial and radial measurements. Using this design, it was possible to make "flame maps" showing the distribution of gas species concentration and temperature from the burner nozzle exit till the exit of the chamber under the test conditions presented in Chapters 4 and 5.

3.3.1   Temperature measurements

Among the temperature measurement techniques, such as the optical (Raman scattering, CARS and 2-line LIF) and the probe-based techniques (suction pyrometer, thermocouple probes- TC), the most common method in a laboratory or for in-furnace measurements is the use of a thermocouple probe. Thermocouples consist of two different metal wires which are joint together on one end to create a junction, such as the type-R thermocouple wires depicted in Figure 3-7. When there is a temperature difference along the length of a metal wire, electrons will start to diffuse from one end to the other, creating an electrical potential. The movement of the electrons is called Seebeck effect; different metals have different Seebeck coefficients and the operation of a thermocouple is based on this difference. As a result, the bead ensures that there is no electrical potential difference at this point but is the initial location where a thermoelectric voltage starts to develop. It should be mentioned that this junction, known as the thermocouple bead, does not measure the local temperature value (ASTM International, 1993).
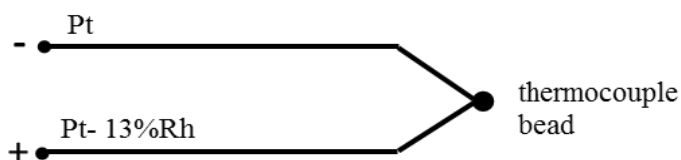
Figure 3-7 Schematic of the structure of thermocouple type-R fine wires.

3.3.1.1 Thermocouple types and limitations

The use of fine wire thermocouples for flame temperature measurements has been extensively used (Heitor and Moreira, 1993, Shaddix, 1999); unsheathed, bare wires are available in different combinations of metal and metal alloys and are known as type J, K, N, R, S or B. Initially, unsheathed thermocouple wires were used as the combination of platinum and 13%-rhodium/platinum (type-R) is ideal for high temperature applications. The thermocouple bead was constructed (by the supplier) by welding two wires off 0.127 mm diameter. The thermocouple wires were mounted in a twin-hole ceramic insulator to protect the wires and connected to a miniature size plug, as seen in Figure 3-8. To avoid any catalytic reactions on the bead surface, which could alter the thermocouple readings, a special coating was applied before taking any measurements. The coating was made by poisoning a gaseous fuel, propane was used here, with a ready solution of HMDSO (hexamethyldisiloxane). The layer of coating was made using a blowtorch with a very high temperature flame which created a thin layer of silicon dioxide (SiO$_2$) on the bead, according to Kaskan (1957). Other types of coating have been reported in Shaddix (1999) study but all of them are prone to degradation after prolonged use and this is the reason for considering to re-apply a layer of coating if it has been visually destroyed. The thickness of the coating layer was measured using a Nikon Profile Projektor, Model V-16D, by measuring the bead before and after coating.

Figure 3-8 Photograph of the fine wire thermocouple probe.

Initial experiments with fine wire thermocouples proved that this method is not suitable for the nature of these experiments as the wires kept breaking. Fine wires after a prolonged use at high temperatures become brittle and susceptible to breakage. In addition, it was difficult to judge the exact spatial location of the bead as when the exposed wires became hot, they tended to shift slightly upwards. The movement of the exposed part of the wires could be justified due to the flame velocity forcing them upwards; this was also a visual observation during the experiments. As reported in Warren (1994), bare wire thermocouples are only suitable for low temperature applications and where the flow is subsonic whereas sheathed thermocouples should

be used at high temperature environments. Together with their high cost and limited availability, a 3 mm mineral insulated thermocouple was used throughout this study.

Type-N sheathed thermocouples are made of nicrobell material, which is a nickel chromium alloy, and the wires consist of a combination of nickel-chromium-silicon (or else known as nicrosil) and nickel-silicon-magnesium (or else known as nisil) alloys. They can withstand temperatures up to 1250 ℃. Sheathed thermocouples cannot capture high temperature fluctuations which are dominant in turbulent flows as their response is slower than bare wires. The highest standard deviation (std) value for the utilised type-N was about 15 ℃ whereas the std values obtained when using the type-R wires could be even up to 28 ℃, depending on the sampling location. However, for the purpose of this study averaged temperature measurements are only needed and the sheathed thermocouples are robust enough and can measure accurately within the flame zone. The temperature readings were recorded using a data-logger device and monitored through an in-house written LabView programme.

3.3.1.2 Errors associated with temperature measurements

The thermocouple probe does not measure the actual temperature of the flame due to complex heat transfer phenomena occurring along the wire and the bead and/or the sheath. A simple description of these complicated mechanisms is presented in this section, conventionally we will refer to the wires and bead as this is a more general reference to any type of thermocouple. The flame heats up the bead and the cooler walls of the combustion chamber (convection heat gain); the bead radiates heat to the walls (radiant heat loss); a temperature gradient occurs along the length of the wires (conduction heat loss); if chemical reactions occur at the wire surface, then its temperature is higher than the flame (surface-induced catalytic reactions- heat loss). According to Blevins and Pitts (1999), in the cooler regions of the flame, the surrounding environment could emit significant heat to the thermocouple (radiant heat gain) and in the case of a diffusion flame, the emissivity of the soot particles should be accounted for (radiant heat gain). Shaddix (1999) agreed with the conclusions of Blevins and Pitts (1999) and emphasised that the environment around a thermocouple probe introduces many different sources of thermal radiation, such as the hot combustion products with infrared emission (CO, CO$_2$ and H$_2$O), the soot particles and the surrounding walls. Consequently, the correction of the measured temperature measurements for heat exchange becomes a difficult task. If the convective heat

transfer dominates the heat transfer mechanism, then there wouldn't be a need for correcting the measured temperature data because the thermocouple measurements would define the local gas temperature.

For fine-wire thermocouples, conduction heat loss is relatively less important compared to the convection heat transfer whereas the radiation energy loss is a function of the fourth power of the absolute temperature. In order to eliminate the conduction heat losses, the smallest possible diameter and sufficiently long wires are chosen. Larger diameter wires show higher thermal inertia and a longer response time is required (Shannon and Butler, 2003). According to Heitor and Moreira (1993), the conduction heat losses become negligible for length-to-diameter ratio above 200. In order to eliminate any catalytic reactions, a special non-catalytic thin layer of coating should be applied on the thermocouple bead to inhibit any chemical reactions (Shaddix, 1999). Shannon and Butler (2003) concluded that for flames where high temperatures exist, the proportionality of the radiation heat loss to T^4 makes the surrounding environment colder than the thermocouple probe and thus it does not emit radiation back to the bead. For the sheathed thermocouple probe that was finally used for the presented results, only radiation heat loss will be accounted for and the correction methodology is presented below.

3.3.1.3 Radiation heat loss corrections

Bradley and Matthews (1968), and later Blevins and Pitts (1999), had extensively studied models to quantify the heat transfer mechanisms between a thermocouple probe and its surrounding environment. All models are based on the energy balance on the thermocouple probe as described as follows:

$$\dot{Q}_{cat} + \dot{Q}_{conv} + \dot{Q}_{rad} + \dot{Q}_{cond} = \rho \, C_p \, V \, \frac{dT_{TC}}{dt} \qquad \text{(Equation 3-1)}$$

For sheathed thermocouples, the sheath material is not prone to catalytic reactions and thus this term can be neglected ($\dot{Q}_{cat}$). Conduction heat losses are minimised by long thermocouple wires and as such, long thermocouple probes ($\dot{Q}_{cond}$). Therefore, the convection heat gain ($\dot{Q}_{conv}$) and the radiation heat loss ($\dot{Q}_{rad}$) become the dominant heat transfer mechanisms from/to the sheathed thermocouple probe. The convection-radiation temperature error can be expressed as follows (Kaskan, 1957):

$$\Delta T_{\text{conv-rad}} = \frac{1.25 \, \varepsilon \, \sigma \, T_{TC}^4 \, D^{0.75}}{\lambda} \left(\frac{\eta}{\rho \, U} \right)^{0.25} \qquad \text{(Equation 3-2)}$$

where ε is the emissivity of the thermocouple, estimated approximately to be 0.19 from the nickel emissivity which is the main component of the sheath and of the wires (above 80 %), σ is the Stefan-Boltzmann constant (5.67 10^{-8} J / s m^2 K^4), λ is the thermal conductivity of the fluid (W / m K) at the measured temperature, T_{TC}, (K), η is the dynamic viscosity of the fluid at the measured temperature (kg / m s), ρ is the density at the measured temperature (kg / m^3), U is the fluid flow velocity (m / s) and D is the bead diameter (m). The thermal conductivity and viscosity are calculated assuming that the fluid is air using the available data from Svehla (1962) for a wide range of temperatures. The convection-radiation temperature error is added to the measured thermocouple temperatures and the data presented in Chapters 4 and 5 are after applying this correction. The detailed methodology for temperature corrections is presented in Appendix D.

3.3.2 Gas species measurements

Gas samples were taken from multiple points within the flame and at the exit of the combustion chamber to create flame maps of the distribution of combustion species for the different test conditions as presented in Chapters 4 and 5.

3.3.2.1 Gas sampling probes

Samples were withdrawn from the flame zone using an uncooled quartz probe in a right-angle shape, as depicted in Figure 3-9. Quartz is commonly used in high temperature applications and especially, when low catalytic sensitivity becomes an important characteristic. The probe is connected via a PTFE line to a series of gas analysers. Its right-angle shape allows for alignment with the flow and minimises the disturbance to the flow; its length should be at least six tube diameters downstream of the sampling volume area, according to Drake et al. (1987). At the exit of the chamber, a straight ceramic probe is used as there is no concern about interfering with the flow and is positioned at the centre since the exhaust gases are fully mixed downstream of the flame zone.
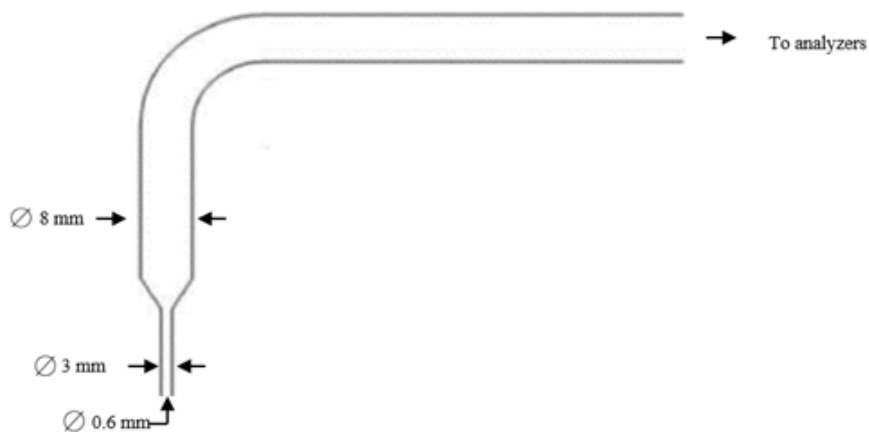
Figure 3-9 Sketch of the quart right angle probe employed.

The greatest errors in the probe sampling method originate from the effects of the probe size and shape on the flame due to the radial shift in the flow streamlines around the probe tip and also, the continuation of the combustion reactions within the probe. Most of the reactions depend strongly on the temperature and/or pressure and thus a successful in-flame sampling method is the one that provides the most rapid reduction in the sample temperature and pressure to suppress any radical recombination reactions within the probe (Fristrom, 1983). Successful suppression of the chemical reactions means that the species measurements will be representative of the species local concentration at the sampling volume area (Chiappetta and Colket, 1984). In order to reduce the flame disturbance by inserting a probe, a narrow width probe tip and a right-angle shaped probe should be used.

There are three different types of probes: convective cooling or isokinetic, aerodynamic quenching and dilution sampling probes. Quenching is essential when equilibrium conditions have not been reached and the reactions can continue within the probe (Colket et al., 1980). To reduce the temperature of the gas sample, the heat released by combustion should be transferred to the cooled walls of the probe (convective heat transfer). Another option is to expand the probe diameter rapidly so that supersonic speeds are achieved inside the probe and cooling through the walls will eventually reduce the sample temperature (aerodynamic quenching). The last option is to dilute the sample with a low temperature inert additive which will absorb the heat of the hot flame gases (dilution effect) (Colket et al., 1980, Chiappetta and Colket, 1984). In this study, aerodynamic quenching is chosen as it yields higher quenching rates.

Other researchers have used similar type of probes, such as Colket et al. (1982) who studied the effects of the probe size on achieving aerodynamic quenching and investigated experimentally microprobes (orifice diameter of 75 μm) and macroprobes (diameter of 2000 μm) and developed a model to predict under which conditions aerodynamic quenching is achievable. One of the reactions greatly affected by sampling errors is the conversion of NO to NO$_2$ within the probe due to the temperature drop. Drake et al. (1987) conducted a detailed study using four different quartz and stainless steel probes, of different designs and both cooled and uncooled probes, in order to reveal the probe sampling effects on the formation of thermal NO$_x$ emissions in diffusion flames. They suggested that sampling with uncooled quartz probes in fuel-lean regions can convert most of the NO to NO$_2$ within the probe. However, in fuel-rich flame regions, these species are not affected substantially by the probe size and shape (Drake et al., 1987). In post-flame regions, probe reactions are eliminated due to the low local flame temperatures and low radical concentrations which inhibit any further reactions within the probe.

During the experimental campaigns presented in Chapters 4 and 5, right-angle shaped uncooled quartz probes were utilised to sample within the flame. Whereas at post-flame regions and at the exit of the chamber, ceramic straight probes were used as they withstand high temperatures and are less fragile which makes them easier to handle.

3.3.2.2 Sampling system

Gas samples are extracted using customised quartz and ceramic probes from multiple locations within the flame and at the exit of the chamber. Despite the differences in the probe types, the rest of the sampling system is the same and thus it can be seen in Figure 3-10.

Gases from the hot combustion chamber were drawn into the probe and then using PTFE lines they were passed through suitable traps (Drechsel bottle) to remove moisture and particulates from the sample before being introduced into the gas analysers. A series of filters follows to remove the majority of the large soot particles. Initially, a pre-filter system, consisting of glass microfiber filters for 2.7 μm particle size, is used as they are capable of attaining a high volume of particles at elevated temperatures and they are resistant to moisture. After this level of filtration, the sample is introduced to a ceramic based filter for removal of 2 μm particles to ensure that a

soot-free sample will enter the set of analysers. The conditioning unit of the analysers filters again the incoming sample for much finer particles, 0.7 μm particulate filter, and then pressurises it via a heated sample pump fitted with a bypass flow control. The bypass flow is essential to ensure that a constant flow of the necessary amount of gas is drawn by the analysers and any excess amount is vented out. Afterwards, the sample is dried by a chiller for any water condensation. Finally, a manifold distributes the sample to the five analyser units.
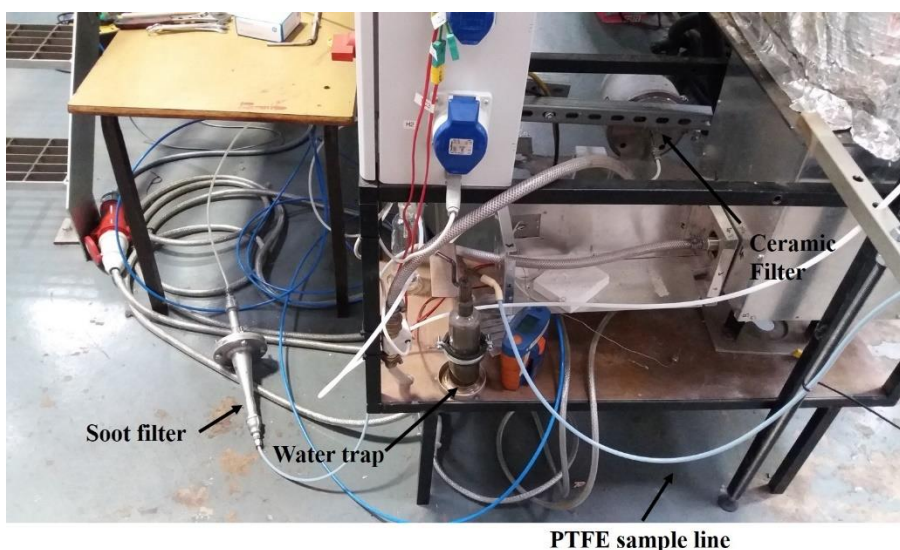
Figure 3-10 Photograph of the sampling system.

3.3.2.3 Oxygen analyser

A Signal multi gas analyser, fitted with a paramagnetic analyser, is utilised for measuring the dry oxygen concentration. The principle method of this analyser is the positive magnetic susceptibility property of oxygen. Most substances possess magnetic properties, either positive (are attractive to magnetic fields) or negative. Other common gases have paramagnetic susceptibilities, such as NO and NO$_2$, but they are present in traces compared to the oxygen concentration. In addition, the susceptibility property of O$_2$ is hundreds of times greater than NO$_x$ or other gases (Signal Group, 2009).

3.3.2.4 Carbon dioxide and carbon monoxide analysers

Signal infrared analysers are used to measure the concentration of CO$_2$ and CO emissions. Most gases absorb infrared light and particular gases absorb well at specific wavelengths. Therefore, the wavelength can be used to discriminate between the

different gases being absorbed. Inside the analyser unit there are two separate sealed cells with the sample and a non-absorbing gas. The radiation light passes through each cell in turn and when radiation passes through the sample with the infrared active molecules, part of it is absorbed. The difference in signal is measured by the detector and is related to the amount of the absorbing gas being present in the detector cell (Signal Group, 2002).

3.3.2.5 Nitric oxide analyser

A Signal chemiluminescence analyser is used to measure simultaneously the concentration of NO, NO$_x$ and NO$_2$. Chemiluminescence can only detect NO and a converter is used to convert any NO$_2$ to NO. The conversion is accomplished by passing the sample gas through a heated tube containing a carbon material. For measuring nitrogen dioxide, the analyser automatically cycles between NO and NO$_x$ and subtracts the NO readings from the NO$_x$ ones to give the NO$_2$ concentration. The converter is designed as such to prevent any reactions between NO, CO and ammonia by selecting a special carbon material instead of stainless steel and by sustaining an elevated temperature to avoid side reactions with ammonia (Signal Group, 2008).

3.3.2.6 Total unburnt hydrocarbon analyser

A Signal flame ionisation analyser is used to measure the hydrocarbon concentration in a gas sample. Any carbon-hydrogen bonded molecules present in a hydrogen flame can form carbon ions. The detector responds to the carbon ions and gives an output proportional to the carbon count. The concentration is either in methane or propane equivalent; e.g. 10 ppm of C$_3$H$_8$ give an output of either 40 ppm in methane equivalence or 13.33 ppm in propane equivalence. The model used here is setup in methane equivalence (Signal Group, 2004).

3.3.2.7 Fourier transform infrared analyser

Fourier Transform Infrared gas analysis (FTIR) is a spectroscopic technique that is based on the absorption of infrared light which can change the vibrational and rotational status of a molecule. The IR spectrum of a molecule is a unique fingerprint and thus it is easy to distinguish the absorption spectra of multiple IR active molecules. In high efficient combustion systems, the dominant gases are water vapour and carbon dioxide which both absorb in the IR spectrum in broad bands and due to their high

concentration, their absorption is much higher than the absorption of trace species. As reported by Amand (1999), it is possible to measure species in trace levels where water vapour and carbon dioxide can interfere. Various researchers have used an FTIR analyser to monitor emissions from combustion devices or from exhaust stacks, such as Hilton, 1998 and Marran, 2000. The only traditional analyser that FTIR cannot compete with is the paramagnetic oxygen analyser since elemental diatomic gases do not have infrared spectra.

The model used in this study is the Gasmet Dx-4000 by Quantitech. It is a portable multicomponent FTIR gas analyser which is setup to detect 12 species simultaneously in this study. The analyser comes with a portable sampling system which includes a heated sample pump, a heated filter element (of 0.1 μm particle retention) and heated sample lines; all parts are heated to 180 °C (Gasmet Technologies Qy, 2013). This analyser is used for measuring at post-flame regions as within the flame zone the sample spectra were saturated and could not be resolved. Enhanced spectral analysis with added interfering species and manual peak fitting were attempted but the final signal was too saturated and the highest peaks of the dominant species could not be resolved for the in-flame measurements.

3.3.2.8 Measuring system

The sampling and temperature probes are fitted into the ports which are welded onto the sliding metal plate, ½" ports in diameter, and reducing unions with compression fittings are used to accommodate the different size probes used in this study. Temperature probes could be used in both the smaller, ¼", and the larger diameter ports, ½", whereas the quartz and ceramic probes were used only in the larger diameter ports, ½", at the front side of the chamber, as seen in Figure 3-11. Compression fittings with PTFE ferrules are used in all ports to allow for easy and quick adjustment of the radial location of the probes; PTFE ferrules allowed for short "radial movements". In addition, these fittings provided ease on locking the probe accurately at a specific location and provided a good gas tight seal around the probe by eliminating air ingress during measurements.

The positioning of the probes is mainly calculated from the CAD drawings of the combustion chamber but is also verified visually through the window port for the low axial positions. These checks are carried out daily prior to any sampling and thus any

discrepancies are taken into account when reporting the axial and/or radial position of the probes. The accuracy of the axial/radial location is ± 0.5 mm. To accurately locate the probe within the combustion chamber, the distance between the welded ports on the sliding plate and the end of the probe is measured and correlated to the depth until the centre of the chamber; Figure 3-12 depicts the measuring method.
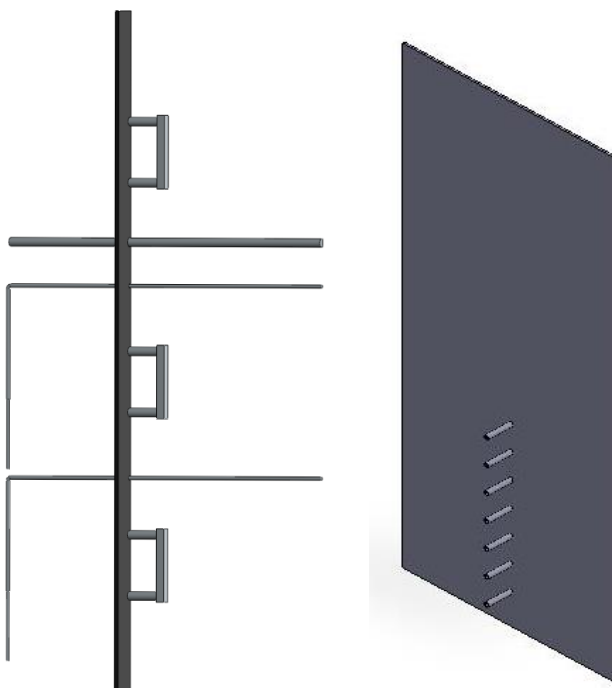
Figure 3-11 Schematic of the sliding metal plate with fitted multiple probes, ½" (left side), thermocouple ports, ¼", at the back side of the chamber (right side).

All the radial measurements are then calculated from the centre of the chamber and the same procedure was followed for the thermocouple probes. For aligning the quartz probe tip into the flame, a metal pointer was used and its alignment was checked every day before sampling, see Figure 3-13.
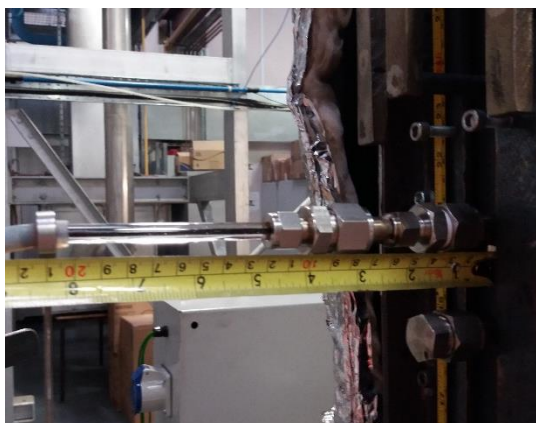
Figure 3-12 Photograph illustrating the measuring method.

Figure 3-13 Photograph of the probe alignment procedure using a pointer.

3.4 Experimental Methodology

3.4.1   Typical testing day

A typical testing day starts with turning on the Signal analysers to warm-up which takes at least 2 hours. If the quartz probe is to be used, alignment is needed to ensure the correct position of the probe tip within the flame. The Drechsel bottle is emptied and resealed using silicone grease and the soot filter is replaced by a new filter. The rig is purged with air for a few minutes and after a quick check that it is safe to be lit, the burner is ignited according to the light-up process. Always firing up begins with over 3 % excess air to ensure that the exit CO emissions are very low. A second analyser is used to monitor the O$_2$ and CO$_2$ exit emissions throughout the day to check for any leaks or issues with the gas supply system and this analyser is left on during the night. The next step is to calibrate this portable analyser and proceed to leak testing the sampling system, as described in the following Section 3.4.2. At this point, the desired air baseline flow rates are set according to the experimental matrix spreadsheet. After a successful leak test on the sampling system, the recording of the exit emissions starts and typically after 45 minutes the rig reaches its steady state condition. Once the air baseline has been established the flow rates can change to reflect the conditions of the day's test. During this time period, the Signal analysers have warmed up and the operator proceeds to calibrate them, as explained in section 3.4.3. Upon successful achievement of steady state of the day's test conditions, the measurements can start. When temperature measurements are about to be collected, then the start-up process begins with the light-up of the burner, the calibration of the

portable analyser and the leak test of the sampling system. All the other processes remain the same.

Usually during a testing day, the test conditions do not need to change to another test condition but if is necessary then the air baseline conditions are reached first for half an hour and then the new test conditions are set and steady state is reached after at least 30 minutes. During this changeover, the exit emissions are continuously logged. During a day, every one hour in the morning and every two hours in the afternoon it is necessary to stop sampling and check if there is any drift from the morning calibration values of the Signal analysers. The same process applies to the portable O_2/CO_2 analyser which monitors the exit emissions. Moreover, the soot filter is changed periodically, every 2.5 hours. Real-time data is displayed in an in-house made software for species concentration and in an in-house made LabView programme for temperature measurements.

At the end of a testing day, if the CO_2 supply is on, its supply is shut down first and then the fuel supply. The maximum air flow is set in order to promote a faster cooling of the rig and the rig is safe to be left unattended after 1hour. Within this time the gas sampling lines and probes are purged with compressed air to remove any soot and water. In addition, a last check of the analysers drift is carried out and then they are left for sampling ambient air for at least 30 minutes to remove any soot in the lines and purge their internal cells.

3.4.2   Leak testing procedure

Two leak tests are carried out daily prior to any sampling to check the air tightness of the sampling system and the sampling line to the Signal rack. Leaks are detected by introducing N_2 to the system and monitoring the O_2 level as an indicator of any air entrainment. This procedure also reveals any carbon particles remaining in the sampling line to the Signal rack as all species are monitored during the leak test.

During the commissioning of the burner rig, "smoke tests" were performed to reveal the location of the leaks. Smoke pellets were inserted through the window port, it was then sealed back, the exit of the rig was also blocked and blowing air through one of the small diameter temperature ports, the smoke could only escape through the leaking points. This was not a regular procedure as the new rig was leak-free and the exit emissions of the chamber were monitored throughout the day.

3.4.3 Calibration procedure of Signal analysers

Analysers with linear response need to be calibrated at two points, namely the zero and the span point. The latter one should correspond to about 75-80 % of the maximum expected species concentration. The calibration gases were permanently piped to the Signal rack, thus allowing for quick calibration checks during and at the end of a testing day. The manual calibration process always begins with establishing the zero point of all analysers using zero grade nitrogen as a zero gas. The span points were calibrated with Beta Standard calibration gases, $\beta = \pm 2$ % accuracy. A "cocktail" gas cylinder consisting of 91.2 ppm CH_4, 147 ppm CO, 14.85 % CO_2 and 3.01 % O_2 in balance of N_2 was used for calibrating the span points of the IR CO and CO_2, paramagnetic O_2 and THC FID analysers. To calibrate the span point of the NO chemiluminescent analyser, a gas cylinder with 414 ppm of NO and 2 ppm of NO_2 in balance of N_2 was used. The span gas concentrations are selected according to the expected measurements and therefore, two more cylinders were used to check the linear response of the analysers at higher measuring ranges. For the FID analyser, a propane gas cylinder off 1004 ppm propane in balance of N_2 was utilised and for high levels of CO, a 2 % CO in balance of N_2 was used.

When a drift in the zero point, low and high span points is reported, the collected data need to be corrected accordingly. When only a zero drift is identified, the offset is simply added to the measured values. For a span drift, interpolation between the zero and span points and the zero and span calibration drift points is carried out.

3.4.4 Gas flow rates calculations

The utilised manual flow controllers were calibrated by the manufacturer using air at 15 ℃ and 1 bar absolute pressure and calibration charts were produced. These charts provide the conversion of the rotameter tube reading (in cm) into air flow rates (l/min at the above temperature and pressure conditions). The indicated flow rate is corrected for different operating pressure and density to represent the actual gas flow rate. The pressure correction is achieved using a pressure gauge at the outlet of the rotameter and the density correction is needed to account for the different density of methane and carbon dioxide. Changes in the temperature of the gases negligibly affected the flow rate and thus they are not taken into account.

3.4.5   Mass balance calculations

An experimental spreadsheet was made to perform simple mass balance calculations assuming complete combustion of natural gas. The outlet gas concentration of oxygen and carbon dioxide are used as a guide to setup the fuel and oxidant flow rates.

3.4.6   Processing of experimental results

3.4.6.1 Emission index

Depending on the combustion system, such as boilers or gas turbine engines, the emissions level is expressed in different units, such as kg/m^3 or gm/kW, and as a result, a method to normalise the emissions level is necessary. For this purpose, the emission index, EI, a non-dimensional quantity, is used and is defined as the ratio of the amount of emitted pollutant species (in grams) per unit mass of the fuel burnt (in kilograms), independently of the dilution level of the exhaust gases.

To calculate the emission index of NO$_x$ at post-flame regions and further downstream (at the exit of a combustion system), where it is safe to assume that all carbon is oxidised to CO$_2$, the following equation is utilised:

$$\text{EINO}_x = \frac{x_{\text{NO}_x} \; \text{MW}_{\text{NO}_2}}{x_{\text{CO}_2} \; \text{MW}_{\text{CH}_4}} \times 1000 \; (\text{g/kg}) \qquad \text{(Equation 3-3)}$$

Equation (3-3) has been derived by the study carried out by Takeno and Nishioka (1993), x represents the mole fraction of a species and MW is the molecular weight of a species. The molecular weight of NO$_2$ is conventionally used here as all the NO emissions eventually are converted to NO$_2$ emissions in the atmosphere and regulations on NO$_x$ exhaust emissions are reported as NO$_2$ equivalent. Moreover, radial measurements of NO and NO$_x$ at the exit of the combustion chamber, used in this study verify that the NO$_x$ emission index does not vary in the radial direction, where well-mixed conditions occur; this is in excellent agreement with the experimental study of Driscoll et al. (1992).

3.4.6.2 Mixture fraction

Mixture fraction calculations, Z, are computed on a carbon atom balance basis taking into account the emission measurements of fuel (assumed to be pure CH$_4$), CO and

CO$_2$, according to the Equation (3-4). The mass fractions, Y, are calculated on a wet basis and $Y_{c,j}$ denotes the mass fraction of the carbon atoms included in the fuel jet stream which is equal to 0.75 for a methane fuel stream. Another way of representing the progress on the combustion process within the flame is plotting the species measurements in the mixture fraction space; the mixture fraction is basically the fraction of the fuel stream in the total mixture. For regions below the stoichiometric mixture fraction ($Z_{st} = 0.055$ for methane-air mixtures), the fuel is in shortage (fuel-lean zone) and the combustion terminates when the mass fraction of the fuel becomes zero (fuel is consumed) (Masri et al., 1988, Masri and Bilger, 1986):

$$Z = \frac{\left(\frac{12}{16.032} \, Y_{CH_4} + \frac{12}{28} \, Y_{CO} + \frac{12}{44} \, Y_{CO_2} \right)}{Y_{c,j}} \qquad \text{(Equation 3-4)}$$

3.4.6.3 Conversion from wet to dry basis

The experimental data collected using the Signal analysers are on a dry basis as moisture is removed prior to analysis. For the mixture fraction calculations, the mole fractions of the species need to be converted to a wet basis. Therefore, Equation (3-5) is used to convert the reported gas species from dry to wet basis as follows:

$$\text{Wet mass fraction} = \frac{\text{Dry mass fraction}}{1 + \text{dry mass fraction of water}} \qquad \text{(Equation 3-5)}$$

3.4.7 Error analysis

This section describes all sources of measurement errors concerning the collected data. The most significant error source comes from the precision of the measurement devices (Signal and FTIR gas analysers and thermocouples). To extract the total error, a statistical analysis is used since all errors are random, cannot be entirely eliminated by good experimental practices and are independent of each other. Random errors can be reduced by averaging over a large number of data and that is the reason for presenting averaged gas species concentration and temperature data in Chapters 4 and 5. In addition, errors must be independent so that they can counteract their effects. The total error can be calculated as follows, according to Taylor (1997):

$$E_{\text{total}} = \sqrt{E_1^2 + E_2^2 + \ldots + E_n^2} \qquad \text{(Equation 3-6)}$$

where E symbolises any error source and n is the total number of error sources. The statistical uncertainty was determined as $\pm$ 1 standard deviation or $\pm$ 2 standard deviations or $\pm$ 3 standard deviations from the averaged measurement value. Table 3-2 presents the sources of measurement errors related to the species gas analysis using the Signal analysers.

In Table 3-2, a summary of all the experimental error sources originating from the use of the Signal gas analysers (from the instrument and the calibration gases) is presented as taken from the manuals of the analysers (which are indicated with an *asterisk) or the factory calibration certificates (without the asterisk). FSD (full scale deflection) refers to the analyser range used during the measurements and pk-pk (peak to peak) refers to the error between the minimum and the maximum signal during the factory error calibration process. In addition, for the THC, NO$_x$, CO and O$_2$ analysers it was taken into account the two different measuring ranges as the measurements were within both ranges. Some errors from Table 3-2 are neglected when calculating the total error uncertainty, which is summarised in Table 3-3. These errors are the NO$_x$ converter efficiency, since only NO$_x$ measurements are reported in this study, and the analysers' drift (zero and span), as calibration checks were performed every 1 or 1.5 hours during sampling. Any drift was noted and the collected data presented in Chapters 4 and 5 were corrected. In addition, drift due to changes in the ambient temperature are not taken into consideration as the analysers were allowed to warm up and reach full accuracy before any measurements were taken and the regular calibration checks incorporated any drifts due to temperature changes. Finally, cross sensitivities are found to be negligible for the range of the measurements.

The measurement error originating from the thermocouple probe is $\pm$ 0.0075 * T, where T is the measured temperature. This measurement accuracy is collected from the manufacturer certification.

Finally, Table 3-4 introduces the FTIR measurement uncertainty for the O$_2$, CO, NO, NO$_2$, N$_2$O, CO$_2$ and H$_2$O species as specified by the supplier.

Table 3-2 A summary of the experimental error sources originating from the species sampling method using the Signal analysers.

Analyser					
Error source	THC	NOx	CO	CO2	O2
Accuracy/ Repeatability*			≥ 1% FSD		≥ 0.02% FSD
Linearity			≤ 0.5 % FSD		
Detector noise					
Zero	< 0.08 ppm pk-pk	≤ 0.04 ppm pk-pk	≤ 5 ppm pk-pk	300 ppm pk-pk	0.005 % pk-pk
Span			≤ 0.5 % FSD pk-pk		
Drift					
Zero	< 0.1 ppm/day	≤ 0.02 ppm/day	≤ 2.5 ppm/day	< 1584 ppm/day	< 0.008 %/day
Span			≤ 0.5 % FSD/hr		
Ambient temperature effect					
Zero	n/a	≤ 0.027 ppm/ºC	≤ 2 ppm/ºC	< 250 ppm/ºC	< 0.008 %/ºC
Span*	< 0.1% FSD/ºC	< 1% FSD/3ºC	0.2% FSD/ºC		< 0.1% (5-40ºC)
Cross sensitivities_ correction factor		n/a	-20 ppm in 100% CO2	-0.03% in 100% CH4	n/a
NOx converter efficiency	n/a	96%		n/a	
Calibration gases_ accuracy on certified values			± 2%		

Table 3-3 Total error uncertainty originating from the Signal gas analysers.

	THC		NOx		CO		CO2		O2	
Range	1000 ppm	10 %	100 ppm	400 ppm	5000 ppm	5 %	25 %	5 %	25 %	
Error	71 ppm	0.1 %	8 ppm	10 ppm	62 ppm	0.1%	0.4%	0.2%	0.1%	

Table 3-4 FTIR measurement uncertainty.

Analyser	O_2	CO	NO	NO_2	N_2O	CO_2	H_2O
Measurement uncertainty (%)	2.4	6.0	6.5	5.7	4.4	5.0	6.2

3.5 Introduction to Numerical Calculations

The aim of modeling gaseous combustion is to obtain an insight into the coupling of the exothermic combustion processes with the turbulent mixing processes occurring in reacting systems and develop an appropriate model to account for this interaction. Gaseous combustion modeling is achieved by solving the governing partial differential equations for the conservation of mass, momentum, species and energy. Most practical combustion systems involve turbulent reactive flows and the inclusion of detailed chemical kinetic mechanisms, which increase greatly the computational time because reliable kinetic mechanisms include tens of species, hundreds of reactions and many different chemical time scales. Therefore, the computational models of turbulent diffusion flames have two main approaches for including chemical mechanisms, one is to create libraries with tables of scalar values and temperature by performing laminar flame calculations and including detailed kinetic mechanisms. The other approach is to include reduced mechanisms (of a few reaction steps) but provide detailed species and temperature profiles (Norton et al., 1993). This study computes the species and temperature profiles in the mixture fraction space by adopting a steady flamelet model which uses a detailed kinetic mechanism and can cheaply complete these calculations for laminar opposed diffusion flames.

For the laminar flame calculations, a small variety of models are available to be used in Fluent pre-processor as described below. Once perfect mixing is achieved in a combustion system, combustion chemistry can be modelled with the Equilibrium model, if combustion is close to a chemical equilibrium state, the Steady Diffusion Flamelet model can be used and if the combustion significantly departs from equilibrium, the Unsteady Diffusion Flamelet model should be used. For chemical systems departing from equilibrium, there are three available models, the Rich Flammability Limit option of the Equilibrium model, the Steady Diffusion Flamelet model, which is the extension of the mixture fraction formulation to take into account and non-equilibrium effects, or the Unsteady Diffusion Flamelet model. The aim of

this study is to investigate the CO$_2$ dilution effects on natural gas combustion experimentally and numerically and in this section, the flamelet calculations are presented as computed using the OPPDIF code as is embedded in ANSYS Fluent software.

3.6 Numerical Model

3.6.1 Conservation equations in reacting flows

The conservation equations of species and energy (in terms of total enthalpy) in reactive flows are described as follows (Poinsot and Veynante, 2005):

$$\frac{\partial}{\partial t}(\rho \, Y_i) + \frac{\partial}{\partial x_a}(\rho u_a Y_i) + \frac{\partial j_{ia}}{\partial x_a} = \dot{\omega}_i \qquad \text{(Equation 3-7)}$$

$$\frac{\partial}{\partial t}(\rho h) + \frac{\partial}{\partial x_a}(\rho u_a h) - \frac{\partial}{\partial x_a}\left(\frac{\lambda}{c_{pi}}\frac{\partial h}{\partial x_a}\right) =$$
$$- \frac{\partial}{\partial x_a}\sum_{i=1}^{n} h_i\left(\frac{\lambda}{c_{pi}}\frac{\partial Y_i}{\partial x_a} + j_{ia}\right) + \frac{\partial P}{\partial t} + \dot{\omega}_h \qquad \text{(Equation 3-8)}$$

where Y_i is the mass fraction of species, i, ρ is the density, u_α is a component of the velocity vector, x_α is a spatial coordinate, $\dot{\omega}_i$ is the net mass chemical reaction rate of species i, λ is the thermal conductivity, c_{pi} is the specific heat capacity of species i at constant pressure, P is the pressure, h is the total enthalpy accounting for both the sensible and the chemical energy, $\dot{\omega}_h$ is the heat source term and $j_{i\alpha}$ is the molecular diffusion flux of species i, which is determined as follows (Poinsot and Veynante, 2005):

$$j_{ia} = - \rho \, D_i \, \frac{\partial Y_i}{\partial x_a} \qquad \text{(Equation 3-9)}$$

The diffusion coefficients, D_i, are usually characterised using the Lewis number, Le_i, which is defined as (Poinsot and Veynante, 2005):

$$Le_i = \frac{\lambda}{\rho \, c_{pi} \, D_i} = \frac{D_T}{D_i}, \quad i=1,2,\dots,n \qquad \text{(Equation 3-10)}$$

where $D_T = \lambda /(\rho c_P)$ is the thermal coefficient and the Lewis number is the ratio between the thermal and species diffusivity. The numerical model used in this study

assumes that the molecular diffusivities of the fuel and the oxidiser species are equal and therefore, the Le_i number is unity for all species i. The assumption of a single unity Lewis number, or else, neglecting the differential diffusion, is generally acceptable for turbulent flows (high Reynolds flames) as turbulence transports all scalars equally by convection and turbulent mixing dominates the molecular diffusion (Nilsen and Kosály, 1999, Goldin et al., 2012, Poinsot and Veynante, 2005). However, in many combustion applications, the molecular transport coefficients differ from each other, namely "differential diffusion", and especially in laminar flows. As reported by Guo and Smallwood (2010), neglecting differential diffusion for all species does not predict accurately the soot formation rate in laminar flames and also, it could have an impact on modeling turbulent flames. On the other hand, the study by Mauss et al. (2006) on the modeling of soot formation using an unsteady flamelet approach concluded that good predictions of the soot volume fraction can be achieved without considering the differential diffusion effect as they focused on investigating different parameters. Therefore, the choice of assuming unity Lewis number or not depends a lot on each investigation. In this study, there is no intention to develop the existing flamelet model or is there the option of a non-uniform Lewis number, and so, we can only address the discussion over this assumption. Furthermore, as mentioned in Section 3.6.4, this assumption is in compliance with the restrictions of the flamelet model; the flamelet concept can only be used when the flow is turbulent. Therefore, the Lewis number unity assumption gives the following approximation (Peters, 1984):

$$\rho \, D_i \equiv \frac{\lambda}{c_{pi}} \qquad \text{(Equation 3-11)}$$

In the majority of combustion models, several assumptions are introduced to allow for simplifications of the equations. Using the simplified diffusion law (known as Fick's law), all the diffusion coefficients, D_i, of the chemical species i are equal to D. In addition, transport properties can be simplified by neglecting the Dufour and Soret effects; the former effects refer to the heat flux due to species mass fraction gradients and the latter to molecular species diffusion due to temperature gradients (Poinsot and Veynante, 2005). For non-premixed combustion systems, the aforementioned approximation leads to important simplifications as it allows the introduction of only one conserved scalar variable and thus the element mass fractions are linearly related to it (Peters, 1984). In addition, the specific heat capacities of all chemical species i, c_{pi}, are assumed to be constant for simplicity reasons and equal to the mean specific

heat capacity at constant pressure, c$_P$, and independent of temperature (Peters, 1997, Poinsot and Veynante, 2005). Another essential simplification taken into account when modelling diffusion flames is the assumption of constant pressure. The Mach number, M$_\alpha$, which is defined as the ratio of flame speed to speed of sound, is low in a reactive flow since the flame speed is much lower than the sound speed. Also, in high Reynolds number steady flows, the changes in mean pressure are of the order of M$_\alpha^2$ and therefore it can be reasonably accepted that the pressure term in the energy equation (Equation (3-8)) is neglected; $\partial P/\partial t = 0$ (Poinsot and Veynante, 2005).

Subsequently, combining Fick's law for the molecular diffusion flux, Equation (3-9), with Lewis assumption for equal diffusivities for all species i and temperature, Equation (3-11), leads to a simplified form of the energy equation. In turbulent flames, the molecular transport plays an important role only near the reaction zone and elsewhere the turbulent transport is dominant and all scalars are transported equally by convection. Taking into account all the above mentioned simplifications and assumptions, the energy balance equation can be determined as, (Peters, 1986):

$$\frac{\partial}{\partial t}(\rho\, h) + \frac{\partial}{\partial x_a}(\rho\, u_a h) - \frac{\partial}{\partial x_a}\left(\rho\, D\, \frac{\partial h}{\partial x_a}\right) = \dot\omega_h \qquad \text{(Equation 3-12)}$$

and the species balance equation becomes (Peters, 1986):

$$\frac{\partial}{\partial t}(\rho Y_i) + \frac{\partial}{\partial x_a}(\rho\, u_a Y_i) - \frac{\partial}{\partial x_a}\left(\rho\, D\, \frac{\partial Y_i}{\partial x_a}\right) = \dot\omega_i \qquad \text{(Equation 3-13)}$$

3.6.2 Mixture fraction

In non-premixed flames, the fuel and oxidiser flows are not mixed before they enter the reaction zone and therefore mixing of reactants becomes important for initiating and sustaining the combustion process. The two fundamental processes in a diffusion flame are firstly the mixing process and when mixing is achieved then the combustion process (directly related to the flame structure) can take place (Poinsot and Veynante, 2005). Therefore, mixing at the molecular level becomes more important than chemical reactions, which are usually much faster in non-premixed systems. It is apparent that the burning rate is mainly controlled by molecular diffusion and thus the name, diffusion flames, comes from their rate controlling step. The combustion process is the balance between the heat loss (as carried out of the reaction zone by the

products) and the heat gain (as released by the exothermic combustion reactions). When the heat loss rate is greater than the chemical heat production rate, the flame will extinguish.

The structure of a steady diffusion flame is characterised by the ratio between characteristic time scales which represent the molecular diffusion (or also known as mass transport) and the combustion chemistry. In a reactive system, this ratio can change substantially and as a result, a parameter indicating which of these two processes is the rate controlling step in a combustion system is needed. This parameter is called the Damköhler number, is defined as the ratio between a characteristic diffusion and a chemical time scale and is described as follows (Glassman and Yetter, 2008, Peters, 1986):

$$D_a = \frac{\tau_D}{\tau_C}$$
(Equation 3-14)

When D_α is >>1, the chemical reactions are much faster than molecular diffusion and so, the reactions can be assumed to be infinitely fast. Whereas when D_α is <<1, diffusion occurs much faster and the combustion is limited by the chemical kinetics (Glassman and Yetter, 2008).

The internal structure of diffusion flames is characterised by the extent of mixing between reactants and thus it is suitable to introduce a parameter to quantify that extent. This parameter is called the mixture fraction, is symbolised by Z and is defined as the local mass fraction of burnt and unburnt fuel stream elements (such as C, H) in all the participating combustion species (such as CO, CO_2, etc.). It is widely known that in chemical reactions, the atomic elements are conserved and thus the mixture fraction becomes a conserved scalar quantity; a "chemistry-independent" variable (Veynante and Vervisch, 2002, Peters, 1984). Most studies on diffusion flames assume ideal conditions, such as a single step reaction mechanism with N species for complete combustion (Peters, 1997):

$$\nu'_F \, F + \, \nu'_{O_2} O_2 \leftrightarrow \nu'_{CO_2} CO_2 + \, \nu'_{H_2O} \, H_2O$$
(Equation 3-15)

where F represents the fuel stream, O_2 the oxygen in the oxidiser stream, CO_2 and H_2O the products and ν'_F and ν'_{O_2} are the stoichiometric coefficients of the fuel and oxygen streams, accordingly. The mixture fraction is defined as the local ratio of the

fuel stream (index 1) mass flux to the sum of the fuel and oxidiser stream (index 2) mass fluxes and is described as follows (Peters, 1997):

$$Z = \frac{\dot{m}_1}{\dot{m}_1 + \dot{m}_2} \qquad \text{(Equation 3-16)}$$

By denoting the fuel mass fraction in the fuel stream by $Y_{F,1}$ and the oxygen mass fraction in the oxidiser stream by $Y_{O_2,2}$, i.e. $Y_{O_2,2}$ is 0.23 in an air stream, the mixture fraction of a homogeneous system can be determined as follows (Peters, 1997):

$$Z = \frac{v\,Y_F - Y_{O_2} + Y_{O_2,2}}{v\,Y_{F,1} + Y_{O_2,2}} \qquad \text{(Equation 3-17)}$$

Where v is the stoichiometric oxidiser-to-fuel mass ratio. A stoichiometric mixture is defined by $vY_F = Y_{O_2}$ and thus the stoichiometric mixture fraction, Z_{st}, is defined as follows (Peters, 1997):

$$Z_{st} = \left[1 + \frac{v\,Y_{F,1}}{Y_{O_2,2}}\right]^{-1} \qquad \text{(Equation 3-18)}$$

In methane-air mixtures, the stoichiometric mixture fraction is calculated to be 0.055, in a hydrogen-air mixture it is 0.028, and in a propane-air mixture is 0.06; for complete combustion, the required mass of air is about 20 times more than the fuel mass (Peters, 1997). The equivalence ratio, Φ, is defined as the actual fuel-to-oxygen ratio in a mixture divided by the stoichiometric ratio, as explained in Equation (3-17). Thus, the equivalence ratio and the mixture fraction are related as follows (Peters, 1997):

$$\Phi = \frac{Y_{F,u}/Y_{O_2,u}}{\left(Y_{F,u}/Y_{O_2,u}\right)_{st}} = \frac{v\,Y_{F,u}}{Y_{O_2,u}} \qquad \text{(Equation 3-19)}$$

$$\Phi = \left(Z/Z_{st}\right)\left((1 - Z_{st})/(1-Z)\right) \qquad \text{(Equation 3-20)}$$

where $Y_{F,u}$ and $Y_{O_2,u}$ are the local mass fractions of the fuel and oxygen, respectively and Equation (3-20) shows that the Z can be regarded as an expression of only the equivalence ratio.

In a jet diffusion flame, the fuel and oxidiser streams diffuse towards each other after exiting from the burner nozzle and a stoichiometric mixture plane is created.

Combustion takes place in a thin surface around the region of the stoichiometric plane. This thin surface, and the region around it, is called a laminar diffusion flamelet. The mixture fraction of a flamelet is given in a flow field as a function of the space and time and also, defines the location of a thin reaction zone at $Z(x_a, t) = Z_{st}$ (Peters, 1984, Peters, 1986). The mixture fraction can be defined by solving a convective diffusive equation because it is a conserved scalar quantity and its chemical source term in the balance equation is zero (Peters, 1997):

$$\frac{\partial}{\partial t}(\rho\, Z) + \frac{\partial}{\partial x_a}(\rho\, u\, Z) - \frac{\partial}{\partial x_a}(\rho D \frac{\partial Z}{\partial x_a}) = 0 \qquad \text{(Equation 3-21)}$$

The diffusion flame is fully determined when the mixture fraction, Z, and any of the scalars T or Y_i are known. An orthogonal coordinate system x_1, x_2, x_3, t is assumed to be attached on the surface of the stoichiometric plane and x_1 is replaced by Z following the transformation rules as explained comprehensively in Peters (1984) and Bilger (1976). The mass fraction and temperature balance equations can now be re-organised and transformed from the physical space, where x is the independent variable, to the mixture fraction space, where Z is the independent variable. As such, all scalars are functions of the mixture fraction, Z, and the time, t. Therefore, the flamelet formulation, as described by the Y_i and T transport equations, leads to a one-dimensional structure as attached to the stoichiometric mixture plane (Peters, 1984).
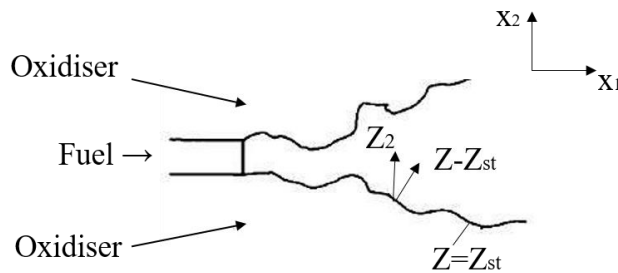
Figure 3-14 Schematic of the coordinate transformation rules for the physical space (Peters, 1986).

3.6.3 Conserved scalar approach

To sum up, the conserved scalar approach can only be applied to non-premixed flames and for systems which are close to local chemical equilibrium when the chemistry is fast enough and mixing becomes the rate limiting process. Only combustion systems with two inlets, one for fuel and the other for the oxidiser mixture, can account for into this formulation and modelled using a single conserved variable. This approach

includes the general transformation to a coordinate-free system with the use of the mixture fraction since it is a chemistry-independent conserved scalar variable. This transformation, as explained in Section 3.6.2, leads to a one-dimensional flamelet structure where all scalar profiles, such as density, temperature and concentration, are linearly correlated and dependent on the mixture fraction, if only fast reactions are assumed. The conserved scalar approach has been extensively described by Bilger (1976) and therefore it is not repeated here.

The assumption of fast chemical kinetics is well supported and has been successfully used for diffusion flames, especially for H_2 diffusion flames. Local equilibrium implies the elimination of the complicated chemical kinetic mechanisms from any analysis which is an essential simplification for chemical calculations as valuable computational time is gained. However, turbulence alters the local diffusion time scales within the flame zone and therefore the equilibrium concept is not a realistic approach. Moreover, chemical time scales can also vary greatly in a reacting system and consequently, heat generated by combustion can be a fast process compared to the formation of pollutant species, such as NO_x and soot. As a result, in practice the combustion systems are designed such that they are efficient in terms of achieving complete combustion, when most fuel is oxidised and the flame is fairly stable, and emit low pollutant levels (Peters, 1986, Peters, 1984).

In the case of hydrocarbon flames, the assumption of rapid chemistry overestimates the concentration of, for example, CO and H_2 in the fuel-rich regions. In addition, in diffusion flames, equilibrium conditions cannot be met and local flame quenching is likely to occur when the diffusion time is equal to the chemical time scale. Local quenching could lead to lift-off and possibly to the blow-out of diffusion jet flames. Therefore, it became of paramount importance to characterise diffusion flames from their equilibrium state (fast chemistry) until their extinction limit (or else called the quenching limit) (Peters, 1986, Peters, 1984).

3.6.4 Steady diffusion flamelet model

The steady flamelet concept is based on modelling turbulent flames whose reacting surface is considered to consist of a number of thin, laminar diffusion flames. Therefore, this model assumes that in turbulent flow fields combustion occurs in thin flame sheets which are known as diffusion flamelets (Peters, 1986). Williams (1975) was the first to present the idea of laminar diffusion flamelets embedded within a

turbulent diffusion flame. The basis of this concept is that a diffusion flamelet has the same structure as a laminar diffusion flame of a simple configuration, such as the counter-flow diffusion flames. The configuration of a counter-flow flame is a convenient representation of the structure of laminar flames because its governing equations can be reduced to one-dimensional equations using similarity transformation rules (Peters, 1984). Counter-flow diffusion flames have been studied extensively by a number of investigators because their simple configuration favours, for the purposes of modelling, the inclusion of both the complex chemical kinetic mechanisms and the transport processes occurring in non-premixed flames (Williams, 1975, Peters, 1984, Dixon-Lewis et al., 1984, Rogg et al., 1986, Smooke et al., 1986, Puri, 1987).

As shown in Figure 3-15 (a) and (b), in counter-flow flames, the fuel and oxidiser streams enter the reaction zone from two opposed jets; the oxygen diffuses towards the fuel stream and the two streams meet at the location of the stagnation point and diverge radially outwards. At the stoichiometric plane, chemical reactions take place and create a steady planar diffusion flame close to the stagnation point. Counter-flow flames are maintained at steady-state because a continuous supply of fuel and oxidiser enters the reaction zone and all the heat produced in the reaction zone comes from the exothermic combustion chemical reactions (Dixon-Lewis et al., 1984, Veynante and Vervisch, 2002). When the two jet inlets get closer in distance, or the velocity or the flow rate of the two streams is increased above a certain limit, the flame temperature decreases and so, the reactions cannot be sustained. The jet velocity gradient is inversely proportional to the flame residence time. When the jet velocities increase, high velocity gradients are applied to the flow close to the stagnation point, also known as strain rates, and the residence time becomes almost equal to the required chemical time scale which brings the flame close to extinction; known as the counter-flow flame extinction limit (Smooke et al., 1986). When counter-flow flames are presented in the mixture fraction space, we represent the fuel inlet as Z=1 and the oxidiser inlet as Z=0 and the value of the mixture fraction parameter changes along the formed thin diffusive layer, as shown in Figure 3-15 (b) (Veynante and Vervisch, 2002, Peters, 1984).

(a)

b)
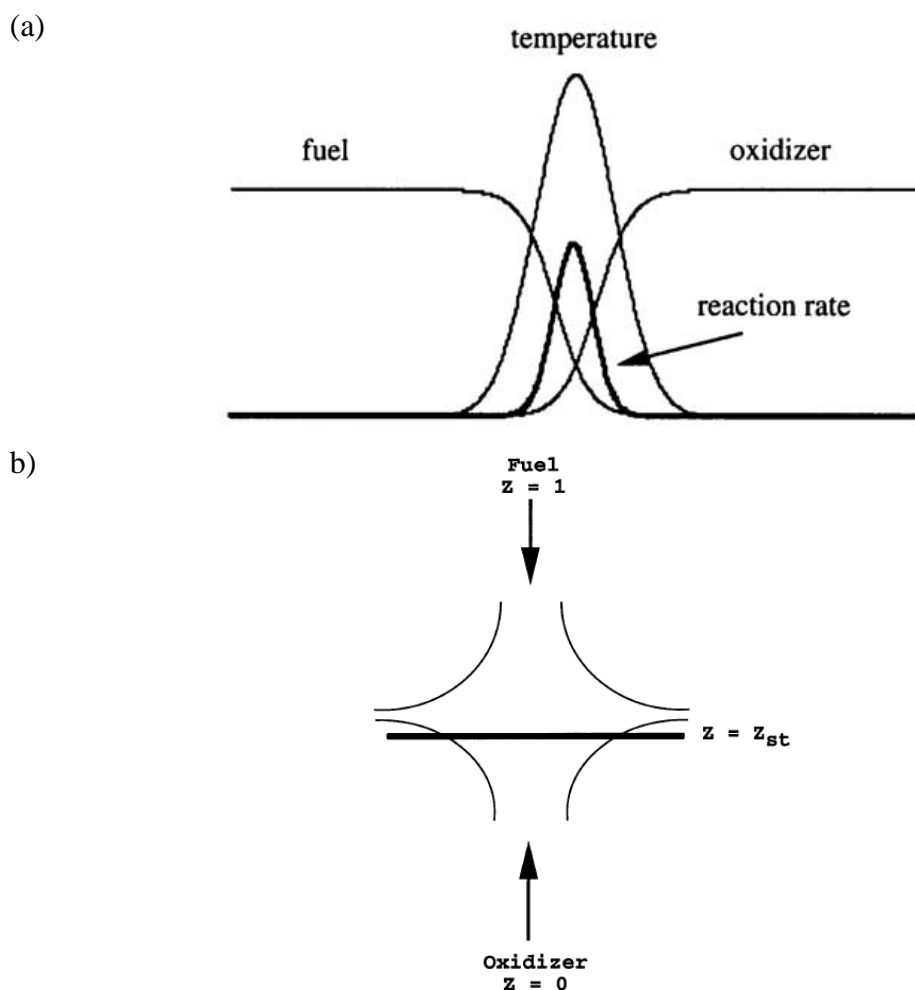
Figure 3-15 (a) Schematic of the structure of a laminar diffusion flame (Veynante and Vervisch, 2002) and (b) schematic of a counter-flow diffusion flame (Puri et al., 1987).

When a flame is stretched significantly, it departs from chemical equilibrium, and any further stretching could lead to flame blown-out. In near-equilibrium conditions, the time for the completion of the chemical reactions is shorter than the time needed for the transport processes. Away from equilibrium, turbulence has a strong impact on flame stretching (or straining) which in turn causes radicals and even more heat to diffuse out of the flame at a faster rate. As a result, the species don't reach equilibrium and local non-equilibrium effects become important and need to be accounted for in the turbulent combustion modelling.

The need for developing a model for non-premixed combustion that could include both the conserved scalar formulation and non-equilibrium effects is the purpose of the existence of the flamelet concept. To implement this, an additional parameter needs to be incorporated which can indicate quantitatively how close or far a system is from reaching equilibrium. This may be done either by using the characteristic strain

rate for a counter-flow diffusion flamelet, a_s, or the instantaneous scalar dissipation, χ_{st}. The strain rate is the ratio between the relative speed of both jets, v, and the distance between the jets, d, is given as follows (Veynante and Vervisch, 2002):

$$a_s = v/d \qquad \text{(Equation 3-22)}$$

It is more common between the two parameters to use the instantaneous scalar dissipation which is defined as the inverse of a characteristic diffusion time, $\tau_\chi = \chi_{st}^{-1}$, and its units are s^{-1} (Peters, 1984):

$$\chi = 2D \left(\frac{\partial Z}{\partial x_j} \frac{\partial Z}{\partial x_j} \right) = 2D|\nabla Z|^2 \qquad \text{(Equation 3-23)}$$

Due to the coordinate transformation, instantaneous scalar dissipation includes the influence of convection and diffusion, and it is intrinsically defined at the stoichiometric plane, $\chi_{st} = \chi(Z_{st})$, and directly related to the strain rate (Peters, 1984):

$$\chi_{st} = \frac{a_s \exp\left[-2 \left(\text{erfc}^{-1} \left(2 Z_{st} \right) \right)^2 \right]}{\pi} \qquad \text{(Equation 3-24)}$$

where erfc^{-1} is the inverse of the complementary error function. The instantaneous scalar dissipation is related to the reacting flow field and so, when χ_{st} is very small (gets close to zero), the equilibrium limit is reached and the flamelet structure depends only on the mixture fraction, Z, which is an independent variable, as χ is a function of Z, as shown in Equation (3-23). When it exceeds a critical value, heat loss cannot be balanced by the chemical heat generation and the flamelet is quenched. Therefore, the balance between diffusion and chemical heat release, as indicated by the Damköhler number, which can now be expressed via Equation (3-25), affects the structure of a flame (Veynante and Vervisch, 2002):

$$Da = \left({}^{\tau_\chi} / _{\tau_c} \right) = \left(\tau_c \, \chi_{st} \right)^{-1} \qquad \text{(Equation 3-25)}$$

Therefore, a single flame can now be parameterised by only Z and χ_{st}.

If the balance equations for the species and enthalpy are re-written in a local orthogonal coordinate system attached to Z=Z$_{st}$, as explained in Section 3.6.2, using also the assumption of unity Lewis number and constant species heat capacities, the

conservation equations of enthalpy, Equation (3-12) and species, Equation (3-13, may be recast as follows (Wang and Chen, 2005):

$$\rho\frac{\partial T}{\partial t} - \rho\frac{\chi}{2}\frac{\partial^2 T}{\partial Z^2} + \sum_{i=1}^{n} h_i\omega_i = 0 \qquad \text{(Equation 3-26)}$$

$$\rho\frac{\partial Y_i}{\partial t} - \rho\frac{\chi}{2}\frac{\partial^2 Y_i}{\partial Z^2} - \omega_i = 0 \qquad \text{(Equation 3-27)}$$

where the enthalpy is expressed in terms of the temperature in Equation (3-26). If the time derivative terms are omitted, the local flamelet scalar structure can be defined only by the mixture fraction, Z, and the scalar dissipation, χ_{st}. To model turbulent flames, the mean values of the fluctuating scalars, such as density, temperature and species mass fractions are required instead of the instantaneous values. According to the flamelet concept, the mean turbulent flame structure can be computed from multiple laminar flamelets where each flamelet could be pre-calculated and saved in a flamelet library with Z and χ_{st} serving as the independent variables. The flamelets are then embedded in a turbulent flame using statistical methods as presented in Peters (1997) and Wang and Chen (2005) but it is not part of this study to investigate it further.

3.7 Methodology for the Numerical Calculations

In this study, flamelet calculations have been carried out using a detailed chemical kinetic mechanism to generate laminar opposed diffusion flamelets. The advantage of the flamelet library is the low computational cost when coupled with a computational fluid dynamics code. The strong asset of the steady flamelet model is that it takes into account the realistic kinetic effects of the turbulent flames but its strong weakness is that it can only model relatively fast chemistry. This assumption implies that the flame response to any aerodynamic strain caused by turbulence can be instantaneous and as such, strong non-equilibrium and slow chemistry phenomena, which are present in turbulent flames, will not be taken into account in these laminar flamelet calculations (Peters, 1984). Any reactive system can be in a non-equilibrium condition when chemical and diffusion time scales are almost the same. In such conditions, the model cannot predict accurately any sudden phenomena that occur away from equilibrium, such as flame ignition and extinction, and the formation of NO$_x$ species and the CO oxidation process, which are both slowly occurring processes. Another explanation of

the instantaneous reaction of a flame to a strain rate is that when the imposed strain is negligible (close to zero), the chemical system tends to reach equilibrium and when a high strain value is applied, the flame is close to its extinction limit (Veynante and Vervisch, 2002).

The initial step in the modeling turbulent combustion is to compute counter-flow diffusion flamelet calculations using the GRI Mech 3.0 mechanism for natural gas flames. In laminar flamelet modeling, a laminar flame in a simple 1D configuration is parameterised by two scalars, as explained in Section 3.6.4, the mixture fraction and the scalar dissipation. Laminar flames can be computed in two and three dimensions, however, flamelets can only be calculated in one or zero dimensions. There are several one-dimensional configurations but for the non-premixed flames, the opposed flow configuration is usually used (Goldin et al., 2012).

In this study, the numerical calculations adopted the detailed GRI-Mech 3.0 chemical reaction scheme, which is the newest released version of this kinetic mechanism. It is a compilation of 325 chemical reactions along with rate coefficient expressions and thermodynamic data for the 53 participating species. The GRI-Mech 3.0 has been selected due to its optimisation for modelling the combustion of natural gas and/or methane fuels. It has been optimised for temperature conditions between 1000 and 2500 K, pressure conditions from 10 Torr up to 10 atm and equivalence ratios from 0.1 to 5 for premixed systems (Gas Research Institute, 2000). This mechanism includes C_1 and C_2 chemistry to describe the oxidation of methane, the NO formation, and NO reburn chemistry, and reactions that are involved in the combustion of other hydrocarbon constituents of natural gas (Gas Research Institute, 2000). The kinetic mechanism used for these calculations is shown in Appendix C. A recently published study by Metcalfe et al. (2013) presented detailed chemical kinetic mechanisms for the oxidation of small hydrocarbon and oxygenated hydrocarbon fuels, including methane. In this study, sensitivity analyses were performed to determine the values of the rate constants of important reactions taking place in the C_1- C_2 oxidation mechanisms of these fuels. A compilation and optimisation of the already published mechanisms, such as the Leeds mechanism, the GRI- Mech, the San Diego Mech, the USC Mech II, the Politecnico di Milano CRECK mechanism and the Model Fuels Consortium mechanism, yielded to the mechanisms proposed by Metcalfe et al. (2013).

3.7.1 Boundary conditions

The numerical calculations are made only at atmospheric pressure conditions for pure methane as a fuel; the natural gas composition is considered to be equal to pure methane for simplicity reasons. The fuel and oxidiser composition for all the cases are presented in Table 3-5. The composition of the oxidiser stream is chosen to represent the experimental test conditions, apart from the 3 % CO$_2$ in volume which is added to the numerical calculations to reveal in a more comprehensive way the effects of adding CO$_2$ in the oxidiser stream.

Table 3-5 Boundary conditions for all the numerical case studies investigated.

Mole composition				
		Oxidiser		
	Fuel	O$_2$	N$_2$	CO$_2$
	1	0.21	0.79	0.00
P = 1atm, T = 293K	1	0.20	0.77	0.03
	1	0.20	0.75	0.05
	1	0.19	0.71	0.10

3.7.2 Solution method

Multiple steady diffusion flamelets are computed for a range of scalar dissipation values to include various strain rate levels; starting from equilibrium until a very high strain rate, close to extinction. For every case study, the first flamelet is computed with the same initial, low, value of scalar dissipation, $\chi_{st}= 0.01$ s^{-1}, and the next diffusion flamelet is computed according to the specified scalar dissipation step, $\Delta\chi$. The generation of flamelets ends when the flamelet is extinguished. In this study, the maximum number of flamelets is chosen such that the flamelet reaches extinction. For each case study, the scalar dissipation step is varied such that the total number of the flamelets generated is at least 20, which is chosen after several trials to give a wide range of flamelets. An adaptive algorithm approach is selected for the grid refinement of steady diffusion flamelets. A number of trials has shown that the selected values for the tolerances does not affect the solution. As such, a steady flamelet solution is calculated initially on a coarse grid (32 grid points) and when converged, more points are added according to the input parameters. The refined grid is then re-converged and this process is repeated until the values of the control parameters are reached. Several

trials indicate that the solution is independent of the values of the control parameters and of the selected number of the grid points.

It is worth mentioning that the steady diffusion flamelet model cannot predict precisely the exact extinction limit of a flamelet but it gives a good estimation of the extinction limit. This limitation is observed during the calculations, when the scalar dissipation step is slightly varied for the same boundary conditions, the final scalar dissipation value at the stoichiometric mixture fraction changes slightly. A summary of the final solution values of the flamelet calculations is presented in Table 3-6, as an attempt to explain the aforementioned solution process. The high χ_{st} values are an estimation for the extinction dissipation rate and the average χ_{st} is an intermediate value which is used to show the effect of strain rate on the scalar profiles and temperature.

Table 3-6 Final solution values of the flamelet calculations.

	Air	3% CO_2	5 % CO_2	10 % CO_2
Scalar dissipation step (s^{-1})	1.5	1.0	0.6	0.4
Total number of generated flamelets	21	21	24	15
Low χ_{st}	0.01	0.01	0.01	0.01
Average χ_{st}	13.0	9.0	6.4	2.6
High χ_{st}	25.0	17.0	12.4	5.4

3.8 Summary

Chapter 3 described in detail the experimental setup and instrumentation used during the test campaigns presented in Chapters 4 and 5. It includes the drawings of the in-house built chamber, a description of the type of the gas burner used along with the different types of gas sampling probes, thermocouple probes and the range of gas analysers used in this study. The experimental methodology that followed to conduct the planned experiments and analyse the collected data is explained. Furthermore, it contains the theory behind the numerical model used in Chapter 6 to predict the impact of CO_2 on the flame chemistry of methane-air flames.

CHAPTER 4- Experimental Results: Flame A with Equivalence Ratio = 0.58 - 0.64

4.1   Introduction

This chapter provides a description of the data collected during the first experimental campaign, named as "Flame A". The effects of adding CO$_2$ into the oxidiser reactant stream at two dilution levels are investigated. Using the Signal analysers, as described in Section 3.3.2, the concentration of the major combustion species is measured on a dry basis. The flame temperature is measured using a type-N sheathed thermocouple probe and its setup is presented in Section 3.3.1. All measurements are taken utilising the in-house built combustion chamber, as depicted in Section 3.2, which allows for investigating fully controlled confined flames.

Chapter 4 begins with Section 4.2 that introduces the test conditions applied during the test campaign, "Flame A". The experimental results of Flame A are divided into two sections; the first, Section 4.3, introduces the in-flame data and the second, Section 4.4, the data collected at the exit of the combustion chamber. The in-flame measurements were taken axially at different distances from the burner exit surface, and radially at small distances from the centre of the flame. The right-angle shaped quartz probe was used to draw samples from the flame whereas the straight ceramic probe was used at the exit sampling point, as described in Section 3.3.2.1. Two types of graphs are introduced for the in-flame data, the first type is symbol line graphs that present the raw data as obtained from the gas species analysis and from the thermocouple measurements, after correcting them for radiation heat loss; the radiation correction method is discussed in Section 3.3.1.3. The second type of graphs is 2D contour plots used as a graphical technique to illustrate the relationship between three variables in two dimensions; one variable is the distribution of the concentration or temperature in the axial and radial axis (the other two variables). In Section 4.4, the exit emissions are presented for the air and the CO$_2$-diluted flames, as measured at the central axis of the final part of the combustion chamber. Furthermore, Section 4.5

includes a discussion on the experimental data and the chapter concludes with Section 4.6 that contains the main key outcomes of the test campaign "Flame A".

4.2   Test Conditions

The fuel utilised throughout this study is natural gas and without using a gas booster, the maximum achievable Reynolds number was 4725; as calculated for the cold fuel stream. The flow rate of natural gas was kept the same for both experimental campaigns. The oxidiser mixture comprised of either air or air blended with pure CO$_2$ at two dilution levels. The dilution levels investigated in the two campaigns are 5 and 10 % CO$_2$ in volume. The staged enhancement of the air stream with CO$_2$ will reveal the reactivity of CO$_2$. Both dilution levels led to stable lifted flames. As shown in Table 4-1, the velocity of the oxidiser stream is kept constant at about 0.53 m/s for the air and the CO$_2$-diluted flames. The constant velocity was achieved by decreasing the amount of air when adding CO$_2$ and thus the equivalence ratio increased slightly.

The in-flame measurements are taken at various axial sampling locations, x/D_i, where x is the actual axial distance from the burner exit surface and D_i is the internal diameter of the fuel jet pipe, 4.57 mm. Closer to the burner surface, the measurements are denser as flame kinetics are important. Further downstream of the burner exit, the axial step is larger but the radial step remains constant and equal to 10 mm. Species sampling is conducted between 90 mm and 570 mm above the burner exit surface but measurements with the thermocouple probe are taken between 10 mm and 570 mm above the burner exit. Due to a technical issue with the Signal pump, there was not enough sample for all the Signal analysers. Therefore, the right-angle quartz probe was shortened in length and could no longer reach as low as 10 mm above the burner exit surface. On the other hand, the thermocouple probe had access to such low axial locations. At the final convergent part of the combustion chamber, gas samples were withdrawn using a straight ceramic probe and the results are shown in Section 4.4.

Table 4-1 summarises the test conditions investigated during the experimental campaign "Flame A". It includes the dilution levels for each flame type, the velocity of the reactant streams, the Reynolds number based on the fuel stream, the equivalence ratio of each flame type and finally, the axial sampling locations.

Table 4-1 Test conditions of "Flame A" campaign.

Case study- Flame A	Air	5 % CO₂-diluted	10 % CO₂-diluted
Inlet CO₂ mole fraction	0.00	0.05	0.10
Average Fuel Jet Velocity (m/s)	18.7		
Reynolds Number	4725		
Average Oxidiser Flow Velocity (m/s)	0.53		
Sampling Locations (x/Dᵢ)	2, 11, 20, 28, 37, 46, 63, 81, 125, 372		
Equivalence ratio (Φ)	0.58	0.61	0.64

4.3 In-flame Measurements

All in-flame measurements are taken using the Signal gas analysers and are reported in either vol% or ppm units depending on the species; 1 % equals 10,000 ppm. The temperature data are plotted in Kelvin degrees upon applying the correction for radiation heat loss. In the symbol line plots, the X axis represents the radial distance from the centreline of the fuel jet pipe, as such the zero value represents the centreline of the jet where the fuel issues. Radial distances from the jet centreline are represented by the negative and positive values. The Y axis represents the raw data, either corrected temperature measurements or averaged gas species measurements. Furthermore, the in-flame data are presented also in contour plots where the X axis represents the radial distance and the Y axis the axial distance. The third variable of the contour plots is the data collected.

4.3.1 Temperature profile

In Figure 4-1, corrected temperature measurements for radiation heat losses are presented in the physical space. The highest temperature difference between the uncorrected and corrected measurements was about 300 K and occurred at high temperature values. Since the radiation correction term increases with the T_{meas}^4, it is expected the heat loss to be higher in regions of elevated flame temperatures. Two additional sampling locations, x/D_i= 2 and 11, are included in the temperature plots because the thermocouple probe could reach as low as 10 and 50 mm above the burner exit surface. The low values of the temperature at these low axial locations indicate that there is no visible flame at these regions. As reported by Vanquickenborne and

van Tiggelen (1966), the lift-off region is a premixed unreactive zone. This is the reason for a flatter shape in the distribution of the temperature at these low axial locations. Whereas when turbulence dominates, the shape of the profiles is curved, indicating a reactive flow. It is then concluded that the air and CO_2-diluted flames are lifted, not attached to the burner rim.

The sampling location $x/D_i = 20$ reveals the location of the stabilisation point of the air flame because the profile of the temperature for the diluted flames is fairly uniform at this location. It is suggested that the stabilisation point of the lifted air flame is located at about 90 mm above the burner exit surface whereas the equivalent point of the CO_2-diluted flames occurs at a higher axial location. This observation leads to the conclusion that the CO_2 acts as a destabilisation parameter, shifting the flame stabilisation point further downstream with a simultaneous change in the flame streamlines. Therefore, a direct comparison between axial locations for the air and the diluted flames is meaningless as the sampling locations were kept constant.

It is clear that there are differences in the shape of the temperature profiles between the various axial locations, which is an indication of the combustion progress. Within the lift-off region, the temperature profile is flat and there is an insignificant variation in the temperature values. Within the mid-flame zone, the temperature is minimum on the jet centreline and increases on moving radially outwards. In diffusion flames, the maximum flame temperature is found to be at the shear layer of the fuel and oxidiser streams where stoichiometric conditions exist and reactants are almost fully consumed. Moving further downstream, the temperature profiles become again smoother and flatter but now high temperatures exist, thus indicating the heat released by the chemical reactions. At $x/D_i = 125$, there is not a significant radial distribution in the mean flame temperature for all flame types and thus it implies that this location is close to the flame tip where fuel decomposition occurs.

Figure 4-1 shows that for the air flame, at x/D_i between 28 and 63 the maximum temperatures are located at $r = \pm 10$ mm. For the 5 % CO_2-diluted flame, at x/D_i between 28 and 37 the maximum values are found at $r = \pm 20$ mm and at x/D_i between 46 and 81 at $r = \pm 10$ mm. Furthermore, for the 10 % CO_2-diluted flame, at x/D_i between 28 and 37 the maximum values are at $r = \pm 20$ mm and at x/D_i between 46 and 81 the peaks are found on the centreline. Figure 4-2 illustrates the temperature field of the air and diluted flames in a contour plot as a function of the axial distance, from the burner

exit, and the radial distance, from the centreline. The temperature contour plots are a good indication that the CO_2 changes the shape and volume of the reaction zone, as discussed above. The temperature peaks for the flame types investigated during this experimental campaign, "Flame A", are found to be 1585 K, 1532 K and 1517 K for the air, 5 % and 10 % CO_2-diluted flames. Lower temperatures occurring in the CO_2-diluted flames are due to the higher heat capacity of the CO_2.

The standard deviation (std) in the averaged temperature data shows the degree of turbulence within the flame zone. However, the low std values that were observed are due to the thickness of the sheathed thermocouple probe. Fluctuations in the temperature readings are observed to change significantly in the radial direction, indicating the intensity of the chemical reactions. The highest temperature std for the air flame was $\pm 7.9\,^{\circ}C$, located at $x/D_i= 20$ and $r= \pm 10$ mm, for the 5 % CO_2-diluted flame it was $\pm 6.5\,^{\circ}C$ at $x/D_i= 63$ and $r= \pm 30$ mm and for the 10 % CO_2-diluted flame was $\pm 6.7\,^{\circ}C$ at $x/D_i= 63$ and $r= \pm 20$ mm.

Contour plots of the averaged flame temperature measurements are illustrated in Figure 4-2 to give a more representative illustration of the flow field and the changes caused by the addition of CO_2 in the oxidiser stream. The additional sampling locations are not included in the temperature contour plots and the downstream shift of the stabilisation point of the three lifted flame types is illustrated here. The effect of CO_2 on the flame structure is noticeable by the wider flame zone observed in the CO_2-diluted flames. Additionally, the contour plots reveal the cooling effect caused due to dilution.

4.3.2   Species profiles

Concentration profiles of the major combustion species are illustrated in Figures 4-3 to 4-10. In Figures 4-3, 4-5, 4-7 and 4-9, the concentration is presented in ppm or vol% and is plotted against the radial distance, r, for axial locations between 90 and 570 mm above the burner exit surface. In Figures 4-4, 4-6, 4-8 and 4-10, two-dimensional contour plots illustrate the concentration of these species in the physical space; the X axis represents the radial distance, from the centreline and the Y axis represents the axial distance, x, above the burner exit surface.
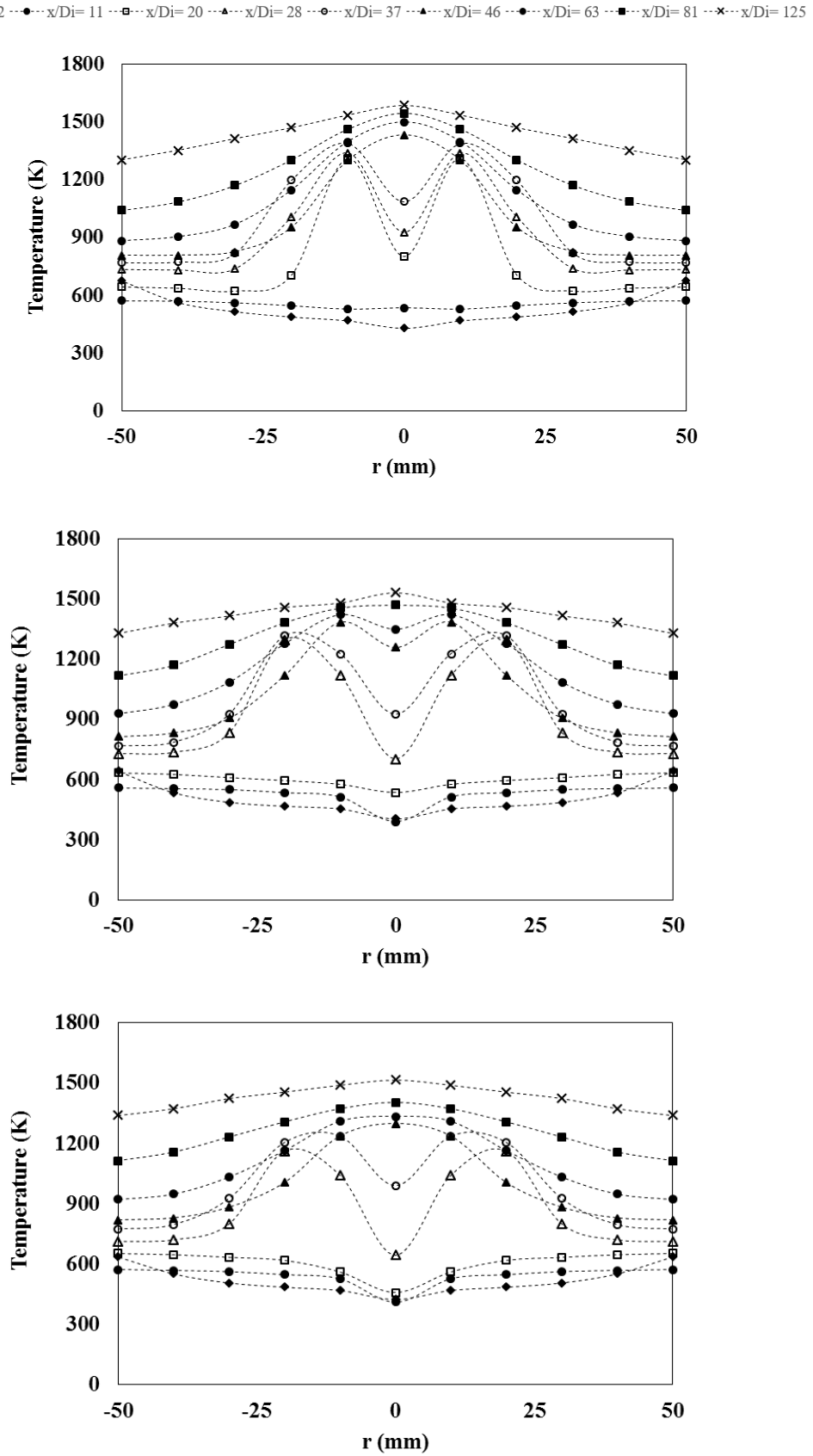
Figure 4-1 Radial distribution of the temperature measurements at all axial locations for the air, 5 % and 10 % CO$_2$-diluted flames, respectively.
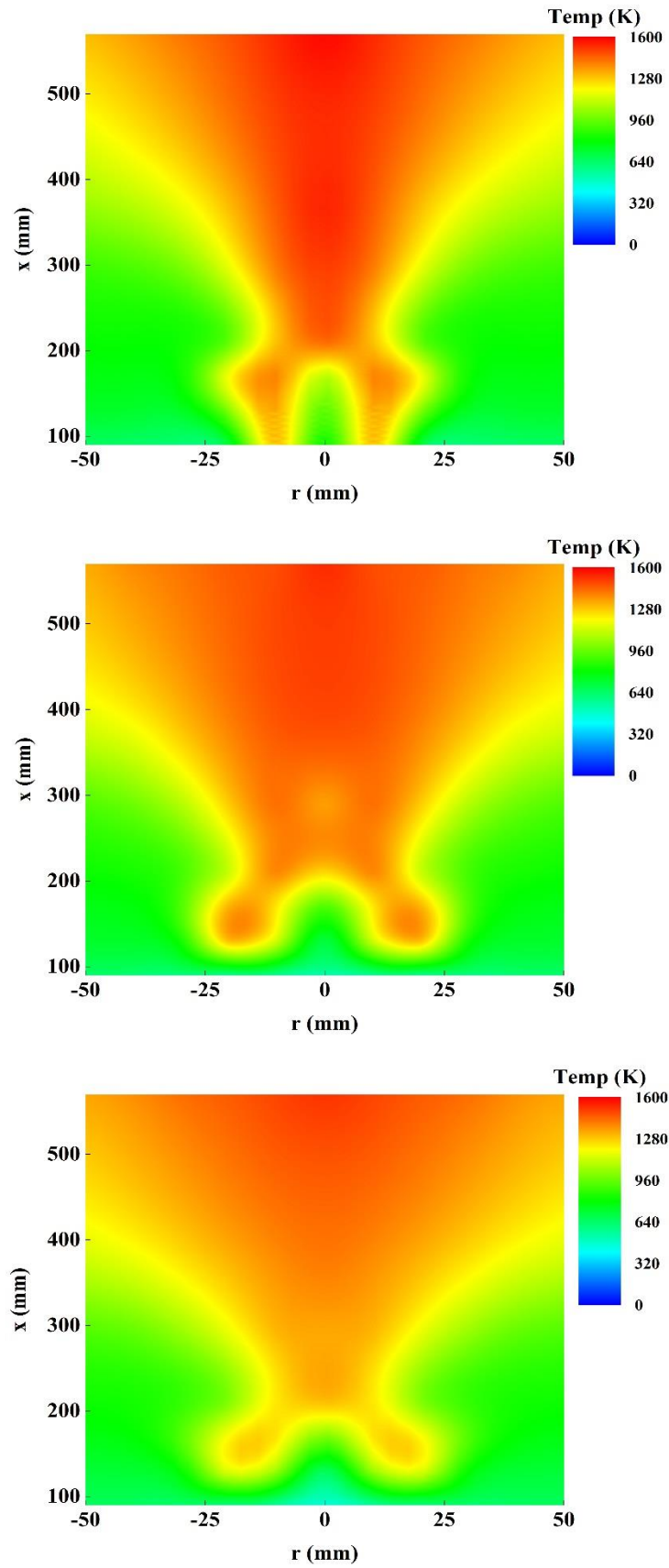
Figure 4-2 Contour plots with the temperature measurements for the air, 5 % and 10 % CO$_2$-diluted flames, respectively.

The dilution effect of CO$_2$ causes a reduction in the inlet O$_2$ concentration since the total volume of the oxidiser stream was kept constant between the three case studies examined in this chapter. The lower inlet O$_2$ concentration can be observed at the sampling location x/D$_i$= 20 and r= ±50 mm for the CO$_2$-diluted flames as this sampling point is outside of the flame where the oxidiser stream dominates. The flame instabilities caused by the CO$_2$ dilution can be evidenced also by the O$_2$ concentration at x/D$_i$= 20 apart from the temperature profiles. Between the diluted flames the change observed in the stabilisation point is due to the dilution level. The measured O$_2$ level at x/D$_i$= 20 is high enough, indicating the existence of a non-reaction zone for the diluted flames.

Close to the vicinity of the centreline, a gradual axial drop in the O$_2$ concentration is noticed. The reduction in the O$_2$ concentration depends on the mixing rate of the fuel and the oxygen and thus the combustion progress. The combustion process proceeds along the flame axis and the O$_2$ consumption becomes higher on moving away from the burner exit surface. Furthermore, high measured concentrations of O$_2$ are observed for the 10 % diluted flame which is an interesting finding as it suggests that the fuel does not react with the oxygen in a fast way. As reported in the literature and is evident by the O$_2$ concentration, the addition of CO$_2$ causes a reduction in the fuel burning rate.

In diffusion flames, fuel and oxidant are mixed through turbulent diffusion and molecular mixing. The blending of the separate volumes of fuel and oxidant, called turbulent mixing, occurs via large eddies. On the other hand, molecular mixing occurs at the interface of these distinct volumes and increases when mixing proceeds from the surface into the inner of these eddies. The combustion progress rate is determined by a comparison between the time scales of molecular mixing and chemical reaction. Any delay in the mixing process, which occurs prior to the reactions, is evident by the phenomenon called unmixedness (Lewis et al., 1956). Unmixedness is found where fuel species and O atoms are found in the centreline in a stoichiometric proportion and at a flame height well below the location where most fuel is completely burnt. In Figure 4-4, the O$_2$ contour plot of the air flame reveals the existence of this phenomenon which is a characteristic of the turbulent non-premixed flames. The O$_2$ is supposed to be consumed along the flame axis in a progressive manner but as is illustrated for the air flame, oxygen becomes again available downstream of the

stabilisation point. The distribution of the O$_2$ concentration within the flame zone is better understood if the distribution of THC is also considered.

Figure 4-5 presents the radial distribution of the THC concentration in a logarithmic scale for all axial locations. The characteristics of these plots are representative of a diffusion flame where the peak concentration of the THC occurs on the centreline and reduces gradually to zero when moving radially outwards from the centreline. The pyrolysis of the fuel mixture occurs through molecular transport of the fuel molecules to the flame front which is located at a radial distance from the centreline (Gollahalli, 1998). In a gas diffusion flame, the fuel concentration decreases in a slow rate as moving away from the burner exit surface. The axial drop in the THC concentration is more prominent in the air flame and indeed at x/D$_i$= 81 and 125, a very low concentration of THC is measured. This axial drop becomes less noticeable with increasing the dilution level. However, at x/D$_i$= 81 and 125, a low concentration of THC is also measured for the diluted flames. This observation suggests what other studies have concluded, namely the CO$_2$ addition causes the suppression of the fuel oxidation mechanism (Lee et al., 2001, Park et al., 2002). The contour plot of the THC concentration in Figure 4-6 reveals the existence of a strong fuel pocket formed at the centreline and confirms that the decomposition of the fuel mixture occurs in a radial direction from the centreline and is due to the mixing of the fuel with the oxidant stream. The unmixedness, as observed in the air flame, is illustrated here by the two separate red regions and is related to the lower mixing rate as compared to the combustion rate. Furthermore, it is clear that the fuel mixture is eventually oxidised where high temperatures occur and oxygen is available.

One of the main combustion products is CO$_2$ and its profile within the flame zone is used to determine the effects of adding CO$_2$ into the combustion air stream. The peak concentration of CO$_2$ for all types of flame is found to be at the highest in-flame sampling location, x/D$_i$= 125, where the consumption of the fuel is intense due to the high flame temperatures which are present. The maximum measured concentration of CO$_2$ is 7.6 %, 12.6 % and 15.8 % for the air, 5 % and 10 % CO$_2$-diluted flames, respectively. For the diluted flames, x/D$_i$= 20 is located upstream of the stabilisation point where premixing is dominant and it should be mentioned that the high concentration of CO$_2$ at this region is due to the CO$_2$ addition. As shown in Figure 4-7, the concentration of the main combustion product, the CO$_2$, peaks at the flame front, away from the centreline. In the vicinity of the reaction zone of non-premixed flames,

fuel molecules have been transported from the centreline to be consumed by reactive radicals. The flame temperature and the concentration of the major product species, such as water and carbon dioxide, are increased in the reaction zone (Giles et al., 2006). Considering the contour plots in Figure 4-8, it can be concluded that CO$_2$ alters the flame zone significantly. Firstly, the CO$_2$ contour plot for the air flame confirms the delay between the mixing and reaction times due to unmixedness. Secondly, when CO$_2$ is added into the flame zone, two branches of a high CO$_2$ concentration are formed in the diluted flames, indicating the location of the burning surface.

A harmful combustion product is the NO$_x$ species which mainly consist of NO rather than NO$_2$ emissions in jet diffusion flames. As depicted in Figures 4-9 and 4-10, high concentration of NO$_x$ emissions is measured in regions of low O$_2$ concentration, and hence a low concentration of O atoms, and high flame temperatures. The slow Zeldovich mechanism becomes the dominant formation pathway at temperatures above 1800 K. The weakness of the thermal NO pathway to account for the measured NO$_x$ emissions is evident due to the insufficient flame temperatures combined with low O atoms concentration occurring at the locations of high NO$_x$ emissions. The initiation step for the prompt NO mechanism is the reaction of a hydrocarbon radical with the nitrogen molecule, which is observed to occur in the flame front where most fuel molecules have been transported (Fenimore, 1971). Considering the distribution of the THC concentration, the fuel mixture starts to decompose near the reaction zone of the diffusion flame and therefore, it can be assumed that the NO$_x$ formation is mainly attributed to the Fenimore prompt mechanism which is dominant in lower temperatures and in fuel-rich conditions, as described in Section 2.3.1.2. According to Hayhurst and Vince (1980), the diffusion flames are considered to have a slightly fuel-rich reaction zone surrounded by a slightly fuel-lean zone which suppresses the NO destruction mechanism. The proposed formation mechanism for the measured NO$_x$ emissions is consistent with the study of Nishioka et al. (1994) who also found that in pure diffusion flames, NO is generated by the prompt mechanism and the peak concentration of NO is found to be in the vicinity of the temperature peak. In addition, they suggested that the thermal pathway plays a minor role to the total NO$_x$ produced in diffusion flames. Figures 4-1 and 4-9 show that the NO$_x$ profile follows the temperature profile and the NO$_x$ emissions reach a maximum at positions near the temperature maxima where the main reaction zone of the diffusion flames exists.
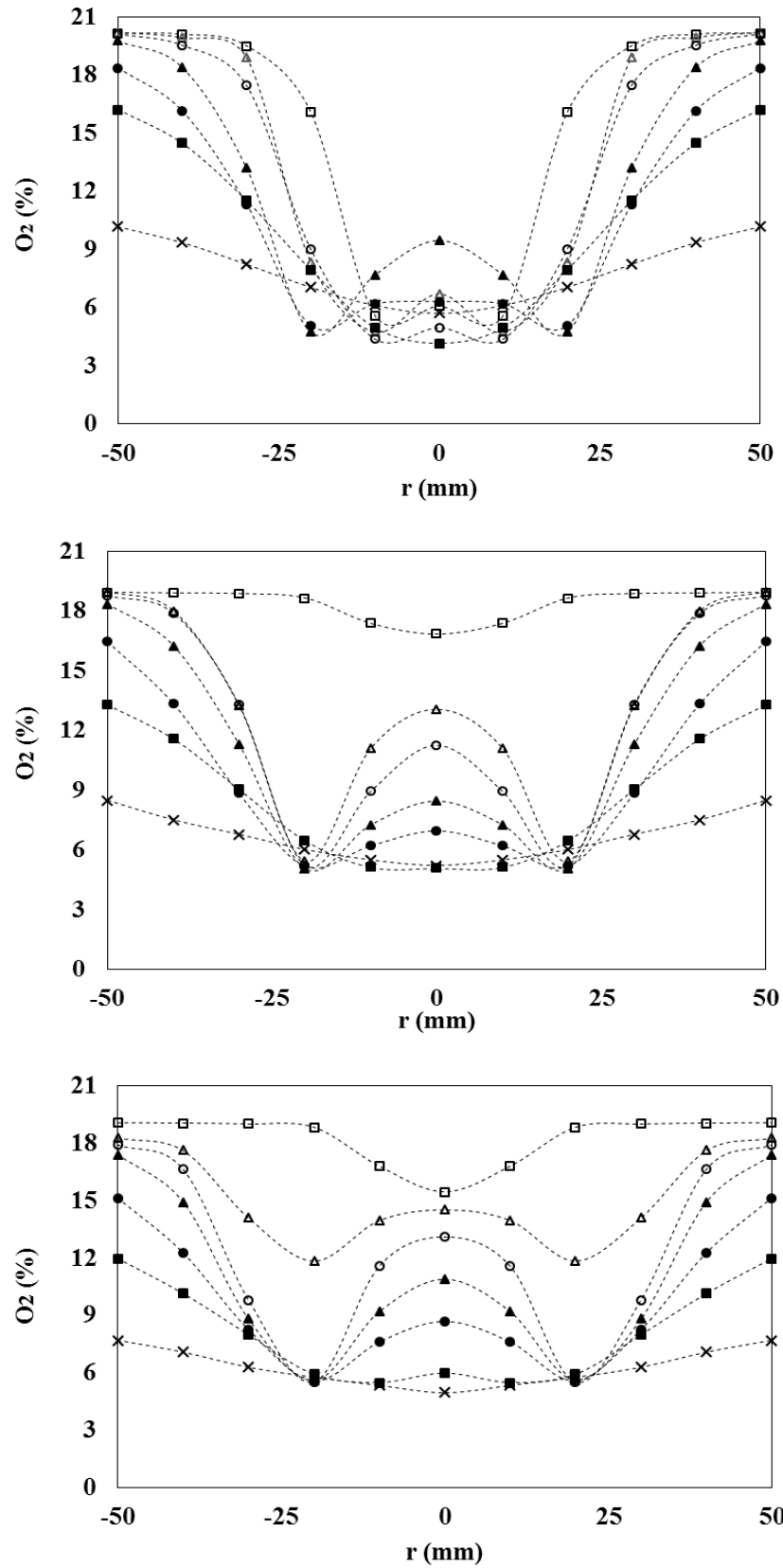
Figure 4-3 Radial distribution of the O$_2$ concentration at all axial locations for the air, 5 % and 10 % CO$_2$-diluted flames, respectively.
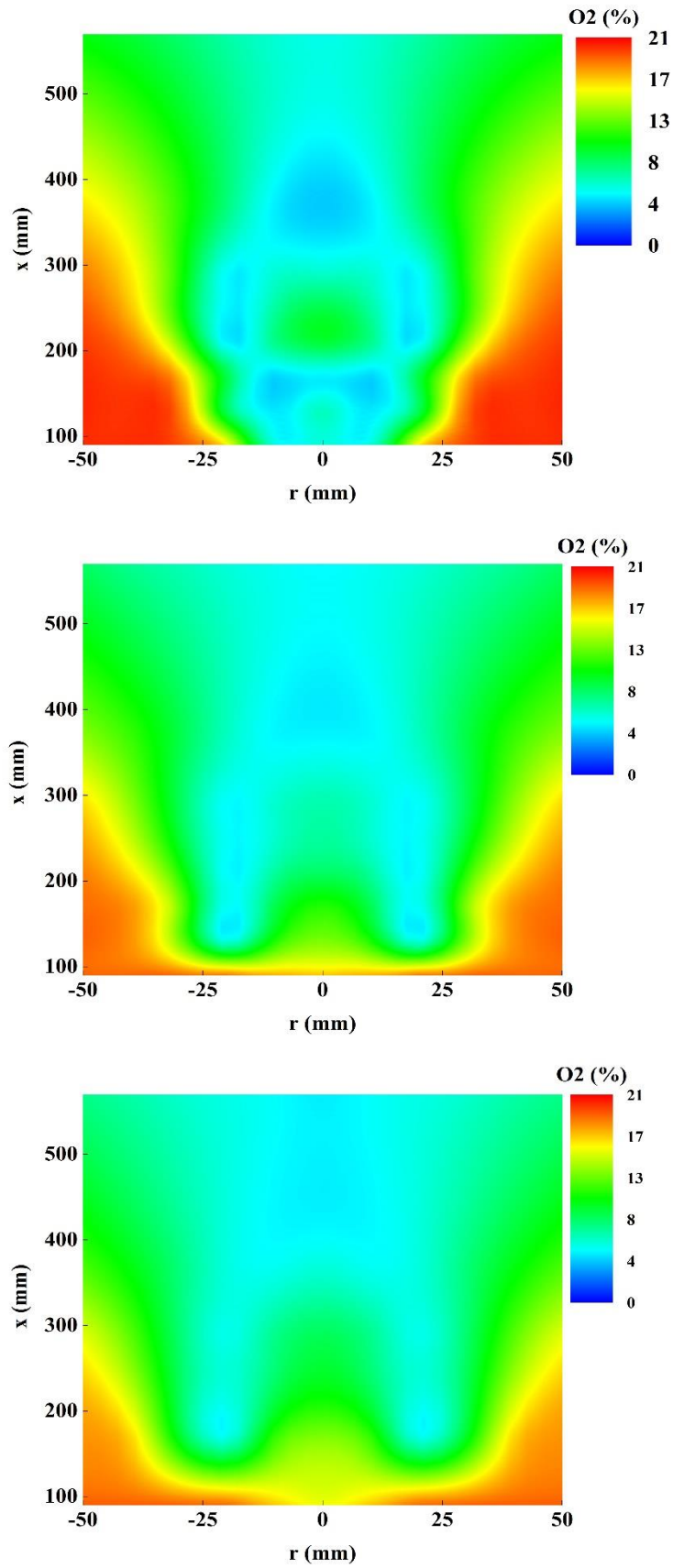
Figure 4-4 Contour plots of the O$_2$ concentration for the air, 5 % and 10 % CO$_2$-diluted flames, respectively.
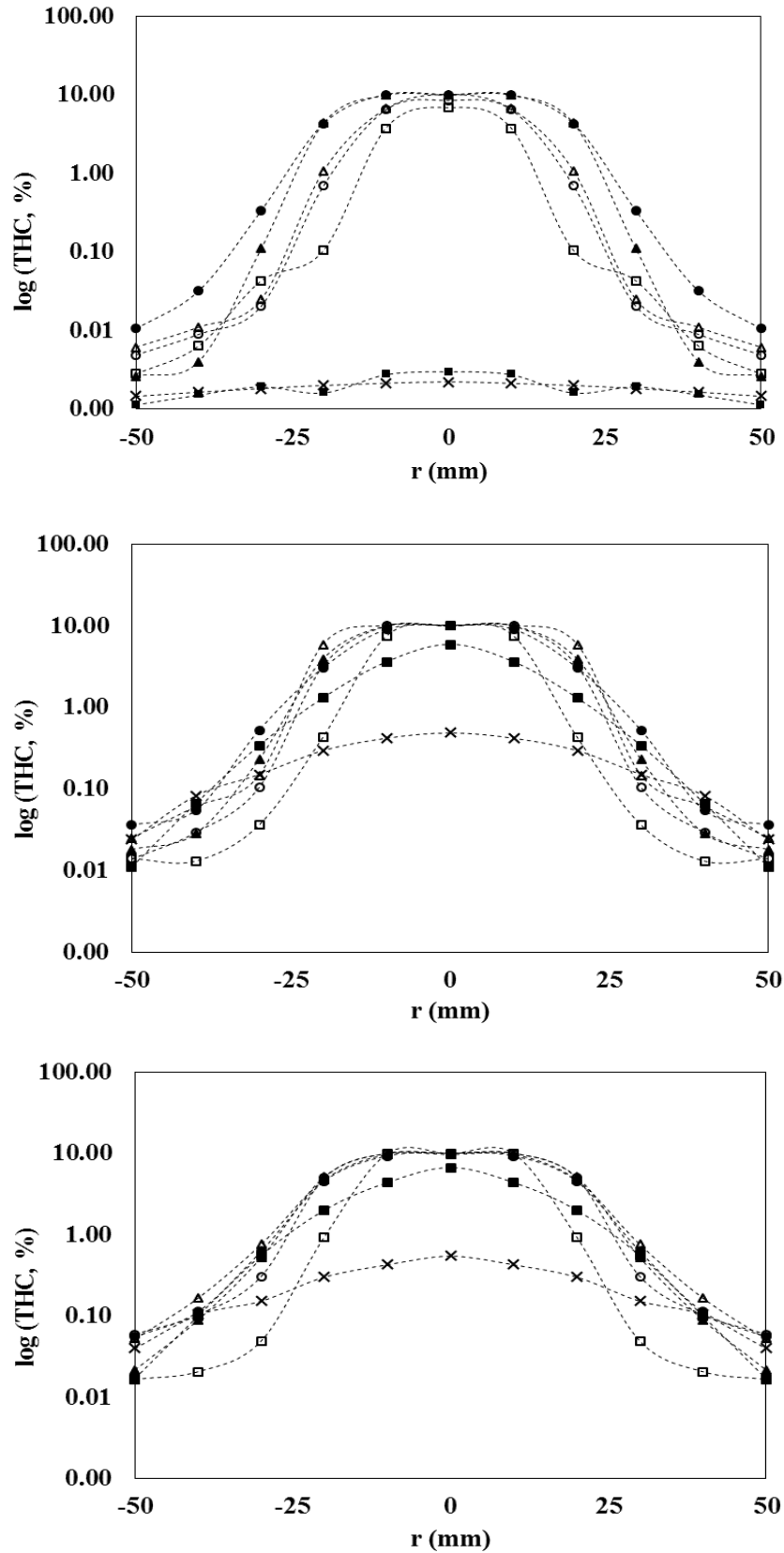
Figure 4-5 Radial distribution of the THC concentration at all axial locations for the air, 5 % and 10 % CO$_2$-diluted flames, respectively.
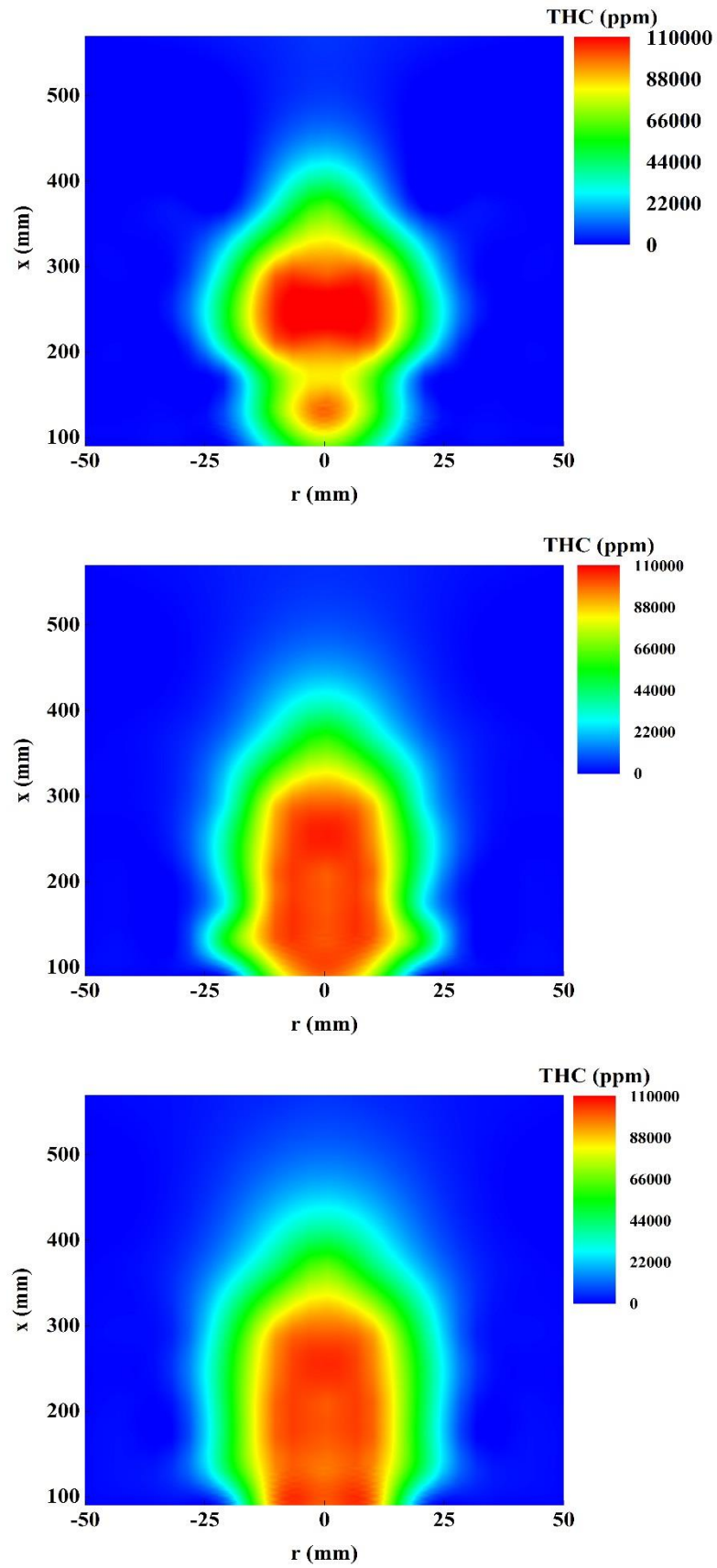
Figure 4-6 Contour plots of the THC concentration for the air, 5 % and 10 % CO$_2$-diluted flames, respectively.
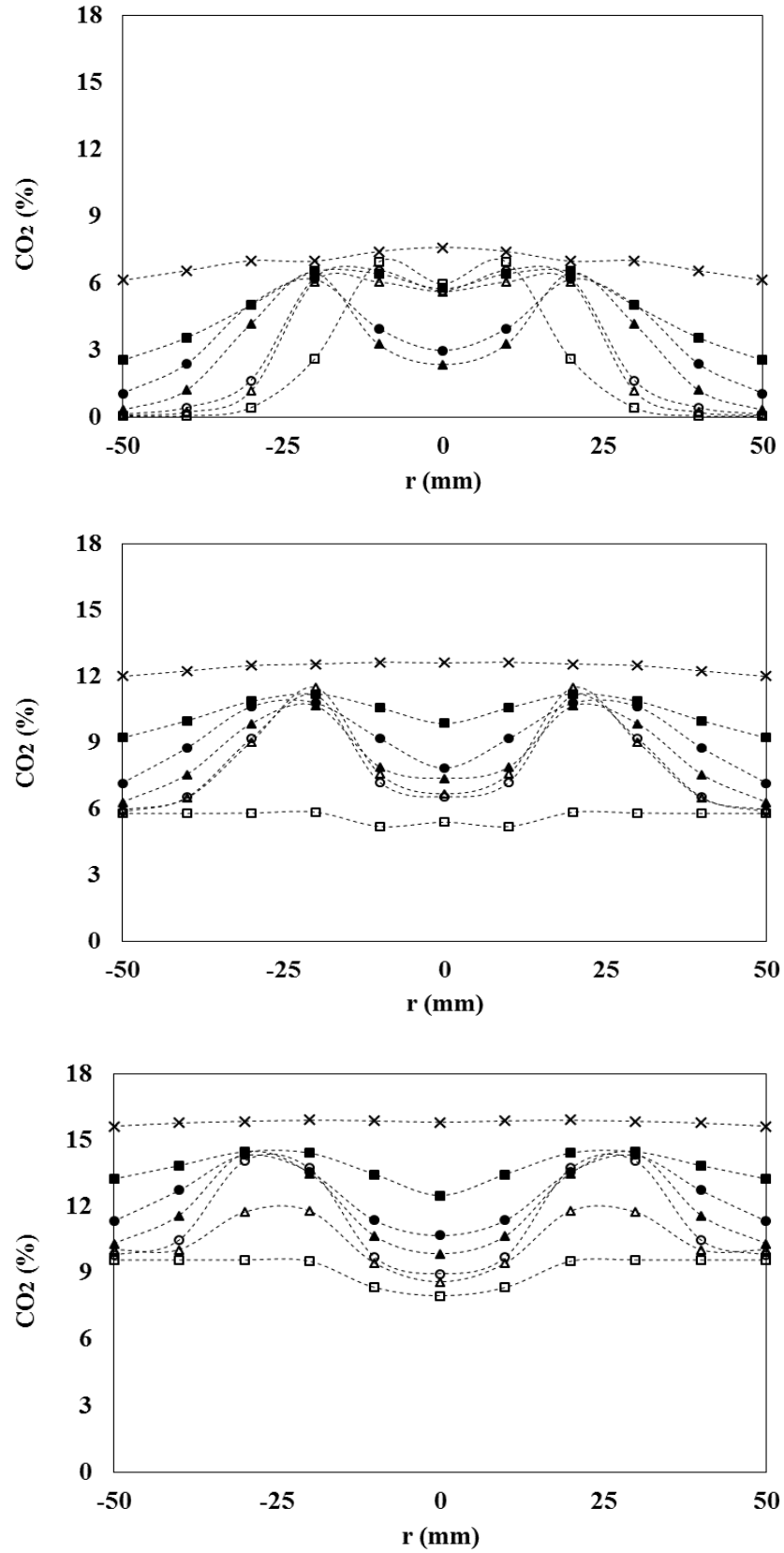
Figure 4-7 Radial distribution of the CO$_2$ concentration at all axial locations for the air, 5 % and 10 % CO$_2$-diluted flames, respectively.
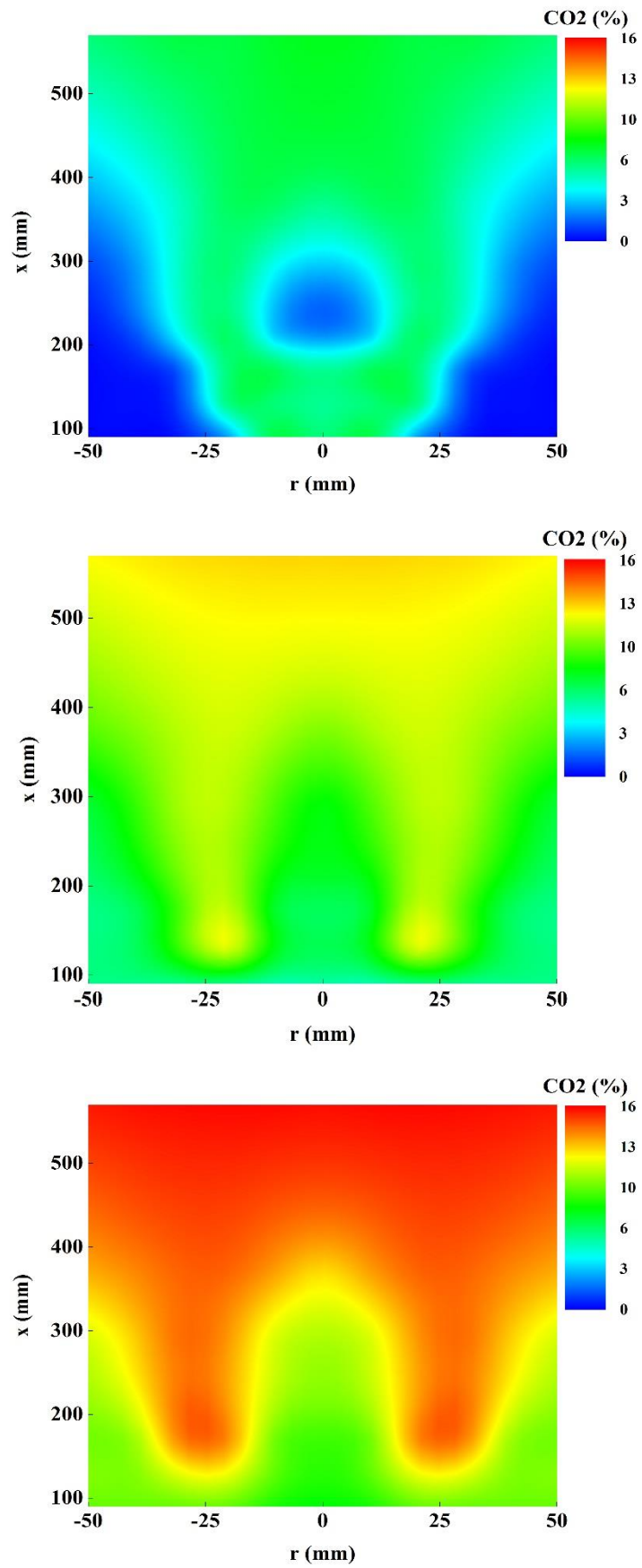
Figure 4-8 Contour plots of the CO$_2$ concentration for the air, 5 % and 10 % CO$_2$-diluted flames, respectively.

The measured maximum concentration of NO_x for the air flame is 204 ppm and is located at $x/D_i= 81$, as seen in Figure 4-9. There is a significant reduction in the NO_x level with the addition of CO_2 as the maximum measured concentration fell to 144 ppm and 112 ppm for the 5 % and 10 % CO_2-diluted flames, respectively. The reduction in NO_x emissions is in excellent agreement with the anticipated behaviour of CO_2 in a reacting system. Lee et al. (2001) has concluded that CO_2 changes the methane reaction pathways in a favourable way for the reduction of total NO_x emissions, as explained in Section 2.5.2.2. It is observed that at $x/D_i= 125$ the measured NO_x level is lower than at 81 which can be attributed to the fact that radical recombination reactions are close to completion at this point and the fuel decomposition rate has dropped significantly.

The distribution of the CO concentration at various sampling locations within the flame zone is shown in Figures 4-11 and 4-12. As has been already evidenced, the addition of CO_2 moves the lifted flame base further downstream, the flame streamlines are in turn affected and thus a direct comparison between the axial locations of each flame type is not meaningful. In all cases, CO is found to be maximum in regions of a low O_2 and a high THC concentration. As reported by Chen and Ghoniem (2014), CO emissions are mainly produced in the fuel-rich regions of diffusion flames and is the main indicator of incomplete combustion conditions. This is illustrated in Figure 4-12 where the maximum concentration of CO is located closer to the fuel-rich zone of the diffusion flame sheet, the centreline, rather than the on the oxidiser-rich zone. The experimental results reveal that the addition of CO_2 affects the formation of the CO emissions due to the significant reduction in the flame temperature. Temperature plays an important role in chemical reactions; the lower the flame temperature is, the more time the fuel needs to be oxidised to CO or CO_2.

Similar studies have reported that the reduction in flame temperature due to dilution leads to lower fuel burning rates (Røkke and Hustad, 2005, Jansohn et al., 2011). Moreover, Marsh et al. (2017) have shown that for flame temperatures below 2400 K the CO_2 dissociation reaction is not important and cannot account for the increased CO emissions.
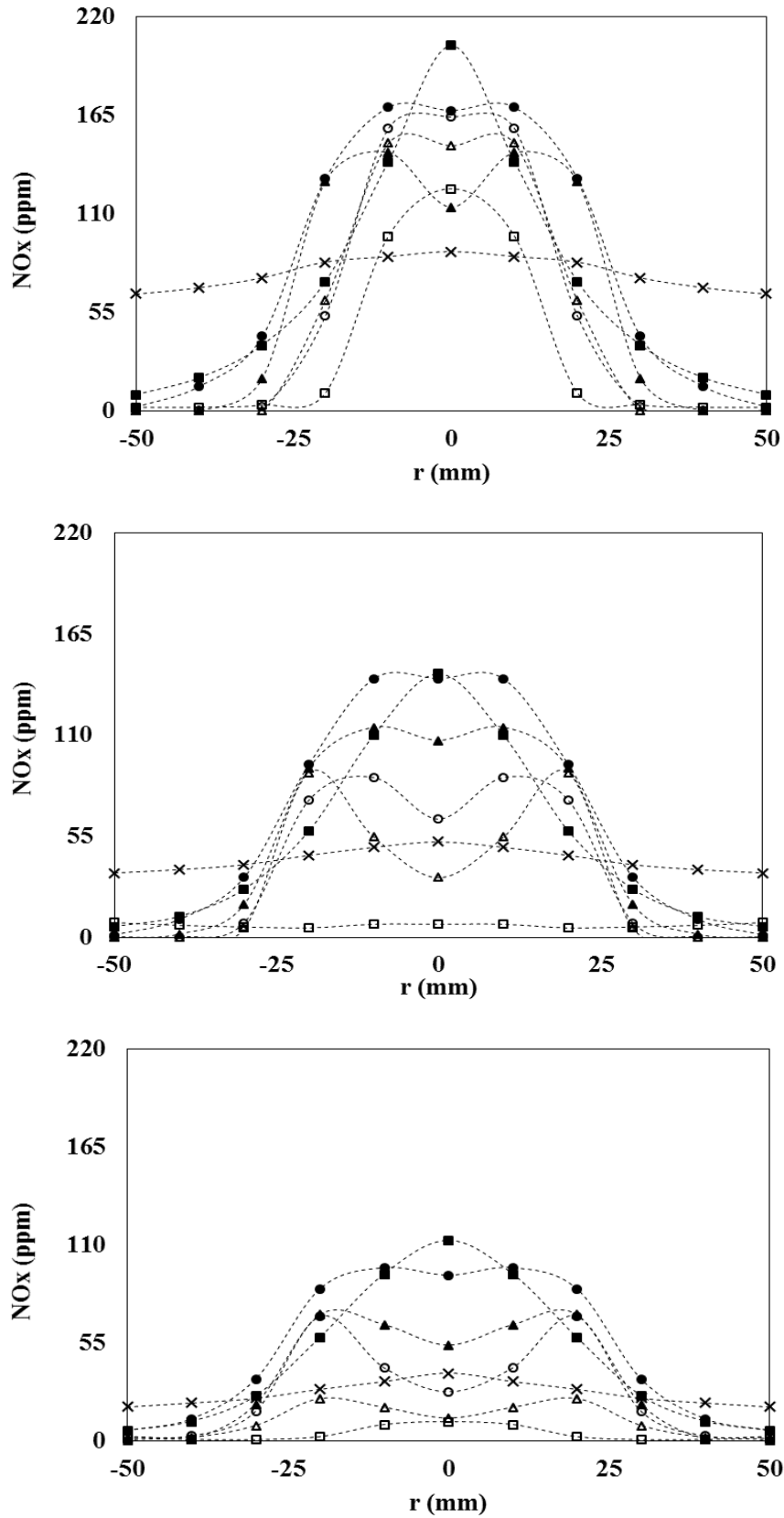
Figure 4-9 Radial distribution of the NO$_x$ concentration at all axial locations for the air, 5 % and 10 % CO$_2$-diluted flames, respectively.
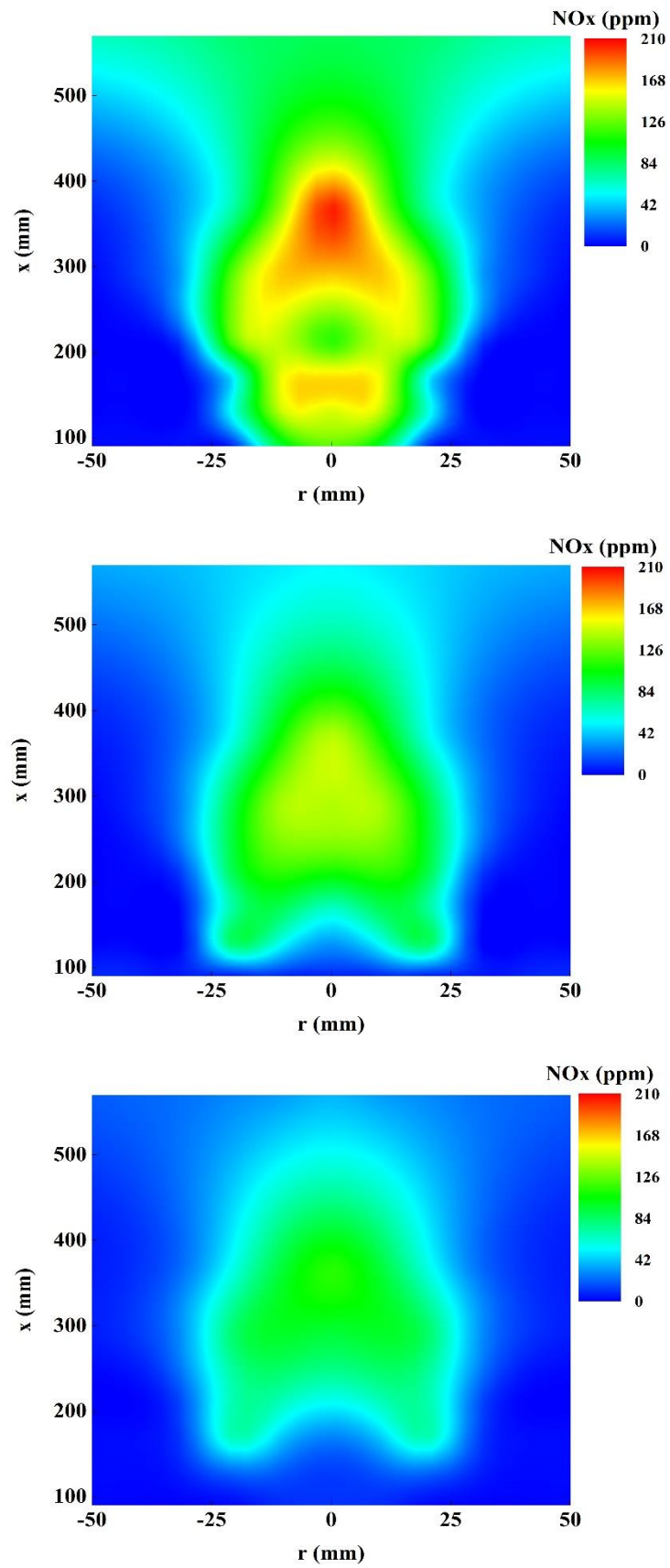
Figure 4-10 Contour plots of the NO$_x$ concentration for the air, 5 % and 10 % CO$_2$-diluted flames, respectively.
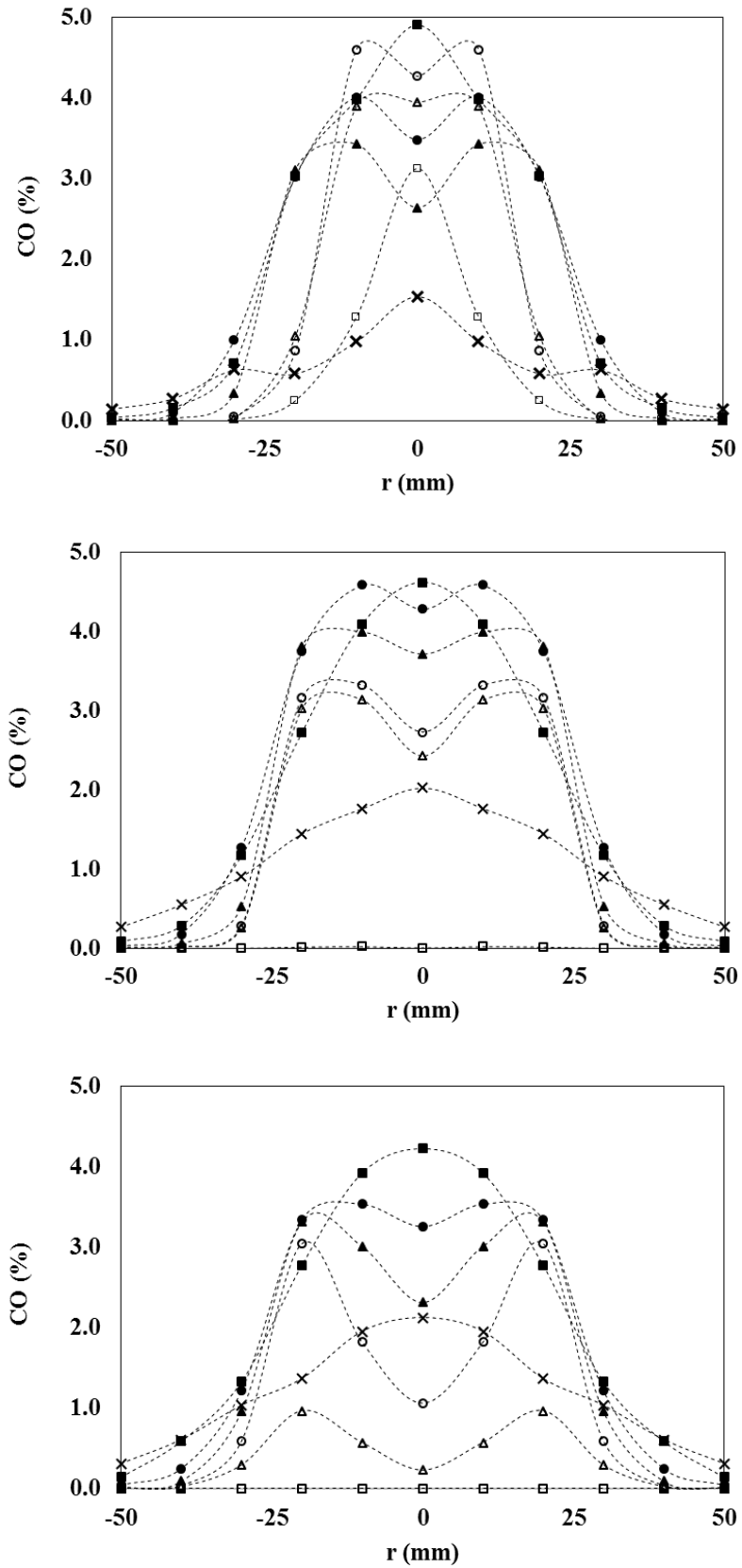
Figure 4-11 Radial distribution of the CO concentration at all axial locations for the air, 5 % and 10 % CO$_2$-diluted flames, respectively.
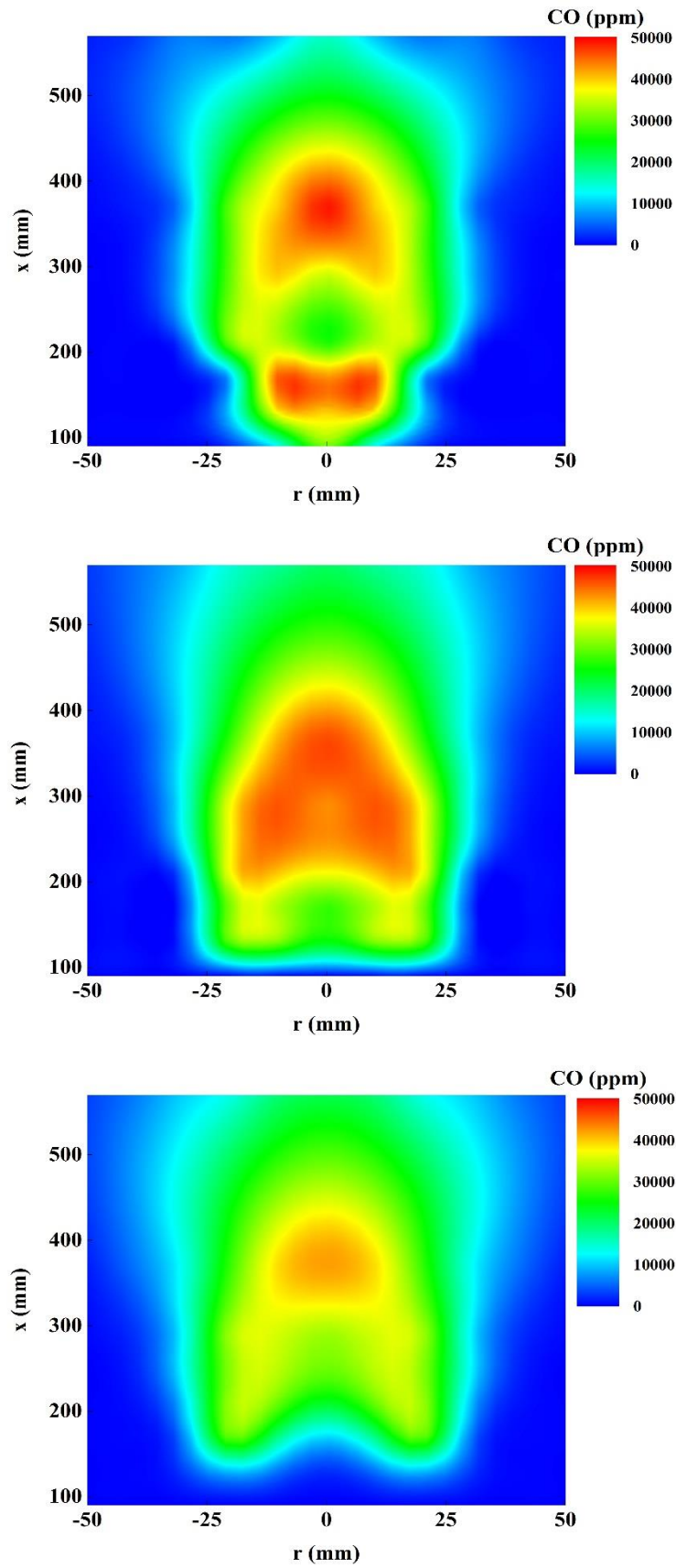
Figure 4-12 Contour plots of the CO concentration for the air, 5 % and 10 % CO$_2$-diluted flames, respectively.

4.4   Exit Measurements

Gas species measurements are also taken at the exit of the chamber, which is located at about 1700 mm above the burner surface, $x/D_i = 372$, to further demonstrate the effect of CO_2 on the combustion of natural gas. At the exit of a combustion system, radical recombination reactions are completed and the temperature has significantly dropped to a level that cannot sustain chemical reactions and minor traces of THC are usually found. Table 4-2 presents the temperature of the exhaust gases as measured at the central axis of the final convergent part of the chamber. It appears that the temperature is almost the same for the air and CO_2-diluted flames but significantly lower than the measured averaged temperatures occurring within the flame zone. As the addition of CO_2 increases the lift-off distance, the flame volume and length are also affected and therefore, the exit temperature does not vary with dilution.

Table 4-2 Measured exit temperatures in Kelvin.

"Flame A"	T_exit (K)
Air flame	850
5 % CO₂-diluted flame	848
10 % CO₂-diluted flame	849

Figure 4-13 illustrates the exit emissions of CO_2 as a function of its inlet volumetric percent which is added to the oxidiser stream. It is expected that the addition of CO_2 as a reactant inevitably increases its concentration as a product. The increase in the CO_2 emissions is more prominent between the air and the 5 % diluted flames. The dilution effect of CO_2 leads to the decreased exit O_2 concentration as the inlet air amount was reduced accordingly in order to keep constant the total oxidiser flow rate. The reduction of the exit O_2 emissions as a function of the CO_2 inlet volumetric percent is outlined in Figure 4-14. The impact is more prominent between the air and the CO_2-diluted flames rather than between the 5 % and 10 % CO_2-diluted flames.
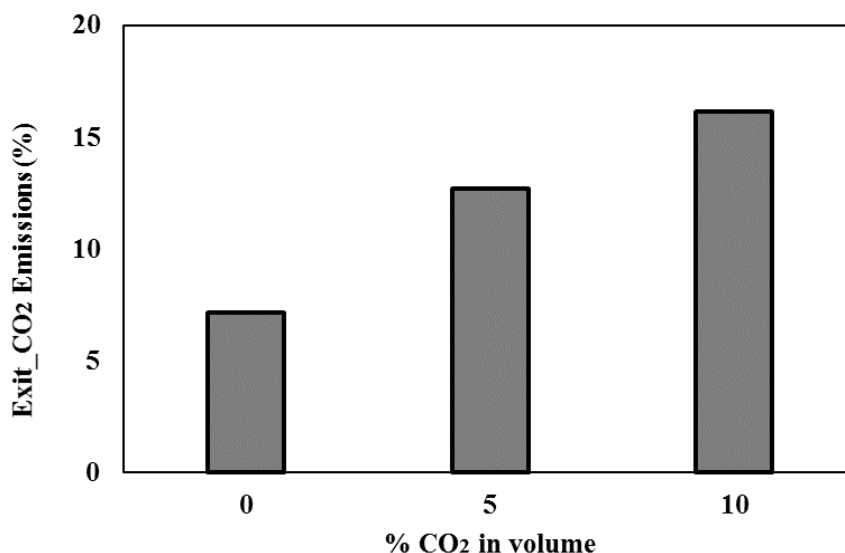
Figure 4-13 Exit CO_2 emissions in vol% as a function of the inlet volumetric percent of CO_2.
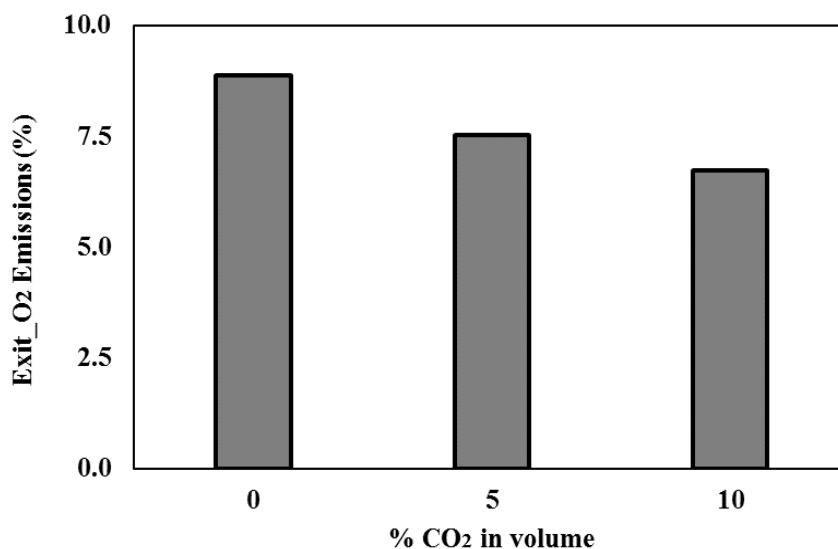
Figure 4-14 Exit O_2 emissions in vol% as a function of the inlet volumetric percent of CO_2.

Figure 4-15 presents the THC emissions as measured at the exit of the chamber as a function of the added CO_2 percent. For the air flame, almost any unburnt fuel was detected indicating complete combustion of the natural gas mixture. Whereas for the 10 % CO_2-diluted flame, a low concentration of THC, at about 75 ppm, is measured. The addition of 5 % CO_2 is observed to have a minor impact on the exit THC emissions. As combustion reactions have terminated at this sampling location, the exit emissions are representative of the negative thermal and chemical effects of the addition of CO_2.
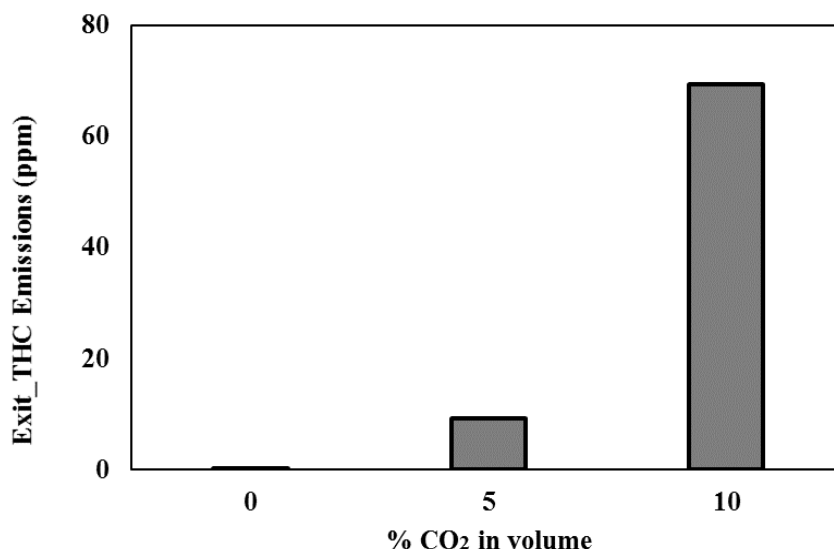
Figure 4-15 Exit THC emissions in ppm as a function of the inlet volumetric percent of CO$_2$.

Similarly, Figure 4-16 outlines the impact of the added CO$_2$ in the air stream on the CO emissions for the air and the diluted flames. As hardly any THC emissions were measured at the exit of the chamber under air combustion, emissions of CO are not expected to be found because complete combustion leads to a complete oxidation of CO to CO$_2$. However, there is a clear increase in the exit CO emissions when 10 % CO$_2$ in volume is added to the oxidiser stream, leading to about 75 ppm to be measured. A slight increase is observed when 5 % CO$_2$ is added, which is equivalent to 10 ppm being measured. The trend in the profile of the exit CO emissions follows the emissions trend of THC which is expected as CO is the intermediate product formed during the oxidation of any carbonaceous fuel.
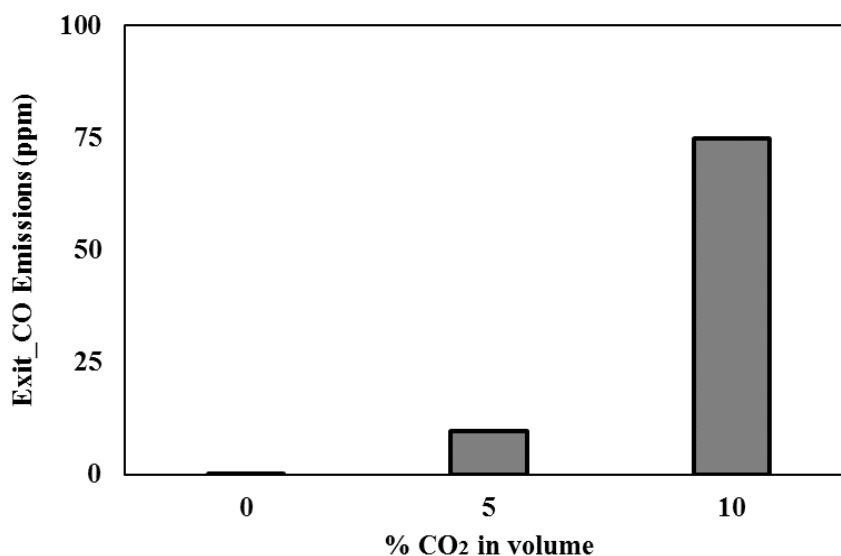
Figure 4-16 Exit CO emissions in ppm as a function of the inlet volumetric percent of CO$_2$.

The in-flame measurements of NO_x emissions suggested that CO_2 as part of the reactant stream alters the formation pathways of NO_x and thus reduces their formation. Figure 4-17 illustrates the exit emissions of NO_x as a function of the inlet concentration of CO_2 and indicates its strong impact which causes a 28% and a 50% reduction in the NO_x emissions for the 5 % and 10 % CO_2-diluted flames, respectively, as compared to the level of NO_x emissions measured in the air flame. The reduction is caused by the flame temperature drop which inhibits the thermal NO formation and does not enhance the prompt initiation step. Furthermore, the prompt pathway, which is the dominant mechanism for the in-flame emissions, is suppressed by the lower availability of fuel species, such as CH, due to dilution, as explained in Section 2.3.1.2.
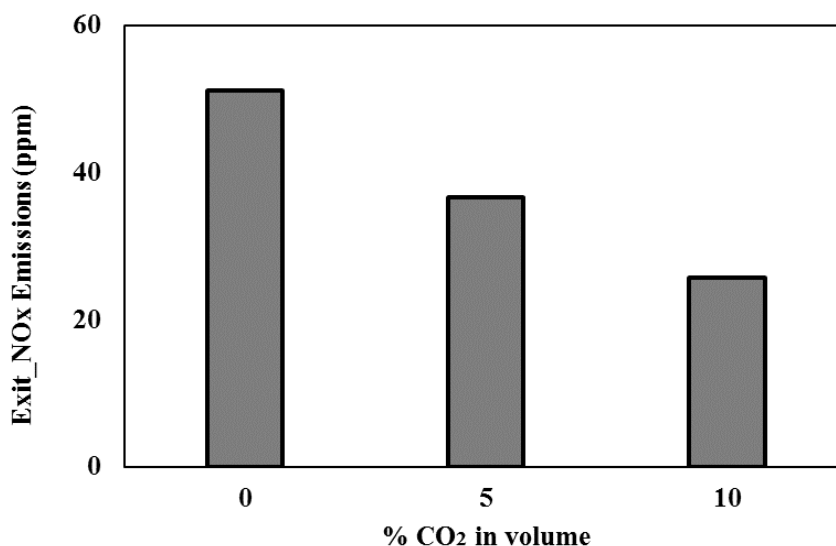
Figure 4-17 Exit NO_x emissions in ppm as a function of the inlet volumetric percent of CO_2.

It is common to report metrics, such as NO_x and CO, taken at the exit of a reactive system, in terms of the fuel mass consumption or the net power output. Within this study, it is not possible to report the emissions on a power basis as only a gas burner was utilised. However, the emissions are reported based on the mass of fuel burnt so that they can be compared under different test conditions and/or technologies and useful information can be extracted in terms of the levels of the pollutant emissions of a combustion system. As explained in Section 3.4.6.1, the emission index (EI) of a pollutant represents the mass of the pollutant emitted per the mass of the burnt fuel, (g/kg). Figure 4-18 shows the $EINO_x$ and EICO values as a function of the inlet volumetric percent of CO_2 added to the oxidiser stream. The $EINO_x$ are represented by the black "x" symbols and the EICO by the black-filled triangle symbols.

It is noted that by increasing the concentration of the CO_2 in the oxidiser stream, both $EINO_x$ and EICO are significantly affected. The decrease in the $EINO_x$ is consistent with the reduction of the in-flame NO_x emissions with dilution. The thermal and chemical impact of CO_2 on the NO_x attribute considerably to their emissions by lowering the flame temperature and affecting their kinetic mechanism. Furthermore, the temperature of the exhaust gases is significantly lower than the temperature required to sustain the Zeldovich reaction mechanism. In addition, at the exit of the chamber, a very low concentration or traces of THC are measured and thus the absence of fuel radicals cannot maintain the production of NO_x via the Fenimore reaction mechanism.

Similar to the in-flame CO data, the calculated EICO value for the CO_2-diluted flames is higher than the equivalent value for the air flame, which is consistent with the literature. Particularly, for the air flame, traces of CO were measured at the exit of the utilised chamber. The presence of CO_2 in the oxidiser stream causes an increase in the exit CO measured emissions, and hence increase the EICO value because the reduced flame temperature due to CO_2 slows down the oxidation reaction of CO through the suppression of the reaction of CO with OH.
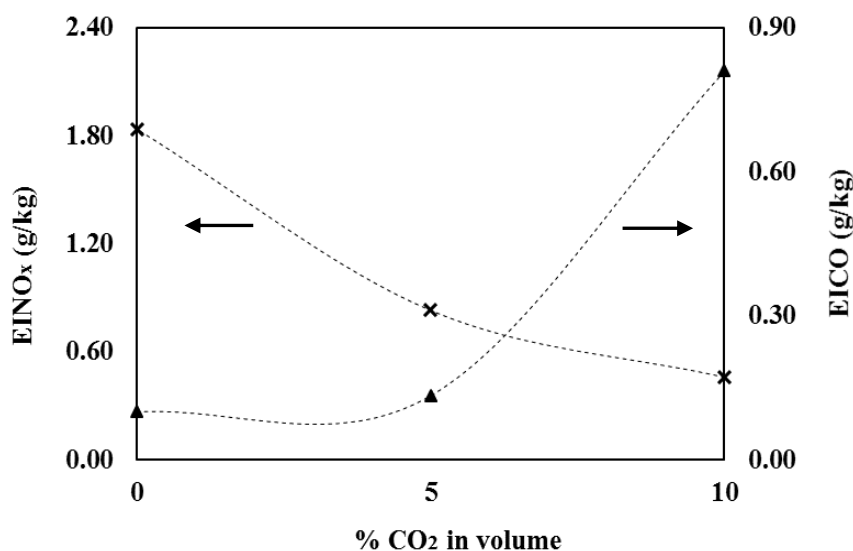
Figure 4-18 Calculated $EINO_x$, black "x" symbols, and EICO, black-filled triangle symbols, as a function of the inlet CO_2 volumetric percent.

4.5 Discussion

A summary of the main key experimental findings as observed during the test campaign "Flame A" is presented below. The main conclusions are as follows:

- The reduction in the flame temperature due to the enhancement of the air stream with CO$_2$ is evident through the temperature fields. The peak in-flame temperatures were measured at x/D$_i$= 125, which is equal to 570 mm above the burner surface. The maximum in-flame averaged temperature was at about 1585 K, 1532 K and 1517 K for the air, 5 % and 10 % CO$_2$-diluted flames, accordingly. The temperature drop of the air and the 5 % CO$_2$-diluted flame is more prominent than the temperature difference between the diluted flames.

- The added CO$_2$ is replacing part of the air stream and thus the level of the inlet O$_2$ decreases. The dilution effect of CO$_2$ is shown at x/D$_i$= 20 and r= ±50 mm for all three case studies where the maximum inlet O$_2$ concentration is measured as there is no flame at this sampling point and the oxidiser stream is dominant. As depicted in the O$_2$ contour plots, Figure 4-4, CO$_2$ affects negatively the stability of the flame because it lifts the flame base further downstream. The velocity ratio of the fuel and oxidiser streams was kept constant and hence the downstream shift of the flame base can only be attributed to the addition of CO$_2$ and its ability to absorb more heat. At x/D$_i$= 125, the O$_2$ concentration was measured to be 5.7 %, 5.2 % and 5 % and at x/D$_i$= 372, to be 8.9 %, 7.5 % and 6.7 % for the air, 5 % and 10 % CO$_2$-diluted flames, accordingly. Due to the excess air added to the combustion system, high levels of O$_2$ are measured at the exit of the utilised burner test rig. The exit O$_2$ emissions are higher than the levels measured at x/D$_i$= 125 as chemical reactions are completed at this sampling point and oxygen can no longer be consumed.

- The distribution of the THC refers to the overall combustion progress. In Figure 4-5, it is clear that the burning of the fuel mixture under air combustion occurs progressively between x/D$_i$= 20 to 63 with a steep drop at x/D$_i$= 81 and in turn at x/D$_i$= 125. Whilst the addition of CO$_2$, slows down the fuel burning process, as indicated by the existence of a fuel pocket between x/D$_i$= 20 to 81, at x/D$_i$= 125 there is a significant reduction in the THC concentration. The exit THC emissions are considered to be negligible for the air and 5 % diluted flames, 0.1 ppm and 9 ppm, respectively, and low for the 10 % diluted flame, 70 ppm. On the other hand, the THC concentration at x/D$_i$= 125 was found to be 4000 ppm, 4865 ppm and 5476 ppm for the air, 5 % and 10 % CO$_2$-diluted flames, accordingly. The difference in the concentration between these two axial sampling locations, x/D$_i$=

125 and 372, indicates the continuation of the combustion reactions at post-flame regions which leads to the complete burning of the fuel.

- The maximum in-flame measured CO$_2$ concentration was 7.6 %, 12.6 % and 15.8 % in the air, 5 % and 10 % CO$_2$-diluted flame flow fields, respectively. Due to the peak flame temperature being measured at x/D_i= 125, the peak concentration of CO$_2$ was also measured at this axial sampling location. As shown above, the reactions continue downstream the flame zone at higher axial locations, the post-flame regions, and terminate before the exit of the chamber. Consequently, the exit emissions of CO$_2$ are higher than the levels at x/D_i= 125, particularly, they are measured to be 8 %, 12.7 % and 16.2 % for the air, 5 % and 10 % CO$_2$-diluted flames.

- The averaged peak concentration of the NO$_x$ emissions was measured at x/D_i= 81 for all flame types and is 204 ppm, 144 ppm and 112 ppm for the air, 5 % and 10 % CO$_2$-diluted flames, accordingly. The experimental data analysis in Section 4.3.2 suggests that the NO$_x$ emissions are mainly produced via the prompt mechanism which depends mostly on stoichiometry and less on the flame temperature. Therefore, NO$_x$ emissions peak where fuel radicals are in abundance, as indicated by the fuel decomposition and the steep drop in the THC concentration. Therefore, their peak values are measured at x/D_i= 81 as it appears that the fuel decomposition is more intense at this region. Similar to the temperature drop, the reduction in the NO$_x$ emissions with the addition of CO$_2$ is clear and mainly noticeable between the air and the 5 % diluted flame rather than the reduction between the CO$_2$-diluted flames. The exit emissions of NO$_x$ species are found to be 51 ppm, 37 ppm and 26 ppm for the air, 5 % and 10 % CO$_2$-diluted flames. It is remarkable the influence of CO$_2$ on the NO$_x$ species.

- The in-flame CO emissions at x/D_i= 81 were measured to be 4.9 %, 4.6 % and 4.2 % and at x/D_i= 125 to be 1.5 %, 2 % and 2.2 % for the air, 5 % and 10 % CO$_2$-diluted flames, respectively. The in-flame measurements taken below x/D_i= 81, lead to the false conclusion that the air flame produces more CO than the diluted flames despite the addition of CO$_2$ and its chemical impact. The exit emissions of CO are 0.1 ppm, 10 ppm and 75 ppm for the air, 5 % and 10 % CO$_2$-diluted flames, accordingly. Negligible amount of CO is found under air and 5 %-diluted combustion and a low concentration for the 10 % diluted flame. The reporting of the emissions at x/D_i= 125 and 372 can suggest that the addition of CO$_2$ has an

impact on the formation of CO as is reported in the literature. The CO emissions follow the same trend as the THC as CO is the intermediate oxidation product of the fuel mixture. It is concluded that the formation of CO depends strongly on the flame temperature and residence time and its oxidation is a slow chemical process.

4.6   Conclusions

In Chapter 4, the impact of the addition of CO_2 into fuel-lean natural gas diffusion flames with an initial equivalence ratio, $\Phi = 0.58$, is presented. The experimental methodology followed in this study was to keep the velocity ratio of the oxidiser and fuel streams constant. Because varying the fuel flow rate was out of the range of interest of this study, to keep the velocity ratio constant, the flow rate of the oxidiser mixture needed to be kept the same. Therefore, there is a slight variation in the equivalence ratio between the air and the diluted case studies due to dilution of the total mixture. The in-flame and exit species concentration and the flame temperature along with the emission index of the NO_x and CO species are presented at various axial locations. The experiments are conducted utilising the in-house built combustion chamber, as presented in Chapter 3, to allow for the characterisation of confined natural gas flames. In this section, a summary of the dilution, thermal and chemical effects of CO_2 on fuel-lean gas flames (Flame A) is presented.

The burning surface of turbulent diffusion flames is located where the amount of fuel and oxygen is in a stoichiometric proportion. At the flame front, the maximum temperature is located and this is due to the stoichiometric conditions being present (Lewis et al., 1956). The presence of CO_2 in the air stream has shown that CO_2 alters the location of the flame front by widening the flame zone and thus increasing the flame volume. In addition, it acts as a destabilising parameter that pushes further downstream the flame base from the burner exit surface.

The dilution effect of CO_2 is shown by the lower excess O_2 concentration in the oxidiser stream. The thermal effect of CO_2 is indicated by the lower measured flame temperatures in the diluted flames. As discussed above, the thermal impact of the addition of CO_2 is a critical consequence of the composition of the new oxidiser mixture. The higher heat capacity of CO_2 raises the total heat capacity of the oxidiser mixture and this results in slowing down the combustion chemical kinetic rates required for the complete conversion of the fuel to CO_2. By inhibiting the burning of

the fuel, increasing the chemical reaction times of the CO$_2$-diluted oxidiser mixture, and hence lowering the CO oxidation rate, the generated CO emissions are found to be higher in the diluted flames. In non-premixed flames, most part of the NO$_x$ generated consists of NO. Due to the relatively low flame temperatures and the slow reactions consisting the Zeldovich mechanism, the NO$_x$ emissions are mainly produced via the Fenimore prompt pathway. The addition of CO$_2$ alters the methane oxidation mechanism in an unfavourable way for the production of CH$_i$ radicals which are found to be responsible for initiating the prompt mechanism according to the reaction (R 2-4). Therefore, NO$_x$ emissions are found to decrease substantially with increasing the inlet concentration of CO$_2$. The chemical effect of CO$_2$, as defined by its direct participation in the chemical reactions, was not identified. The reverse reaction of (R 2-12) is the dominant reaction pathway for CO$_2$ in order to participate actively in the combustion process. However, the dissociation reaction of CO$_2$ is found to be very slow for flame temperatures below about 2400 K (Marsh et al., 2017).

CHAPTER 5- Experimental Results: Flame B with Equivalence Ratio = 0.75 - 0.83

5.1   Introduction

This chapter provides a description of the data collected during the second experimental test campaign, named as "Flame B". Two CO$_2$-dilution levels are investigated during this test campaign, 5 % and 10 %. Using the Signal analysers, as described in Section 3.3.2, the concentration of the major combustion species (THC, O$_2$, CO$_2$, CO, NO$_x$) was measured on a dry basis within the flame zone and at the exit of the combustion chamber. During this experimental campaign, post-flame measurements of 12 major and minor combustion species were performed using the FTIR analyser; the principles of FTIR are explained in Section 3.3.2.7. The flame temperature was measured using the type-N sheathed thermocouple probe, whose setup was presented in Section 3.3.1. All measurements were taken utilising the in-house built combustion chamber, as depicted in Section 3.2.

In Chapter 5, the effects of the added CO$_2$ in the air stream are presented for natural gas non-premixed flames with an air equivalence ratio, Φ= 0.75. The test conditions followed during this test campaign are presented in Section 5.2. Sections 5.3 to 5.5 include the collected experimental data of the "Flame B" campaign. The in-flame measurements were taken axially, sampling initially close to the burner zone and moving further downstream, and radially, starting at the centreline and moving radially outwards at distances of 10 mm. The right-angle shaped quartz probe was used to draw samples from the flame whereas the straight ceramic probe was used at the post-flame regions and at the highest sampling point, the exit of the chamber; the types of the probes are described in Section 3.3.2.1. Two types of graphs are introduced for the in-flame data, the first type is symbol line graphs that present the raw data as obtained from the gas species analysis and from the thermocouple measurements, after correcting them for radiation heat loss according to the method explained in Section 3.3.1.3. The second type of graphs is 2D contour plots used as a graphical technique to illustrate the relationship between the concentration or temperature and the axial

and radial distances. The data collected at post-flame regions using the FTIR analyser are shown in Section 5.4 and the data taken at the central axis of the final part of the combustion chamber are shown in Section 5.5. Furthermore, Section 5.6 presents the key findings of this experimental campaign and in Section 5.7, a comparison of "Flame A" and "Flame B" is performed. The chapter 5 concludes with a summary of the main outcomes of the experimental campaign "Flame B".

5.2   Test Conditions

The fuel utilised throughout "Flame B" campaign was natural gas and the maximum technically achievable Reynolds number was 4725; the same Re as in "Flame A". The oxidiser mixture comprised of either air or air blended with CO$_2$ at two dilution levels, 5 % and 10 %. As shown in Table 5-1, the velocity of the oxidiser stream is kept constant at about 0.42 m/s, for the air and the CO$_2$-diluted flames. The constant velocity was achieved by decreasing the amount of air when adding CO$_2$ and thus the equivalence ratio increased slightly; Φ= 0.75, 0.78 and 0.83 for the air, 5 % and 10 % CO$_2$-diluted flames. The in-flame measurements are taken at various axial sampling locations, x/D_i, where x is the actual axial distance from the burner exit surface and D_i is the internal diameter of the fuel jet pipe, 4.57 mm. Close to the burner zone, the measurements are taken at short axial distances and sampling away from the burner the axial step increased, keeping though the radial step at 10 mm at all axial locations. The gas species sampling was conducted between 90 mm and 1160 mm above the burner exit surface but the measurements with the thermocouple probe are taken between 10 mm and 570 mm above the burner exit. The use of FTIR was only possible at the post-flame regions and thus simultaneous analysis of 12 major and minor species was performed. Exit emissions and temperature were also collected at about 1700 mm above the burner exit surface. All the sampling locations along with other important test conditions, such as the velocity of the fuel and oxidiser streams, are summarised in Table 5-1.

Table 5-1 Test conditions of "Flame B" campaign.

Case study- Flame B	Air	5 % CO₂-diluted	10 % CO₂-diluted
Inlet CO_2 mole fraction	0	0.05	0.10
Average Fuel Jet Velocity (m/s)		18.7	
Reynolds Number		4725	
Average Oxidiser Flow Velocity (m/s)		0.42	
Sampling Locations (x/D_i)		2, 11, 20, 28, 37, 46, 63, 81, 125, 138, 149, 254, 372	
Equivalence ratio (Φ)	0.75	0.78	0.83

5.3   In-flame Measurements

5.3.1   Temperature profile

The temperature measurements are collected using the sheathed thermocouple described in Section 3.3.1.1 and the results in Figures 5-1 and 5-2 are corrected for radiation heat loss, according to the method described in Section 3.3.1.3. The maximum difference between uncorrected and corrected measurements occurs at higher temperatures as the radiation correction term, ΔT_{rad}, is proportional to T_w^4, where T_w is the measured temperature. Thermocouple measurements were taken axially and radially along the whole flame length to create a detailed flame temperature map; the axial step increases while scanning farther downstream of the burner exit surface as the temperature distribution becomes smoother due to the gradual quenching of the combustion reactions. Therefore, the initial axial step is 40 mm, then it increases to 80 mm, 100 mm and 180 mm whereas the radial step is kept constant throughout the measurements and is equal to 10mm. Figure 5-1 shows the data taken between 10 mm ($x/D_i= 2$) and 570 mm ($x/D_i= 125$) above the burner exit surface. Figure 5-2 includes also the measurements taken at 10 mm and 50 mm above the burner exit.

In Figure 5-1, the temperature profiles of the 5 % and 10 % CO₂-diluted flames are compared against the air flame to reveal the thermal effect of adding CO₂ into the oxidiser mixture. The different physical properties of the CO₂-diluted oxidiser mixture, such as the heat capacity, as compared to the air mixture result in lower flame

temperatures because of the higher heat capacity of CO_2. The peak temperatures were found at x/D_i= 125 and are equal to 1714 K for the air flame, 1665 K and 1642 K for the 5 % and 10 % CO_2-diluted flames, respectively. Due to the addition of CO_2, it is observed that there is a change in the trend of the profiles that is correlated to a change in the location of the flame front. In diffusion flames, combustion takes place at the boundary layer between the fuel and oxidiser streams where stoichiometric conditions are met. At this location, the reactants concentration is at minimum while the concentration of the products and the flame temperature are at maximum (Hottel and Hawthorne, 1948). As seen in Figure 5-1, for the 10 % CO_2-diluted flame and axial locations x/D_i= 20 to 63, the temperature is found to be minimum at the centreline, where fuel jet dominates, and maximum adjacent to the centreline, at a radial distance between 10 and 20 mm. On the other hand, for the air flame and at x/D_i= 20 to 37, the temperature peaks at a radial distance of 10mm. This is an indication of the change in the reaction zone due to addition of CO_2. When sampling at higher axial locations, it is noticed that the temperature profile takes progressively a smoother profile with the peak being located at the centreline. The smoother variation in temperature indicates the gradual quenching of the reactions. In Figure 5-2, the temperature profiles are illustrated in two-dimensional contour plots which show the temperature distribution along the axial (Y axis) and radial direction (X axis). The additional axial locations are useful in visualising the destabilising effect of CO_2, which forces the flame base further downstream of the burner exit surface. Consequently, the axial locations cannot be compared directly from one flame type to the other as flame streamlines are shifted whereas the sampling locations are kept constant. It is observed that the sampling location x/D_i= 11 is within the lifted air flame base whereas the x/D_i= 2 and 11 are outside the visible length of the lifted diluted flames.
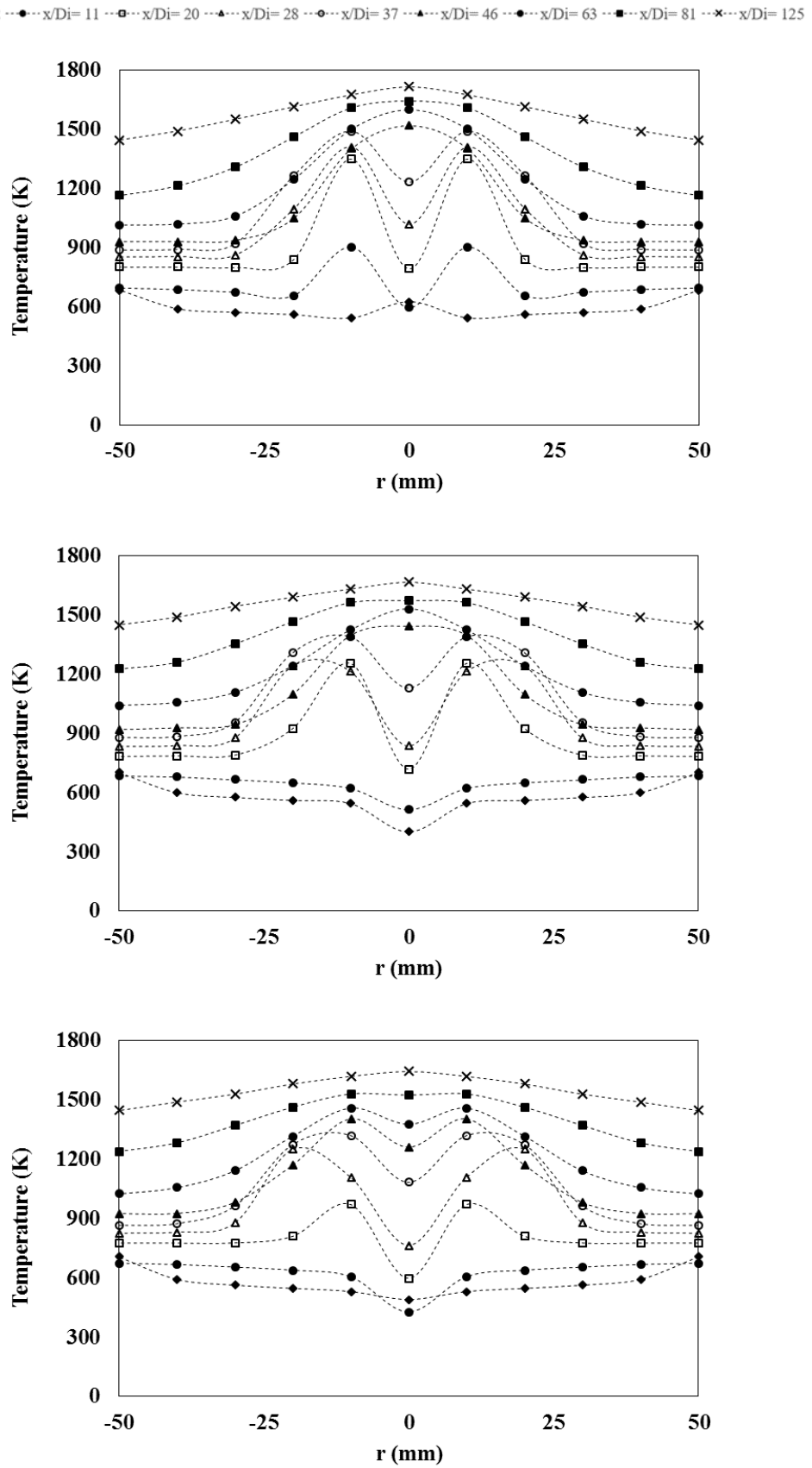
Figure 5-1 Radial distribution of the temperature measurements at all axial locations for the air, 5 % and 10 % CO$_2$-diluted flames, respectively.
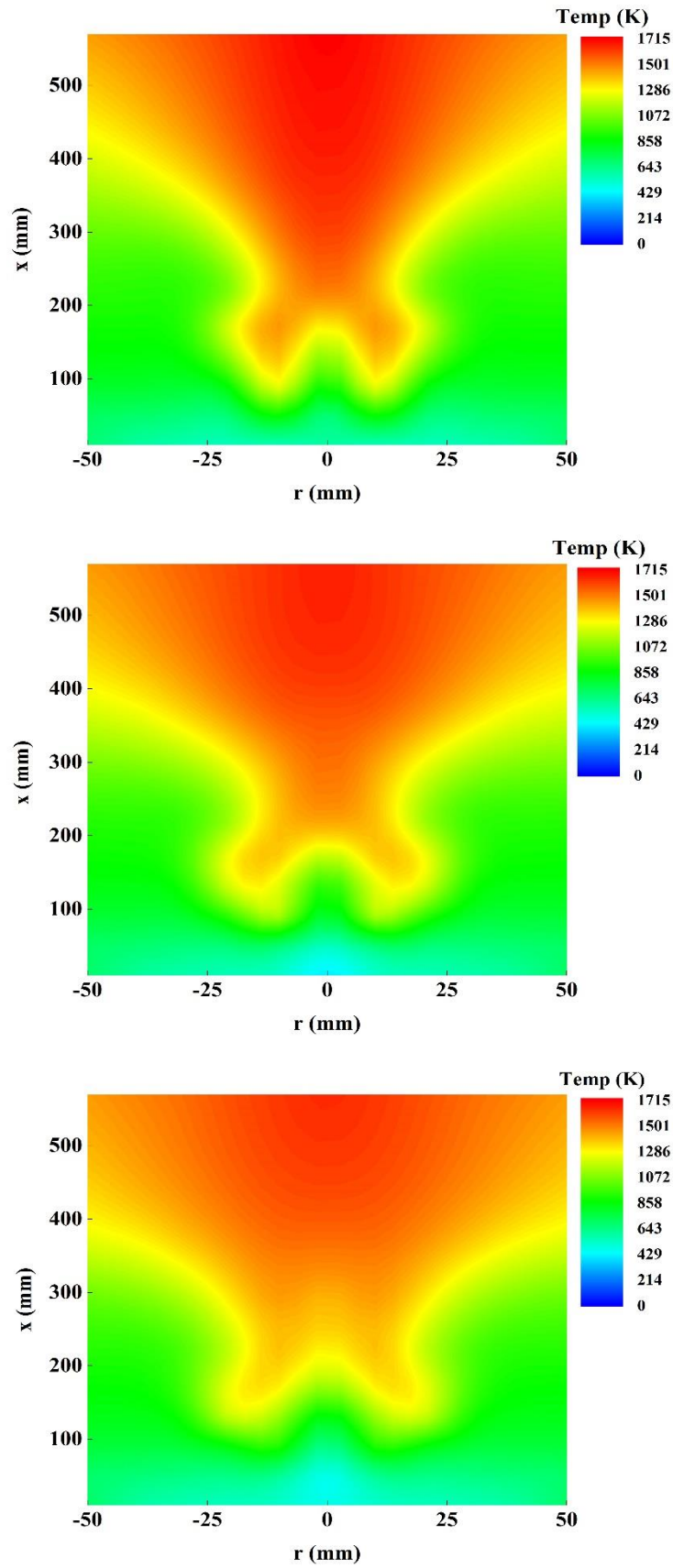
Figure 5-2 Contour plots with the temperature measurements for the air, 5 % and 10 % CO$_2$-diluted flames, respectively.

5.3.2 Species profiles

The O_2, THC, CO_2, NO_x and CO species measurements, taken during the experimental campaign "Flame B", are collected using the Signal analysers described in Section 3.3.2. Measurements are taken axially and radially to create a detailed species flame map; the axial and radial steps are kept the same with the temperature measurements for consistency.

The addition of CO_2 in the oxidiser mixture causes a significant change in the profile of the O_2 concentration, as seen in Figures 5-3 and 5-4. According to Hottel and Hawthorne (1948), in non-premixed flames, the reactants are not present at the flame front which indicates fast chemical reaction rates. In the air case, the O_2 concentration is minimum on the centreline, remains very low at a radial distance of 10 mm away from the centreline and peaks radially outwards. Moving downstream of the burner exit surface the O_2 level reduces gradually, indicating the consumption of O_2 due to the intensity of the combustion process. The distribution of the O_2 in the air flame is observed to be substantially different from the CO_2-diluted flames. In the CO_2-diluted flames, a relatively higher concentration of O_2 is found on the jet centreline for the lowest axial locations which is an evidence of a lifted flame base and is due to the premixing of the fuel with the oxidiser. It is observed that the minimum O_2 concentration is located at a radial distance of 20 mm for the diluted flames and not at the jet centreline. The O_2 contour plots in Figure 5-4 illustrate the spreading of the flame zone due to CO_2 dilution, particularly as seen at r= ±50 mm and x= 300 mm for every flame type.

Figures 5-5 and 5-6 reveal the distribution of the concentration of THC as measured at 90 mm to 570 mm above the burner surface. The concentration of THC peaks on the centreline because the fuel jet stream issues in the centre of the burner and reduces radially outwards. With the CO_2 dilution, a higher concentration of THC is found on the centreline and adjacent to it for the diluted flames. Moreover, for the diluted flames, lower flame temperatures, due to the presence of CO_2, occur at low and mid axial locations which do not allow for the fuel to be oxidised and thus slows down its decomposition. It is seen that the concentration of THC appears to be relatively unchanged for x/D_i= 28 to 63 in the case of the diluted flames. Nevertheless, at x/D_i= 125, most of the fuel is eventually burnt out as the local flame temperatures are at their maximum and enhance the fuel oxidation mechanism. The contour plots in Figure 5-

6 reveal the formation of a strong fuel pocket around the centreline in the case of the CO$_2$-diluted flames which is not observed in the same intensity in the air flame.

The main combustion products are steam and carbon dioxide. The Signal gas analysers remove all the moisture from the gas samples prior to analysis and thus the water concentration cannot be measured. Therefore, the measured concentration profile of CO$_2$ is plotted in Figures 5-7 and 5-8. For the air combustion, the maximum CO$_2$ concentrations are found on the centreline at x/D_i= 20 to 28 and then a wider peak of CO$_2$ is observed when sampling further downstream. Carbon dioxide is greatly produced at higher axial locations rather than close to the burner exit surface because the oxidation of the fuel progresses gradually along the flame length, as is also indicated by the consumption of O$_2$. Increased flame temperatures are present away from the burner exit which attribute to the oxidation of CO to CO$_2$. As already mentioned, the dilution of the oxidiser mixture with CO$_2$ results in a significant change in the reaction zone. For the CO$_2$-diluted flames, the concentration of CO$_2$ is low and equal to the added amount at low axial locations, its maximum concentrations are found at a radial distance from the centreline, at about 20 mm. At x/Di= 125, high levels of CO$_2$ are measured but above these locations the production rate of CO$_2$ declines, indicating the decline of the combustion reaction rates. Figure 5-8 illustrates the increase in the CO$_2$ profile on the centreline (air flame) and radially outwards (diluted flames).

Emissions of NO$_x$ are considered to contribute to the photochemical smog and air pollution. Strict regulations on NO$_x$ emissions are now in force and therefore research is driven to the development of low NO$_x$ burners for the elimination of NO$_x$ emissions from gaseous power generation units. Consequently, the impact of CO$_2$ addition on the NO$_x$ emissions becomes an important issue. The plots in Figures 5-9 and 5-10 depict the concentration of NO$_x$ emissions in ppm as measured using a chemiluminescent analyser. During the experiments, both NO and NO$_x$ emissions are measured but due to uncertainties in the conversion of NO to NO$_2$ in the sampling system, only the NO$_x$ emissions are presented in this study. However, both data are analysed and it can be concluded that NO$_2$ is found in traces compared to the NO levels. Hence, the formation of NO$_x$ emissions is explained according to the formation mechanisms of the NO species.
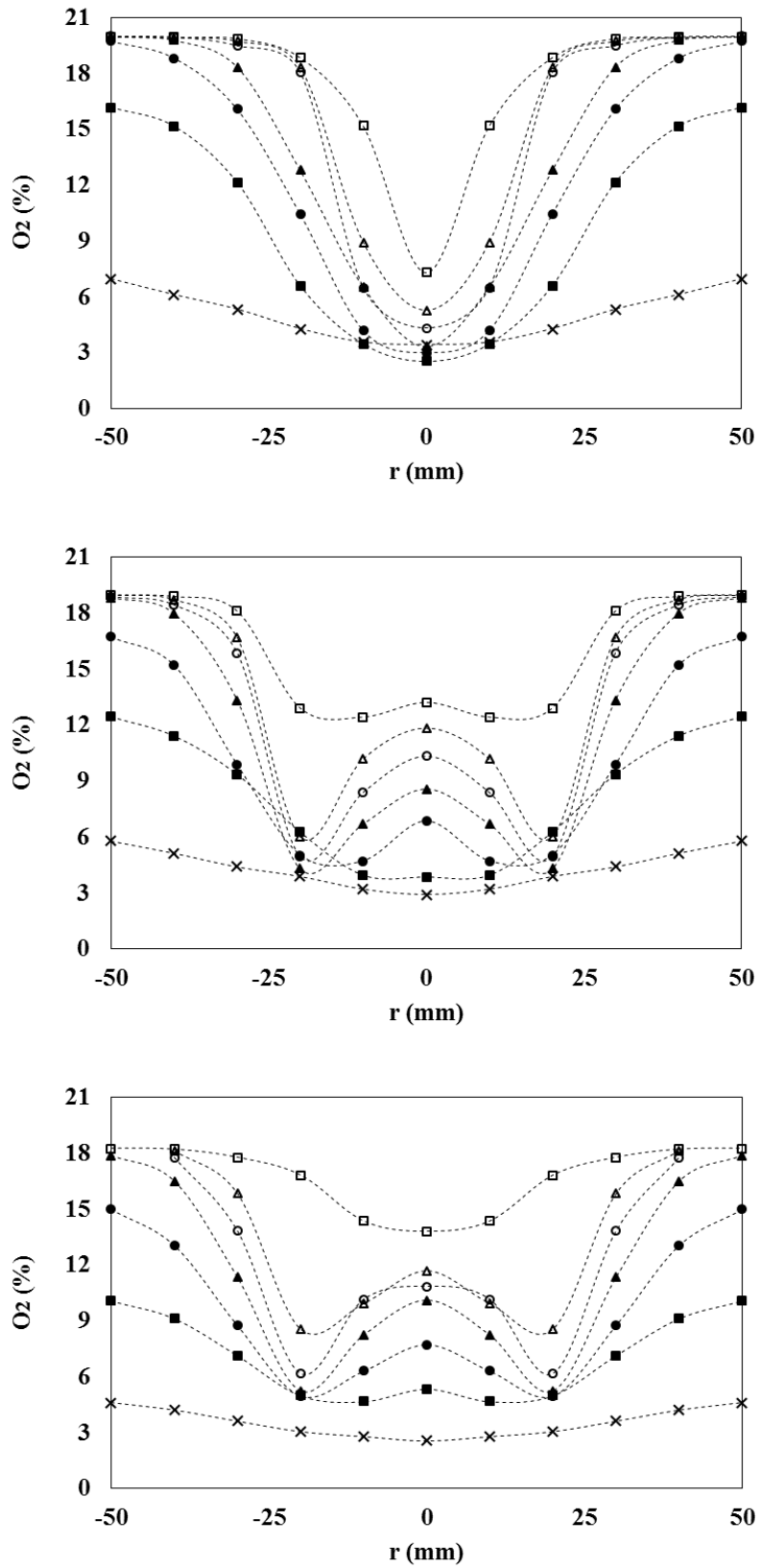
Figure 5-3 Radial distribution of the O$_2$ concentration at all axial locations for the air, 5 % and 10 % CO$_2$-diluted flames, respectively.
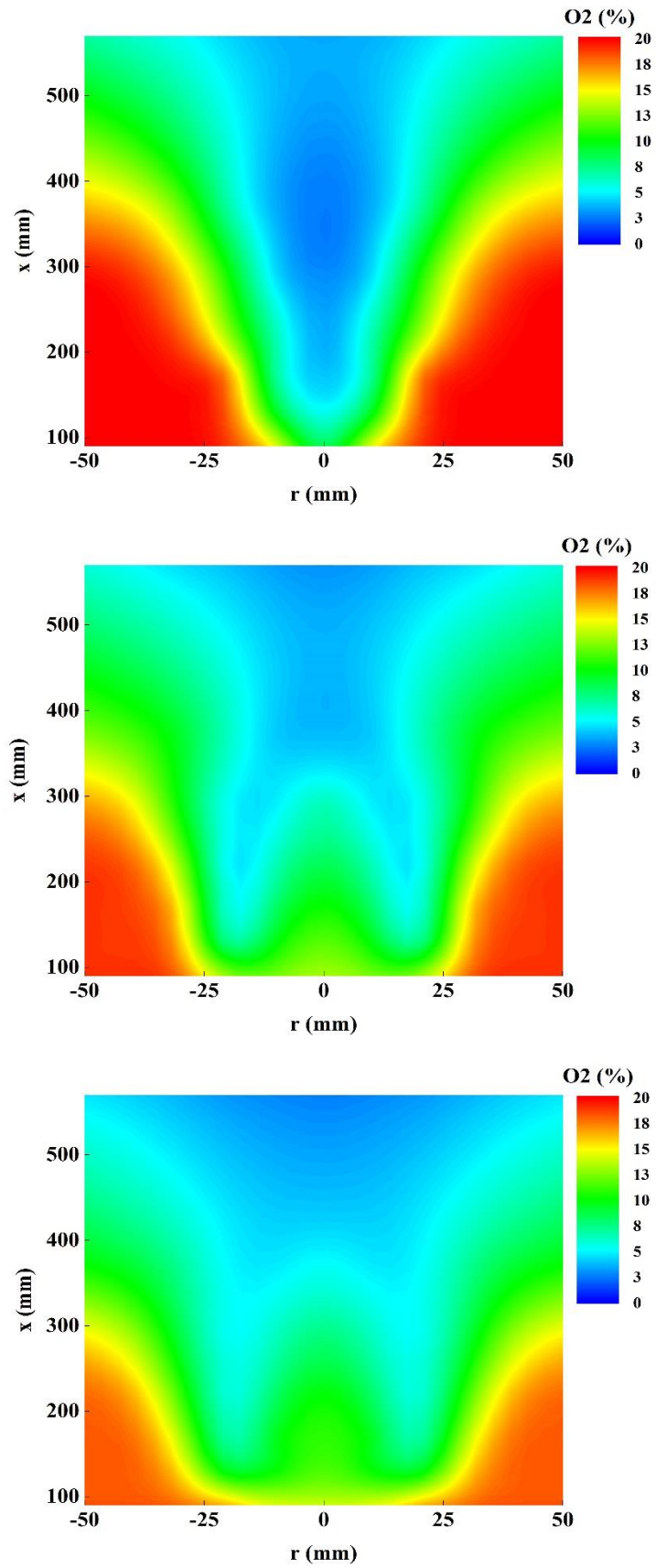
Figure 5-4 Contour plots of the O$_2$ concentration for the air, 5 % and 10 % CO$_2$-diluted flames, respectively.
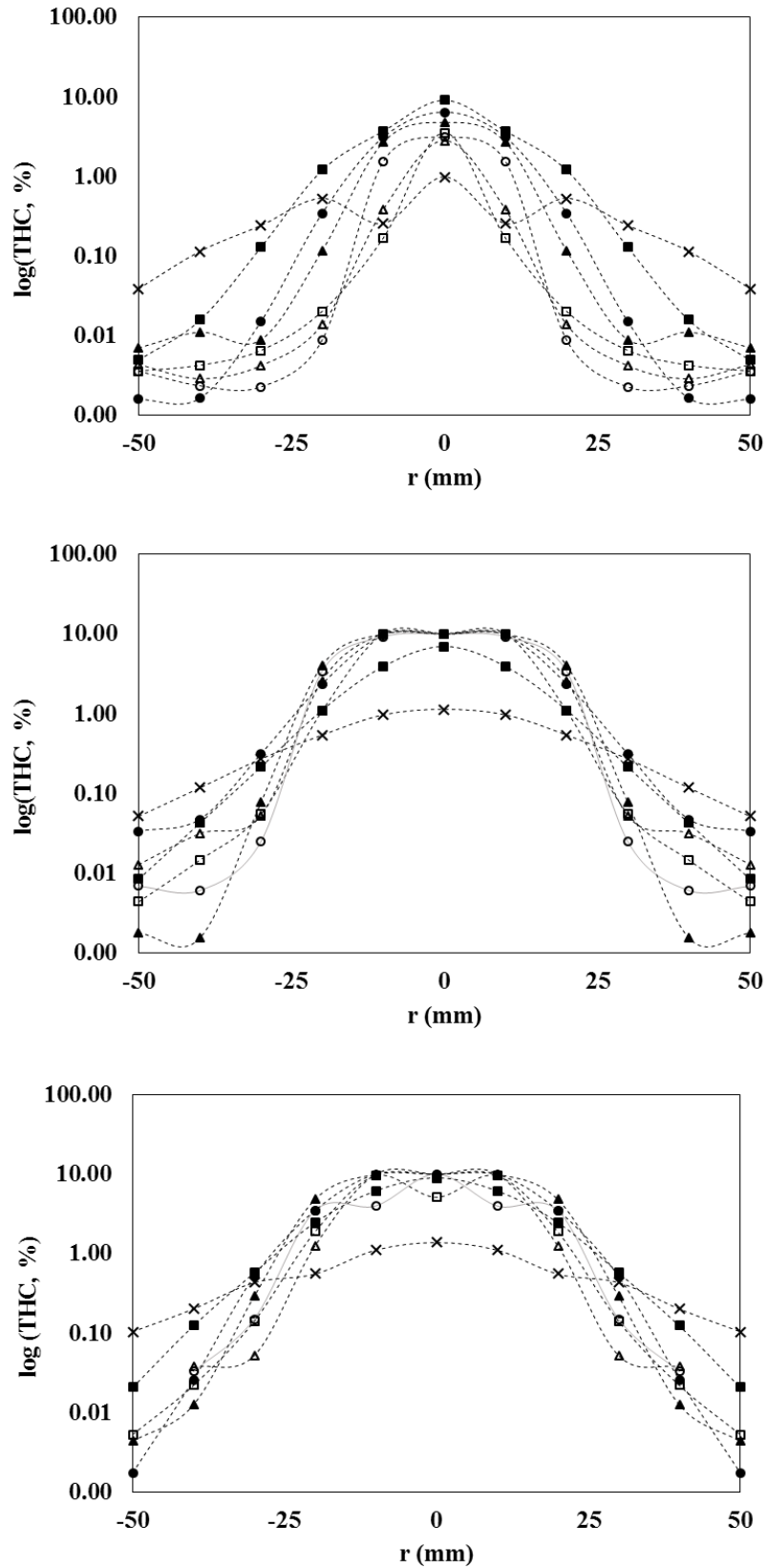
Figure 5-5 Radial distribution of the THC concentration at all axial locations for the air, 5 % and 10 % CO$_2$-diluted flames, respectively.
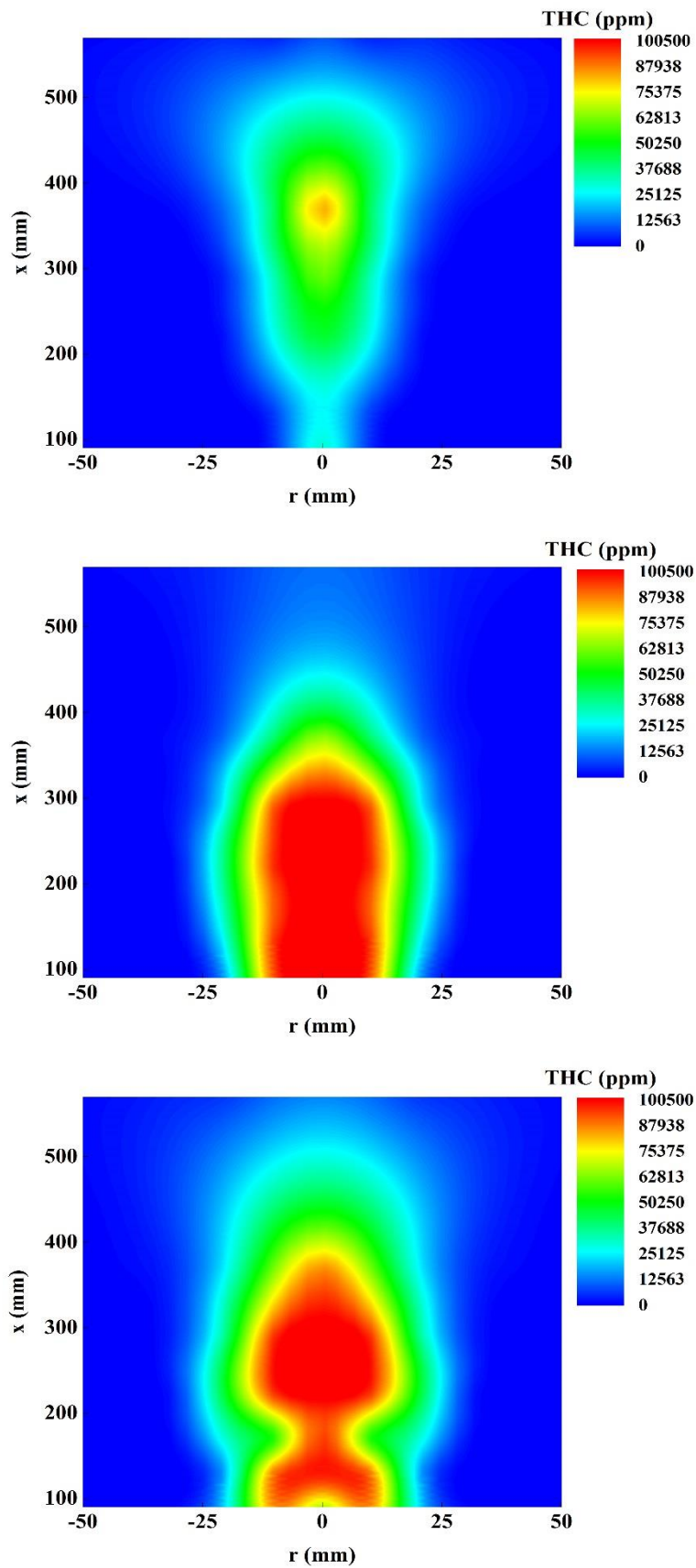
Figure 5-6 Contour plots of the THC concentration for the air, 5 % and 10 % CO$_2$-diluted flames, respectively.
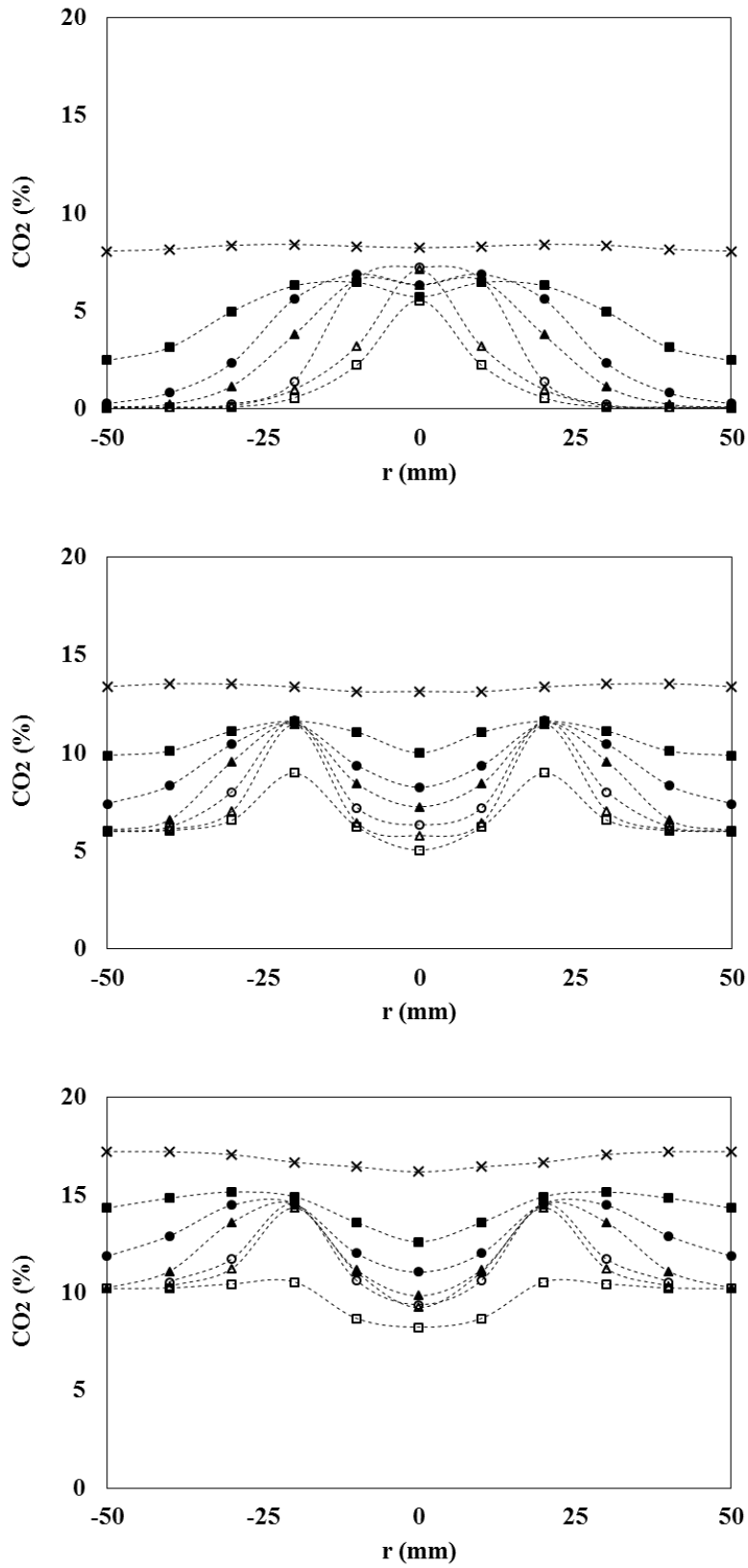
Figure 5-7 Radial distribution of the CO$_2$ concentration at all axial locations for the air, 5 % and 10 % CO$_2$-diluted flames, respectively.
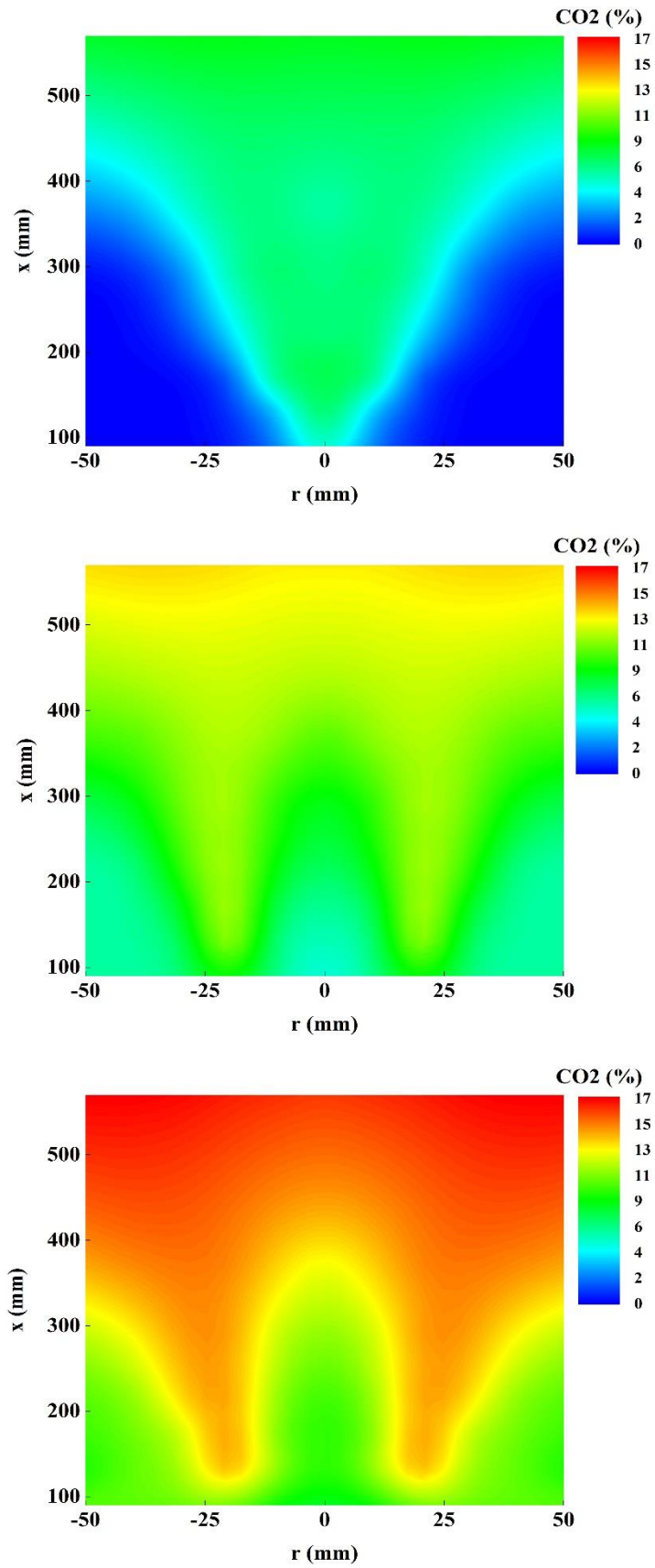
Figure 5-8 Contour plots of the CO$_2$ concentration for the air, 5 % and 10 % CO$_2$-diluted flames, respectively.

The thermal NO pathway is fuelled by high flame temperatures, above 1800 K, and the availability of O atoms, whereas the prompt formation depends mostly on the local stoichiometry. To understand which mechanism is dominant, the formation of the major species and the flame temperature play a key role. The peak concentration of NO$_x$ emissions occurs on the centreline of the air flame and the minimum is found at the flame boundaries. On the centreline, the fuel species are in abundance, O$_2$ is found to be in a low concentration and the flame temperature increases progressively while moving away from the burner exit surface. The location of the maximum NO$_x$ emissions coincides with the location of fuel decomposition. As the prompt formation mechanism depends on stoichiometry and is dominant where fuel species, such as CH, are present, it can be concluded that this reaction pathway forms most of the measured NO$_x$ emissions. For the CO$_2$-diluted flames, the impact of CO$_2$ is prominent and contributes to the reduction of NO$_x$ emissions through mainly its chemical effect but also its thermal effect. For the 5 % CO$_2$-diluted flame, the concentration of NO$_x$ is lower on the centreline for axial locations x/D$_i$= 20 to 63 and peaks on the centreline at higher axial sampling locations. If the NO$_x$ profile is combined with the profile of O$_2$, it can be concluded that the level of O$_2$ is found to be very low at locations with a high concentration of NO$_x$. The consumption of O$_2$ is due to the fuel decomposition at these locations and the presence of fuel radicals promotes the formation of NO. A similar behaviour is observed when 10 % CO$_2$ in volume is added to the combustion air stream. The level of NO$_x$ emissions is significantly lower in this case and can be attributed to the slower burning rate of the fuel stream and the cooler flame temperatures which inhibit the prompt initiation step, the reaction (R 2-4) (Lim et al., 2000).

Carbon monoxide is an undesirable combustion product which is formed because of the incomplete combustion of the fuel mixture. The fast reaction of fuel and oxygen leads to the early presence of CO, at low axial locations, x/D$_i$= 20 to 37. The formation of CO is located on the centreline where the fuel species are plentiful and the highest concentration is found at x/D$_i$= 81 for all flame types, as seen in Figures 5-11 and 5-12. Fuel oxidation is accompanied by an increase in the flame temperature and the O$_2$ consumption rate. The contour plot of CO emissions for the 5 % CO$_2$-diluted flame is a good example of its formation process; the peak concentration of CO is located 250 mm above the burner surface and continues to be high until 400 mm downstream of the burner exit. Considering the contour plots of THC, O$_2$ and flame temperature

(Figures 5-2, 5-4 and 5-6), it is observed that CO is formed where O$_2$ is progressively consumed for the fuel decomposition. Intense production of CO is measured at 280 mm above the fuel jet exit for the 10 % CO$_2$-diluted flame. At this axial location, 280 mm, the O$_2$ level reduces to a significantly low limit and the temperature increases substantially assisting the fuel oxidation process. It is suggested that the flame temperature plays an important role to the formation of CO and thus when adding CO$_2$ into the air stream, the temperature reduces significantly as noticed schematically in Figure 5-2. Therefore, it is suggested that at x/Di= 48 to 81 the higher in-flame CO emissions measured for the air flame are attributed to the higher flame temperatures. However, as will be presented below, the increase in the CO emissions due to CO$_2$ dilution is evident at the in-flame sampling location x/D$_i$= 125 and at the post-flame regions.

5.4 Post-flame Measurements

The FTIR analyser could not be used for in-flame measurements because the sample spectrum was saturated by some species; the peaks of dominant species overlapped the peaks of other present species. Nevertheless, this type of gas analysis was possible to be used in post-flame regions; 630 mm, 680 mm and 1160 mm above the burner exit surface (x/D$_i$= 138, 149, 254, respectively). The advantage of using an FTIR analyser is the simultaneous measurement of 12 major and minor combustion species, apart from diatomic molecules, such as O$_2$, which do not absorb infrared light. Therefore, Tables 5-2, 5-3 and 5-4 present the concentration of nine major and minor combustion products at x/D$_i$= 138, 149, 254 for the air flame, the 5 %- and 10 % CO$_2$-diluted flames. The concentration of N$_2$O, NO$_2$ and C$_3$H$_8$ was also measured but is not presented here as is only present in traces, below 7 ppm.

From Tables 5-2 to 5-4, it is observed that the concentration of H$_2$O remains almost the same, the concentration of CO$_2$ increases and the concentration of CO decreases while sampling farther away from the burner. As discussed in this study, the chemical effect of CO$_2$ on the CO emissions is to cause the increase of CO. At x/D$_i$= 138, the measured concentration of CO for the air flame is 0.9% and for the diluted flames is 1.2 % and 1.7 % in volume. A similar trend is noticed at x/D$_i$= 149, higher CO emissions due to dilution, but the level of concentration is lower due to the progressive oxidation of CO which leads to very low levels (about 0.01-0.02 %) at x/D$_i$= 254.
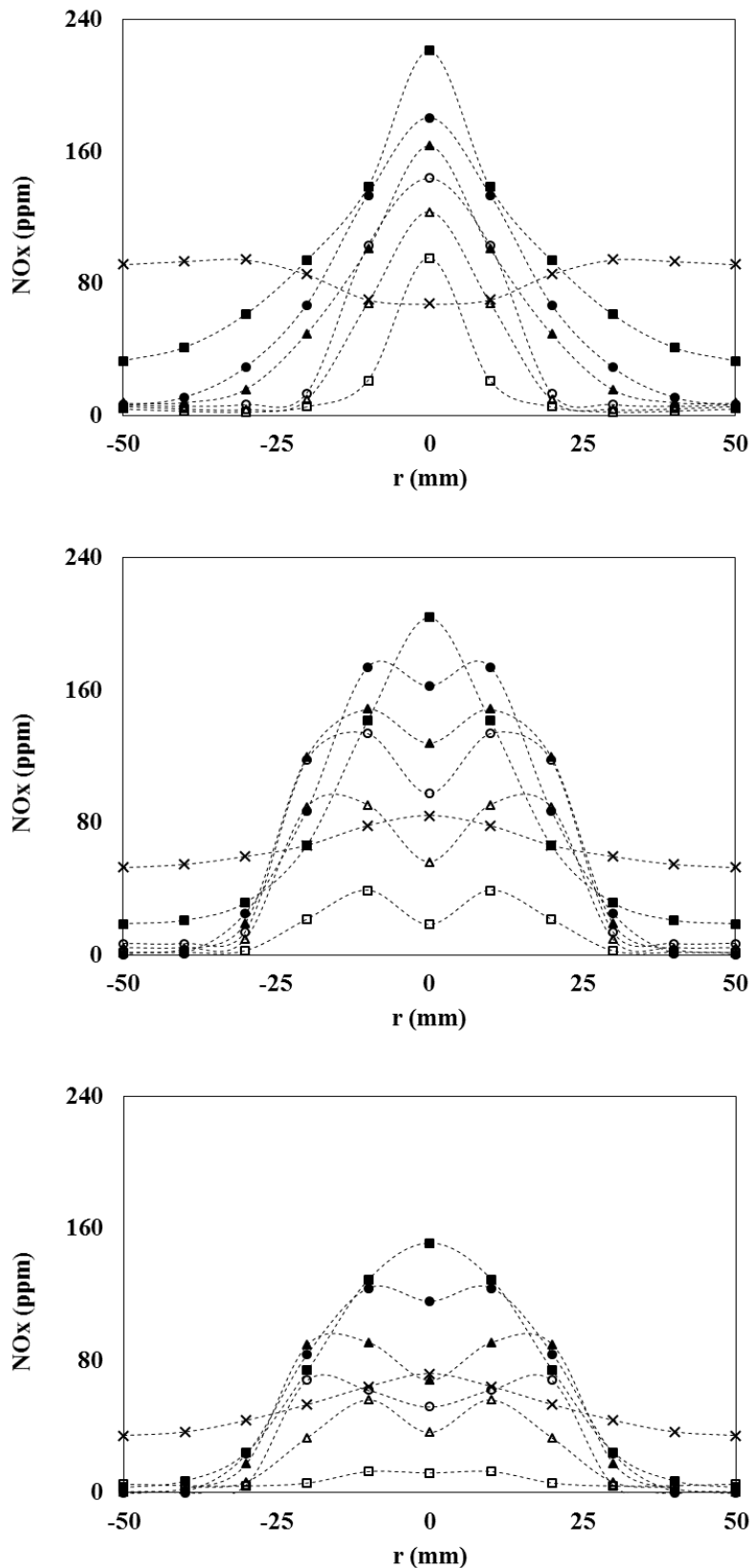
Figure 5-9 Radial distribution of the NO$_x$ concentration at all axial locations for the air, 5 % and 10 % CO$_2$-diluted flames, respectively.
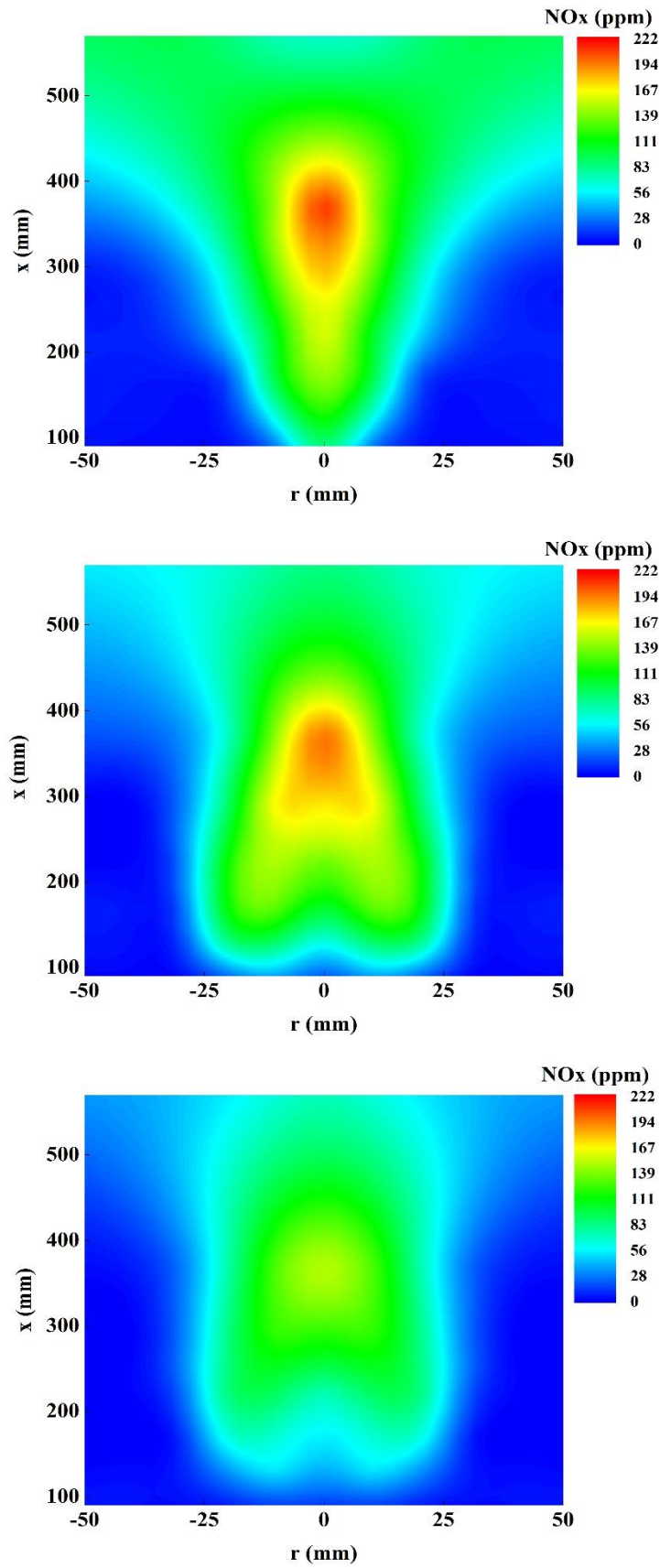
Figure 5-10 Contour plots of the NO$_x$ concentration for the air, 5 % and 10 % CO$_2$-diluted flames, respectively.
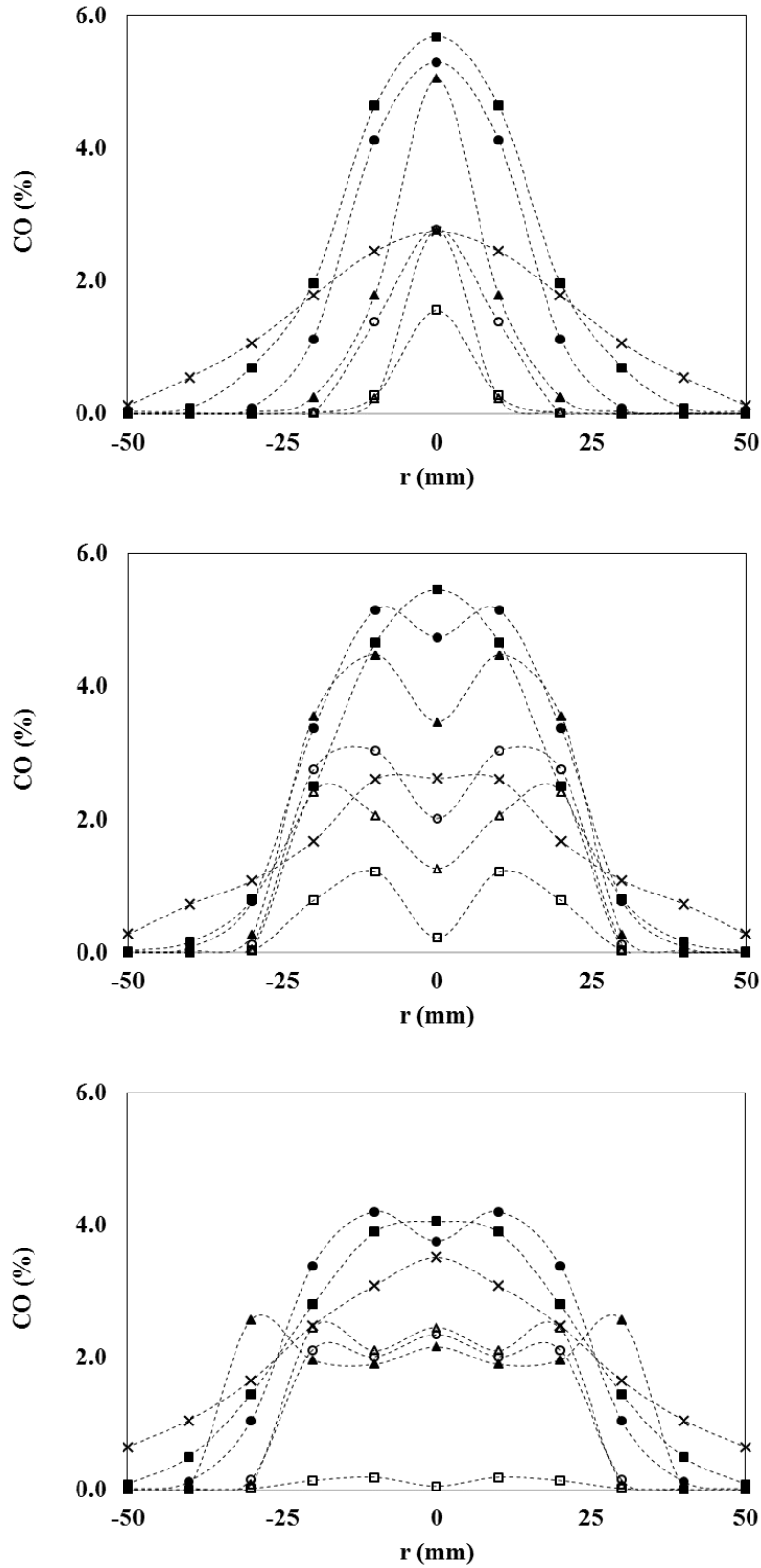
Figure 5-11 Radial distribution of the CO concentration at all axial locations for the air, 5 % and 10 % CO$_2$-diluted flames, respectively.
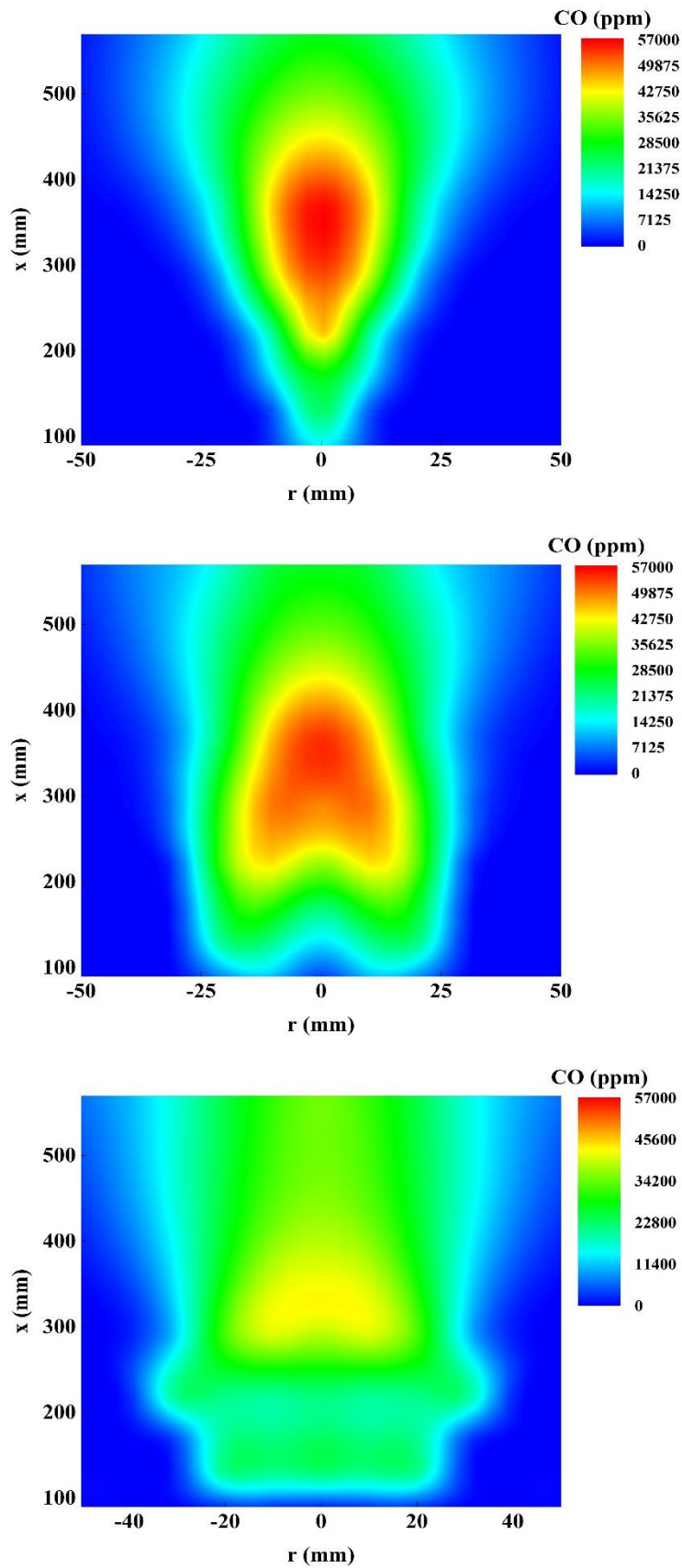
Figure 5-12 Contour plots of the CO concentration for the air, 5 % and 10 % CO$_2$-diluted flames, respectively.

The comparison between the in-flame and the post-flame results are in an excellent agreement showing that the measured post-flame levels of CO are lower, and of CO_2 are higher, than the corresponding in-flame levels. For example, the CO level for the air flame is 2.8 % at x/D_i= 125 and 0.9 % at x/D_i= 138. The FTIR analyser can measure simultaneously NO, NO_2 and N_2O species. The experimental results have shown that the concentration of NO_2 and N_2O are in traces and thus, are not included in Tables 5-2, 5-3 and 5-4. The reduction of NO emissions due to the CO_2 dilution and also, the reduction while sampling away from the burner exit due to the reduction of the fuel species is clearly shown from the post-flame measurements. It was shown in Sections 4.3 and 5.3 that the addition of CO_2 into the combustion air stream slows down the fuel-burning rate and as a result, the concentration of the measured fuel species, CH_4, C_2H_4, C_2H_2, HCN, is higher at the post-flame areas of the diluted flames compared to the air flame. For example, the concentration of CH_4 at x/D_i= 149 for the 10 % CO_2-diluted flame is found to be 997 ppm whereas for the air flame 204 ppm. Furthermore, the concentration of the fuel species is higher at lower axial locations (x/D_i= 138) than at higher (x/D_i= 149) which indicates the continuation of the fuel burning process with its termination occurring at x/D_i=254 where only trace amounts could be detected.

Table 5-2 Post-flame measurements taken at x/D_i= 138.

x/D_i=138	Air flame	5 % CO_2-diluted flame	10 % CO_2-diluted flame
H_2O (%)	2.05	2.45	2.60
CO_2 (%)	8.43	14.20	17.54
CO (%)	0.90	1.20	1.70
NO (ppm)	120.00	61.00	40.00
HCN (ppm)	30.00	40.00	45.00
CH_4 (ppm)	500.00	1158.00	2193.00
C_2H_4 (ppm)	10.00	30.87	94.43
C_2H_2 (ppm)	400.00	600.00	1000.00

Table 5-3 Post-flame measurements taken at x/Di= 149.

x/D$_i$=149	Air flame	5 % CO$_2$-diluted flame	10 % CO$_2$-diluted flame
H$_2$O (%)	2.24	2.34	2.44
CO$_2$ (%)	8.65	14.32	18.03
CO (%)	0.55	0.80	0.95
NO (ppm)	115.00	58.00	35.00
HCN (ppm)	6.50	17.73	29.37
CH$_4$ (ppm)	204.00	459.00	997.00
C$_2$H$_4$ (ppm)	4.60	13.15	28.70
C$_2$H$_2$ (ppm)	100.00	312.00	514.00

Table 5-4 Post-flame measurements taken at x/Di= 254.

x/D$_i$=254	Air flame	5 % CO$_2$-diluted flame	10 % CO$_2$-diluted flame
H$_2$O (%)	2.37	2.59	2.61
CO$_2$ (%)	8.80	14.39	18.78
CO (%)	0.013	0.020	0.023
NO (ppm)	112.00	41.00	30.00
HCN (ppm)	0.53	0.77	0.78
CH$_4$ (ppm)	0.72	1.43	2.09
C$_2$H$_4$ (ppm)	0.38	0.41	0.44
C$_2$H$_2$ (ppm)	0.34	0.47	0.60

5.5 Exit Measurements

For a full characterisation of the flame types investigated during the test campaign "Flame B", gas species and temperature measurements were also taken at the central axis of the exit of the chamber which is located at about 1700 mm away from the

burner exit surface, x/D_i = 372. At this sampling point, all radical recombination reactions are completed and a very low amount of fuel is usually present in traces. As Table 5-5 shows, there isn't a major difference in the exit temperature between the three test conditions; the exit temperature is found to be T= 863 K, 865 K and 868 K for the air, 5 % and 10 % CO_2-diluted flames respectively. This might be attributed to the change in the flame volume and hence the flame length due to the dilution of the air stream with CO_2. Figure 5-13 shows the exit emissions of CO_2 as a function of the inlet volumetric amount of CO_2 for the three case studies investigated in this test campaign. When a product is added as part of the reactant stream in a combustion system, it is expected that its concentration at the exit of the system will be increased and thus the exit concentration of the CO_2 was measured to be 9.3 %, 14.8 % and 18.4 % for the air, 5 % and 10 % CO_2-diluted flames, accordingly.

Table 5-5 Measured exit temperatures in Kelvin.

"Flame B"	T_exit (K)
Air flame	863
5 % CO₂-diluted flame	865
10 % CO₂-diluted flame	868

On the other hand, the exit concentration of the other reactant species, the O_2, decreases with adding CO_2 in the oxidiser stream, as shown in Figure 5-14; 5.1 %, 3.9 % and 3.0 % are the exit levels of O_2 for the air, 5 % and 10 % CO_2-diluted flames, respectively. The reduction in the exit averaged concentration of O_2 is more remarkable between the air and the 5 % diluted flames rather than between the two diluted flames.

In Figure 5-15, the level of THC as measured at the exit of the chamber is illustrated for the air, 5 % and 10 % CO_2-diluted flames. Hardly any fuel concentration is measured in the three case studies and the averaged measured concentration refers to traces of THC in ppm, 1.6 ppm, 5.3 ppm and 8.4 ppm for the air, 5 % and 10 % diluted flames, respectively.
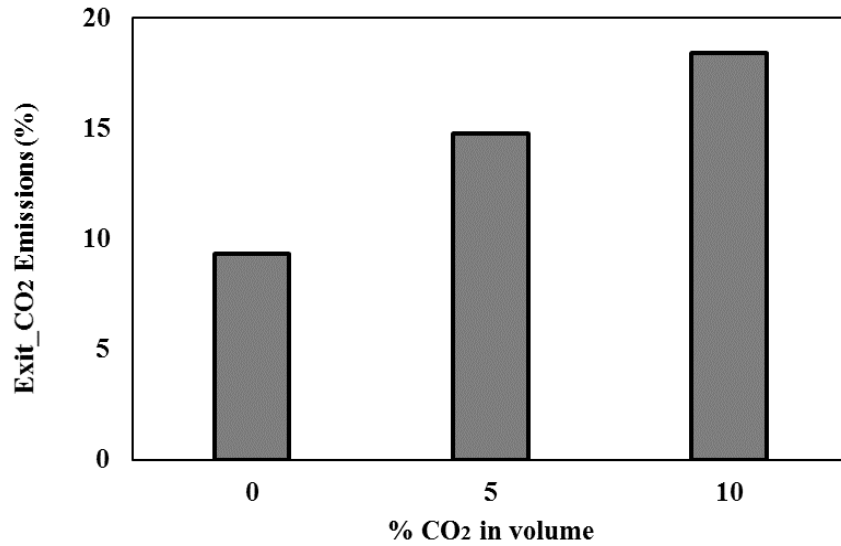
Figure 5-13 Exit CO$_2$ emissions in vol% as a function of the inlet volumetric amount of CO$_2$.
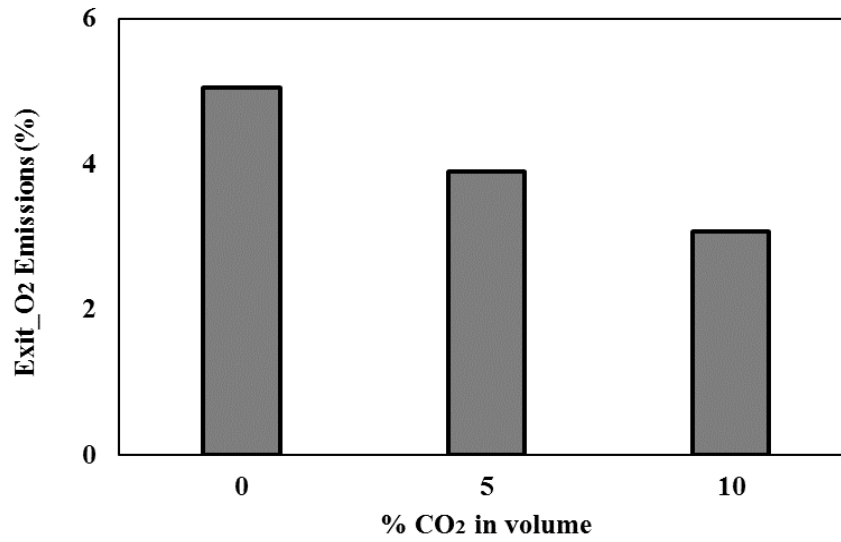
Figure 5-14 Exit O$_2$ emissions in vol% as a function of the inlet volumetric amount of CO$_2$.
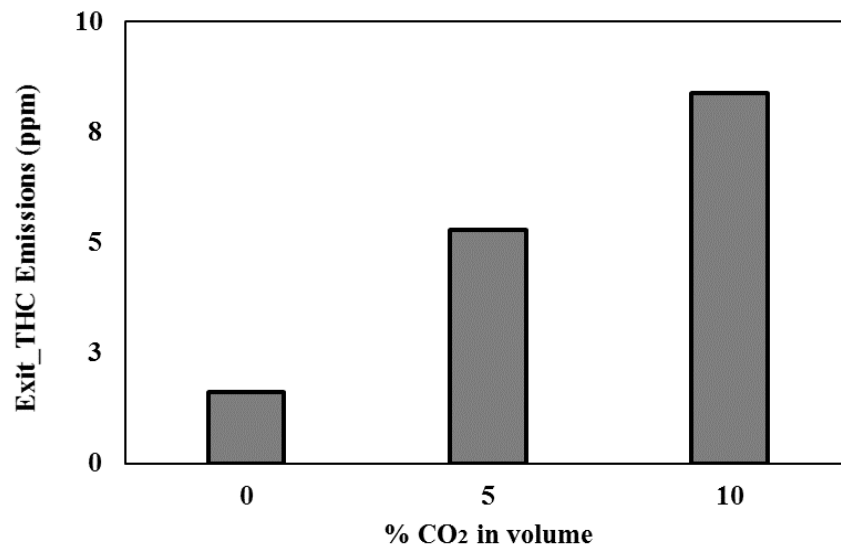
Figure 5-15 Exit THC emissions in ppm as a function of the inlet volumetric amount of CO$_2$.

As discussed above, at the exit of the utilised combustion test rig hardly all the fuel has been burnt and oxidised to CO and CO_2. Figure 5-16 illustrates the exit emissions of CO in ppm as a function of the added amount of CO_2 in the oxidiser reactant stream. Under air combustion, 10 ppm of CO were measured and 30 ppm and 80 ppm were measured for the 5 % and 10 % diluted flames, respectively. Overall, these concentration levels are relatively low when compared to the in-flame levels. Furthermore, the level of the exit CO emissions indicates the efficiency of a combustion system since the emission levels of CO together with THC are an indication of the completeness of a combustion process.

On the other hand, the impact of the CO_2 addition on the NO_x emissions is positive as shown in Figure 5-17 which outlines the exit emissions of NO_x as a function of the added volumetric amount of CO_2. The NO_x pollutant emissions reduce substantially when adding CO_2; 107 ppm, 54 ppm and 34 ppm were the concentration of NO_x for the air, 5 % and 10 % diluted flames, respectively.
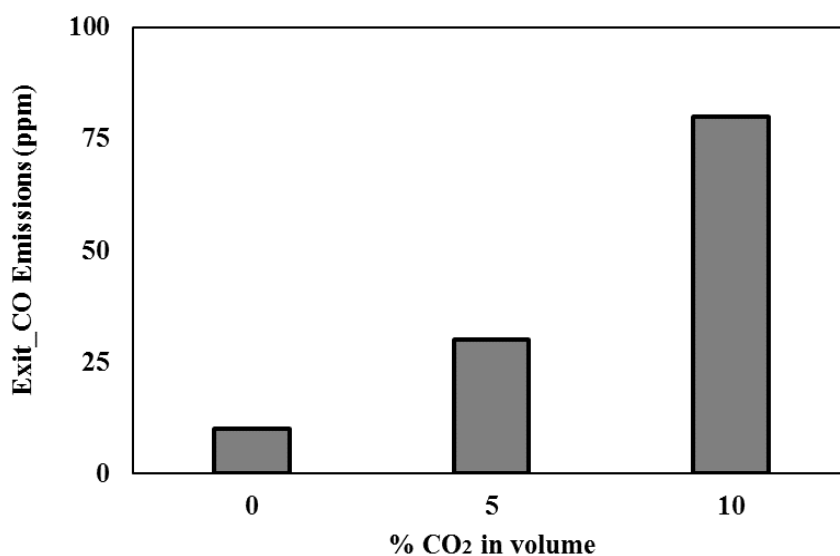
Figure 5-16 Exit CO emissions in ppm as a function of the inlet volumetric amount of CO_2.

To compare the exit emissions with a different experimental setup or different technologies, the emissions need to be reported under the same basis and thus the emission indices of NO_x and CO are calculated for the mass of fuel being burnt, as explained in Section 3.4.6.1. In Figure 5-18, the effect of CO_2 dilution on the emission indices of NO_x, symbolised by the black "x" symbols, and CO emissions, symbolised by the black-filled triangle symbols, is presented. It is shown that the inlet concentration of CO_2 in the oxidiser mixture has an impact on both the $EINO_x$ and EICO.
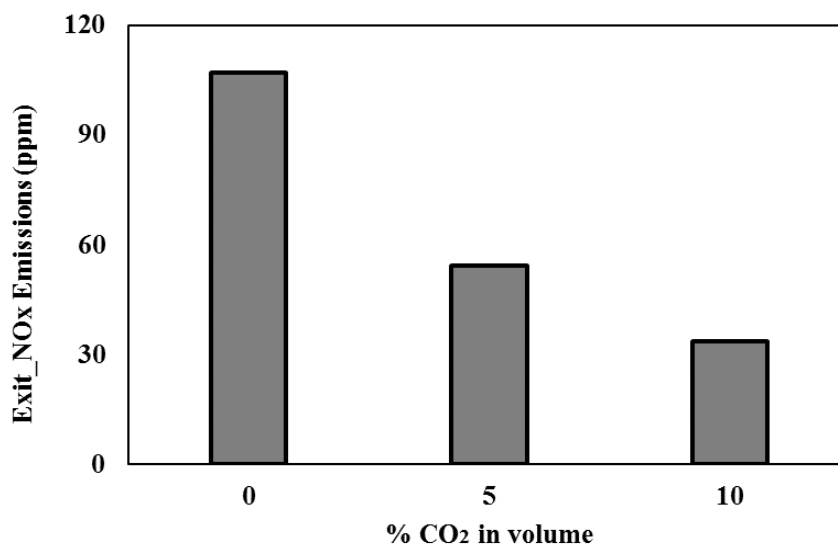
Figure 5-17 Exit NO_x emissions in ppm as a function of the inlet volumetric amount of CO_2.

The $EINO_x$ were calculated based on the exit emissions of NO_x emissions and are found to be 3.30, 1.06 and 0.53 g/kg for the air, 5 % and 10 % diluted flame, accordingly. The reduction in the $EINO_x$ is expected because the in-flame NO_x emissions were considerably lower for the diluted flames, the exit temperature of the exhaust gases is relatively low to sustain any reactions and the absence of fuel radicals at this sampling location inhibit the continuation of the prompt formation mechanism. The reduction in $EINO_x$ is more prominent between the air and the 5 % diluted flames when compared to the levels of $EINO_x$ between the 5 % and 10 % diluted flames. Furthermore, the emission index of the exit CO emissions is increased with the CO_2 addition; the EICO values for the air, 5 % and 10 % diluted flames are 0.19, 0.36 and 0.76 g/kg, respectively. The difference in EICO values between the two dilution levels is more remarkable when compared to the difference between the air and the 5 % EICO values.
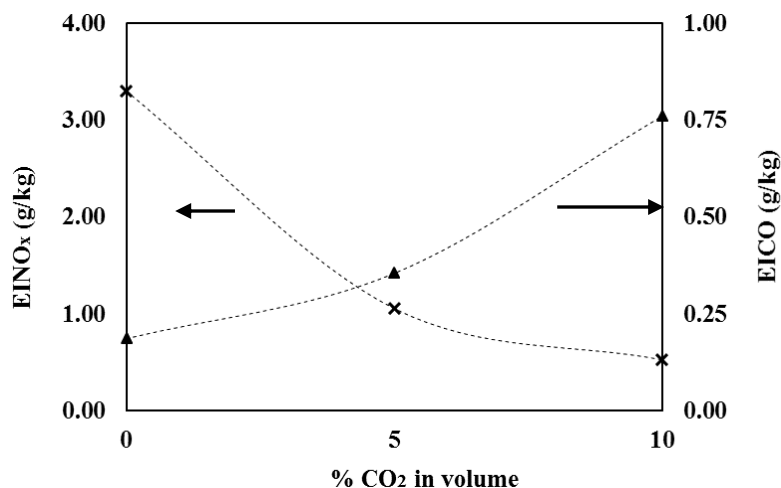
Figure 5-18 Calculated EINO$_x$, black "x" symbols, and EICO, black-filled triangle symbols, as a function of the inlet CO$_2$ volumetric percent.

5.6   Discussion

During this experimental test campaign, "Flame B", gas species measurements were performed at in-flame regions, at axial locations x/D$_i$= 20, 28, 37, 46, 63, 81, 125, at post-flame regions, x/D$_i$= 138, 149 and 254, and at the exit of the chamber, x/D$_i$= 372. A summary of the main key experimental findings as observed during this test campaign is discussed as follows:

- The peak values of the flame temperature are measured at the axial location x/D$_i$= 125 and are found to be 1714 K, 1665 K and 1642 K for the air, 5 % and 10 % diluted flames, accordingly. The highest temperature drop is observed when 5 % CO$_2$ in volume is added to the air stream. However, the peak temperature reduces further when 10 % CO$_2$ in volume is added. Although the flame volume temperature changes substantially due to dilution, no significant difference is observed in the exit temperatures due to dilution.

- The change in the distribution of the O$_2$ concentration due to dilution is rather interesting. At x/D$_i$= 20, the concentration of O$_2$ in the diluted flames is clearly higher than in the air flame. Carbon dioxide moves the flame stabilisation point further downstream and the high O$_2$ level found at low axial locations is due to premixing of fuel and oxidiser. However, regardless of dilution or not, the O$_2$ is consumed at relatively high axial locations within the flame. It was not possible to measure the O$_2$ concentration with the FTIR analyser at the post-flame regions. However, gas sample measurements taken at x/D$_i$= 125 and 372 can be used as an evidence of the termination of the combustion reactions at the exit of the

134

combustion chamber. At the axial location x/D$_i$= 125, the measured averaged concentration of O$_2$ was found to be 3.4 %, 3 % and 2.6 % and at x/D$_i$= 372, it was found to be 5.1 %, 3.9 % and 3.1% for the air, 5 % and 10 % diluted flames, respectively. The decrease in the O$_2$ level between the air and the diluted flames is prominent and is due to dilution of the oxidiser stream. Finally, the higher O$_2$ levels at the exit of the chamber indicate that the chemical reactions taken place during the combustion of natural gas are completed.

- In diluted flames, the in-flame concentration of THC is high enough even at high axial locations as compared to the progressive reduction of the level of the THC in the air flame. Comparing the concentration of THC at x/D$_i$= 125, 149 and 372, it is evident that the fuel oxidation process occurs slowly but complete conversion to CO$_2$ is achieved at the exit of the chamber. For example, in the 5 % diluted flame, the measured averaged concentration of THC is found to be 11309 ppm, 459 ppm and 5.3 ppm at x/D$_i$= 125, 149 and 372, respectively.

- The NO$_x$ formation mechanism is influenced by the addition of CO$_2$. At the exit of the chamber, the NO$_x$ emissions were found to be 107, 54 and 34 pm for the air flame, 5 % and 10 % diluted flames, respectively. At x/D$_i$= 125, the level of NO$_x$ is measured at 117, 84 and 72 ppm for the air flame, 5 % and 10 % diluted flames, respectively. Firstly, the added CO$_2$ in the air stream has an impact on NO$_x$ and secondly, it is clear that NO$_x$ emissions reduce as sampling closer to the exit of the chamber due to reduced temperatures and limited availability of fuel radicals.

- The concentration of CO emissions is relatively low at low axial locations (x/D$_i$= 20 to 37) and peaks gradually with an increase in flame temperature and in the fuel decomposition process. Higher in-flame levels for the air flame are observed due to higher in-flame temperatures promoting fuel oxidation. However, at x/Di= 125 the peak concentration of CO is 2.4 %, 2.6 % and 3.5 for the air, 5 % and 10 % CO$_2$-diluted flames, respectively. This increase in CO emissions due to dilution is evident also at the post-flame regions.

5.7   Comparison of Flame A and Flame B

A comparison between the two experimental campaigns, "Flame A" and "Flame B", reveals the impact of varying the equivalence ratio, Φ, of the natural gas non-premixed flames. "Flame A" included lower Φ values compared to "Flame B" moving further away from stoichiometry, Φ= 1. All the experiments were conducted keeping the flow

rate of the natural gas constant. The difference between the test campaigns is the total oxidiser flow rate which leads to the different equivalence ratio. The main conclusions from investigating different equivalence ratios are as follows:

- Increasing the equivalence ratio between "Flame A" and "Flame B" campaigns, higher flame temperatures occur and a lower amount of O_2 is available for burning the same amount of fuel. The lower the Φ, the cooler the flame is as the maximum flame temperature is achieved at stoichiometric conditions, where Φ is equal to 1.

- Changing the Φ parameter results in changing the velocity ratio between the fuel and the oxidiser streams. Variation in the strain rate has an impact on the flame stability and flame lift-off height. The flame stabilisation point is shifted downstream of the burner exit surface when decreasing the Φ.

- As the flame volume changes, due to the variation in Φ, only the exit emissions can be compared between the two experimental campaigns. At the exit of the chamber, traces of THC were measured as complete combustion was achieved during all test conditions. Also, a higher O_2 concentration is measured under lower Φ conditions, as expected.

- The change in the Φ influences the formation of the NO_x emissions. The peak concentration of the NO_x emissions is found to be 220 ppm for the air flame of Flame A whereas is found to be 240 ppm for the air flame of Flame B. The difference is attributed to the increased flame temperatures with increasing the Φ. The temperature parameter is crucial for both the thermal and the prompt NO mechanisms.

- Exit emissions showed that higher concentrations of CO and CO_2 are achieved for Flame B conditions. The flame temperature is responsible for this phenomenon as it assists the fuel to oxidise and the CO to be converted to CO_2.

5.8 Conclusions

In Chapter 5, fuel-lean natural gas diffusion flames, with an air equivalence ratio $\Phi = 0.75$, are investigated under air and CO_2-enhanced combustion conditions. The total flow rate of the oxidiser mixture is kept constant during the addition of CO_2 which keeps the velocity of the oxidiser mixture constant to exclude any strain rate effects. Simultaneous measurement of in-flame, post-flame and exit emissions and temperature is performed.

The impact of the addition of CO$_2$ into the combustion air stream is prominent on the flame structure, stability, volume and composition. The flame stabilisation point is lifted downstream of the burner exit surface with dilution. In addition, adding CO$_2$ in the air stream causes the flame volume to expand. The concentration of the major species is significantly affected by the compositional change in the oxidiser mixture due to dilution. It is concluded that even the lower CO$_2$-dilution level, 5%, affects greatly the combustion process of natural gas.

The higher heat capacity of CO$_2$ leads to cooler in-flame temperatures for the diluted flames. The consequences of the temperature drop are on the fuel and CO oxidation mechanisms and the formation of NO$_x$ emissions. In-flame and post-flame measurements gave a deeper insight into the progress of the fuel oxidation process, the O$_2$ consumption and the formation of CO$_2$, NO$_x$ and CO emissions. Although in-flame levels of THC are high for the diluted flames, the fuel is gradually oxidised in the post-flame regions and only traces of THC are measured at the exit of the chamber. Experimental results clearly indicate that the addition of CO$_2$ causes a drop in the fuel decomposition rate, as is indicated by the high in-flame concentration of THC at high axial sampling locations for the diluted flames. The slow burning of natural gas influences in turn the formation-destruction of the pollutant emissions. The early formation of CO is due to the rapid reaction of the fuel and O$_2$ but incomplete combustion of the fuel is responsible for the elevated concentration of the CO emissions. It is observed that higher in-flame emissions of CO under air combustion occur which are attributed to the higher air flame temperatures. However, as experimental data shown, the impact of CO$_2$ on the CO is observed at axial locations above x/D$_i$= 125. Post-flame and most importantly, the exit CO emissions, suggest that the oxidation of CO to CO$_2$ is affected by the residence time as much as by the flame temperature. Furthermore, the consequences of the addition of CO$_2$ have a positive impact on the NO$_x$ emissions. The findings of "Flame B" show undoubtedly the significant reduction in NO$_x$ emissions which is attributed to the change caused in the prompt formation mechanism by dilution. Finally, the main outcome of the comparison between the experimental campaigns is that the equivalence ratio can play an important role on the formation of the pollutant emissions through changing the amount of available oxygen and flame temperatures occurring in a combustion system.

CHAPTER 6- Numerical Results

6.1 Introduction

In Chapter 3, the theory of the steady flamelet model is explained and in this chapter, the numerical results are presented. This model can include realistic kinetic effects when computing turbulent flames, where the chemistry is pre-processed and stored in tables, thus allowing for great savings in the computational time. Nevertheless, the model is developed for simulating turbulent diffusion flames with relatively fast chemistry. Consequently, the flame responds instantaneously to flame stretching caused by turbulence and the model cannot capture deep non-equilibrium effects, including slow chemistry.

This numerical study demonstrates the effects of increasing the concentration of CO$_2$ into the combustion air stream on the mass fractions of the major and minor combustion species and radicals and the flame temperature. The main objective is to consider the chemical and thermal effects of CO$_2$ on the flame chemistry. The results are plotted against the mixture fraction as it acts as an independent variable. Firstly, the species composition and temperature of laminar opposed diffusion flames are presented. Secondly, the effect of the strain rate on the flame structure is investigated; variation in the scalar dissipation gives information on different turbulent intensities. Furthermore, the effects of CO$_2$ are investigated by varying its inlet concentration.

6.2 Numerical Results

6.2.1 Species and temperature profiles

This section provides data on the chemical composition and temperature of a methane-air flame, related to the counter-flow flame structure, which are plotted against the mixture fraction space at a specific value of the scalar dissipation, χ_{st}. The purpose of this numerical study is to generate flamelet libraries, which are stored in tables with values of the flame temperature and the major and minor species mass fractions for a wide range of scalar dissipation values; from near equilibrium (low χ_{st} values) to near extinction conditions (highest χ_{st} values). This methodology allows to study the sensitivity of the species concentration and temperature distribution with increasing the value of the scalar dissipation departing from near equilibrium (initial value, χ_{st_o},

taken in all the case studies as 0.01 s^{-1}) and solving until close to extinction. The quenching scalar dissipation value, χ_{st_q}, varies in each case study as the boundary conditions have a strong effect on the extinction limit. It should be emphasised that the steady flamelet model cannot accurately predict any sudden phenomena that occur significantly away from the equilibrium state, including extinction limits. However, as mentioned in Section 3.7.2, an attempt is made to estimate the extinction limits for every case study. Flamelets were solved using the Equations (3-20) and (3-21) and multiple flamelets were generated starting with a minimum value of the scalar dissipation, χ_{st_o}, and progressing with a scalar dissipation step, $\Delta\chi$, as shown in Table 3.5. In the computed air cases, the stoichiometric mixture fraction value, Z_{st}, is calculated to be 0.055, which is the value for a stoichiometric methane-air mixture, and is represented by a vertical dashed line in the following plots.

In Figures 6-1 to 6-5, the mass fractions of the reactants along with the major and minor product species and radicals are illustrated for a methane-air flame. The predicted adiabatic flame temperature is also plotted. The presented values are plotted against the mixture fraction and are computed for an average scalar dissipation value, χ_{st}= 13 s^{-1}. An average scalar dissipation value can represent more accurately an experimental database compared to equilibrium or close to extinction limits. Norton et al. (1993) followed the same approach to compare their experiments against their numerical results.

In Figure 6-1, the flamelet structure of a laminar opposed diffusion flame is presented via the mass fractions of the reactants (CH$_4$, O$_2$), the major combustion products in the flame (H$_2$O, CO$_2$, CO) along with the calculated flame temperature. The scalar profiles are illustrated in the mixture fraction space and are in accordance with the representation of a one-dimensional counter-flow flame as described by Veynante and Vervisch (2002). The boundaries of the mixture fraction space represent the oxidiser inlet (Z= 0) and the opposed fuel stream inlet (Z= 1). Therefore, the fuel mass fraction is zero on the oxidiser side, as denoted by Z= 0, and after the stoichiometric plane increases rapidly. Similar behaviour is observed for the O$_2$ mass fraction but on the opposite side of the mixture fraction space, maximum concentration is found at Z=0 and minimum at Z=1. The stoichiometric plane, as depicted by the black dashed line in the figures, indicates where diffusion and mixing are intense and most chemical reactions are initiated. Within the reaction zone of non-premixed flames, fuel species

are transported to and consumed whereas the temperature and the mass fractions of the major product species, such as H_2O and CO_2, are increased. Therefore, it is observed that close to the stoichiometric plane the concentration of O_2 and CH_4 are minimum and the peak values of the main combustion products and of the flame temperature are reached (Giles et al., 2006). The maximum concentration of the CO emissions is predicted to be on the fuel-rich side of the mixture fraction space where incomplete oxidation of methane is dominant due to the lack of available oxygen. The CO emissions along with the THC are strongly related to the combustion efficiency as high emissions indicate an incomplete combustion system. On the other hand, the peak of stable product species, such as H_2O and CO_2, and the peak temperature are found on or adjacent to the stoichiometric plane but typically on the fuel-rich side. The profiles of the major species and the temperature are in excellent agreement with Norton et al. (1993) who compared their experimental against their numerical calculations.

As reported by Smyth et al. (1985), the calculated peak flame temperature for a methane-air mixture at stoichiometric conditions is 2225 K. However, most laminar flame calculations that have been reported for counter-flow methane-air flames have resulted in lower T_{max} values; usually peak temperatures were found to be near 2000 K and just on the fuel-rich side (Puri et al., 1987, Smooke et al., 1986 Barlow et al., 1990, Seshadri et al., 1990 and Norton et al., 1993). The main reason for this discrepancy is due to the aforementioned assumptions made during the numerical calculations; the possible reasons are either the assumption of finite rate chemistry or the non-inclusion of radiation heat losses or the simplified transport assumptions, such as unity Lewis number and constant heat capacity (Norton et al., 1993, Seshadri et al., 1990). Furthermore, the location of the peak temperature varies across several experimental and numerical studies but most authors have reported that the peak is close to the stoichiometric mixture fraction either on the fuel-lean or fuel-rich flame side (Norton et al., 1993).

Figure 6-2 illustrates the mass fractions of the NO and NO_2 emissions along with the adiabatic temperature profile. Nitrogen dioxide emissions are calculated to be close to the oxidiser side where the peak value of the radical HO_2 is found, which is the precursor for its formation pathway, as indicated by the reaction (R 2-5) in Section 2.3.1.3. Nitrogen dioxide emissions are predicted to be much lower than the NO emissions as they don't form at the hottest parts of a diffusion flame and usually

contribute to less than 10 % of the total NO$_x$ emissions (Li and Williams, 1999). For flame temperatures above 1800 K, the thermal NO formation mechanism is highly temperature dependant and increases linearly with the availability of O atoms. As expected, the peak concentration of O atoms is found to be on the oxidiser side, as shown in Figure 6-4. Similar numerical studies have found that the prompt mechanism is dominant in fuel-rich flame regions of diffusion flames where temperature does not play a key role but only stoichiometry does (Li and Williams, 1999). Also, the rate of the prompt initiation reaction is greater than the thermal reaction rate in methane-air diffusion flames even over a range of air preheat temperatures, which are expected to favour mainly the thermal pathway (Lim et al., 2000). For non-premixed counter-flow flames, NO is consumed and produced mainly through the Fenimore mechanism whereas the thermal contribution is less significant. According to Nishioka et al. (1994), the peak NO is always located close to the temperature peak. Some studies on opposed flow flames have shown that the GRI Mech overpredicts the concentration of CH species and thus, the calculated prompt NO emissions are higher than the measured ones as CH is the main precursor of the prompt pathway. According to Li and Williams (1999), this inaccuracy could be attributed to the prompt NO$_x$ chemistry database included in the GRI Mech and particularly the C$_2$ chemistry. Similar conclusions were reached by Lim et al. (2000) who also studied the effect of air preheat on species profiles for methane-air counterflow diffusion flames.

Methane oxidation occurs through either the attack by reactive radicals like OH, O or H to form CH$_3$, or thermal decomposition, as reported by Westbrook and Dryer (1984). Smooke et al. (1986) highlighted the importance of computing the flame structure including the C$_2$ chemistry which allows for a better prediction of the mass fractions of H$_2$ and CO. For these flamelet calculations, the detailed GRI- Mech 3.0 was utilised which contains all the necessary reactions to predict accurately the flow field of a methane flame. Figures 6-3 and 6-5 illustrate the mass fractions of major and minor species and trace radicals as found in a diffusion flame, such as C$_2$H$_2$, C$_2$H$_4$, C$_2$H$_6$, O, H, OH and CH$_3$. The peak values of HC species are observed on the fuel-rich side of the flame and their concentration increases on the fuel side. The peak values of O, H and OH radicals are located on the fuel-lean side of the flame and their concentration reduces significantly in the reaction zone where most reactions between hydrocarbon intermediate species and these radicals occur (Westbrook and Dryer, 1984). This is due to the high tendency of these radicals to attack fuel molecules (Barlow et al.,

1990). For counter-flow flames, the peak concentration of the radical species, such as CH, H, OH and O is found close to the reaction zone. In particular, the peak of the H and CH radicals is located on the fuel-rich side while O-atoms are located on the fuel-lean side, as also reported by Giles et al. (2006).
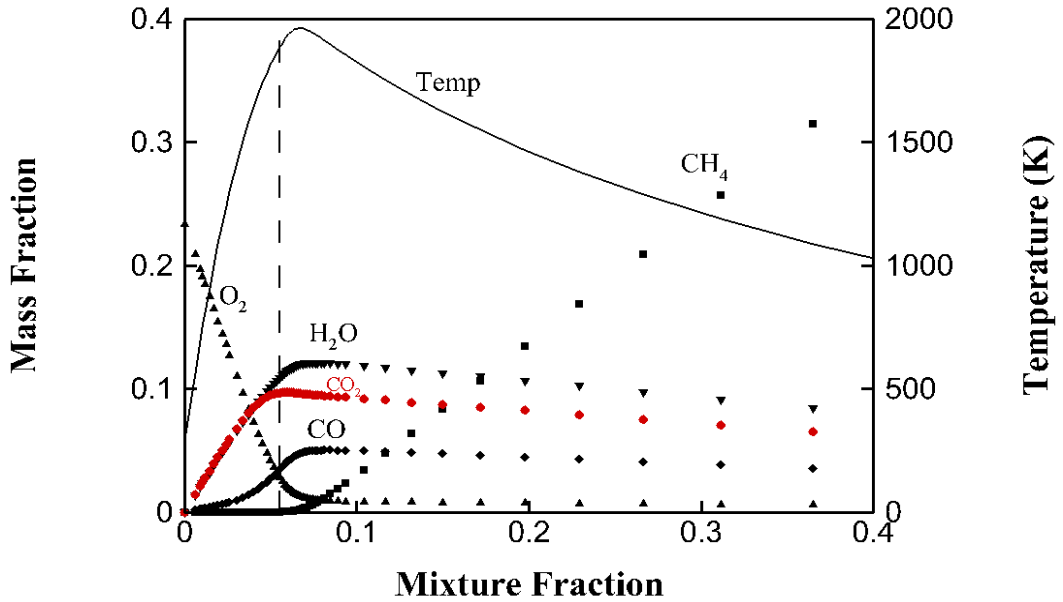
Figure 6-1 Calculated mass fractions of CH_4, O_2, H_2O, CO_2, CO and calculated adiabatic flame temperature presented as a function of the mixture fraction as calculated at $\chi_{st}= 13$ s^{-1}. Black-filled square symbols used for CH_4, black-filled left-triangle symbols for O_2, black-filled triangle symbols for H_2O, red-filled diamond symbols for CO_2, black-filled diamond symbols for CO and solid black line for temperature.
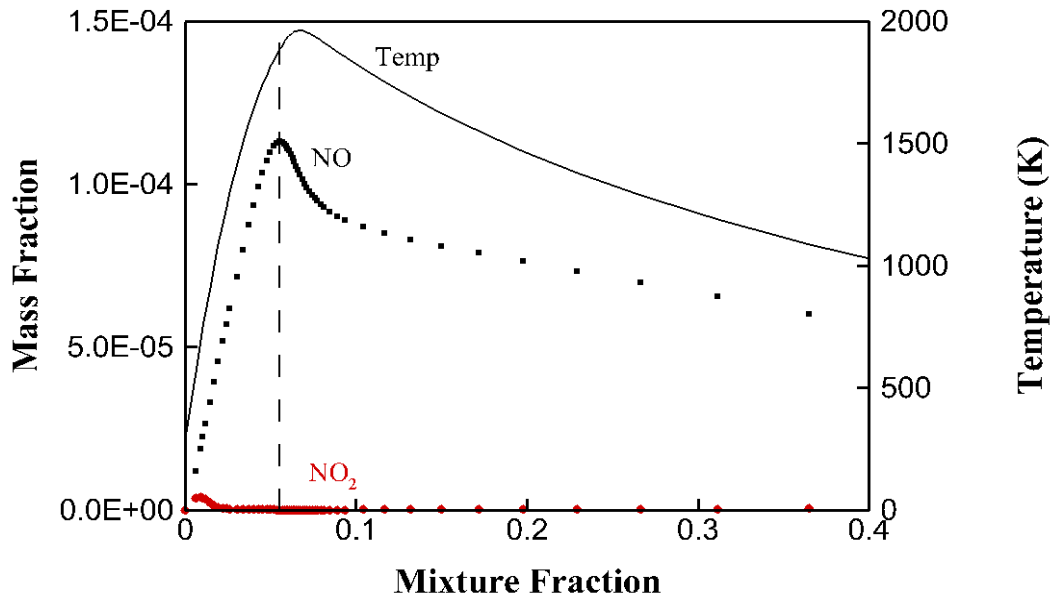
Figure 6-2 Calculated mass fractions of NO and NO_2 and calculated adiabatic flame temperature presented as a function of the mixture fraction as calculated at $\chi_{st}= 13$ s^{-1}. Black-filled square symbols used for NO, red-filled diamond symbols for NO_2 and solid black line for temperature.
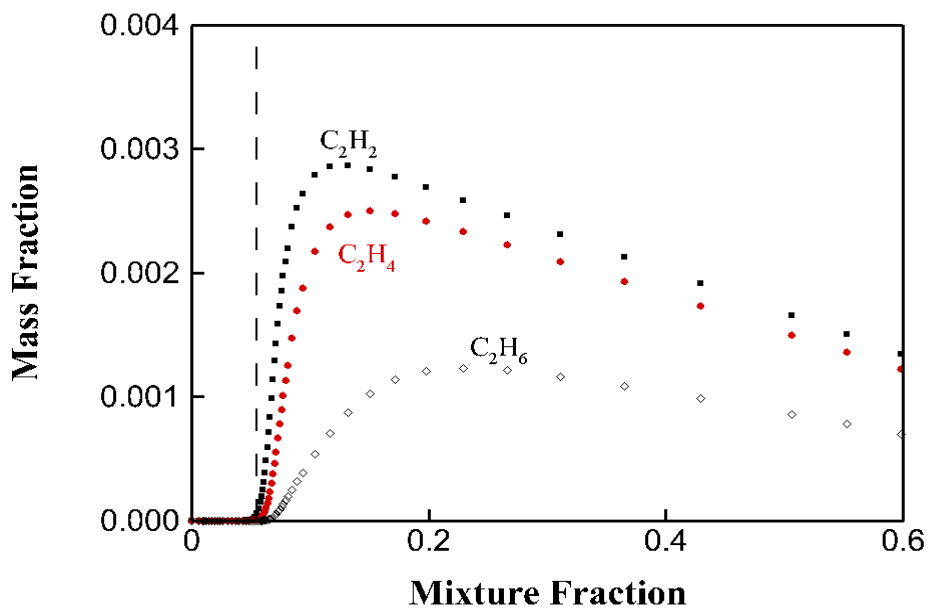
Figure 6-3 Calculated mass fractions of C$_2$H$_2$, C$_2$H$_4$ and C$_2$H$_6$ presented as a function of the mixture fraction as calculated at χ_{st}= 13 s^{-1}. Black-filled square symbols used for C$_2$H$_2$, red-filled circle symbols for C$_2$H$_4$ and black diamond symbols for C$_2$H$_6$.
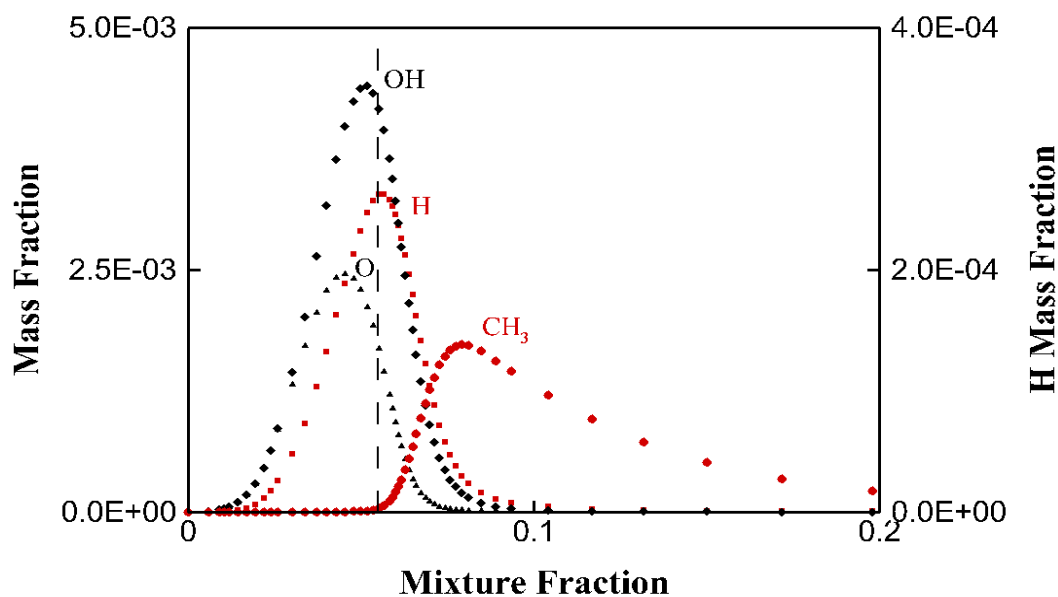
Figure 6-4 Calculated mass fractions of H, O, OH and CH$_3$ presented as a function of the mixture fraction as calculated at χ_{st}= 13 s^{-1}. Red-filled square symbols used for H, black-filled triangle symbols for O, black-filled diamond symbols for OH and red-filled circle symbols for CH$_3$.
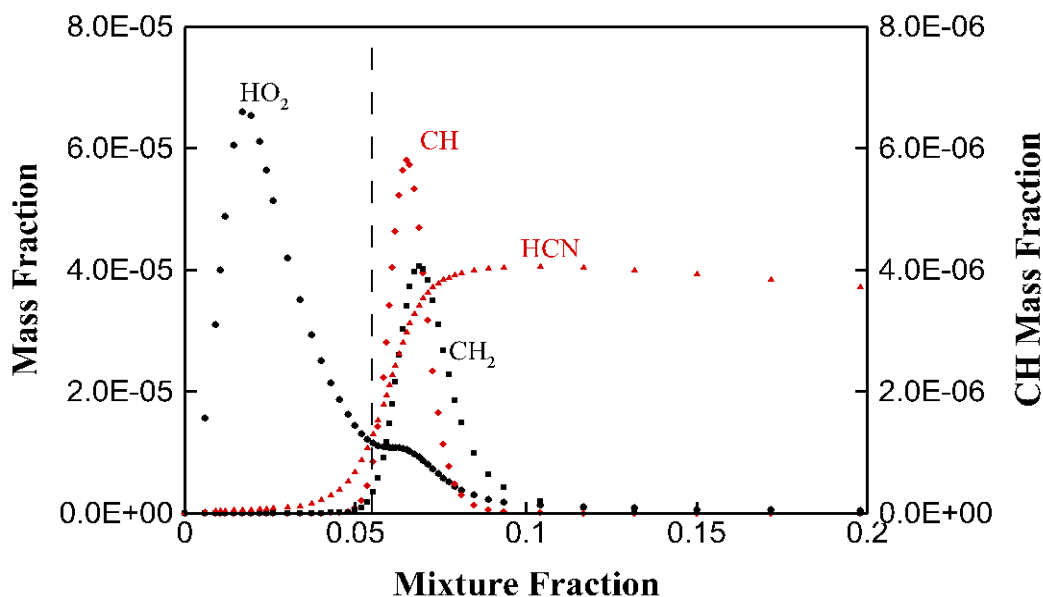
Figure 6-5 Calculated mass fractions of CH$_2$, HO$_2$, HCN and CH presented as a function of the mixture fraction as calculated at χ_{st}= 13 s^{-1}. Black-filled square symbols used for CH$_2$, black-filled diamond symbols for HO$_2$, red-filled triangle symbols for HCN and red-filled diamond symbols for CH.

6.2.2   Impact of scalar dissipation

As mentioned in Section 3.6.4, the steady flamelet model is an extension of the scalar conserved approach to include more features of the diffusion flames. The structure and properties of laminar flamelets are expressed via the mixture fraction and the scalar dissipation value. The latter represents the molecular mixing rate between the reactants and defines any changes in the inner structure of a flame due to stretching (Peters, 1984, Peters, 1986). Consequently, the influence of the scalar dissipation value on the flamelet structure is important. The scalar dissipation is the inverse of a diffusive time, when this time decreases, the scalar dissipation increases enhancing the mass and heat transfer close to the stoichiometric plane. As the scalar dissipation is directly related to the strain rate, as seen in Equation (3-24), when the χ_{st} increases, the flame stretching increases and the combustion intensity drops (Veynante and Vervisch, 2002). The plots in Figures 6-6 to 6-12 depict the mass fractions of the main flame species, CH$_4$, O$_2$, H$_2$O, CO$_2$, CO, NO and the adiabatic flame temperature against the mixture fraction variable, Z, for a range of scalar dissipation values. To examine the effect of the straining rate on the flame structure, three scalar dissipation values are investigated below. Each case study has a similar reactant concentration but the flamelets are computed at a different scalar dissipation value.

A low value close to the equilibrium limit, $\chi_{st\_1}= 0.01$ s^{-1}, an average value, $\chi_{st\_2}= 13$ s^{-1}, and a high value representing conditions near extinction, $\chi_{st\_3}= 25$ s^{-1}, have been selected. The results suggest that the impact of the scalar dissipation is seen to be significant on the scalar profiles and the local stoichiometry, as expressed via the mixture fraction parameter.

As the flame is stretched and strained by turbulence, species concentration and temperature gradients increase and radicals and heat diffuse quicker out of the flame. At a critical value of the strain rate, the imbalance created by the local loss of heat and active species, as enhanced by flame stretching, will lead to quenching (Liew et al., 1984). Consequently, the diffusion time decreases significantly while increasing the strain rate. Therefore, it can be concluded that high strain rates result in less intense combustion and lower concentration of products. Continuing to increase the scalar dissipation, there is a considerable impact on the concentration of the reactants (O_2, CH_4) which is increased, as seen in Figures 6-6 and 6-7. The reason for this increase is that the reactant residence time becomes shorter than the chemical reaction time (Cheng et al., 2006).

The decreased residence time affects in turn the flame temperature that decreases (Som et al., 2007). The adiabatic flame temperature decreases substantially close to the stoichiometric plane and the peak temperature shifts to a higher Z value, which was also observed by Liew et al. (1984). The most interesting feature is the change in the trend at about Z= 0.08, as seen in Figures 6-8, 6-9 and 6-10 which illustrate the adiabatic flame temperature and the mass fractions of CO_2 and CO in the mixture fraction space, accordingly. On the oxidiser side and at the stoichiometric plane, the impact of the scalar dissipation is different compared to the fuel side. It appears that relatively higher values of χ_{st} at fuel-rich regions result in a more efficient fuel oxidation as indicated by the higher temperature, a higher CO_2 mass fraction and a reduction in the CO level. This trend is a good indication of the relation between strain rate and diffusion processes, confirming the fact that the burning rate, heat and mass transport in the reaction zone is gradually enhanced until very high values of scalar dissipation where chemistry cannot be anymore maintained due to large heat losses and intense flame stretching.

Figure 6-11 illustrates the relatively minor impact of χ_{st} on the mass fraction of H_2O which in fact diminishes gradually on the fuel side. On the other hand, Figure 6-12

reveals the major impact of flame stretching on the mass fraction of NO emissions, which decrease drastically due to the reduced residence time and the temperature decrease. Similar behaviour is observed by Cheng et al. (2006) and Drake and Blint (1989). The study of Drake and Blint (1989) is a comprehensive investigation of the effect of flame stretching on NO_x formation which suggests that the net formation rate of NO_x and most importantly the residence time in flame regions of high flame temperature are the crucial parameters.
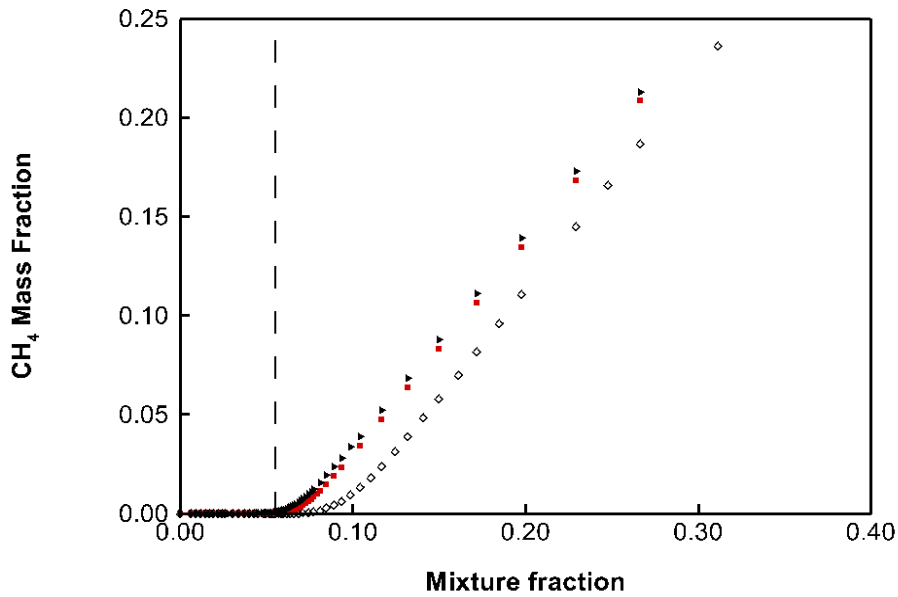
Figure 6-6 Calculated mass fraction of CH_4 as a function of the mixture fraction at a low χ_{st}, black diamond symbols, at an average χ_{st}, red-filled square symbols, and at a high χ_{st}, black-filled triangle symbols.
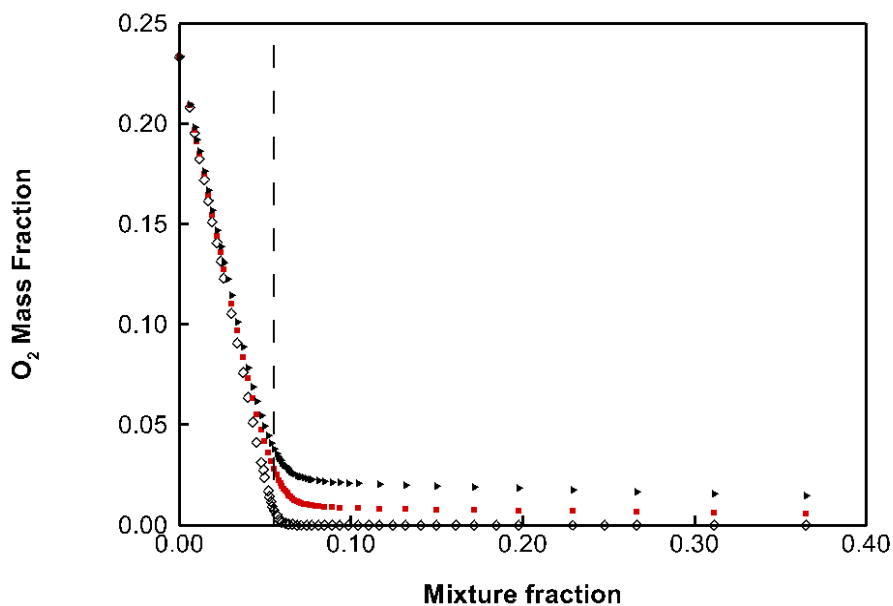
Figure 6-7 Calculated mass fraction of O_2 as a function of the mixture fraction at a low χ_{st}, black diamond symbols, at an average χ_{st}, red-filled square symbols, and at a high χ_{st}, black-filled triangle symbols.
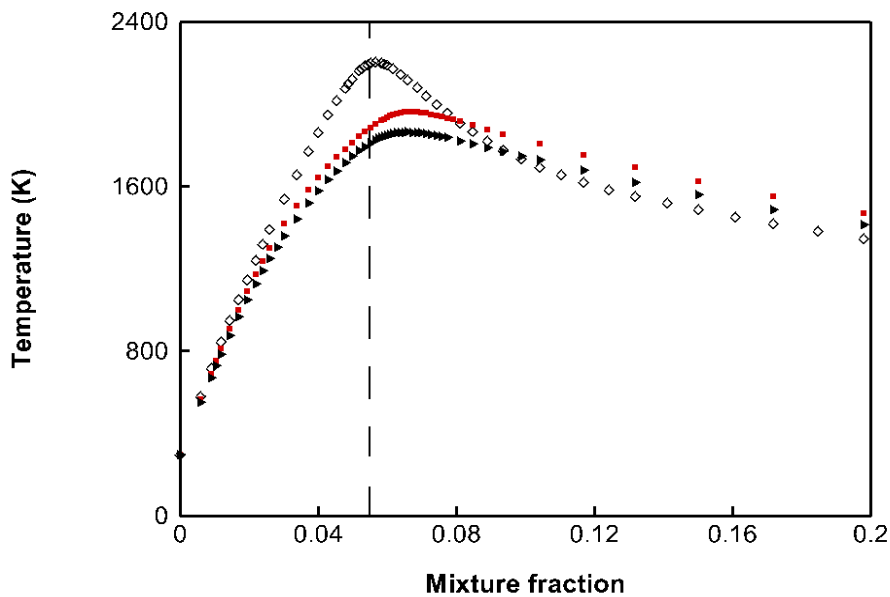
Figure 6-8 Calculated adiabatic flame temperature as a function of the mixture fraction at a low χ_{st}, black diamond symbols, at an average χ_{st}, red-filled square symbols, and at a high χ_{st}, black-filled triangle symbols.
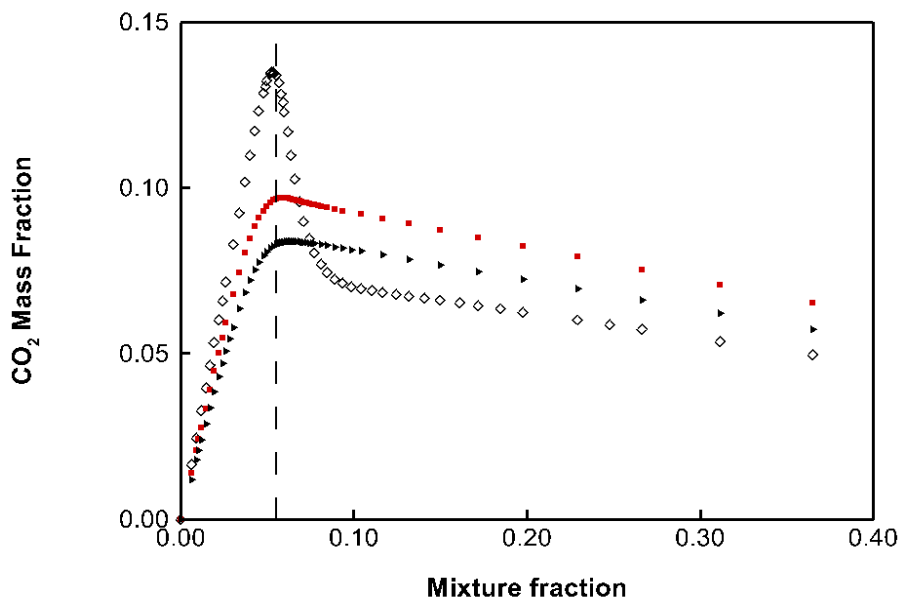
Figure 6-9 Calculated mass fraction of CO$_2$ as a function of the mixture fraction at a low χ_{st}, black diamond symbols, at an average χ_{st}, red-filled square symbols, and at a high χ_{st}, black-filled triangle symbols.
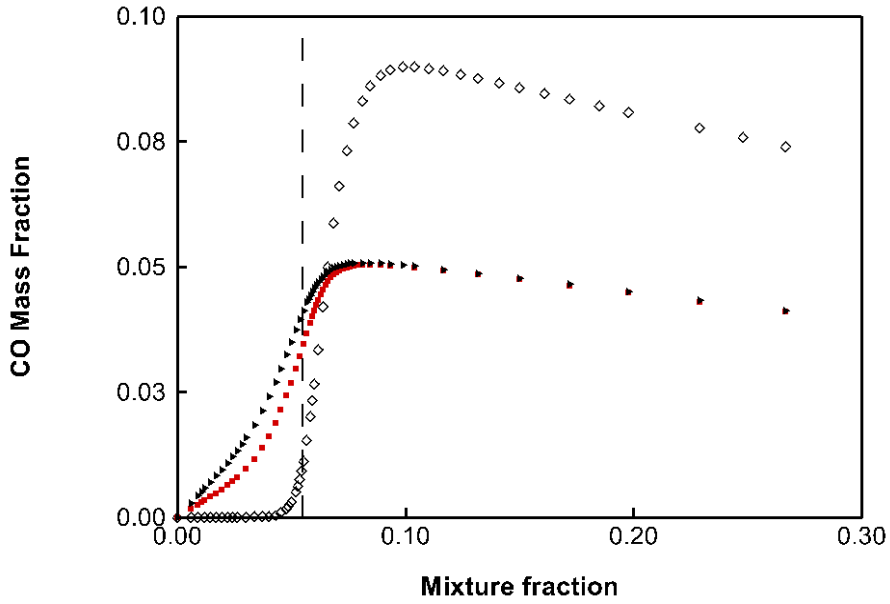
Figure 6-10 Calculated mass fraction of CO as a function of the mixture fraction at a low χ_{st}, black diamond symbols, at an average χ_{st}, red-filled square symbols, and at a high χ_{st}, black-filled triangle symbols.
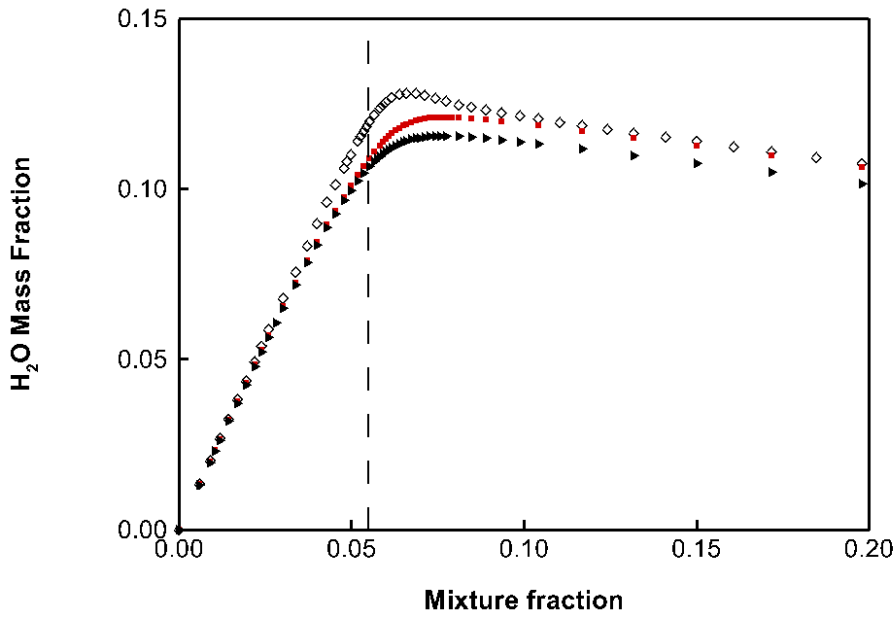
Figure 6-11 Calculated mass fraction of H$_2$O as a function of the mixture fraction at a low χst, black diamond symbols, at an average χst, red-filled square symbols, and at a high χst, black-filled triangle symbols.
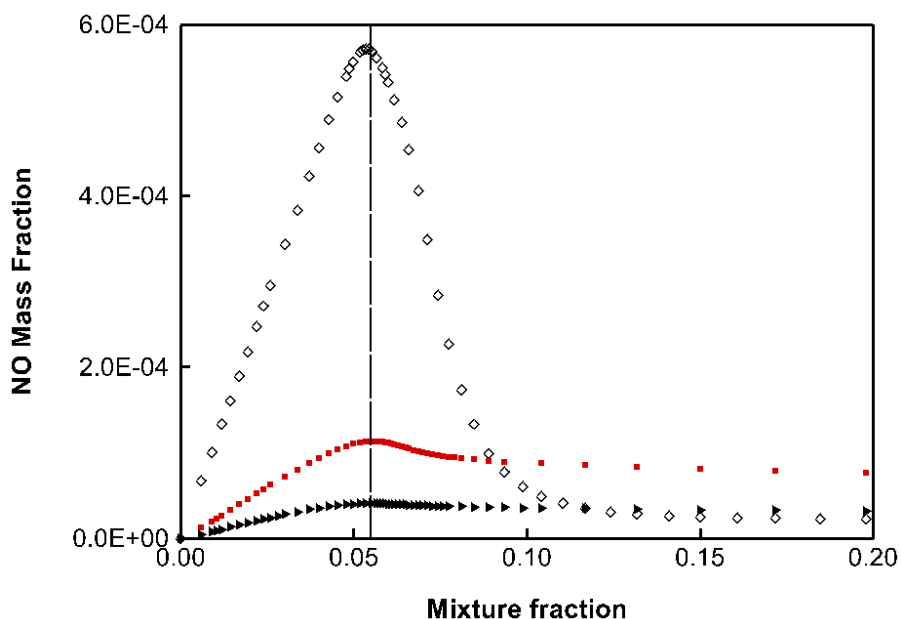
Figure 6-12 Calculated mass fraction of NO as a function of the mixture fraction at a low χ_{st}, black diamond symbols, at an average χ_{st}, red-filled square symbols, and at a high χ_{st}, black-filled triangle symbols.

6.2.3 Impact of CO₂ dilution

The main objective of this study is to investigate experimentally and numerically the chemical and thermal effects of CO_2 dilution on flame chemistry. In this section, the performance of the steady flamelet model to predict the flow field under CO_2-enhanced combustion environments is examined. The 1D flamelet calculations have been proved to be a cheap method, in terms of computational time, of calculating the temperature and species mass fractions in the mixture fraction space. An average value of the scalar dissipation is selected for each of the four case studies described below. The values of the χ_{st} for each test condition can be found in Table 3-6.

Figures 6-13 to 6-19 depict the mass fraction of major and minor flame species and radicals (O_2, CH_4, H_2O, OH, H, O, NO, N, C_2H_2, C_2H_6, HCN, CH, CO, CO_2) and the adiabatic flame temperature in the mixture fraction space for four case studies. The flamelet structure of the methane-air flame is compared against the structure of 3 %, 5 % and 10 % CO_2-diluted methane-air flames to reveal the impact of the increased inlet CO_2 concentration.

Diluting the oxidiser stream yields a lower O_2 concentration in the oxidant stream and higher levels of CH_4 on the fuel side, as plotted in Figure 6-13. The reaction zone is defined where the concentration of the reactants drops drastically and the concentration of product species reach high levels. Since a higher mass fraction of the

THC is found due to CO$_2$ dilution, it is suggested that the presence of CO$_2$ slows down the combustion burning rate through altering the methane reaction pathways (Park et al., 2002, Lee et al., 2001). Lower reaction rates are also justified due to lower temperatures within the reaction zone which inhibits the promotion of the fuel oxidation. The distribution of the mass fraction of the main reactive radicals (OH, O and H) is shown in Figure 6-14; the radicals are found in abundance in the oxidiser side and due to CO$_2$ dilution, their peak values are reduced. The significant reduction in the concentration of these radicals with increasing the dilution level is combined with the reduction in the fuel burning rate and thus, the overall combustion rate. The OH consumption is achieved via the reactions (R 2-12) or (R 2-13) or the oxidation reactions of methane between CH$_i$ species and OH which yield higher reaction rates compared to the reactions (R 2-12) and (R 2-13). The decreased oxidation of the fuel leads in turn to a reduced production of water with increasing the CO$_2$ dilution level as water is one of the main combustion products.

The higher heat capacity of CO$_2$ is expected to lead to a reduction in the calculated adiabatic flame temperature with increasing the CO$_2$ dilution level in the combustion air stream. The temperature drop has several consequences on the combustion process. The chemical and thermal impact of the temperature drop on the fuel burning process has been already discussed. The other considerable impact of the addition of CO$_2$ in the reactant mixture is on the NO emissions. In diffusion flames, NO$_x$ emissions consist mainly of NO and less of NO$_2$ emissions and therefore, only the mass fraction of NO is plotted in Figure 6-15. The dramatic reduction in the mass fraction of NO emissions with increasing the CO$_2$ dilution level is driven by changes in the thermal and prompt mechanisms.

In Figures 6-16 to 6-18, the mass fractions of important minor species (N, C$_2$H$_2$, C$_2$H$_6$, HCN and CH) for the formation of NO are plotted as a function of the mixture fraction, Z. Although the thermal contribution to the NO formation is minor compared to the prompt, the consideration of this mechanism is important. Due to the strong dependence of thermal NO on the flame temperature and the availability of O atoms, the thermal NO emissions are reduced with the presence of CO$_2$. Decrease in the O$_2$ mass fraction leads to a significant reduction in the mass fractions of O and OH in the flame which are crucial radicals for the thermal pathway through the reactions (R 2-1) and (R 2-3). The N atoms are produced via the reaction (R 2-1) and are then converted to thermal NO via the reactions (R 2-2) and (R 2-3). The significant

reduction in the mass fraction of N atoms, and the lack of active radicals, yield a significant reduction in the thermal NO formation (Ju and Niioka, 1997), as shown in Figure 6-16.

Figure 6-17 illustrates the mass fraction of important hydrocarbon species, the acetylene, C_2H_2, and ethane, C_2H_6, generated during the oxidation process of methane. The addition of CO_2 in the reactant mixture reduces significantly the concentration of these hydrocarbon species due to alterations in the methane oxidation reactions which is an indication of the slower decomposition rate of the fuel and the higher CH_4 mass fraction. As reported by Lee et al. (2001), the peak concentration of the hydrocarbon species shifts to the oxidiser side when CO_2 is added to the air stream where active radicals, such as O, H and OH, are in abundance. As reported by Giles et al. (2006), the large reduction in the peak of HCN mass fraction caused by the addition of CO_2 is attributed to the chemical impact of CO_2 as the mass fractions of C_2H_2 and CH drop significantly. Acetylene is the dominant contributor to the prompt mechanism via its oxidation pathway which leads to the formation of CH radicals. The reaction between CH and N_2 to form HCN is the initiation step for the formation of prompt NO (Miller and Bowman, 1989). Consequently, the reduced formation of C_2H_2 caused by CO_2 dilution, results in a decreased formation of CH radicals in flames and thereby of the formation of HCN, as outlined in Figure 6-18. The study of Li and Williams (1999) concludes also that the concentration of CH species is strongly affected by the concentration of CO_2 and this relationship is due to the chemical-kinetic interactions and not only to the reduction of reaction rates due to dilution. Several studies have concluded that the GRI mechanism overpredicts the formation of prompt NO in methane diffusion flames through overpredicting the concentration of CH and thereby, the mass fraction of the NO species should be considered only qualitatively (Giles et al., 2006, Li and Williams, 1999, Barlow et al., 2001, Lim et al., 2000).

Figure 6-19 depicts the behaviour of the mass fraction of CO and CO_2 under air and CO_2-enhanced combustion conditions. The peak of the mass fraction of CO_2 is found on the oxidiser side of the stoichiometric mixture fraction and shifts more to the oxidiser direction with CO_2 dilution as CO_2 competes with CH_i species for the OH radicals. Similarly, the peak mass fraction of CO shifts towards the oxidiser direction with increasing the CO_2 dilution level. The most interesting feature on the CO mass fraction profile is the change of its trend between the air and the CO_2-diluted cases. On the fuel side, the 10 % CO_2-diluted flame produces significantly less CO compared

to the air flame which is not expected to occur under CO$_2$-enhanced combustion conditions. The presence of CO$_2$ in the oxidiser reactant stream has a negative impact on the oxidation reaction of methane because it slows down its burning and alters its reaction pathways by decreasing the amount of important fuel species. Moreover, the different physical properties of CO$_2$ are responsible for the decreased flame temperature which is another inhibitor to the oxidation process. Consequently, it is expected that the CO emissions will increase with CO$_2$ dilution. However, the flamelet calculations predict a decrease in the formation of CO species. The recent study of Goldin et al. (2012) suggests that a model accounting for unsteady flows is required to accurately account for the CO emissions at fuel-lean conditions. Moreover, the major limitation of the flamelet model is that it accounts for fast chemistry which does not apply for the formation process of CO under a diluted combustion environment.
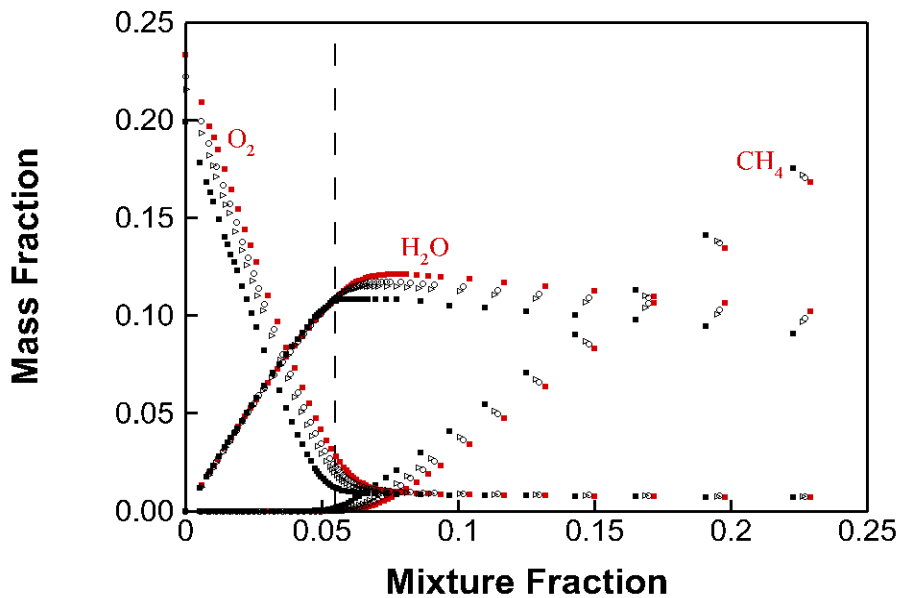
Figure 6-13 Calculated mass fractions of CH$_4$, O$_2$ and H$_2$O as a function of the mixture fraction at an average χ_{st} for the air flame, red-filled square symbols, for the 3% CO$_2$-diluted flame, black circle symbols, for the 5 % CO$_2$-diluted flame, black triangle symbols, and for the 10 % CO$_2$-diluted flame, black-filled square symbols.
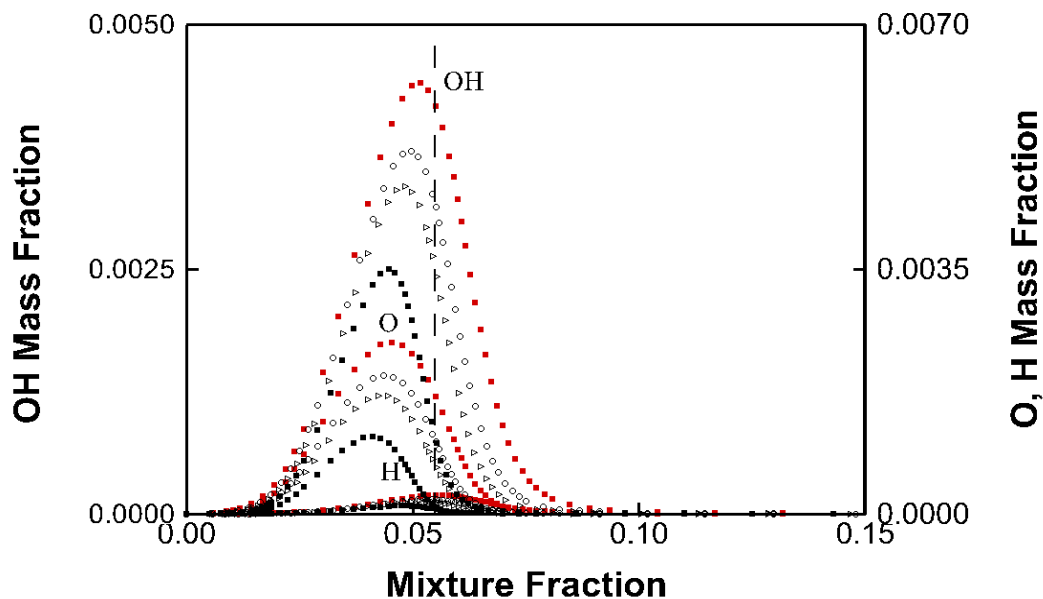
Figure 6-14 Calculated mass fractions of OH, H and O as a function of the mixture fraction at an average χ_{st} for the air flame, red-filled square symbols, for the 3% CO$_2$-diluted flame, black circle symbols, for the 5 % CO$_2$-diluted flame, black triangle symbols, and for the 10 % CO$_2$-diluted flame, black-filled square symbols.
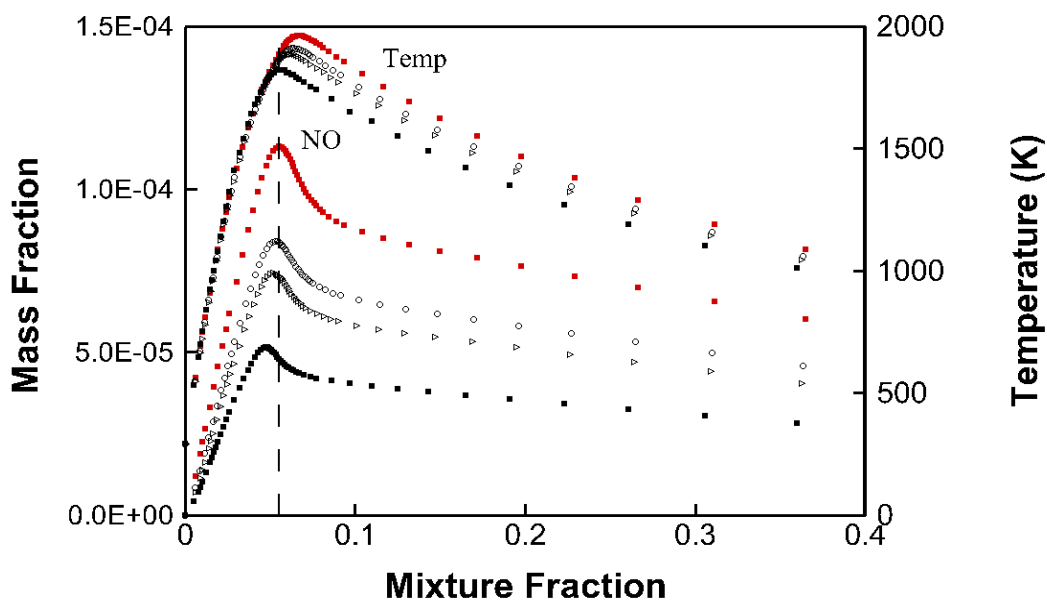
Figure 6-15 Calculated mass fraction of NO and calculated adiabatic flame temperature as a function of the mixture fraction at an average χ_{st} for an the flame, red-filled square symbols, for the 3% CO$_2$-diluted flame, black circle symbols, for the 5 % CO$_2$-diluted flame, black triangle symbols, and for the 10 % CO$_2$-diluted flame, black-filled square symbols.
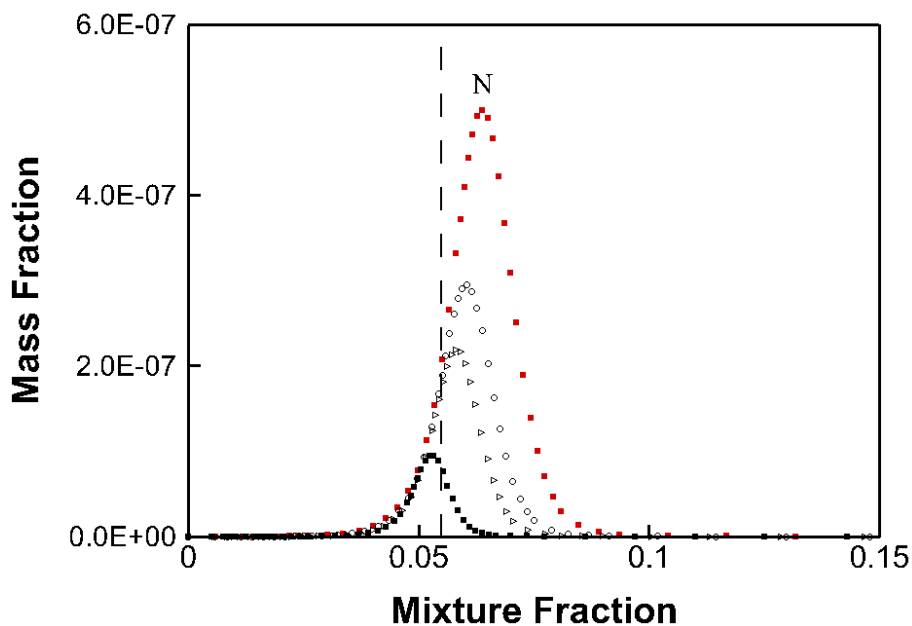
Figure 6-16 Calculated mass fractions of N as a function of the mixture fraction at an average χ_{st} for the air flame, red-filled square symbols, for the 3% CO$_2$-diluted flame, black circle symbols, for the 5 % CO$_2$-diluted flame, black triangle symbols, and for the 10 % CO$_2$-diluted flame, black-filled square symbols.
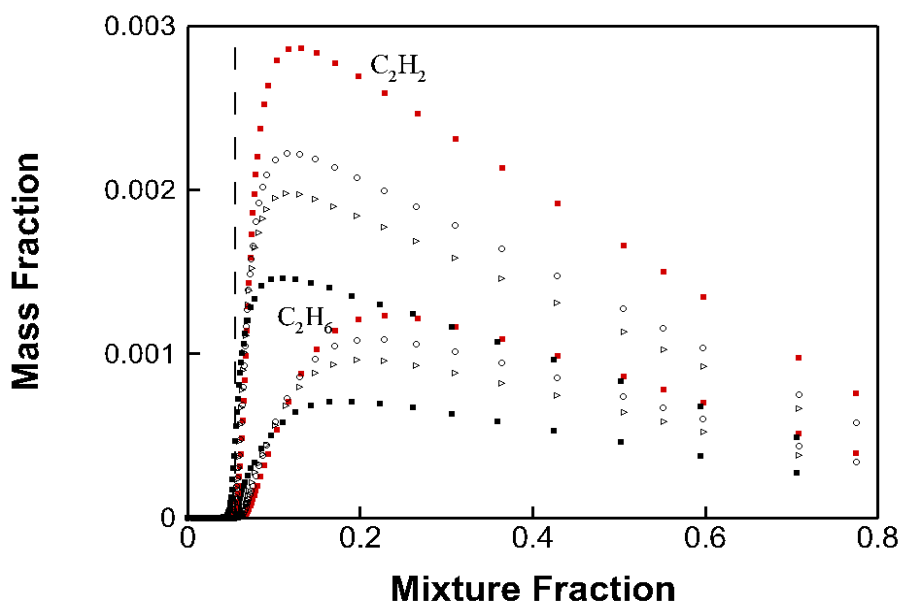
Figure 6-17 Calculated mass fractions of C$_2$H$_2$ and C$_2$H$_6$ as a function of the mixture fraction at an average χ_{st} for an the flame, red-filled square symbols, for the 3% CO$_2$-diluted flame, black circle symbols, for the 5 % CO$_2$-diluted flame, black triangle symbols, and for the 10 % CO$_2$-diluted flame, black-filled square symbols.
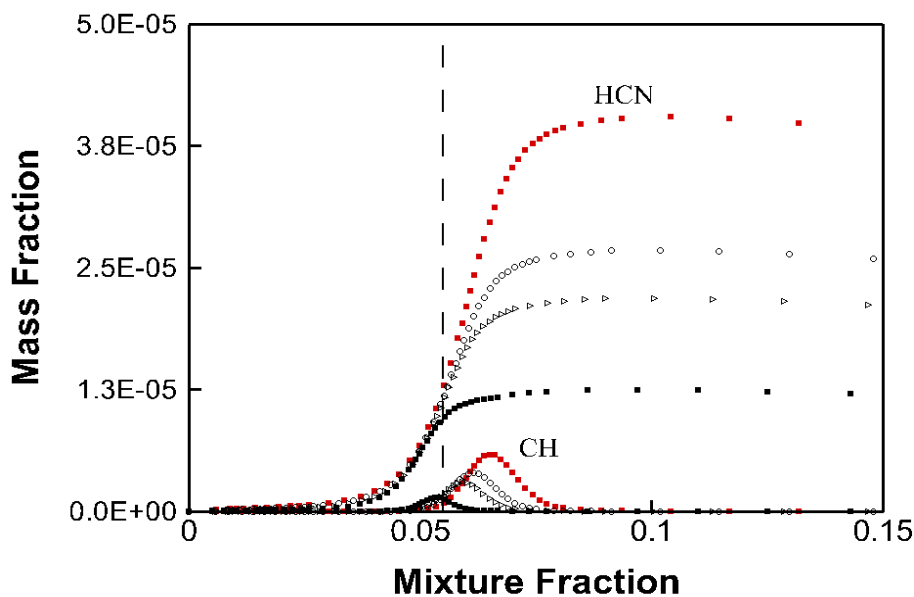
Figure 6-18 Calculated mass fractions of HCN and CH as a function of the mixture fraction at an average χ_{st} for the air flame, red-filled square symbols, for the 3% CO$_2$-diluted flame, black circle symbols, for the 5 % CO$_2$-diluted flame, black triangle symbols, and for the 10 % CO$_2$-diluted flame, black-filled square symbols.
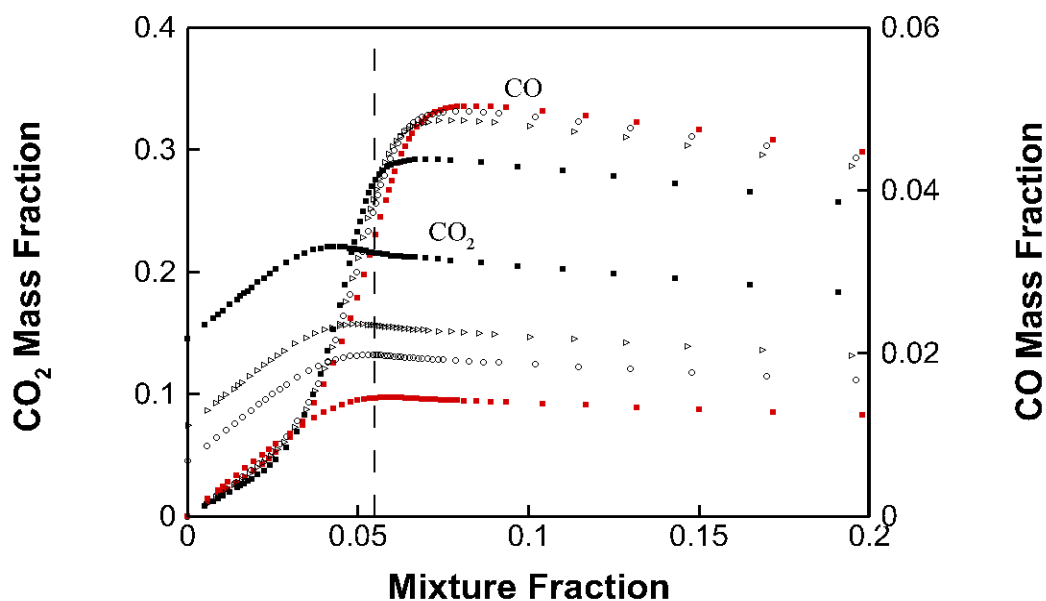
Figure 6-19 Calculated mass fractions of CO$_2$ and CO as a function of the mixture fraction at an average χ_{st} for the air flame, red-filled square symbols, for the 3% CO$_2$-diluted flame, black circle symbols, for the 5 % CO$_2$-diluted flame, black triangle symbols, and for the 10 % CO$_2$-diluted flame, black-filled square symbols.

6.2.4 Discussion

In Section 6.2, the numerical results as obtained from the 1D steady flamelet model are reported. The purpose of using this model was to investigate numerically the dilution, thermal and chemical effects of the presence of CO$_2$ in the oxidiser stream

on the flame chemistry and composition. The chemical kinetic mechanism GRI-Mech 3.0 was incorporated within the flamelet solver and cheaply calculations, in terms of computational time, were completed with respect to predicting the changes in flame composition as caused by dilution. Section 6.2 was divided into three parts in order to understand how this numerical model, the flamelet model, works; first, the major species and the adiabatic flame temperature were plotted in the mixture fraction space to reveal the performance of the model to predict the configuration of methane-air counter-flow non-premixed flames. Secondly, the impact of the scalar dissipation on the flame structure and finally, the impact of CO$_2$ on the flame chemistry were investigated. In summary, the main conclusions from the numerical calculations are as follows:

- It has been found that the flamelet structure of a laminar opposed diffusion flame is predicted reasonably well via the mass fractions of the reactants (CH$_4$, O$_2$), the major combustion products in the flame (H$_2$O, CO$_2$, CO) along with the calculated adiabatic flame temperature. In diffusion flames, close to the stoichiometric mixture fraction plane, the concentration of O$_2$ and CH$_4$ are minimum and the concentration of the main combustion products and the flame temperature are close to their peak values.

- The structure and properties of laminar flamelets are expressed via two parameters, the mixture fraction, Z, and the instantaneous scalar dissipation, χ_{st}. The impact of the strain rate is significant on the flame structure and thus it was part of this study. It is found that flame stretching leads to a drop in the combustion intensity. This drop was indicated by the increased mass fractions of the reactants, the reduced mass fractions of the main combustion products and the lower flame temperatures. A sensible increase in the scalar dissipation above the equilibrium state is beneficial as increased diffusion time scales promote mixing and diffusion. However, further increase in the strain rate is not sustainable as the diffusion time increases dramatically, leading to much shorter residence time for the reactants if compared to the chemical reaction time. Then, heat and radicals diffuse quickly out of the flame forcing the flame to quench.

- The performance of the flamelet model on predicting accurately the dilution, thermal and chemical effects of the addition of CO$_2$ is of major interest in this study. The utilised chemical kinetic mechanism, GRI-Mech 3.0, includes reactions with C$_2$ species which are crucial to the prediction of the methane oxidation

pathway. It is concluded that the model can predict quite well the changes in the flame chemistry with the exemption of the behaviour of the CO emissions. The slow burning rate of methane due to the presence of CO$_2$ leads to an increase in the CO concentration. However, the model is based on fast chemistry and predicted that the CO emissions will decrease with CO$_2$ dilution. The oxidation of CO emissions is a relatively slow process that requires sufficient residence time and thus is inhibited by dilution.

6.3   Comparison of Numerical Results with Flame B

Further to examining how the flamelet model works and its performance on predicting satisfactory the effects of the addition of CO$_2$, a direct comparison between the experimental campaign "Flame B" and the numerical results is performed. The direct comparison will conclude on the suitability of the model to predict turbulent diffusion flames and their interaction with strong chemical kinetic phenomena. The mixture fraction calculations for the experimental data are made according to the methodology explained in Section 3.4.6.2. In all figures, experimental data are represented by symbols whereas calculated data by solid lines.

6.3.1   Air case study

Figure 6-20 depicts the measured flame temperature and the calculated adiabatic temperature and Figures 6-21 to 6-24 illustrate the mass fractions of the major species in the mixture fraction space. The vertical dashed line denotes the location of the stoichiometric mixture fraction, $Z_{st} = 0.055$, for a methane-air flame. The best matched value of the scalar dissipation over the range described in Table 3-6 from the flamelet calculations is found to be $\chi_{st} = 19$ s^{-1} for the air flame.

The flamelet model does not account for any heat loss/gain due to radiation and heat transfer to the walls and hence the numerical solution gives the adiabatic flame temperature. Consequently, the adiabatic temperature is higher than the measured temperature, as shown in Figure 6-20. As explained in Section 3.3.1.3, the thermocouple measurements were corrected so as to include the radiation heat loss. Nevertheless, there is a good agreement of the location of the peak temperature which is found to be on the fuel-rich side.
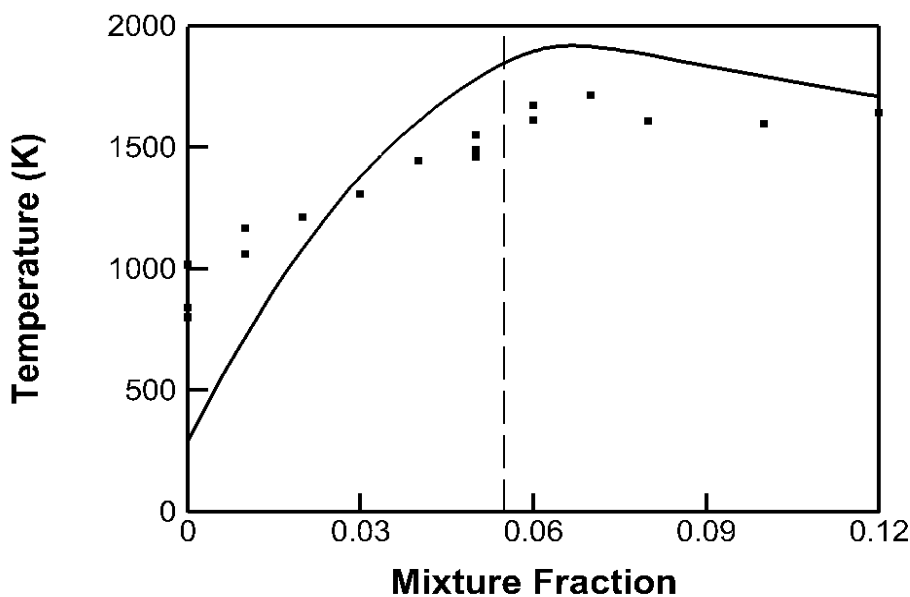
Figure 6-20 Radiation-corrected temperature experimental data (black symbols) and calculated adiabatic temperature (black solid line) as a function of the mixture fraction for the air case study. Dashed line represents the stoichiometric mixture fraction.

There is an excellent agreement between the measured mass fraction of THC and the calculated mass fraction of CH_4 in the mixture fraction space, as indicated by Figure 6-21. It should be noted that the FID analyser used for measuring the concentration of THC was calibrated to give the values in methane equivalent and, as a result, it can be directly compared to the calculated mass fraction of CH_4. In Figure 6-22, an excellent agreement is also observed between the calculated and the measured mass fraction of O_2 in the mixture fraction space; results agree more on the oxidiser side than on the fuel side. The CO_2 experimental data for the air flame match perfectly well with the corresponding CO_2 calculated mass fraction, as presented in Figure 6-23. For the CO profile, there is a satisfactory agreement in the trend but for values of the mixture fraction above its stoichiometric value, the experimental mass fraction of CO is lower than the corresponding calculated value.

Figure 6-24 reveals the poor prediction of the NO_x mass fraction using the flamelet model. During the experiments both the NO and NO_x concentrations were measured but due to uncertainties on the NO/NO_2 conversion within the sampling system, only measured NO_x emissions are reported in this study. However, it should be noted that the measured NO_2 emissions were insignificant compared to the emissions of the NO. Consequently, the calculated mass fraction of the NO can be compared against the measured mass fraction of NO_x.
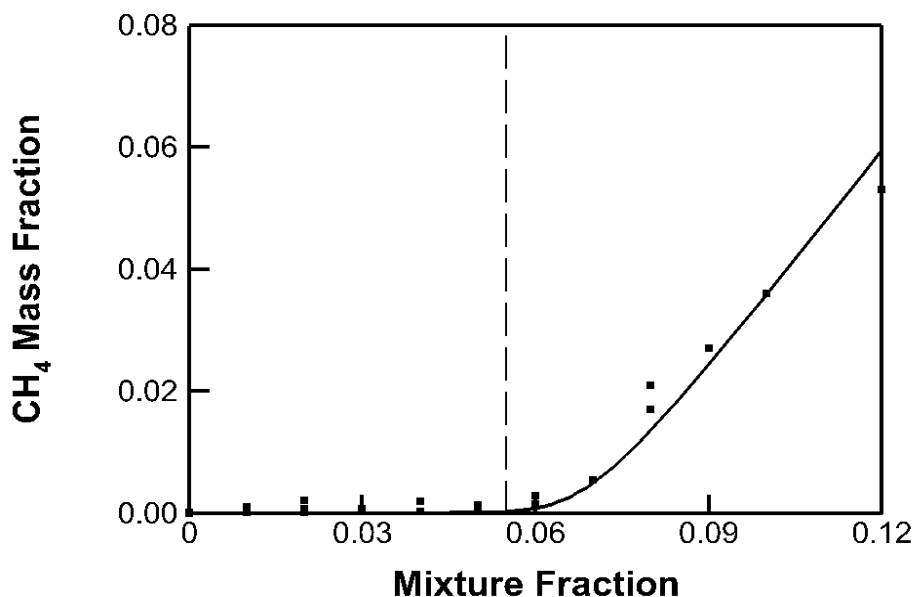
Figure 6-21 Measured mass fraction of THC (black symbols) and calculated mass fraction of CH$_4$ (black solid line) as a function of the mixture fraction for the air case study. Dashed line represents the stoichiometric mixture fraction.
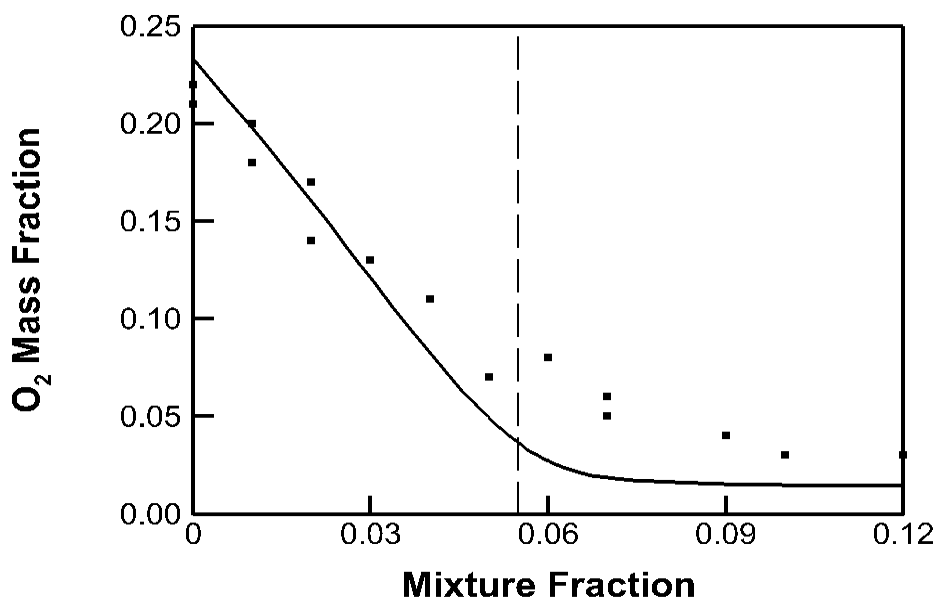
Figure 6-22 Measured mass fraction of O$_2$ (black symbols) and calculated mass fraction of O$_2$ (black solid line) as a function of the mixture fraction for the air case study. Dashed line represents the stoichiometric mixture fraction.

As explained in Section 5.3.2, most of the NO$_x$ emissions found within the flame zone of a turbulent diffusion flame is attributed to NO rather than NO$_2$ due to high flame temperatures. The formation of NO$_x$ species is a slow process due to the strong triple bond of N$_2$ molecule (thermal pathway) and the production of the CH species (prompt pathway) which occurs in fuel-rich regions and are a product of the fuel oxidation. It has been extensively discussed in Section 3.6 that the steady flamelet model cannot

predict accurately slow chemical processes since it assumes fast chemistry. It is concluded that a NO$_x$ model is needed to account for these species and in Fluent the NO$_x$ production is usually evaluated at a post-processing stage. Therefore, for the CO$_2$-diluted cases that follow, the NO profiles are not presented.
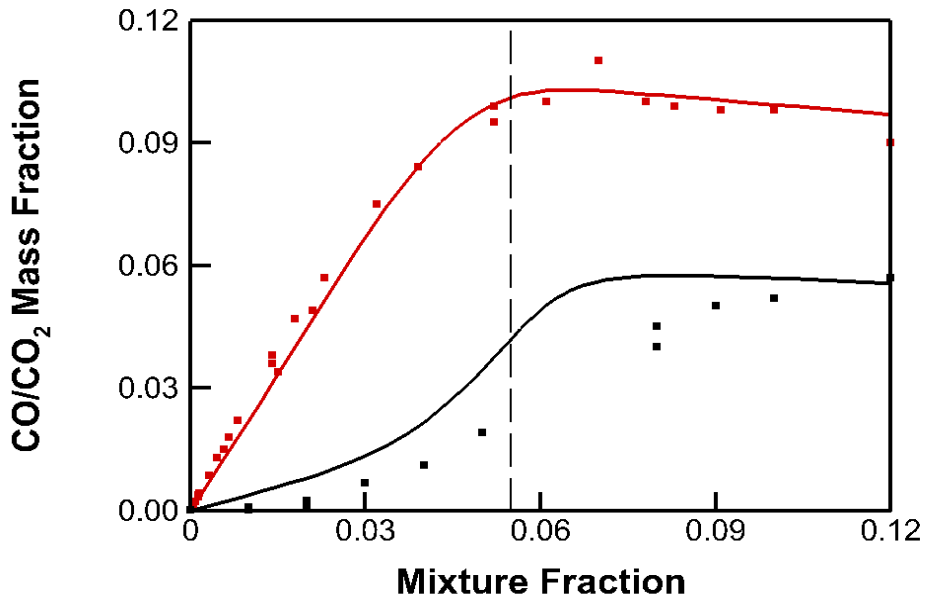
Figure 6-23 Measured mass fraction of CO$_2$ (red symbols) and of CO (black symbols). Calculated mass fraction of CO$_2$ (red sold line) and of CO (black solid line) as a function of the mixture fraction for the air case study. Dashed line represents the stoichiometric mixture fraction.
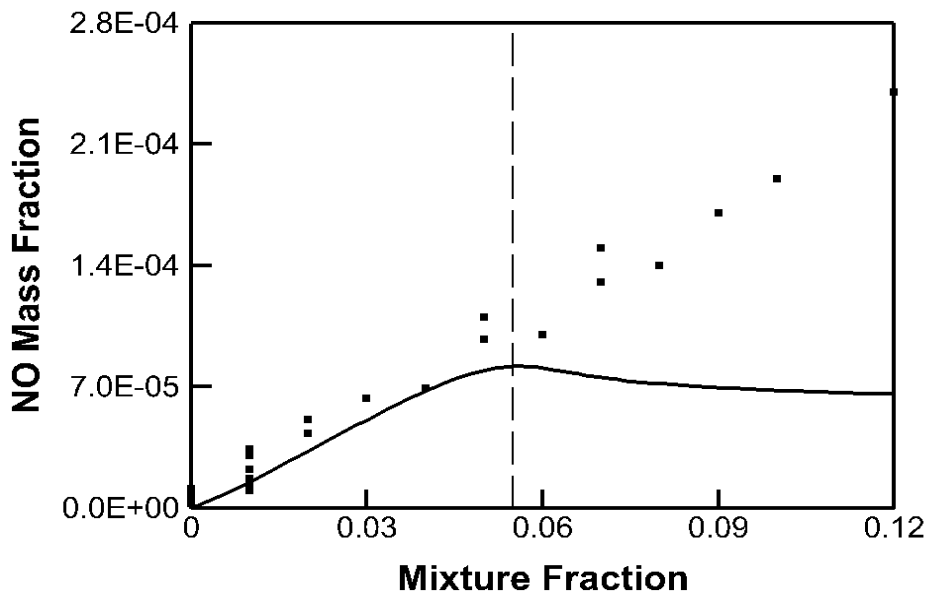
Figure 6-24 Measured mass fraction of NO$_x$ (black symbols) and calculated mass fraction of NO (black solid line) as a function of the mixture fraction for the air case study. Dashed line represents the stoichiometric mixture fraction.

6.3.2 CO$_2$-diluted case studies

Figures 6-25 to 6-26 depict the measured flame temperature and the calculated adiabatic temperature in the mixture fraction space for the 5 % and 10 % CO$_2$-diluted flames. Figures 6-27 to 6-32 illustrate the mass fractions of the major species (O$_2$, CH$_4$, CO, CO$_2$) in the mixture fraction space for the diluted flames. In all figures, the experimental data are represented by symbols whereas calculated data by solid lines. The best matched value for the scalar dissipation from the flamelet calculations is found to be $\chi_{st}= 9.4$ s^{-1} and 5 s^{-1} for the 5 % and 10 % CO$_2$-diluted flames, accordingly. As explained above, the NO mass fraction profile is not presented because there is a significant discrepancy between the numerical and the experimental data.

There is no doubt that a poor agreement between the measured and the calculated mass fractions and the temperature is observed. The shape of the profiles of the scalars illustrated in the mixture fraction space is predicted quite accurately however, the measured and calculated peak values are found at a different mixture fraction value. This discrepancy can be attributed due to the main limitation of the flamelet model that it assumes fast chemistry even under diluted combustion environments. The experimental results showed clearly that CO$_2$ slows down the fuel burning rate and the CO oxidation mechanism.
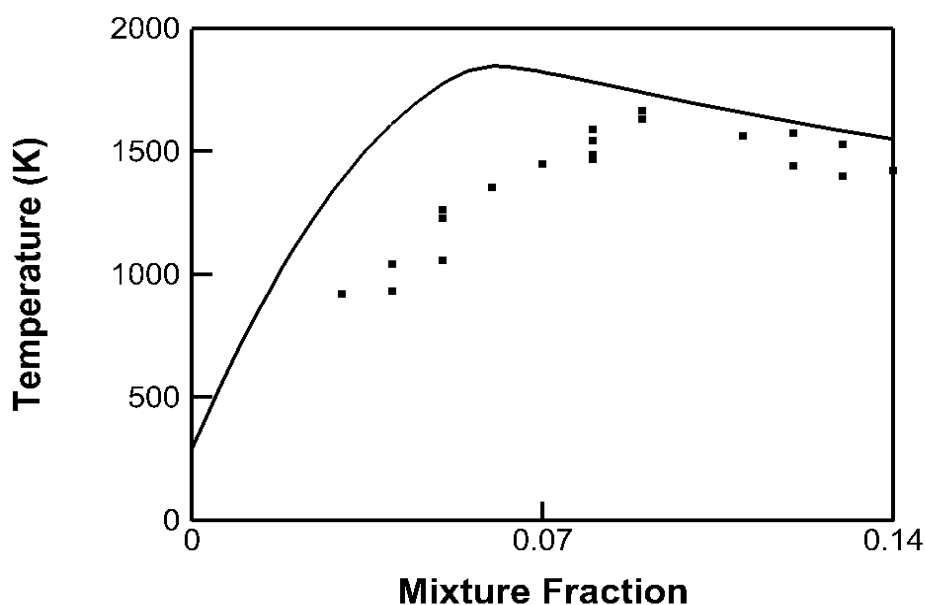
Figure 6-25 Radiation-corrected temperature experimental data (black symbols) and calculated adiabatic temperature (black solid line) as a function of the mixture fraction for the 5 % CO$_2$-diluted case study.
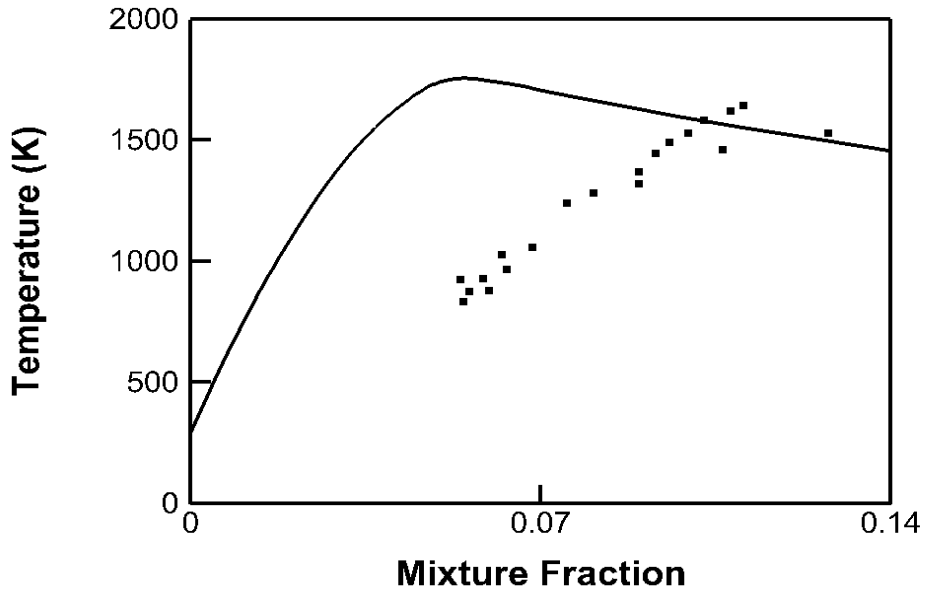
Figure 6-26 Radiation-corrected temperature experimental data (black symbols) and calculated adiabatic temperature (black solid line) as a function of the mixture fraction for the 10 % CO$_2$-diluted case study.
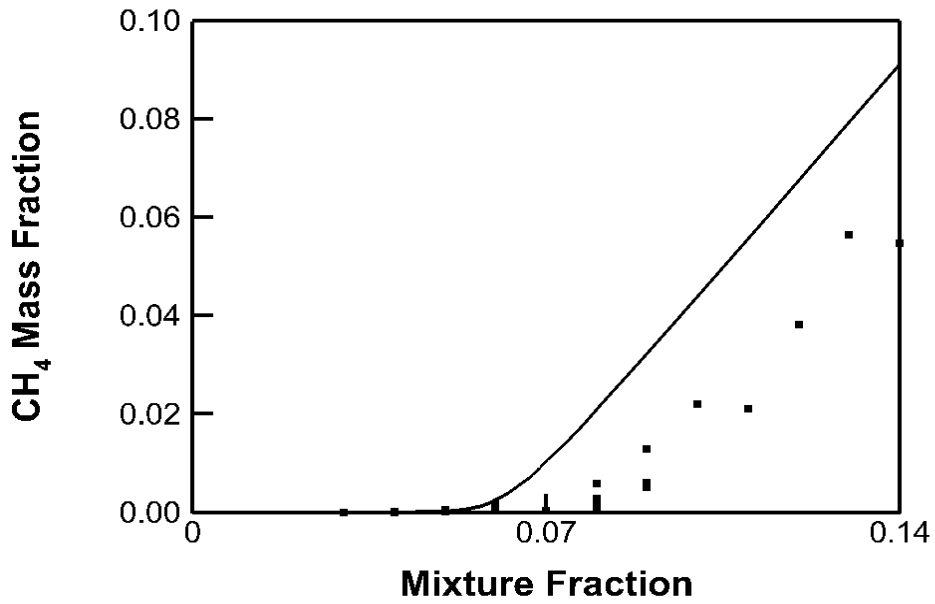
Figure 6-27 Measured mass fraction of THC (black symbols) and calculated mass fraction of CH$_4$ (black solid line) as a function of the mixture fraction for the 5 % CO$_2$-diluted case study.
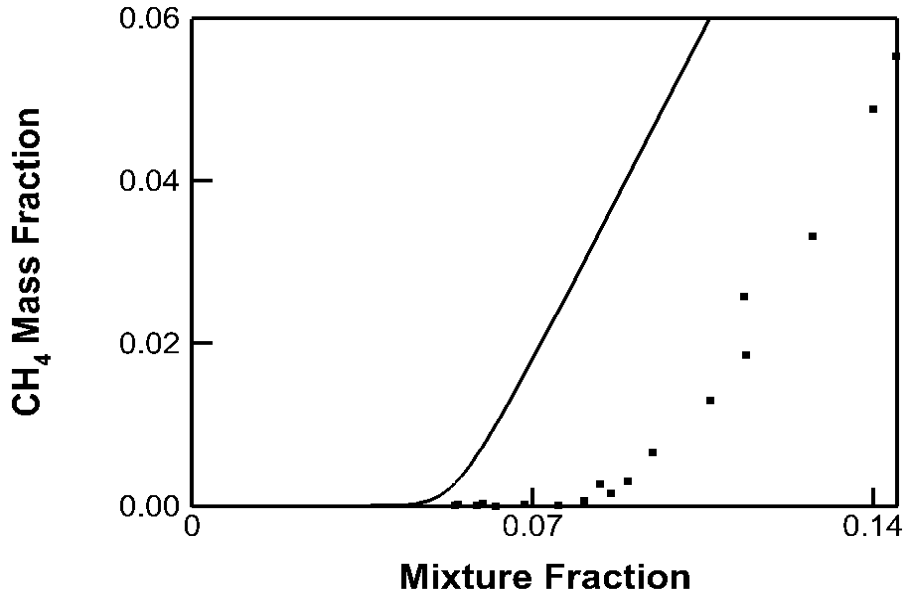
Figure 6-28 Measured mass fraction of THC (black symbols) and calculated mass fraction of CH$_4$ (black solid line) as a function of the mixture fraction for the 10 % CO$_2$-diluted case study.
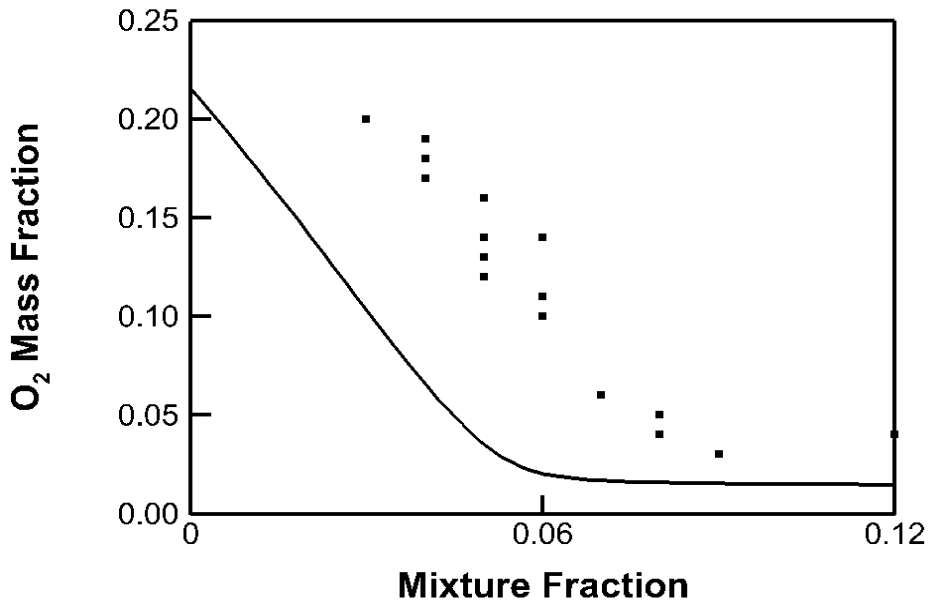
Figure 6-29 Measured mass fraction of O$_2$ (black symbols) and calculated mass fraction of O$_2$ (black solid line) as a function of the mixture fraction for the 5 % CO$_2$-diluted case study.
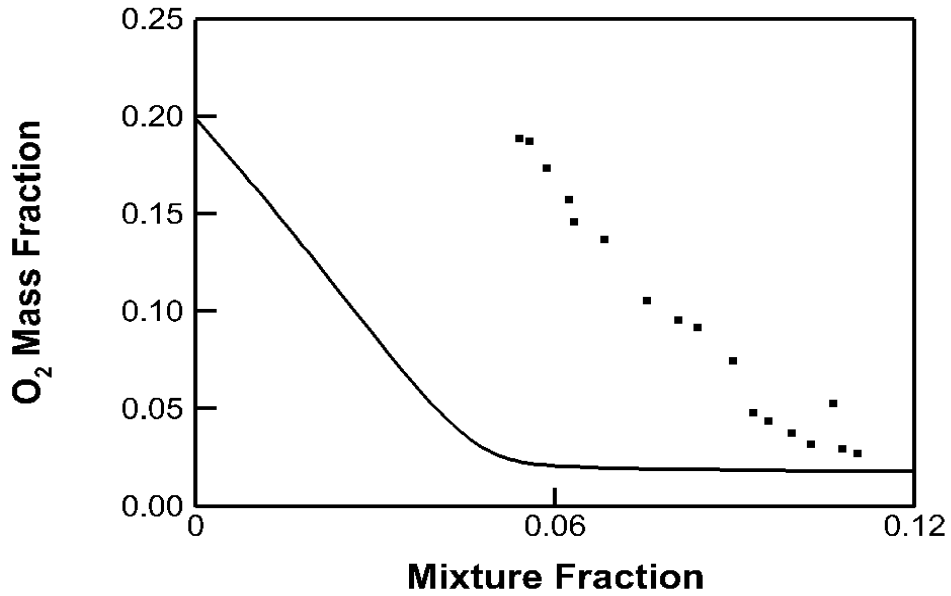
Figure 6-30 Measured mass fraction of O_2 (black symbols) and calculated mass fraction of O_2 (black solid line) as a function of the mixture fraction for the 10 % CO_2-diluted case study.
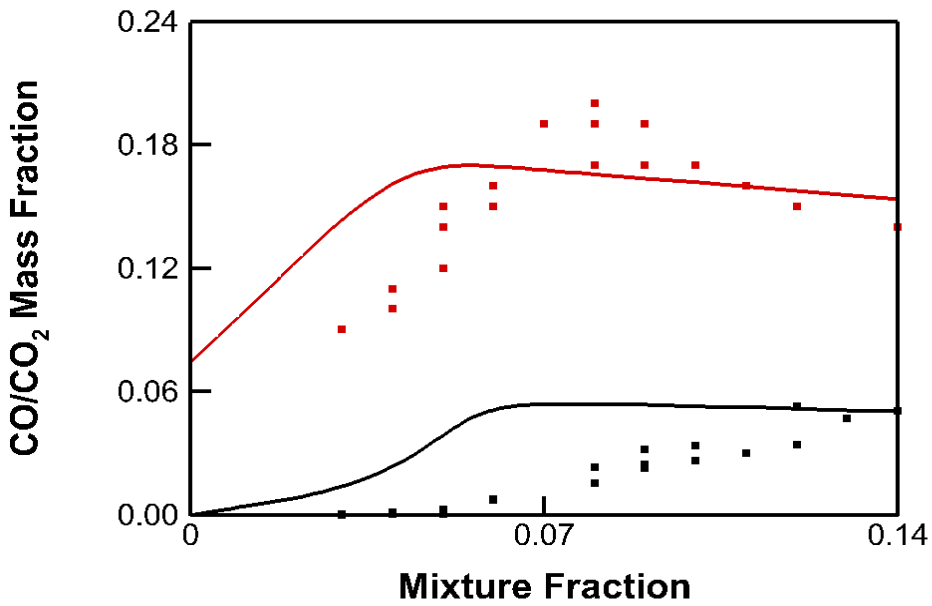
Figure 6-31 Measured mass fraction of CO_2 (red symbols) and of CO (black symbols). Calculated mass fraction of CO_2 (red sold line) and of CO (black solid line) as a function of the mixture fraction for the 5 % CO_2-diluted case study.
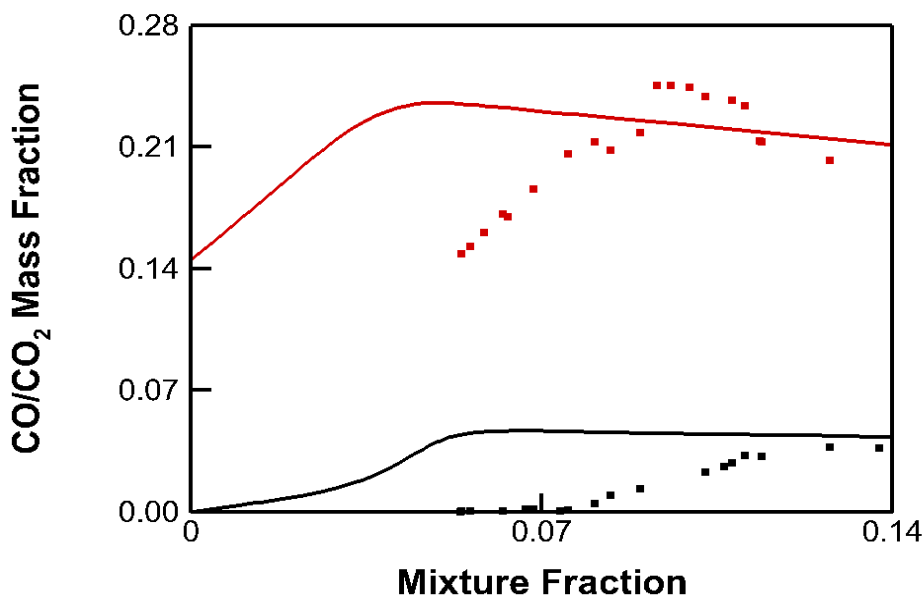
Figure 6-32 Measured mass fraction of CO$_2$ (red symbols) and of CO (black symbols). Calculated mass fraction of CO$_2$ (red sold line) and of CO (black solid line) as a function of the mixture fraction for the 10 % CO$_2$-diluted case study.

6.4 Conclusions

A detailed study using the steady laminar flamelet model has been performed in order to evaluate the performance of the numerical model with respect to predicting the changes in flame composition and chemistry when CO$_2$ is added to the oxidiser stream. A simple 1D numerical model, based on the configuration of counter-flow diffusion flames, is used together with a detailed kinetic mechanism to describe the complexity of the combustion chemistry and its interaction with turbulence. The calculated flame temperature and species concentration are obtained through fast flamelet calculations. The results are stored in tables and can be used when modeling gaseous combustion systems to reduce the amount of computational time required for including complex chemical kinetic mechanisms.

The study concluded that the flamelet model works well in predicting the characteristics of a turbulent flow field as found when varying the scalar dissipation parameter. Imposing different strain rates on the flamelets led to reduced combustion intensity; reduced flame temperature, increased fuel concentration and reduced concentration of the combustion products. The GRI-Mech 3.0 kinetic mechanism, which was incorporated into the model, includes all the necessary reactions for the methane oxidation process. However, other numerical studies have shown that it overpredicts the concentration of the CH species and as a result, it overpredicts the

prompt NO concentration. Therefore, it can be concluded that the numerical results for NO can be used only qualitatively.

The numerical results indicated that the thermal and chemical effects of adding CO_2 into the combustion air stream are quite well predicted. Due to dilution, reduced temperature peaks, increased mass fraction of CH_4 and reduced mass fraction of important fuel species, which are produced during fuel decomposition, were reported. These are indicators that the model can predict the impact of CO_2 dilution on the flame kinetics.

However, the comparison of the numerical with the experimental results concluded to the fact that the numerical predictions can only be used qualitatively and with caution as the model cannot predict accurately the NO_x and CO emissions under air combustion due to its assumption on fast chemistry. Good agreement was only achieved for the air combustion apart from the NO emissions but significant disagreement was observed for all species and temperature under CO_2-diluted combustion environment.

CHAPTER 7- General Conclusions and Future Work

7.1 General Conclusions

Chapter 1 presents the environmental issue caused by the increased atmospheric levels of the CO$_2$ emissions. Based on recent predictions on CO$_2$ emissions, it can be concluded that CCS will have to play a major role in controlling the GHG emissions in the short, and the medium, term to avoid the rise in the surface temperature above 2 °C. The contribution of this fundamental study is useful information about the implementation of CCS on existing and newly built power plants.

As shown in Chapter 2, a significant number of research studies have been conducted on assessing the impacts of EGR on the performance of the power and capture plants. These studies proved that the post-combustion process is one of the leading carbon capture technologies which, when combined with EGR, can lead to net reduction of the CO$_2$ emissions. Small-scale experiments have been performed utilising gas turbine combustors to reveal the impacts of adding CO$_2$ in the air stream on the exit pollutant emissions. However, the data collected in these studies are taken at the exit of the combustor or at the outlet of the gas turbine. There is a significant lack of experimental data for in-flame measurements. This study contributes significantly to the fundamental understanding of the effects of CO$_2$ on the flame chemistry and structure.

The focus of this study is the fundamental investigation of the dilution, thermal and chemical effects of adding CO$_2$ in the oxidiser stream on natural gas non-premixed flames. These effects are examined for two air equivalence ratios, $\Phi= 0.58$ and 0.75, at a constant Reynolds number, Re= 4725, as calculated for the cold fuel stream. The novelty of this study is that previous experimental studies were focused on the exit emissions of a combustion system whereas in this study, in-flame, post-flame and exit measurements of major and minor species, including trace species, and of the flame temperature are obtained utilising an in-house built combustion chamber. A detailed examination of the effects of the addition of CO$_2$ on the flame structure, flame stability, pollutant emissions and flame temperature of lab-scale diffusion flames is performed.

Two experimental campaigns, "Flame A", with $\Phi = 0.58$, and "Flame B", with $\Phi = 0.75$, revealed that CO_2 has an impact on the flame stability. For nearly lifted flames, the addition of CO_2 had an impact on the flame stabilisation point which was moved further downstream of the burner exit surface. The shift of the flame base is attributed to the difference in the heat capacity between CO_2 and N_2 as CO_2 absorbs more heat. In some industrial applications, lifted flames could be desired near the burner zone to protect the fuel nozzles from encountering high thermal load which could potentially lead to oxidation of the materials used. Therefore, flame instabilities may not be as important as the thermal and chemical effects of the addition of CO_2.

One of the observations from this study showed that the effects of adding CO_2 into the air stream is the reduced flame temperature. Carbon dioxide has different physical properties from oxygen and particularly nitrogen, the main component of air, and its higher heat capacity raises the total heat capacity of the oxidiser mixture. The experimental work in this study provides clear evidence that increasing the CO_2 dilution level from 5 % to 10 % reduces the flame volume temperature significantly although the variation in the exhaust temperature was insignificant. Consequently, the temperature has a major impact on the kinetics, particularly on the formation-destruction mechanism of the traces species. The temperature drop could have an impact on industrial applications by reducing the D-rating of the power generation systems. However, the change in the D-rating can be resolved by controlling the fuel input (varying the air-to-fuel ratio) which will influence in turn the exit temperature.

The experimental results of this study revealed that CO_2-enhanced combustion causes the reduction in the reaction rates of the fuel burning process and as a result, fuel oxidation will take a longer time. This reduction on the kinetic rates is a consequence of the temperature drop and the competition of CO_2 with the fuel molecules to react with radicals, such as OH, O and H. The current thesis supports similar reported studies that the CO_2 addition alters the oxidation pathways of methane which has successive implications on the formation of pollutant species. The formation of NO_x is also influenced by the added amount of CO_2 leading to a significant reduction in its concentration. The NO_x emissions are formed either via the thermal or the prompt pathway. The temperature drop inhibits the initiation step of the slow Zeldovich mechanism which affects the total NO_x emissions. As the current numerical study has shown, the reduction of the C_2H_2 emissions with increasing the CO_2 dilution level is directly related to the prompt NO formation mechanism as C_2H_2 is the main precursor

for HCN production. Furthermore, the reduced flame temperature has an impact on the prompt initiation step. Consequently, the NO$_x$ emissions are reduced remarkably with the CO$_2$ dilution of the air stream. It is expected that since the fuel burning process is influenced by the addition of CO$_2$, the CO emissions are increased. Early formation of CO is found due to the rapid reaction of the fuel with oxygen and its oxidation reaction to CO$_2$ depends strongly on the flame temperature and the residence time. The measured averaged exit concentration of the THC suggests that all the fuel is burnt and converted to products, to CO$_2$. Post-flame measurements indicated that the unburnt fuel mixture is oxidised quicker than CO whose concentration remained to be high at high axial locations above the burner exit surface. It can be concluded that the design of the combustor plays an important role on the CO oxidation process.

It is particularly interesting that increasing the equivalence ratio had a negative impact on the formation of pollutant species. As mentioned above, the flame temperature is a major parameter in the reaction rates. Higher temperatures promote the production of the NO$_x$ emissions but lower concentration of O$_2$ inhibits the oxidation of the CO emissions. Gas turbine combustors operate under fuel-lean conditions and most of the required excess air is used for cooling the exhaust gases. However, combustion takes place under fuel-lean or close to stoichiometry conditions and hence it is important to provide the lowest amount of combustion air needed to achieve complete oxidation of the fuel.

The numerical study performed in the current work aimed at evaluating the performance of a 1D model on predicting the formation of pollutant emissions and temperature under air and CO$_2$-diluted combustion conditions. The numerical results were compared with the experimental data presented in Chapter 5. It is concluded that a reasonably good agreement of the numerical and experimental data is achieved for the air flame with the exemption of NO$_x$ and CO species. However, it is evident that there is a discrepancy for the diluted cases. The major limitation of this numerical model is that it assumes fast chemistry and cannot predict the slow reaction rates imposed by dilution and the slow formation rate of NO$_x$ species. Therefore, complex combustion models are needed to account for the complex combustion chemistry and its interaction with turbulence.

Overall, this study clearly showed that the addition of CO$_2$ has an impact on the flame properties, flame volume and lift-off distance. However, it is clear that all these

parameters are manageable when this technique is employed as part of EGR in gas turbine combustors.

7.2   Future Work

This section addressees two aspects, namely, (i) suggestions for continuing the current study and (ii) suggestions of new topics of investigation that are driven by developments in the current project.

(i) (a) The results in this study are aimed at providing an understanding of the impact of the CO$_2$ dilution level on the stability and emissions of natural gas non-premixed flames. While both experimental campaigns provided valuable information, further work with the current experimental setup is needed over a wider range of test conditions. With minor modifications on the existing experimental setup, a range of different experimental techniques could be performed, as discussed later. The delivery pressure of the natural gas is about 21 mbar and thus utilising a low-pressure gas booster could assist in investigating higher fuel flow rates and the effect of turbulence on the flame structure and emissions. Industrial gas turbine combustors operate in a high power load and high turbulent reactive flows are of major interest for the industry.

(i) (b) Initial testing was carried out with preheating the oxidiser mixture but due to a sudden breakdown in the air supply system, the heaters were burnt out. However, the replacement of the heaters is simple and straightforward and can produce a broad range of useful experimental data. Combustion with air at elevated inlet temperatures occurs in gas turbine systems and heat is recovered in every part of the system. In addition, when exhaust gas recirculation is applied, the inevitably elevated inlet temperatures are present. The higher the temperature of the oxidiser stream, the more the benefits from the combustion point of view. Flame stability is enhanced through better mixing of the fuel with the oxygen. In addition, the temperature is a crucial parameter for the flame chemistry and thus the rates of some elementary reaction steps are affected. These changes affect the flame structure, distribution of species and temperature across the flame length and affect in turn the formation of the pollutant emissions.

(i) (c) The current burner test rig can be connected to oxygen, nitrogen and carbon dioxide supply lines, thus allowing for blending the three gases and creating several compositions. This methodology gives the opportunity to keep the amount of O$_2$ at 21 % in volume and replace only N$_2$ with CO$_2$. Furthermore, this setup can achieve a very

low O$_2$ concentration as required to sustain a stable flame. In this way, the lowest inlet achievable O$_2$ and the highest exit CO$_2$ concentrations can be investigated.

(i) (d) The combustion chamber was designed in a way that only minor modifications are needed to accommodate laser diagnostic techniques. A wide range of laser instrumentation can be used to investigate the velocity field of the current type of flames; LDV or PIV laser non-intrusive techniques are widely used in research studies. Velocity data can reveal the changes in the flame speed caused by the addition of CO$_2$. Studies have shown that CO$_2$ reduces the flame temperature and flame speed, thus leading to further reduced kinetic reaction rates and slower burning of the fuel. Consequently, the investigation of the velocity field is of increased importance. Moreover, laser techniques could be used to measure the concentration of important combustion radicals and minor species. As revealed, CO$_2$ chemical effects result in changes in the fuel oxidation mechanism. During combustion, important elementary chain branching reactions take place which are strongly affected by the addition of CO$_2$ in the oxidiser mixture. Therefore, planar laser-induced fluorescence (PLIF) would be required for measuring OH, NO and CH species. Additional knowledge on the distribution and concentration of minor species and radicals can give deeper insight into the complex flame chemistry.

(i) (e) Industrial type combustors can achieve complete combustion of the fuel by utilising swirl vanes, multiple fuel injection ports and the combination of non-premixed and partially premixed flames. During this study, an in-house built swirl nozzle was fabricated to investigate both jet and swirl-stabilised flames. However, the testing with the swirl nozzle was not completed but promising preliminary data were collected. Swirl-stabilised flames enhance the stability of the flame zone due to increasing the contact region between the fuel and oxidiser streams. Swirling flow fields are characterised by the presence of central and outer recirculation zones which help in flame stability by mixing hot combustion products with fresh reactants. However, their flow field is complicated and useful data can be extracted when using advanced research equipment, such as laser diagnostic instrumentation.

A few technically feasible suggestions on further work with the existing experimental setup and the available instrumentation were briefly discussed above. However, during the completion of this study, new research areas of investigation were found and presented below.

(ii) (a) The current experimental database is of great value for validating and developing CFD combustion models. Modeling gaseous combustion is a powerful tool as expensive experimental tests could be avoided. There is a need of combustion models which can account for the complex combustion chemistry, the turbulence characteristics of the flames, the interaction between chemistry and turbulence, and the radiation heat exchange between the flame and the surroundings and the soot particles.

(ii) (b) Finding ways to use an FTIR analyser within a flame zone could be proved valuable, similar to the use of laser diagnostic techniques. An FTIR system can measure simultaneously major and minor species apart from any diatomic molecules. A possible use of FTIR would be within the gas turbine combustor zone where fuel-lean conditions exist and possibly the spectrum would not be saturated.

(ii) (c) Considerable investment could be spent on expensive experimental setup to implement real exhaust gas recirculation. The two micro turbines at the Pilot-scale Advanced Capture Technology facilities in Sheffield could be utilised to simulate real EGR. An EGR system would emerge other challenges, such as added cooling requirements to prevent compressor issues. Furthermore, combining real EGR with the carbon capture plant at the PACT facilities would be an excellent research achievement. Finally, a real EGR system as combined with a chemical separation plant would also reveal challenges on the capture stage which would lead to the development of new separation methods.

BIBLIOGRAPHY

Amand, L.-E., Tullin, C.J. The Theory Behind FTIR Analysis—Application Examples From Measurement at the 12 MW Circulating Fluidized Bed Boiler at Chalmers, 1999, CECOST, Lund University.

ASTM International. 1993. *Manual on the Use of Thermocouples in Temperature Measurement.* Fourth edition. ASTM Manual Series: MNL 12 Revision of Special Technical Publication.

Barlow, R.S., Dibble, R.W., Stärner, S.H. and Bilger, R.W. 1990. Piloted Diffusion Flames of Nitrogen-diluted Methane near Extinction: OH measurements. *Symposium (International) on Combustion*. **23**(1), pp.583–589.

Barlow, R.S., Karpetis, A.N., Frank, J.H. and Chen, J.-Y. 2001. Scalar profiles and NO formation in laminar opposed-flow partially-premixed methane/air flames. *Combustion and Flame*. **127**(3), pp.2102–2118.

Baukal, J. and Charles, E. 2013. Chapter 13. Pollutant Emissions *In*: *Oxygen-Enhanced Combustion*. Industrial Combustion. Boca Raton, FL: CRC Press.

Bilger, R.W. and Beck, R.E. 1975. Further Experiments on Turbulent Jet Diffusion Flames *In*: *Symposium (International) on Combustion*. Fifteenth Symposium (International) on Combustion. pp. 541–552.

Bilger, R.W. 1976. Turbulent Jet Diffusion Flames. *Progress in Energy and Combustion Science*. **1**(2–3), pp.87–109.

Blevins, L. G., Pitts, W., Modeling of Bare and Aspirated Thermocouples in Compartment Fires, Fire and Safety Journal, Vol. 33, No. 4, 1999, pp. 239-259.

Bolland, O. and Mathieu, P. 1998. Comparison of Two CO2 Removal Options in Combined Cycle Power Plants. *Energy Conversion and Management*. **39**(16–18), pp.1653–1663.

Bolland, O. and Sæther, S. 1992. New Concepts for Natural Gas Fired Power Plants which Simplify the Recovery of Carbon Dioxide. *Energy Conversion and Management*. **33**(5–8), pp.467–475.

Borghi, R. 1988. Turbulent Combustion Modelling. *Progress in Energy and Combustion Science*. **14**(4). pp. 245–292.

Bowman, C.T. 1975. Kinetics of Pollutant Formation and Destruction in Combustion. *Progress in Energy and Combustion Science*. **1**(1). pp. 33–45.

Bowman, C.T. 1992. Control of Combustion-generated Nitrogen Oxide Emissions: Technology driven by Regulation *In*: *Symposium (International) on Combustion*. Twenty-Fourth Symposium on Combustion, pp. 859–878.

Boyce, M.P. 2012. Chapter 10- Combustors *In*: *Gas Turbine Engineering Handbook*. Waltham, Mass: Elsevier, pp. 427–490.

Bradley, D., Mathews, K. J., 1968, Measurement of High Gas Temperatures with Fine Wire Thermocouples, J. Mech. Engr. Science, Vol. 10, No. 4, pp. 299-305.

Broadwell, J.E., Dahm, W.J.A. and Mungal, M.G. 1984. Blowout of Turbulent Diffusion Flames *In*: *Symposium (International) on Combustion*. Twentieth Symposium (International) on Combustion, pp. 303–310.

British Petroleum. 2016. *BP Energy Outlook: 2016 edition*. BP p.l.c.

Burdet, A., Lachaux, T., de la Cruz García, M. and Winkler, D. 2010. Combustion under Flue Gas Recirculation Conditions in a Gas Turbine Lean Premix Burner. *ASME Turbo Expo 2010: Power for Land, Sea, and Air*. **2**(Combustion, Fuels and Emissions, Parts A and B), pp.1083–1091.

Burgess, C.P. and Lawn, C.J. 1999. The Premixture Model of Turbulent Burning to Describe Lifted Jet Flames. *Combustion and Flame*. **119**(1–2). pp. 95–108.

Catalanotti, E., 2011, Theoretical and Experimental Investigation of Alternative Aviation Fuels, Ph.D. thesis, University of Leeds.

Chen, R.-H. and Driscoll, J.F. 1989. The Role of the Recirculation Vortex in Improving Fuel-Air Mixing within Swirling Flames *In*: *Symposium (International) on Combustion*. Symposium (International) on Combustion. pp. 531–540.

Chen, R.-H. and Driscoll, J.F. 1991. Nitric Oxide Levels of Jet Diffusion Flames: Effects of Coaxial Air and Other Mixing Parameters *In*: *Symposium (International) on Combustion*. Twenty-Third Symposium (International) on Combustion. pp. 281–288.

Chen, L. and Ghoniem, A.F. 2014. Modeling CO2 Chemical Effects on CO Formation in Oxy-Fuel Diffusion Flames Using Detailed, Quasi-Global, and Global Reaction Mechanisms. *Combustion Science and Technology*. **186**(7), pp.829–848.

Cheng, T.S., Chao, Y.-C., Wu, D.-C., Yuan, T., Lu, C.-C., Cheng, C.-K. and Chang, J.-M. 1998. Effects of Fuel-Air Mixing on Flame Structures and NOx Emissions in Swirling Methane Jet Flames *In*: *Symposium (International) on Combustion*. Twenty-Seventh Symposium (International) on Combustion Volume 1. pp. 1229–1237.

Cheng, Z., Wehrmeyer, J.A. and Pitz, R.W. 2006. Experimental and Numerical Studies of Opposed Jet Oxygen-Enhanced Methane Diffusion Flames. *Combustion Science and Technology*. **178**(12), pp.2145–2163.

Chiappetta, L. and Colket, M.B. 1984. Design Considerations for Aerodynamically Quenching Gas Sampling Probes. *Journal of Heat Transfer*. **106**(2), p.460.

Chigier, N.A., Beér, J.M., Grecov, D. and Bassindale, K. 1970. Jet Flames in Rotating Flow Fields. *Combustion and Flame*. **14**(2). pp. 171–179.

Colket, M.B., Chiappetta, L., Guile, R.N., Zabielski, M.F. and Seery, D.J. 1982. Internal aerodynamics of gas sampling probes. *Combustion and Flame*. **44**(1–3), pp.3–14.

Colket, M.B., Zabielski, M.F., Chiappetta, L.J., Dodge, L.G. and Guile, R.N. 1980. *Nitric Oxide Measurement Study: Probe Methods, Volume II*. Washington, D.C.: U.S. Department of Transportation, Federal Aviation Administration. FAA report No. FAA-EE-80-29.

Correa, S.M. 1993. A Review of NOx Formation under Gas-Turbine Combustion Conditions. *Combustion Science and Technology*. **87**(1-6). pp. 329–362.

Dillon, D., Grace, D., Maxson, A., Børter, K., Augeli, J. n, Woodhouse, S. and Aspelund, G. 2013. Post-combustion Capture on Natural Gas Combined Cycle Plants: A Technical and Economical Evaluation of Retrofit, New Build, and the Application of Exhaust Gas Recycle. *Energy Procedia*. **37**, pp.2397–2405.

Ditaranto, M., Hals, J. and Bjørge, T. 2009. Investigation on the In-flame NO Reburning in Turbine Exhaust Gas. *Proceedings of the Combustion Institute*. **32**(2), pp.2659–2666.

Dixon-Lewis, G., David, T., Gaskell, P.H., Fukutani, S., Jinno, H., Miller, J.A., Kee, R.J., Smooke, M.D., Peters, N., Effelsberg, E., Warnatz, J. and Behrendt, F. 1984. Calculation of the Structure and Extinction Limit of a Methane-Air Counterflow Diffusion Flame in the Forward Stagnation Region of a Porous Cylinder. *Symposium (International) on Combustion*. **20**(1), pp.1893–1904.

Drake, M.C., Correa, S.M., Pitz, R.W., Shyy, W. and Fenimore, C.P. 1987. Superequilibrium and Thermal Nitric Oxide Formation in Turbulent Diffusion Flames. *Combustion and Flame*. **69**(3), pp.347–365.

Drake, M.C. and Blint, R.J. 1989. Thermal NOx in Stretched Laminar Opposed-flow Diffusion Flames with CO/H2/N2 fuel. *Combustion and Flame*. **76**(2), pp.151–167.

Drake, M.C. and Blint, R.J. 1991. Relative Importance of Nitric Oxide Formation Mechanisms in Laminar Opposed-flow Diffusion Flames. *Combustion and Flame*. **83**(1). pp. 185–203.

Driscoll, J.F., Chen, R.H., Tangirala, V. and Arbor, A. 1987. The Role of Recirculation in Improving Internal Mixing and Stability of Flames. AIAA 25th Aerospace Sciences Meeting. Reno, Nevada: American Institute of Aeronautics and Astronautics.

Driscoll, J.F., Chen, R.-H., Yoon, Y. 1992. Nitric Oxide Levels of Turbulent Jet Diffusion Flames: Effects of Residence Time and Damköhler Number. *Combustion and Flame*. **88**(1), pp.37–49.

Eickhoff, H., Lenze, B. and Leuckel, W. 1985. Experimental Investigation on the Stabilization Mechanism of Jet Diffusion Flames *In*: *Symposium (International) on Combustion*. Twentieth Symposium (International) on Combustion. pp. 311–318.

ElKady, A.M. 2005. *Experimental Investigation of Aerodynamics, Combustion, and Emissions Characteristics within the Primary Zone of a Gas Turbine Combustor*. PhD Thesis. University of Cincinnati.

ElKady, A.M., Evulet, A., Brand, A., Ursin, T.P. and Lynghjem, A. 2008. Exhaust Gas Recirculation in DLN F-Class Gas Turbines for Post-Combustion CO2 Capture *In*: *ASME Turbo Expo: Power for Land, Sea, and Air*. pp. 847–854.

ElKady, A.M., Evulet, A., Brand, A., Ursin, T.P. and Lynghjem, A. 2009. Application of Exhaust Gas Recirculation in a DLN F-Class Combustion System for Post-

combustion Carbon Capture. *Journal of Engineering for Gas Turbines and Power*. **131**(3). pp. 1-6.

ElKady, A.M., Brand, A.R., Vandervort, C.L. and Evulet, A.T. 2011. Exhaust Gas Recirculation Performance in Dry Low Emissions Combustors *In*: *ASME 2011 Turbo Expo: Turbine Technical Conference and Exposition*. pp. 1183–1192.

Evulet, A.T., ElKady, A.M., Branda, A.R. and Chinn, D. 2009. On the Performance and Operability of GE's Dry Low NOx Combustors utilizing Exhaust Gas Recirculation for Post Combustion Carbon Capture. *Energy Procedia*. **1**(1), pp.3809–3816.

Feikema, D., Chen, R.-H. and Driscoll, J.F. 1990. Enhancement of Flame Blowout Limits by the Use of Swirl. *Combustion and Flame*. **80**(2). pp. 183–195.

Fenimore, C.P. 1971. Formation of Nitric Oxide in Premixed Hydrocarbon Flames *In*: *Symposium (International) on Combustion*. Thirteenth Symposium (International) on Combustion. pp. 373–380.

Fristrom, R. M., Comments on Quenching Mechanisms in the Microprobe Sampling of Flames, Combustion and Flame, Vol. 50, No. 2, 1983, pp. 239-242

Gas Research Institute. 2000. GRI Mechanism version 3.0. Available from: http://combustion.berkeley.edu/gri-mech/.

Gasmet Technologies Oy, 2013, Instruction & Operating Manual, Gasmet Portable Sampling System, Finland

Giles, D.E., Som, S. and Aggarwal, S.K. 2006. NOx emission characteristics of counterflow syngas diffusion flames with airstream dilution. *Fuel*. **85**(12–13), pp.1729–1742.

Glassman, I. and Yetter, R.A. 2008. *Combustion.* Fourth edition. Amsterdam Boston: Academic Press.

Global CCS Institute. 2014. *The Global Status of CCS: 2014*. Melbourne, Australia.

Griffin, T., Bücker, D. and Pfeffer, A. 2008. Technology Options for Gas Turbine Power Generation with Reduced CO2 Emission. *Journal of Engineering for Gas Turbines and Power*. **130**(4), pp.041801-041801-8.

Griffin, T. and Mantzaras, I. 2009. Technologies for Gas Turbine Power Generation with CO2 Mitigation. Progress report, Swiss Electric Research.

Griffiths, J.F. and Barnard, J.A. 1995. *Flame and Combustion.* Third edition. London: Blackie Academic & Professional.

Goldin, G., Ren, Z., Forkel, H., Lu, L., Tangirala, V. and Karim, H. 2012. Modeling CO with Flamelet-Generated Manifolds: Part 1—Flamelet Configuration *In*: *Proceedings of ASME Turbo Expo 2012*. Copenhagen, Denmark, pp. 1141–1151.

Gollahalli, S.R. 1978. Aerodynamic and Diluent Effects on the Emission of Nitrogen Oxides from Hydrocarbon Diffusion Flames. *The Canadian Journal of Chemical Engineering*. **56**(4), pp.510–514.

Guethe, F., Stankovic, D., Genin, F., Syed, K. and Winkler, D. 2011. Flue Gas Recirculation of the Alstom Sequential Gas Turbine Combustor Tested at High Pressure *In*: *ASME 2011 Turbo Expo: Turbine Technical Conference and Exposition*, pp. 399–408.

Guo, H. and Smallwood, G.J. 2010. The Effect of Preferential Diffusion on Soot Formation in a Laminar Ethylene/air Diffusion Flame. *Combustion Theory and Modelling*. **15**(1), pp.125–140.

Gupta, A.K., Bolz, S. and Hasegawa, T. 1999. Effect of Air Preheat Temperature and Oxygen Concentration on Flame Structure and Emission. *Journal of Energy Resources Technology*. **121**(3), pp.209–216.

Hayhurst, A.N. and Vince, I.M. 1980. Nitric Oxide Formation from N2 in Flames: The Importance of 'prompt' NO. *Progress in Energy and Combustion Science*. **6**(1), pp.35–51.

Heitor, M. V., Moreira, A. L. N., 1993, Thermocouples and Sample Probes for Combustion Studies, Prog. Energy Combust. Sci., Vol. 19, pp. 259-278

Hottel, H.C. and Hawthorne, W.R. 1948. Diffusion in Laminar Flame Jets *In*: *Symposium on Combustion and Flame, and Explosion Phenomena*. Third Symposium on Combustion and Flame and Explosion Phenomena, pp. 254–266.

Howard, L. M., 1998, An Experimental Investigation of Oxygen-Enriched Methane Turbulent Diffusion Flames, PhD Thesis, University of Leeds.

Jansohn, P., Griffin, T., Mantzaras, I., Marechal, F. and Clemens, F. 2011. Technologies for Gas Turbine Power Generation with CO2 Mitigation. *Energy Procedia*. **4**. pp.1901–1908.

Ju, Y. and Niioka, T. 1997. Computation of NOx emission of a methane - air diffusion flame in a two-dimensional laminar jet with detailed chemistry. *Combustion Theory and Modelling*. **1**, pp.243–258.

IEAGHG. 2012. *CO₂ Capture at Gas Fired Power Plants*. [Online]. [Accessed 10 March 2016]. Available from: https://www.globalccsinstitute.com/publications/co2-capture-gas-fired-power-plants

International Energy Agency. 2013. *World Energy Outlook 2013*. IEA Publications.

IPCC 2013. Summary for Policymakers. In: Climate Change 2013: The Physical Science Basis. Contribution of Working Group I to the Fifth Assessment Report of the Intergovernmental Panel on Climate Change. Cambridge, United Kingdom and New York, NY, USA: Cambridge University Press.

Kaskan, W.E. 1957. The Dependence of Flame Temperature on Mass Burning Velocity *In*: *Symposium (International) on Combustion*. Sixth Symposium (International) on Combustion, pp. 134–143.

Kelman, J.B., Eltobaji, A.J. and Masri, A.R. 1998. Laser Imaging in the Stabilisation Region of Turbulent Lifted Flames. *Combustion Science and Technology*. **135**(1–6). pp. 117–134.

Kent, J.H. and Bilger, R.W. 1973. Turbulent Diffusion Flames *In*: *Symposium (International) on Combustion*. Fourteenth Symposium (International) on Combustion. pp. 615–625.

Kim, M.K., Won, S.H. and Chung, S.H. 2007. Effect of Velocity Gradient on Propagation Speed of Tribrachial Flames in Laminar Co-Flow Jets *In*: *Proceedings of the Combustion Institute*. pp. 901–908.

Ko, Y.S. and Chung, S.H. 1999. Propagation of Unsteady Tribrachial Flames in Laminar Non-Premixed Jets. *Combustion and Flame*. **118**(1–2). pp. 151–163.

Lawn, C.J. 2009. Lifted Flames on Fuel Jets in Co-Flowing Air. *Progress in Energy and Combustion Science*. **35**(1). pp. 1–30.

Lee, B.J. and Chung, S.H. 1997. Stabilization of Lifted Tribrachial Flames in a Laminar Non-Premixed Jet. *Combustion and Flame*. **109**(1–2). pp. 163–172.

Lee, C.E., Lee, S.R., Han, J.W. and Park, J. 2001. Numerical Study on Effect of CO2 Addition in Flame Structure and NOx Formation of CH4-Air Counterflow Diffusion Flames. *International Journal of Energy Research*. **25**(4), pp.343–354.

Lee, C.E., Oh, C.B. and Kim, J.H. 2004. Numerical and Experimental Investigations of the NOx Emission Characteristics of CH4-Air Co-flow Jet Flames. *Fuel*. **83**(17–18), pp.2323–2334.

Lefebvre, A.H. and Ballal, D.R. 2010. *Gas Turbine Combustion. Alternative Fuels and Emissions* Third edition. Boca Raton London New York: Taylor & Francis.

Lewis, B., Pease, R.N. and Taylor, H.S. 1956. *High-speed aerodynamics and jet propulsion. Combustion processes*. London: Oxford University Press.

Li, H., Haugen, G., Ditaranto, M., Berstad, D. and Jordal, K. 2011a. Impacts of Exhaust Gas Recirculation (EGR) on the Natural Gas Combined Cycle Integrated with Chemical Absorption CO2 Capture Technology. *Energy Procedia*. **4**, pp.1411–1418.

Li, H., Ditaranto, M. and Berstad, D. 2011b. Technologies for Increasing CO2 Concentration in Exhaust Gas from Natural Gas-fired Power Production with Post-combustion, Amine-based CO2 Capture. *Energy*. **36**(2), pp.1124–1133.

Li, S.C. and Williams, F.A. 1999. NOx Formation in two-stage Methane–Air Flames. *Combustion and Flame*. **118**(3), pp.399–414.

Liew, S.K., Bray, K.N.C. and Moss, J.B. 1984. A Stretched Laminar Flamelet Model of Turbulent Non-premixed Combustion. *Combustion and Flame*. **56**(2), pp.199–213.

Lim, J., Gore, J. and Viskanta, R. 2000. A Study of the Effects of Air Preheat on the Structure of Methane/air Counterflow Diffusion Flames. *Combustion and Flame*. **121**(1–2), pp.262–274.

Liu, F., Guo, H., Smallwood, G.J. and Gülder, Ö.L. 2001. The Chemical Effects of Carbon Dioxide as an Additive in an Ethylene Diffusion Flame: Implications for Soot and NOx Formation. *Combustion and Flame*. **125**(1–2). pp. 778–787.

Liu, F., Guo, H. and Smallwood, G.J. 2003. The Chemical Effect of CO_2 Replacement of N_2 in Air on the Burning Velocity of CH_4 and H_2 Premixed Flames. *Combustion and Flame*. **133**(4). pp. 495–497.

Lyons, K.M., Watson, K.A., Carter, C.D. and Donbar, J.M. 2005. On Flame Holes and Local Extinction in Lifted-jet Diffusion Flames. *Combustion and Flame*. **142**(3). pp. 308–313.

Lyons, K.M. 2007. Toward an Understanding of the Stabilisation Mechanisms of Lifted Turbulent Jet Flames: Experiments. *Progress in Energy and Combustion Science*. **33**(2). pp. 211–231.

Marran, D., Kenny, P. Markham, J., Jalbert, P., Moyers, R., Gardner, D., The Application of FT-IR Spectroscopy to Turbine Engine Exhaust Measurement, Advanced Fuel Research, 2000, Arnold Engineering Development Center, 21st AIAA Advanced Measurement Technology Conference and Ground Testing Conference.

Marsh, R., Runyon, J., Giles, A., Morris, S., Pugh, D., Valera-Medina, A. and Bowen, P. 2017. Premixed Methane Oxy-combustion in Nitrogen and Carbon Dioxide Atmospheres: Measurement of Operating Limits, Flame Location and Emissions. Proceedings of the Combustion Institute. *Proceedings of the Combustion Institute*. **36**(3), pp.3949–3958.

Masri, A.R. and Bilger, R.W. 1985. Turbulent Diffusion Flames of Hydrocarbon Fuels Stabilised on a Bluff Body *In*: *Symposium (International) on Combustion*. Twentieth Symposium (International) on Combustion. pp. 319–326.

Masri, A.R. and Bilger, R.W. 1986. Turbulent Non-Premixed Flames of Hydrocarbon Fuels near Extinction: Mean Structure from Probe Measurements *In*: *Symposium (International) on Combustion*. Twenty-First Symposium (International on Combustion). pp. 1511–1520.

Masri, A.R., Bilger, R.W. and Dibble, R.W. 1988. Turbulent Non-Premixed Flames of Methane near Extinction: Mean Structure from Raman Measurements. *Combustion and Flame*. **71**(3), pp.245–266.

Masri, A.R., Dally, B.B., Barlow, R.S. and Carter, C.D. 1994. The Structure of the Recirculation Zone of a Bluff-body Combustor *In*: *Symposium (International) on*

Combustion. Twenty-Fifth Symposium (International) on Combustion. pp. 1301–1308.

Masri, A.R., Kelman, J.B. and Dally, B.B. 1998. The Instantaneous Spatial Structure of the Recirculation Zone in Bluff-Body Stabilised Flames *In*: *Symposium (International) on Combustion*. Twenty-Seventh Symposium (International) on Combustion Volume 1. pp. 1031–1038.

Masri, A.R., Kalt, P.A.M. and Barlow, R.S. 2004. The Compositional Structure of Swirl-stabilised Turbulent Non-Premixed Flames. *Combustion and Flame*. **137**(1–2), pp.1–37.

Mauss, F., Netzell, K. and Lehtiniemi, H. 2006. Aspects of Modeling Soot Formation in Turbulent Diffusion Flames. *Combustion Science and Technology*. **178**(10–11), pp.1871–1885.

Metcalfe, W.K., Burke, S.M., Ahmed, S.S. and Curran, H.J. 2013. A Hierarchical and Comparative Kinetic Modeling Study of C1- C2 Hydrocarbon and Oxygenated Fuels. *Int. J. Chem. Kinet.* **45**, pp.638–675.

Michaud, M.G., Westmoreland, P.R. and Feitelberg, A.S. 1992. Chemical Mechanisms of NOx Formation for Gas Turbine Conditions *In*: *Symposium (International) on Combustion*. Twenty-Fourth Symposium on Combustion. pp. 879–887.

Miller, J.A. and Bowman, C.T. 1989. Mechanism and Modeling of Nitrogen Chemistry in Combustion. *Progress in Energy and Combustion Science*. **15**(4). pp. 287–338.

Mletzko, J., Ehlers, S. and Kather, A. 2016. Comparison of Natural Gas Combined Cycle Power Plants with Post Combustion and Oxyfuel Technology at Different CO2 Capture Rates. *Energy Procedia*. **86**, pp.2–11.

Mullinger, P. and Jenkins, B. 2008. Chapter 10 - Emissions and Environmental Impact *In*: *Industrial and Process Furnaces*. Butterworth-Heinemann: Oxford, pp. 375–411.

Nilsen, V. and Kosály, G. 1999. Differential Diffusion in Turbulent Reacting Flows. *Combustion and Flame*. **117**(3), pp.493–513.

Nishioka, M., Nakagawa, S., Ishikawa, Y. and Takeno, T. 1994. NO Emission Characteristics of Methane-Air Double Flame. *Combustion and Flame*. **98**(1), pp.127–138.

Norton, T.S., Smyth, K.C., Miller, J.H. and Smooke, M.D. 1993. Comparison of Experimental and Computed Species Concentration and Temperature Profiles in Laminar, Two-Dimensional Methane/Air Diffusion Flames. *Combustion Science and Technology*. **90**(1–4), pp.1–34.

Park, J., Kim, S.-G., Lee, K.-M. and Kim, T.K. 2002. Chemical Effect of Diluents on Flame Structure and NO Emission Characteristic in Methane-Air Counterflow Diffusion Flame. *International Journal of Energy Research*. **26**(13), pp.1141–1160.

Peters, N. and Williams, F.A. 1983. Lift-off Characteristics of Turbulent Jet Diffusion Flames. *AIAA Journal*. **21**(3). pp. 423–429.

Peters, N. 1984. Laminar Diffusion Flamelet Models in Non-Premixed Turbulent Combustion. *Progress in Energy and Combustion Science*. **10**(3), pp.319–339.

Peters, N. 1986. Laminar Flamelet Concepts in Turbulent Combustion *In*: *Symposium (International) on Combustion*. Twenty-First Symposium (International) on Combustion. pp. 1231–1250.

Peters, N. 1997. Four Lectures on Turbulent Combustion. September 15-19, Institut für Technische Mechanik RWTH Aachen.

Phillips, H. 1965. Flame in a Buoyant Methane Layer *In*: *Symposium (International) on Combustion*. Tenth Symposium (International) on Combustion. pp. 1277–1283.

Pitts, W.M. 1988. Assessment of Theories for the Behaviour and Blowout of Lifted Turbulent Jet Diffusion Flames *In*: *Symposium (International) on Combustion*. pp. 809–816.

Plessing, T., Terhoeven, P., Peters, N. and Mansour, M.S. 1998. An Experimental and Numerical Study of a Laminar Triple Flame. *Combustion and Flame*. **115**(3). pp. 335–353.

Poinsot, T. and Veynante, D. 2005. *Theoretical and Numerical Combustion,* Second edition. R. T. Edwards, Inc.

Puri, I.K., Seshadri, K., Smooke, M.D. and Keyes, D.E. 1987. A Comparison between Numerical Calculations and Experimental Measurements of the Structure of a Counterflow Methane-Air Diffusion Flame. *Combustion Science and Technology*. **56**(1–3), pp.1–22.

Rogg, B., Behrendt, F. and Warnatz, J. 1986. Turbulent Non-premixed Combustion in Partially Premixed Diffusion Flamelets with Detailed Chemistry. *Symposium (International) on Combustion*. **21**(1), pp.1533–1541.

Røkke, P.E. and Hustad, J.E. 2005. Exhaust Gas Recirculation in Gas Turbines for Reduction of CO2 Emissions; Combustion Testing with Focus on Stability and Emissions. *International Journal of Thermodynamics*. **8**(4), pp.167–173.

Sander, F., Carroni, R., Rofka, S. and Benz, E. 2011. Flue Gas Recirculation in a Gas Turbine: Impact on Performance and Operational Behaviour *In*: *ASME Turbo Expo: Power for Land, Sea, and Air*. pp. 123–132.

Shaddix, C. R., 1999, Correcting Thermocouple Measurements for Radiation Loss: A Critical Review, Proceedings of the 33rd National Heat Transfer Conference, August 15-17, Albuquerque, New Mexico, American Society of Mechanical Engineers.

Shannon, K.S., B.W. Butler, 2003, A review of error associated with thermocouple temperature measurement in fire environments, 2nd International Wildland Fire Ecology and Fire Management Congress and 5th Symposium on Fire and Forest Meteorology, November 16-20, 2003, Orlando, FL.

Schefer, R.W., Namazian, M., Filtopoulos, E.E.J. and Kelly, J. 1994a. Temporal Evolution of Turbulence/Chemistry Interactions in Lifted, Turbulent-Jet Flames *In*: *Symposium (International) on Combustion*. Twenty-Fifth Symposium (International) on Combustion. pp. 1223–1231.

Schefer, R.W., Namazian, M. and Kelly, J. 1994b. Stabilization of Lifted Turbulent-Jet Flames. *Combustion and Flame*. **99**(1). pp. 75–86.

Seshadri, K., Mauß, F., Peters, N. and Warnatz, J. 1990. A Flamelet Calculation of Benzene Formation in Co-flowing Laminar Diffusion Flames. *Symposium (International) on Combustion*. **23**(1), pp.559–566.

Signal Group. 2002. 7000FM GFC IR Analyser Operating Manual. Surrey, England.

Signal Group. 2004. 3000HM Heated Total Hydrocarbon Analyser Operating Manual. Surrey, England.

Signal Group. 2008. 4000VMA Heated Non-Vacuum NOx Analyser Operating Manual. Surrey, England.

Signal Group. 2009. 7008MGA- 9000MGA Multi Gas Analyser Operating Manual. Surrey, England.

Smooke, M.D., Puri, I.K. and Seshadri, K. 1986. A Comparison Between Numerical Calculations and Experimental Measurements of the Structure of a Counterflow Diffusion Flame Burning Diluted Methane in Diluted Air *In*: *Symposium (International) on Combustion*. Twenty-First Symposium (International on Combustion). pp. 1783–1792.

Smyth, K.C., Miller, J.H., Dorfman, R.C., Mallard, W.G. and Santoro, R.J. 1985. Soot Inception in a Methane/air Diffusion Flame as Characterised by Detailed Species Profiles. *Combustion and Flame*. **62**(2), pp.157–181.

Smyth, K.C. 1996. NO Production and Destruction in a Methane/Air Diffusion Flame. *Combustion Science and Technology*. **115** (1-3). pp. 151–176.

Som, S., Ramírez, A.I., Hagerdorn, J., Saveliev, A. and Aggarwal, S.K. 2007. Effect of Strain Rate and Pressure on the Flame Structure and Emission Characteristics of Syngas Flames. *ASME. Turbo Expo: Power for Land, Sea, and Air*. **2:** Turbo Expo 2007, pp.829–838.

Su, L.K., Sun, O.S. and Mungal, M.G. 2006. Experimental Investigation of Stabilization Mechanisms in Turbulent, Lifted Jet Diffusion Flames. *Combustion and Flame*. **144**(3). pp. 494–512.

Svehla, R.A. 1962. *Estimated Viscosities and Thermal Conductivities of Gases at High Temperatures*. Cleveland, Ohio: Lewis Research Centre, National Aeronautics and Space Administration.

Takeno, T. and Nishioka, M. 1993. Species Conservation and Emission Indices for Flames described by Similarity Solutions. *Combustion and Flame*. **92**(4), pp.465–468.

Taylor, J.R. 1997. *An Introduction to Error Analysis* Second edition. Sausalito, California: University Science Books.

Turns, S.R. 1995. Understanding NOx Formation in Non-premixed Flames: Experiments and Modelling. *Progress in Energy and Combustion Science*. **21**(5). pp. 361–385.

Turns, S.R. 1996. *An Introduction to Combustion.* Third edition. New York: McGraw-Hill International Edition.

US Environmental Protection Agency 1998. *NOx- How Nitrogen Oxides Affect the Way We Live and Breathe*. EPA Report, EPA-456/F-98-005. Research Triangle Park, NC 27711.

Vanquickenborne, L. and van Tiggelen, A. 1966. The Stabilization Mechanism of Lifted Diffusion Flames. *Combustion and Flame*. **10**(1). pp. 59–69.

Veynante, D. and Vervisch, L. 2002. Turbulent Combustion Modeling. *Progress in Energy and Combustion Science*. **28**(3), pp.193–266.

Wang, H. and Chen, Y. 2005. Steady Flamelet Modelling of a Turbulent Non-premixed Flame considering Scalar Dissipation Rate Fluctuations. *Fluid Dynamics Research*. **37**(3), pp.133–153.

Warren, R.C. 1994. Design of Thermocouple Probes for Measurement of Rocket Exhaust Plume Temperatures. *NASA STI/Recon Technical Report N*. **95**, pp.1–40.

Westbrook, C.K. and Dryer, F.L. 1981. Chemical Kinetics and Modeling of Combustion Processes *In*: *Symposium (International) on Combustion*. Eighteenth Symposium (International) on Combustion. pp. 749–767.

Westbrook, C.K. and Dryer, F.L. 1984. Chemical Kinetic Modeling of Hydrocarbon Combustion. *Progress in Energy and Combustion Science*. **10**(1), pp.1–57.

Westenberg, A.A. and DeHaas, N. 1972. Steady-state Intermediate Concentrations and Rate Constants. Some HO_2 Results. *The Journal of Physical Chemistry*. **76**(11). pp. 1586–1593.

Williams, F.A. 1975. Recent Advances in Theoretical Descriptions of Turbulent Diffusion Flames *In*: *Turbulent Mixing in Nonreactive and Reactive Flows*. New York: Plenum Press, p. 189.

Whitaker, S., Forced convection heat transfer correlations for flow in pipes, past flat plates, single cylinders, single spheres, and for flow in packed beds and tube bundles, AIChE Journal, Vol. 18, No. 2, 1972, pp. 361-371

APPENDIX A- Development of Burner Design

Part of this study was to investigate swirl-stabilised flames and thus various designs of swirled vanes were attempted. In Figure Appendix A-1, various nozzle models are illustrated; the different design features were the vane angle (45° or 60°), the length of the vanes, which gave a total outer diameter of the nozzle off 60 or 80 mm, and the size of the bluff-body area (28 or 34.4 mm). All designs were manufactured using a 3D printer and tested without the combustion chamber (use of open flames). The design (h) showed better flame stability and thus it was used in the experiments. Figure Appendix A-2 is a photograph of the burner equipped with the swirl nozzle. When the combustion chamber was fabricated, initial testing of the swirl-stabilised flames revealed that a significant amount of soot is formed on the bluff-body area of the swirl nozzle. However, preheating the oxidiser stream reduced significantly the formation of soot which did not allow for sampling with the quartz probe as it was blocked. The preliminary results were promising however, the heaters were burnt out after a few tests were conducted and further testing with the swirl nozzle could not be completed. Furthermore, the gas sampling was made using the FTIR analyser and it was concluded that this gas analysis method was no longer possible for in-flame sampling as the sample spectra were saturated and neither adding more interference species on the species spectrum library nor manual peak fitting could resolve the issue.

(a)   (b)   (c)

(d)   (e)   (f)

(g)   (h)   (i)
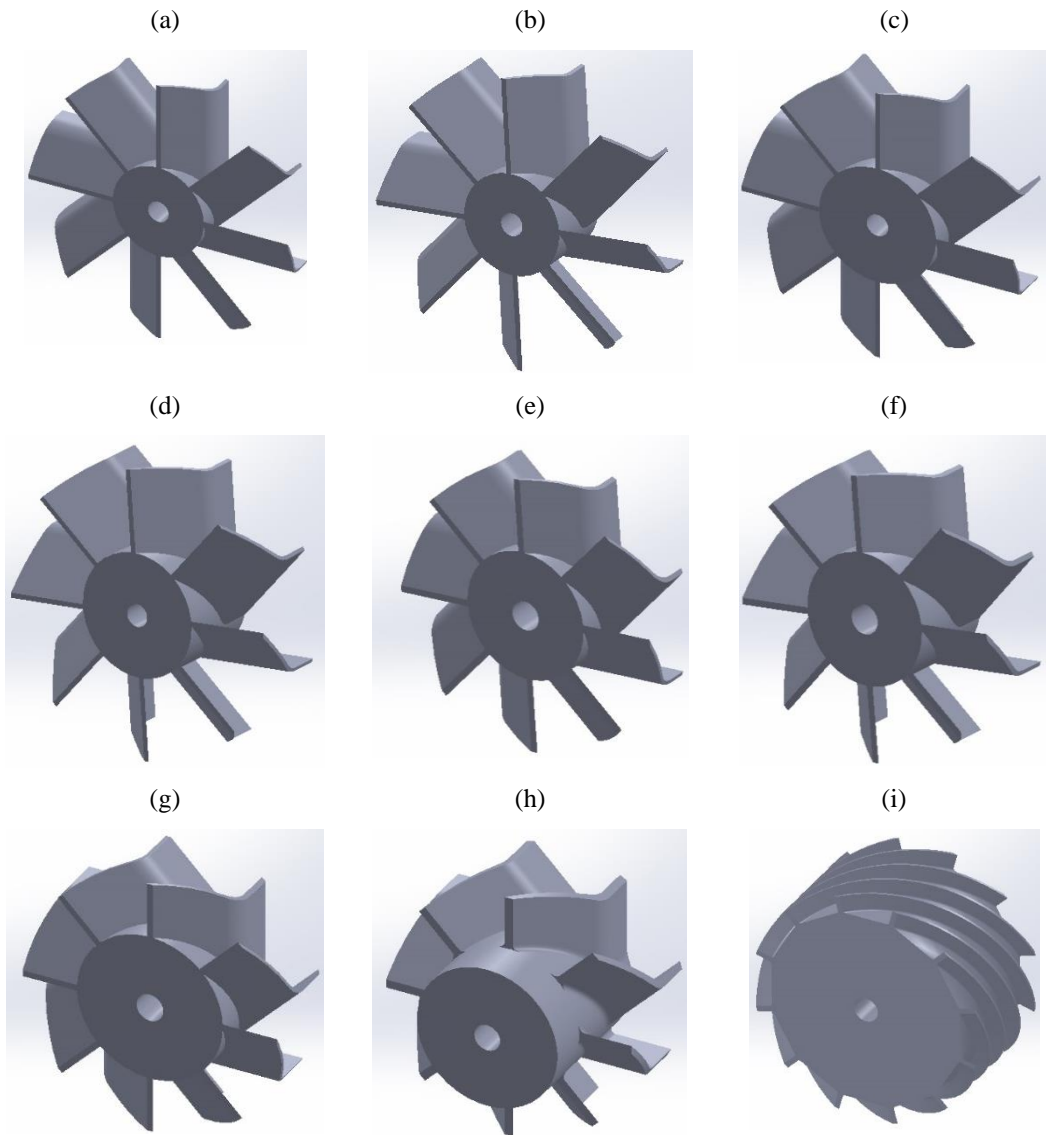
Figure Appendix A- 1 CAD Drawings of the swirl vanned nozzles.
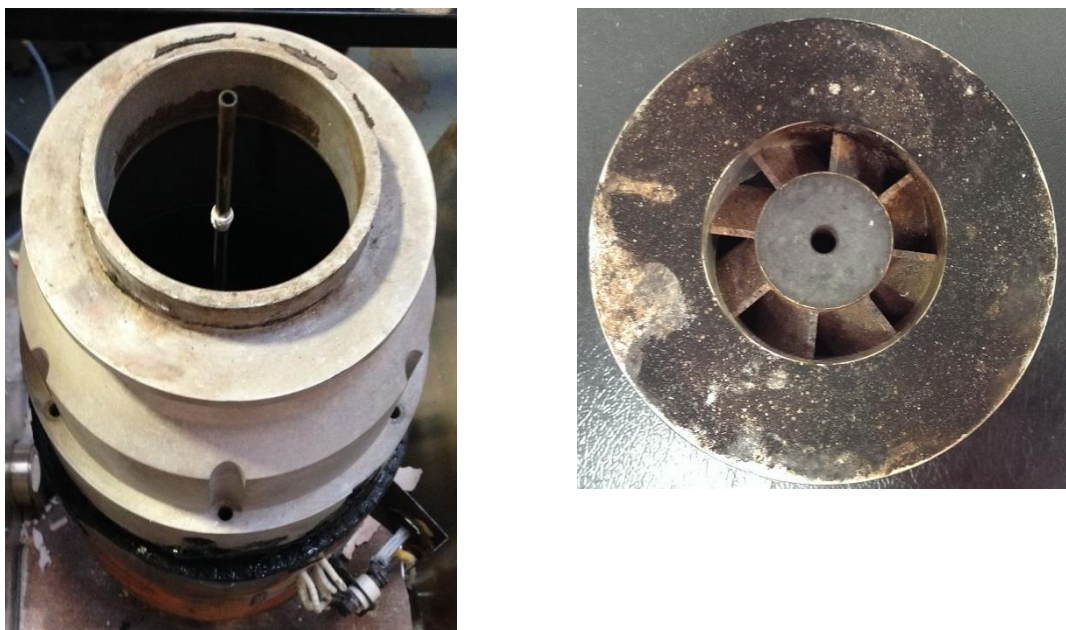
Figure Appendix A- 2 Photographs of the swirl nozzle as fitted into the burner body.

APPENDIX B- Development of Burner Test Rig

During this study, two combustion chambers were designed and tested due to a lack of important design features when it was initially designed. A brief description of the first design is presented below and the CAD drawings are shown in Figure Appendix B-1. This design of the in-house built combustion chamber was made of a combination of quartz glass windows for optical access and access for laser diagnostic techniques. The cross section of the chamber was square with an internal diameter off 340 mm and its height was 1.9 m. It was refractory lined inside (25 mm thick board made of refractory ceramic fibres) with an external high temperature layer of lagging for the operator's safety. The chamber was designed to accommodate gas sampling and temperature measurements inside the flame and at post-flame regions. High temperature silicone bungs are used for sealing the sampling ports. Any laser technique could be used as the chamber was designed with three quartz windows, one for the camera and the other two for the inlet and outlet of the laser light sheet. However, the design was poor in terms of gas tightness and significant air entrainment was observed during extensive testing. The major issues were identified at the assembly point of the chamber and the burner housing, at the top open end of the chamber and the welding method used for the sampling ports. Due to the poor installation of the chamber, neither it was not possible to quantify the air entrainment and correct accordingly the preliminary results nor any maintenance method proved successful in sealing the leaks. Therefore, it was determined to proceed to the second design as presented in Chapter 3.
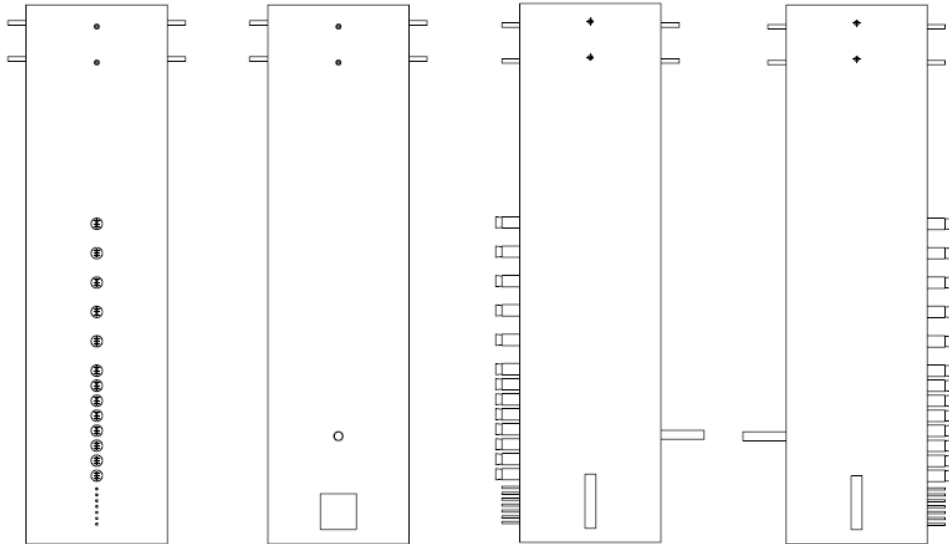
Figure Appendix B- 1 CAD Drawings of the initial design of the combustion chamber.

APPENDIX C- GRI-Mech 3.0 Kinetic Mechanism

All numerical calculations in Chapter 6 were carried out employing the GRI-Mech 3.0 mechanism to describe the chemical reactions taken into account (Gas Research Institute, 2000). The list of the reactions contained in this mechanism is as follows:

$2O + M \leftrightarrow O_2 + M$
$O + H + M \leftrightarrow OH + M$
$O + H_2 \leftrightarrow H + OH$
$O + HO_2 \leftrightarrow OH + O_2$
$O + H_2O_2 \leftrightarrow OH + HO_2$
$O + CH \leftrightarrow H + CO$
$O + CH_2 \leftrightarrow H + HCO$
$O + CH_{2(S)} \leftrightarrow H_2 + CO$
$O + CH_{2(S)} \leftrightarrow H + HCO$
$O + CH_3 \leftrightarrow H + CH_2O$
$O + CH_4 \leftrightarrow OH + CH_3$
$O + CO\ (+M) \leftrightarrow CO_2\ (+M)$
$O + HCO \leftrightarrow OH + CO$
$O + HCO \leftrightarrow H + CO_2$
$O + CH_2O \leftrightarrow OH + HCO$
$O + CH_2OH \leftrightarrow OH + CH_2O$
$O + CH_3O \leftrightarrow OH + CH_2O$
$O + CH_3OH \leftrightarrow OH + CH_2OH$
$O + CH_3OH \leftrightarrow OH + CH_3O$
$O + C_2H \leftrightarrow CH + CO$
$O + C_2H_2 \leftrightarrow H + HCCO$
$O + C_2H_2 \leftrightarrow OH + C_2H$
$O + C_2H_2 \leftrightarrow CO + CH_2$
$O + C_2H_3 \leftrightarrow H + CH_2CO$
$O + C_2H_4 \leftrightarrow CH_3 + HCO$
$O + C_2H_5 \leftrightarrow CH_3 + CH_2O$
$O + C_2H_6 \leftrightarrow OH + C_2H_5$
$O + HCCO \leftrightarrow H + 2CO$
$O + CH_2CO \leftrightarrow OH + HCCO$
$O + CH_2CO \leftrightarrow CH_2 + CO_2$
$O_2 + CO \leftrightarrow O + CO_2$
$O_2 + CH_2O \leftrightarrow HO_2 + HCO$
$H + O_2 + M \leftrightarrow HO_2 + M$
$H + 2O_2 \leftrightarrow HO_2 + O_2$
$H + O_2 + H_2O \leftrightarrow HO_2 + H_2O$
$H + O_2 + N_2 \leftrightarrow HO_2 + N_2$
$H + O_2 + AR \leftrightarrow HO_2 + AR$
$H + O_2 \leftrightarrow O + OH$
$2H + M \leftrightarrow H_2 + M$

$2H + H_2 \leftrightarrow 2H_2$

$2H + H_2O \leftrightarrow H_2 + H_2O$

$2H + CO_2 \leftrightarrow H_2 + CO_2$

$H + OH + M \leftrightarrow H_2O + M$

$H + HO_2 \leftrightarrow O + H_2O$

$H + HO_2 \leftrightarrow O_2 + H_2$

$H + HO_2 \leftrightarrow 2OH$

$H + H_2O_2 \leftrightarrow HO_2 + H_2$

$H + H_2O_2 \leftrightarrow OH + H_2O$

$H + CH \leftrightarrow C + H_2$

$H + CH_2 (+M) \leftrightarrow CH_3 (+M)$

$H + CH_{2(S)} \leftrightarrow CH + H_2$

$H + CH_3 (+M) \leftrightarrow CH_4 (+M)$

$H + CH_4 \leftrightarrow CH_3 + H_2$

$H + HCO (+M) \leftrightarrow CH_2O (+M)$

$H + HCO \leftrightarrow H_2 + CO$

$H + CH_2O (+M) \leftrightarrow CH_2OH (+M)$

$H + CH_2O (+M) \leftrightarrow CH_3O (+M)$

$H + CH_2O \leftrightarrow HCO + H_2$

$H + CH_2OH (+M) \leftrightarrow CH_3OH (+M)$

$H + CH_2OH \leftrightarrow H_2 + CH_2O$

$H + CH_2OH \leftrightarrow OH + CH_3$

$H + CH_2OH \leftrightarrow CH_{2(S)} + H_2O$

$H + CH_3O (+M) \leftrightarrow CH_3OH (+M)$

$H + CH_3O \leftrightarrow H + CH_2OH$

$H + CH_3O \leftrightarrow H_2 + CH_2O$

$H + CH_3O \leftrightarrow OH + CH_3$

$H + CH_3O \leftrightarrow CH_{2(S)} + H_2O$

$H + CH_3OH \leftrightarrow CH_2OH + H_2$

$H + CH_3OH \leftrightarrow CH_3O + H_2$

$H + C_2H (+M) \leftrightarrow C_2H_2 (+M)$

$H + C_2H (+M) \leftrightarrow C_2H_3 (+M)$

$H + C_2H_3(+M) \leftrightarrow C_2H_4 (+M)$

$H + C_2H_3 \leftrightarrow H_2 + C_2H_2$

$H + C_2H_4 (+M) \leftrightarrow C_2H_5 (+M)$

$H + C_2H_4 \leftrightarrow C_2H_3 + H_2$

$H + C_2H_5 (+M) \leftrightarrow C_2H_6 (+M)$

$H + C_2H_5 \leftrightarrow H_2 + C_2H_4$

$H + C_2H_6 \leftrightarrow C_2H_5 + H_2$

$H + HCCO \leftrightarrow CH_{2(S)} + CO$

$H + CH_2CO \leftrightarrow HCCO + H_2$

$H + CH_2CO \leftrightarrow CH_3 + CO$

$H + HCCOH \leftrightarrow H + CH_2CO$

$H_2 + CO (+M) \leftrightarrow CH_2O (+M)$

$OH + H_2 \leftrightarrow H + H_2O$

$2OH (+M) \leftrightarrow H_2O_2 (+M)$

$2OH \leftrightarrow O + H_2O$

$OH + HO_2 \leftrightarrow O_2 + H_2O$ DUPLICATE

$OH + H_2O_2 \leftrightarrow HO_2 + H_2O$ DUPLICATE

$OH + C \leftrightarrow H + CO$

$OH + CH \leftrightarrow H + HCO$

$OH + CH_2 \leftrightarrow H + CH_2O$

OH + CH$_2$ ↔ CH + H$_2$O
OH + CH$_{2(S)}$ ↔ H + CH$_2$O
OH + CH$_3$ (+M) ↔ CH$_3$OH (+M)
OH + CH$_3$ ↔ CH$_2$ + H$_2$O
OH + CH$_3$ ↔ CH$_{2(S)}$ + H$_2$O
OH + CH$_4$ ↔ CH$_3$ + H$_2$O
OH + CO ↔ H + CO$_2$
OH + HCO ↔ H$_2$O + CO
OH + CH$_2$O ↔ HCO + H$_2$O
OH + CH$_2$OH ↔ H$_2$O + CH$_2$O
OH + CH$_3$O ↔ H$_2$O + CH$_2$O
OH + CH$_3$OH ↔ CH$_2$OH + H$_2$O
OH + CH$_3$OH ↔ CH$_3$O + H$_2$O
OH + C$_2$H ↔ H + HCCO
OH + C$_2$H$_2$ ↔ H + CH$_2$CO
OH + C$_2$H$_2$ ↔ H + HCCOH
OH + C$_2$H$_2$ ↔ C$_2$H + H$_2$O
OH + C$_2$H$_2$ ↔ CH$_3$ + CO
OH + C$_2$H$_3$ ↔ H$_2$O + C$_2$H$_2$
OH + C$_2$H$_4$ ↔ C$_2$H$_3$ + H$_2$O
OH + C$_2$H$_6$ ↔ C$_2$H$_5$ + H$_2$O
OH + CH$_2$CO ↔ HCCO + H$_2$O
2HO$_2$ ↔ O$_2$ + H$_2$O$_2$ DUPLICATE
HO$_2$ + CH$_2$ ↔ OH + CH$_2$O
HO$_2$ + CH$_3$ ↔ O$_2$ + CH$_4$
HO$_2$ + CH$_3$ ↔ OH + CH$_3$O
HO$_2$ + CO ↔ OH + CO$_2$
HO$_2$ + CH$_2$O ↔ HCO + H$_2$O$_2$
C + O$_2$ ↔ O + CO
C + CH$_2$ ↔ H + C$_2$H
C + CH$_3$ ↔ H + C$_2$H$_2$
CH + O$_2$ ↔ O + HCO
CH + H$_2$ ↔ H + CH$_2$
CH + H$_2$O ↔ H + CH$_2$O
CH + CH$_2$ ↔ H + C$_2$H$_2$
CH + CH$_3$ ↔ H + C$_2$H$_3$
CH + CH$_4$ ↔ H + C$_2$H$_4$
CH + CO (+M) ↔ HCCO (+M)
CH + CO$_2$ ↔ HCO + CO
CH + CH$_2$O ↔ H + CH$_2$CO
CH + HCCO ↔ CO + C$_2$H$_2$
CH$_2$ + O$_2$ → OH + H + CO
CH$_2$ + H$_2$ ↔ H + CH$_3$
2CH$_2$ ↔ H$_2$ + C$_2$H$_2$
CH$_2$ + CH$_3$ ↔ H + C$_2$H$_4$
CH$_2$ + CH$_4$ ↔ 2CH$_3$
CH$_2$ + CO (+M) ↔ CH$_2$CO (+M)
CH$_2$ + HCCO ↔ C$_2$H$_3$ + CO
CH$_{2(S)}$ + N$_2$ ↔ CH$_2$ + N$_2$
CH$_{2(S)}$ + AR ↔ CH$_2$ + AR
CH$_{2(S)}$ + O$_2$ ↔ H + OH + CO
CH$_{2(S)}$ + O$_2$ ↔ CO + H$_2$O

$CH_{2(S)} + H_2 \leftrightarrow CH_3 + H$

$CH_{2(S)} + H_2O (+M) \leftrightarrow CH_3OH (+M)$

$CH_{2(S)} + H_2O \leftrightarrow CH_2 + H_2O$

$CH_{2(S)} + CH_3 \leftrightarrow H + C_2H_4$

$CH_{2(S)} + CH_4 \leftrightarrow 2CH_3$

$CH_{2(S)} + CO \leftrightarrow CH_2 + CO$

$CH_{2(S)} + CO_2 \leftrightarrow CH_2 + CO_2$

$CH_{2(S)} + CO_2 \leftrightarrow CO + CH_2O$

$CH_{2(S)} + C_2H_6 \leftrightarrow CH_3 + C_2H_5$

$CH_3 + O_2 \leftrightarrow O + CH_3O$

$CH_3 + O_2 \leftrightarrow OH + CH_2O$

$CH_3 + H_2O_2 \leftrightarrow HO_2 + CH_4$

$2CH_3 (+M) \leftrightarrow C_2H_6 (+M)$

$2CH_3 \leftrightarrow H + C_2H_5$

$CH_3 + HCO \leftrightarrow CH_4 + CO$

$CH_3 + CH_2O \leftrightarrow HCO + CH_4$

$CH_3 + CH_3OH \leftrightarrow CH_2OH + CH_4$

$CH_3 + CH_3OH \leftrightarrow CH_3O + CH_4$

$CH_3 + C_2H_4 \leftrightarrow C_2H_3 + CH_4$

$CH_3 + C_2H_6 \leftrightarrow C_2H_5 + CH_4$

$HCO + H_2O \leftrightarrow H + CO + H_2O$

$HCO + M \leftrightarrow H + CO + M$

$HCO + O_2 \leftrightarrow HO_2 + CO$

$CH_2OH + O_2 \leftrightarrow HO_2 + CH_2O$

$CH_3O + O_2 \leftrightarrow HO_2 + CH_2O$

$C_2H + O_2 \leftrightarrow HCO + CO$

$C_2H + H_2 \leftrightarrow H + C_2H_2$

$C_2H_3 + O_2 \leftrightarrow HCO + CH_2O$

$C_2H_4 (+M) \leftrightarrow H_2 + C_2H_2 (+M)$

$C_2H_5 + O_2 \leftrightarrow HO_2 + C_2H_4$

$HCCO + O_2 \leftrightarrow OH + 2CO$

$2HCCO \leftrightarrow 2CO + C_2H_2$

$N + NO \leftrightarrow N_2 + O$

$N + O_2 \leftrightarrow NO + O$

$N + OH \leftrightarrow NO + H$

$N_2O + O \leftrightarrow N_2 + O_2$

$N_2O + O \leftrightarrow 2NO$

$N_2O + H \leftrightarrow N_2 + OH$

$N_2O + OH \leftrightarrow N_2 + HO_2$

$N_2O (+M) \leftrightarrow N_2 + O (+M)$

$HO_2 + NO \leftrightarrow NO_2 + OH$

$NO + O + M \leftrightarrow NO_2 + M$

$NO_2 + O \leftrightarrow NO + O_2$

$NO_2 + H \leftrightarrow NO + OH$

$NH + O \leftrightarrow NO + H$

$NH + H \leftrightarrow N + H_2$

$NH + OH \leftrightarrow HNO + H$

$NH + OH \leftrightarrow N + H_2O$

$NH + O_2 \leftrightarrow HNO + O$

$NH + O_2 \leftrightarrow NO + OH$

$NH + N \leftrightarrow N_2 + H$

$NH + H_2O \leftrightarrow HNO + H_2$

NH + NO ↔ N$_2$ + OH
NH + NO ↔ N$_2$O + H
NH$_2$ + O ↔ OH + NH
NH$_2$ + O ↔ H + HNO
NH$_2$ + H ↔ NH + H$_2$
NH$_2$ + OH ↔ NH + H$_2$O
NNH ↔ N$_2$ + H
NNH + M ↔ N$_2$ + H + M
NNH + O$_2$ ↔ HO$_2$ + N$_2$
NNH + O ↔ OH + N$_2$
NNH + O ↔ NH + NO
NNH + H ↔ H$_2$ + N$_2$
NNH + OH ↔ H$_2$O + N$_2$
NNH + CH$_3$ ↔ CH$_4$ + N$_2$
H + NO + M ↔ HNO + M
HNO + O ↔ NO + OH
HNO + H ↔ H$_2$ + NO
HNO + OH ↔ NO + H$_2$O
HNO + O$_2$ ↔ HO$_2$ + NO
CN + O ↔ CO + N
CN + OH ↔ NCO + H
CN + H$_2$O ↔ HCN + OH
CN + O$_2$ ↔ NCO + O
CN + H2 ↔ HCN + H
NCO + O ↔ NO + CO
NCO + H ↔ NH + CO
NCO + OH ↔ NO + H + CO
NCO + N ↔ N$_2$ + CO
NCO + O$_2$ ↔ NO + CO$_2$
NCO + M ↔ N + CO + M
NCO + NO ↔ N$_2$O + CO
NCO + NO ↔ N$_2$ + CO$_2$
HCN + M ↔ H + CN + M
HCN + O ↔ NCO + H
HCN + O ↔ NH + CO
HCN + O ↔ CN + OH
HCN + OH ↔ HOCN + H
HCN + OH ↔ HNCO + H
HCN + OH ↔ NH$_2$ + CO
H + HCN (+M) ↔ H$_2$CN (+M)
H$_2$CN + N ↔ N$_2$ + CH$_2$
C + N$_2$ ↔ CN + N
CH + N$_2$ ↔ HCN + N
CH + N$_2$ (+M) ↔ HCNN (+M)
CH$_2$ + N$_2$ ↔ HCN + NH
CH$_{2(S)}$ + N$_2$ ↔ NH + HCN
C + NO ↔ CN + O
C + NO ↔ CO + N
CH + NO ↔ HCN + O
CH + NO ↔ H + NCO
CH + NO ↔ N + HCO
CH$_2$ + NO ↔ H + HNCO

$CH_2 + NO \leftrightarrow OH + HCN$

$CH_2 + NO \leftrightarrow H + HCNO$

$CH_{2(S)} + NO \leftrightarrow H + HNCO$

$CH_{2(S)} + NO \leftrightarrow OH + HCN$

$CH_{2(S)} + NO \leftrightarrow H + HCNO$

$CH_3 + NO \leftrightarrow HCN + H_2O$

$CH_3 + NO \leftrightarrow H_2CN + OH$

$HCNN + O \leftrightarrow CO + H + N_2$

$HCNN + O \leftrightarrow HCN + NO$

$HCNN + O_2 \leftrightarrow O + HCO + N_2$

$HCNN + OH \leftrightarrow H + HCO + N_2$

$HCNN + H \leftrightarrow CH_2 + N_2$

$HNCO + O \leftrightarrow NH + CO_2$

$HNCO + O \leftrightarrow HNO + CO$

$HNCO + O \leftrightarrow NCO + OH$

$HNCO + H \leftrightarrow NH_2 + CO$

$HNCO + H \leftrightarrow H_2 + NCO$

$HNCO + OH \leftrightarrow NCO + H_2O$

$HNCO + OH \leftrightarrow NH_2 + CO_2$

$HNCO + M \leftrightarrow NH + CO + M$

$HCNO + H \leftrightarrow H + HNCO$

$HCNO + H \leftrightarrow OH + HCN$

$HCNO + H \leftrightarrow NH_2 + CO$

$HOCN + H \leftrightarrow H + HNCO$

$HCCO + NO \leftrightarrow HCNO + CO$

$CH_3 + N \leftrightarrow H_2CN + H$

$CH_3 + N \leftrightarrow HCN + H_2$

$NH_3 + H \leftrightarrow NH_2 + H_2$

$NH_3 + OH \leftrightarrow NH_2 + H_2O$

$NH_3 + O \leftrightarrow NH_2 + OH$

$NH + CO_2 \leftrightarrow HNO + CO$

$CN + NO_2 \leftrightarrow NCO + NO$

$NCO + NO_2 \leftrightarrow N_2O + CO_2$

$N + CO_2 \leftrightarrow NO + CO$

$O + CH_3 \rightarrow H + H_2 + CO$

$O + C_2H_4 \leftrightarrow H + CH_2CHO$

$O + C_2H_5 \leftrightarrow H + CH_3CHO$

$OH + HO_2 \leftrightarrow O_2 + H_2O$ DUPLICATE

$OH + CH_3 \rightarrow H_2 + CH_2O$

$CH + H_2 (+M) \leftrightarrow CH_3 (+M)$

$CH_2 + O_2 \rightarrow 2H + CO_2$

$CH_2 + O_2 \leftrightarrow O + CH_2O$

$CH_2 + CH_2 \rightarrow 2H + C_2H_2$

$CH_{2(S)} + H_2O \rightarrow H_2 + CH2O$

$C_2H_3 + O_2 \leftrightarrow O + CH_2CHO$

$C_2H_3 + O_2 \leftrightarrow HO_2 + C_2H_2$

$O + CH_3CHO \leftrightarrow OH + CH_2CHO$

$O + CH_3CHO \rightarrow OH + CH_3 + CO$

$O_2 + CH_3CHO \rightarrow HO_2 + CH_3 + CO$

$H + CH_3CHO \leftrightarrow CH_2CHO + H_2$

$H + CH_3CHO \rightarrow CH_3 + H_2 + CO$

$OH + CH_3CHO \rightarrow CH_3 + H_2O + CO$

$HO_2 + CH_3CHO \rightarrow CH_3 + H_2O_2 + CO$

$CH_3 + CH_3CHO \rightarrow CH_3 + CH_4 + CO$

$H + CH_2CO \, (+M) \leftrightarrow CH_2CHO \, (+M)$

$O + CH_2CHO \rightarrow H + CH_2 + CO_2$

$O_2 + CH_2CHO \rightarrow OH + CO + CH_2O$

$O_2 + CH_2CHO \rightarrow OH + 2HCO$

$H + CH_2CHO \leftrightarrow CH_3 + HCO$

$H + CH_2CHO \leftrightarrow CH_2CO + H_2$

$OH + CH_2CHO \leftrightarrow H_2O + CH_2CO$

$OH + CH_2CHO \leftrightarrow HCO + CH_2OH$

$CH_3 + C_2H_5 \, (+M) \leftrightarrow C_3H_8 \, (+M)$

$O + C_3H_8 \leftrightarrow OH + C_3H_7$

$H + C_3H_8 \leftrightarrow C_3H_7 + H_2$

$OH + C_3H_8 \leftrightarrow C_3H_7 + H_2O$

$C_3H_7 + H_2O_2 \leftrightarrow HO_2 + C_3H_8$

$CH_3 + C_3H_8 \leftrightarrow C_3H_7 + CH_4$

$CH_3 + C_2H_4 \, (+M) \leftrightarrow C_3H_7 \, (+M)$

$O + C_3H_7 \leftrightarrow C_2H_5 + CH_2O$

$H + C_3H_7 \, (+M) \leftrightarrow C_3H_8 \, (+M)$

$H + C_3H_7 \leftrightarrow CH_3 + C_2H_5$

$OH + C_3H_7 \leftrightarrow C_2H_5 + CH_2OH$

$HO_2 + C_3H_7 \leftrightarrow O_2 + C_3H_8$

$HO_2 + C_3H_7 \rightarrow OH + C_2H_5 + CH_2O$

$CH_3 + C_3H_7 \leftrightarrow 2C_2H_5$

APPENDIX D- Radiation Heat Loss Calculations for the Sheathed Thermocouple Probe

The energy balance on the sheathed thermocouple probe is given as follows:

$$\dot{Q}_{conv} - \dot{Q}_{rad} = \rho \, C_p \, V \, \frac{\partial T_{TC}}{\partial t} \tag{D1}$$

where $\dot{Q}_{conv}$ is the convective heat gain, $\dot{Q}_{rad}$ is the radiation heat loss, ρ is the fluid density, C_p is the heat capacity of the fluid at constant pressure, V is the fluid volume, and T_{TC} is the measured thermocouple temperature. In steady state conditions, the time derivative becomes zero and as such, the energy balance may be recast as follows:

$$\dot{Q}_{conv} - \dot{Q}_{rad} = 0 \tag{D2}$$

where the convection heat gain and the radiation heat loss terms are defined as follows:

$$h_{conv} \, A_{conv} \, (T_g - T_{TC}) = \varepsilon \, \sigma \, A_{rad} \, (T_{TC}^4 - T_{surr}^4) \tag{D3}$$

and where h_{conv} is the convective heat transfer coefficient, A_{conv} is the surface area for convective heat transfer, T_g is the temperature of the hot gases, ε is the emissivity of the thermocouple probe, σ is the Stefan-Boltzmann constant, A_{rad} is the surface area of radiant body, T_{surr} is the temperature of the surroundings, which include the insulated bead of the sheathed probe. The convection-radiation temperature error is then given by:

$$\Delta T_{conv-rad} = T_g - T_{TC} \tag{D4}$$

Several approaches have been proposed for calculating the convective heat transfer coefficient, h_{conv}. For this purpose, the Nusselt number, Nu, is introduced and is defined as the ratio of the convective to conductive heat transfer across a boundary layer. The Nusselt number is calculated as follows:

$$Nu = \frac{h_{conv}\ D}{\lambda} \tag{D5}$$

where D is a characteristic length, e.g. diameter of the probe, and λ is the thermal conductivity of the fluid. We assume that the surface area of the radiant body, A_{rad}, can be considered to be equal to the surface area available for convection heat transfer, A_{conv}. For estimating the convective heat transfer coefficient, the following correlation between Nu and Re is used for cylinders, according to Kaskan (1957):

$$Nu = 0.8\ Re^{0.25} = 0.8\ \left(\frac{\rho\ D\ U}{\eta}\right)^{0.25} \tag{D6}$$

where U is the fluid velocity and η is the dynamic viscosity of the fluid at the measured temperature. Therefore, the convection heat coefficient is calculated as follows:

$$h_{conv} = \frac{0.8\ \lambda}{D^{0.75}}\ \left(\frac{\rho\ U}{\eta}\right)^{0.25} \tag{D7}$$

Consequently, the convection-radiation temperature error can be calculated as follows:

$$\Delta T_{conv\text{-}rad} = T_g - T_{TC} = \frac{\varepsilon\ \sigma}{h_{conv}}\ (T_{TC}^4 - T_{surr}^4) = \tag{D8}$$

$$\frac{1.25\ \varepsilon\ \sigma\ (T_{TC}^4 - T_{surr}^4)\ D^{0.75}}{\lambda}\ \left(\frac{\eta}{\rho\ U}\right)^{0.25}$$

Since $T_{TC} \gg T_{surr}$, the convection-radiation temperature error is simplified as follows:

$$\Delta T_{conv\text{-}rad} = \frac{1.25\ \varepsilon\ \sigma\ T_{TC}^4\ D^{0.75}}{\lambda}\ \left(\frac{\eta}{\rho\ U}\right)^{0.25} \tag{D9}$$

Finally, the temperature of the hot gases is calculated as follows:

$$T_g = T_{TC} + \Delta T_{conv\text{-}rad} \tag{D10}$$